Spatial organization of electric charges and discharge kinetics of nanofibers elaborated by electrospinning: application to the elaboration of 3D structured nanofibrous materials

Meng Liang

To cite this version:

Meng Liang. Spatial organization of electric charges and discharge kinetics of nanofibers elaborated by electrospinning: application to the elaboration of 3D structured nanofibrous materials. Physics [physics]. Université de Strasbourg, 2020. English. NNT: 2020STRAE002 . tel-03163063

HAL Id: tel-03163063
https://theses.hal.science/tel-03163063
Submitted on 9 Mar 2021

UNIVERSITÉ DE STRASBOURG

ÉCOLE DOCTORALE DE PHYSIQUE ET CHIMIE PHYSIQUE

Institut de Chimie et Procédés pour l'Énergie, l'Environnement et la Santé

(ICPEES – UMR 7515)

THÈSE présentée par :

Meng LIANG

soutenue le : **9 mars 2020**

pour obtenir le grade de : **Docteur de l'Université de Strasbourg**

Discipline/ Spécialité : Physique et chimie-physique

Spatial organization of electric charges and discharge kinetics of nanofibers elaborated by electrospinning: application to the elaboration of 3D structured nanofibrous materials

THÈSE dirigée par :

M. SCHLATTER Guy	Professeur des Universités, Université de Strasbourg

RAPPORTEURS :

M. BOSSARD Frédéric	Professeur des Universités, Université de Grenoble
M. DASCALESCU Lucian	Professeur des Universités, Université de Poitiers

---

AUTRES MEMBRES DU JURY :

Mme DRENCKHAN Wiebke	Directrice de Recherche au CNRS, ICS-UPR22 Strasbourg

Organisation spatiale des charges électriques et cinétique de décharge des nanofibres élaborées par electrospinning: Application à l'élaboration de matériaux nanofibreux structurés en 3D

Spatial organization of electric charges and discharge kinetics of nanofibers elaborated by electrospinning: application to the elaboration of 3D structured nanofibrous materials

Meng LIANG

Contents

PCL	polycaprolactone
PEO	polyethylene oxide
PVP	poly(vinylpyrrolidone)
PLA	polylactic acid
PGA	polyglycolic acid
PLGA	poly(lactic-co-glycolic acid)
PS	polystyrene
DMF	dimethylformamide
DW	deionized water
HA	hyaluronic acid
RH	relative humidity
PVDF–TrFE	Poly (vinylidene fluoride–co–trifluoroethylene)
PET	poly(ethylene terephthalate)
SEM	scanning electron microscope
TSC	using thermally stimulated current
PBT	poly(butylene terephthalate)
PVA	polyvinyl alcohol
PMMA	polymethyl methacrylate
TEBAC	benzyltriethylammonium chloride
DCM	dichloromethane
DMAC	dimethylacetamide

Résumé de la thèse

Introduction, contexte

L'electrospinning est un procédé permettant l'élaboration de matériaux nanofibreux sous l'action d'un champ électrostatique intense. Lors du procédé, une solution de polymère en régime semi-dilué enchevêtrée est acheminée vers une aiguille métallique soumise à un potentiel électrique élevé. Lorsque le champ électrique entre l'aiguille et une contre-électrode métallique reliée à la masse électrique, appelée collecteur, est suffisamment intense (i.e. de l'ordre de 1 kV/cm), un jet de la solution est éjecté violement en direction du collecteur. Lors du trajet entre l'aiguille et le collecteur, le jet est soumis à des instabilités électro-hydro-dynamiques résultant à des mouvements de fouets qui favorisent l'évaporation du solvant et la réduction du diamètre. Après un temps de vol de quelques ms, il se dépose ainsi sur le collecteur une nanofibre de polymère solide sous la forme d'une membrane non tissée. Par ailleurs, en baissant la concentration du polymère dans la solution mise en œuvre, le jet est assujetti à des ruptures conduisant finalement à un dépôt de microparticules : le procédé est alors appelé electrospraying. Au moment de la mise en contact avec le collecteur, la nanofibre chargée électriquement, se décharge graduellement. La cinétique de décharge électrique mais aussi la façon dont sont réparties les charges à la surface du matériau au cours du procédé conditionnent l'organisation et la structuration 3D finale de la membrane.

Le travail de cette thèse a consisté à mesurer les charges électriques portées par la nanofibre dans le cas de l'electrospinning et par les microparticules dans le cas de l'electrospraying. Puis, nous nous sommes intéressés à la répartition des charges électriques sur la membrane au cours de sa fabrication par electrospinning mais aussi à la cinétique de décharge une fois la nanofibre déposée. Cette étude a ensuite été appliquée pour élaborer, par electrospinning/electrospraying, des scaffolds nanofibreux avec une structure 3D contrôlée.

1. Mesure de la densité de charges électriques sur une nanofibre déposée par electrospinning et sur des particules produites par electrospraying

L'electrospinning est une méthode simple et rapide de production de nanofibres sous champ électrique qui a été largement utilisée dans divers domaines. Il a été rapporté que les charges sur les fibres jouent un rôle important pour contrôler la morphologie des fibres ainsi produites. Les charges électriques jouent aussi un rôle important lorsque l'on souhaite fabriquer des membranes avec une structure 3D contrôlée comme par exemple des membranes poreuses avec une taille de pores contrôlée. Enfin, la fabrication d'une membrane chargée électriquement forme un électret poreux qui trouve des applications dans le domaine de la filtration. C'est pourquoi, la mesure précise de la densité de charges portées par une nanofibre est une question importante. Traditionnellement, la densité de charge est obtenue par la mesure du courant électrique induit lors du dépôt de la nanofibre chargée. Toutefois, cette méthode ne permet pas d'évaluer la part des charges électriques qui restent à la surface de la nanofibre après son dépôt. Seules les charges évacuées vers la masse électriques sont quantifiée. Nous avons donc proposé une nouvelle méthode consistant à mesurer l'ensemble des charges portées par la nanofibre juste avant sa mise en contact avec le collecteur. Pour ce faire, un condensateur a été fixé entre un collecteur rotatif et la masse électrique afin de bloquer la dissipation des charges portées par la nanofibre vers la masse. Le potentiel de surface induit par les fibres déposées a été mesuré à l'aide d'un voltmètre électrostatique sans contact. Après avoir évalué la longueur de nanofibre déposée par unité de temps (cad la vitesse de formation des fibres V_f) par imagerie MEB d'échantillons prélevés à différents instants de production, la densité de charge linéique a pu finalement être déterminée. La méthode a également été appliquée pour obtenir la densité de charges de surface des microparticules pulvérisées par electrospraying.

L'effet des paramètres de procédés sur la densité de charge linéique a été étudié tout particulièrement dans le cas de l'élaboration d'une nanofibre de poly(acide lactique) (PLA). Les résultats ont montré que la densité de charge diminue lorsque l'on augmente la concentration de PLA dans la solution mise en œuvre. L'augmentation de la conductivité de la solution, quant à elle, augmente considérablement la densité de charge. L'augmentation de la tension appliquée à l'aiguille d'electrospinning entraîne une augmentation de la vitesse de formation V_f et par conséquent induit une diminution de la densité de charge linéique. Enfin, une augmentation de l'humidité relative de l'air ambiant conduit à l'augmentation de la densité de charge linéique. En ce qui concerne les microparticules produites par electrospraying, le polymère choisi a été le poly(ε-caprolactone) (PCL). Deux PCL ont été étudiés : l'un, ayant une masse molaire de 14 kg/mol permettant la production à haut débit de particules de petit diamètre (entre 1 et 3 μm) et l'autre, ayant une masse molaire de 80 kg/mol permettant de produire à plus faible débit des particules de gros diamètre (entre 10 et 25 μm). Ainsi, la densité de charge de surface a pu être mesurée en fonction du diamètre des particules. Il a été montré que la densité de charges de surface est plus élevée pour les particules produites avec le PCL de 80 kg/mol ce qui s'explique par un ratio surface/volume des particules plus faible que pour celles produites avec le PCL de 14 kg/mol.

2. Accumulation et dissipation des charges résiduelles portées par un scaffold fibreux pendant et après sa fabrication par electrospinning

Comme mentionné précédemment, la densité de charges portée par la nanofibre dépend du procédé et du diamètre de cette dernière. Au cours de la fabrication d'un scaffold fibreux, une partie des charges sont évacuées vers la masse du collecteur alors qu'une autre partie reste accumulée dans la membrane. La manière dont sont libérées et accumulées les charges électriques au sein de la membrane influence la structure de la membrane (porosité et taille des pores principalement) mais aussi l'efficacité de production. Enfin, la capacité qu'a un scaffold fibreux à maintenir dans le temps les charges électriques est une propriété importante lorsqu'on souhaite l'utiliser comme filtre à électret. Ainsi, nous avons étudié l'accumulation et la cinétique de dissipation du potentiel de surface induit par les charges lors du procédé d'electrospinning simple (i.e. avec un collecteur cylindrique lisse) pour deux types de polymères : le PLA et le poly(oxyde d'éthylène) (PEO).

Un montage expérimental original a été développé. Il a consisté à mesurer, en continu pendant l'electrospinning, le courant électrique induit par les charges électriques se dissipant vers la masse, d'une part, et le potentiel à la surface de la membrane résultant de l'accumulation des charges, d'autre part. Les résultats montrent que les fibres de PEO dissipent très rapidement leurs charges électriques : toutes les charges portées par le jet d'electrospinning sont évacuées quasi-instantanément. En ce qui concerne les fibres de PLA, des portions de fibres restent chargées, provoquant une augmentation continue du potentiel de surface dont la cinétique a été étudiée en fonction des paramètres de procédé.

Un modèle a été proposé dans le cadre de cette thèse afin de caractériser la cinétique de formation du potentiel de surface. Grâce au modèle, il a été montré que la mesure du potentiel de surface pendant l'electrospinning est caractérisée par un temps caractéristique τ qui peut être mis en relation avec les caractéristiques électriques aux différentes échelles : (i) le pore, (ii) la couche élémentaire ayant la surface de la membrane et l'épaisseur d'un pore et (iii) l'ensemble de la membrane en cours de construction. Il a été démontré qu'une loi d'échelle permet de prédire l'évolution du diamètre de la fibre en fonction de τ. L'étude de la décroissance du potentiel de surface après l'arrêt de l'électrospinning a montré l’existence de trois mécanismes de dissipation des charges. Une dissipation aux temps courts de l’ordre de quelques secondes se produit sur la surface supérieure de la membrane, puis une dissipation des charges aux temps moyens de l’ordre de plusieurs dizaines de secondes a été attribuée à la dissipation des au sein des pores de la membrane. Enfin, un mécanisme de dissipation aux temps longs de plusieurs centaines ou milliers de secondes a été attribué à la dissipation des charges piégées au cœur des fibres. La persistance des charges résiduelles, grâce en particulier, au ralentissement des mécanismes de dissipation aux temps moyens et longs les deuxième et troisième étapes, est importante pour la construction de membranes à structure contrôlée. Enfin, dans cette partie, il a été montré pour la première fois que la mesure du potentiel de surface, grâce à l'utilisation d'un voltmètre électrostatique, est une méthode simple donnant des informations précises sur la membrane à l'échelle locale du diamètre des pores et des fibres. Une telle méthode devrait permettre de détecter les variations de la morphologie poreuse des membranes au moment même de leur fabrication. De plus, en combinaison avec la mesure du courant, c'est une méthode efficace et complémentaire pour obtenir un suivi en ligne du procédé d’electrospinning.

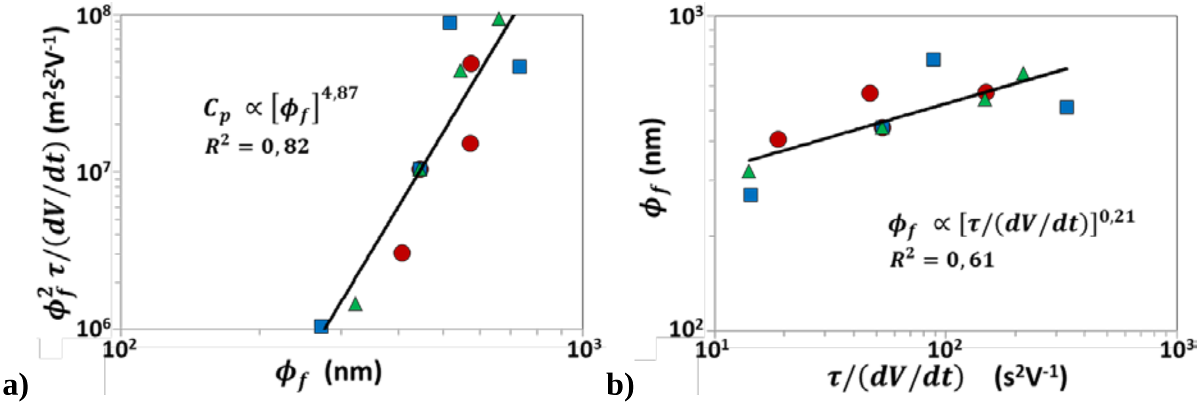

***Figure 1:** Loi d’échelle établie grâce à la corrélation des mesures expérimentales avec le modèle proposé. a) loi d’échelle entre la capacité moyenne des pores et le diamètre moyen des fibres. b) Loi d’échelle entre le diamètre moyen des fibres et le ratio entre le temps caractéristique τ et la dérivée temporelle du potentiel de surface.*

3. Potentiel de surface de fibres suspendues: application à la construction de scaffolds 3D structurés par electrospinning/electrospinning

Le procédé d’electrospinning conduit naturellement à la fabrication de scaffolds 3D avec une organisation pseudo-aléatoire des nanofibres. Bien que ce type de scaffolds montrent un très grand intérêt pour les applications biomédicales telle que l’ingénierie tissulaire, il serait très intéressant de pouvoir contrôler l’organisation fibreuse afin de mimer la structuration 3D de certains tissus comme par exemple le myocarde qui présente une structure hiérarchique avec des cellules fibreuses alignées noyées dans des structures 3D en nid d'abeilles formés par des fibres de collagène ondulés. Par ailleurs, l’electrospinning résulte à la fabrication de scaffolds fibreux avec une faible taille moyenne des pores de l’ordre de quelques microns qui ne permet pas d’assurer une colonisation cellulaire efficace.

Des travaux antérieurs effectués à l’ICPEES ont pourtant montré qu'en utilisant de manière synergique les procédés d’electrospinning et d’electrospraying avec un collecteur formé de protubérances dont la topographie est contrôlée, il est possible de construire des composites dont la structure peut être contrôlée en 2D et même en 3D. Il a été démontré que l’organisation 2D et 3D des nanofibres est régie par la distribution des charges électriques accumulées à la surface du matériau lors de sa fabrication par dépôt alterné de nanofibres par electrospinning et de microparticules par electrospraying. Cette distribution contrôlée de charges électriques, appelée « template électrostatique », est composée d’une part, de zones répulsives dues aux portions de fibres suspendues chargées entre les protubérances du collecteur et, d’autre part, de zones attractives dues aux segments de fibres en contact direct avec les protubérances. Lorsque le « template électrostatique » est bien formé, les microparticules chargées se déposent sélectivement et uniquement sur les zones attractives maintenant ainsi le contact électrique avec les protubérances du collecteur et permettant même lorsque la quantité de microparticules est suffisante de construire de nouvelles protubérances localisées juste au-dessus de celles du collecteur permettant ainsi de redessiner sa topographie. La fabrication de scaffolds structurés en 3D peut alors être assurée par des dépôts successifs et alternés de nanofibres et de microparticules.

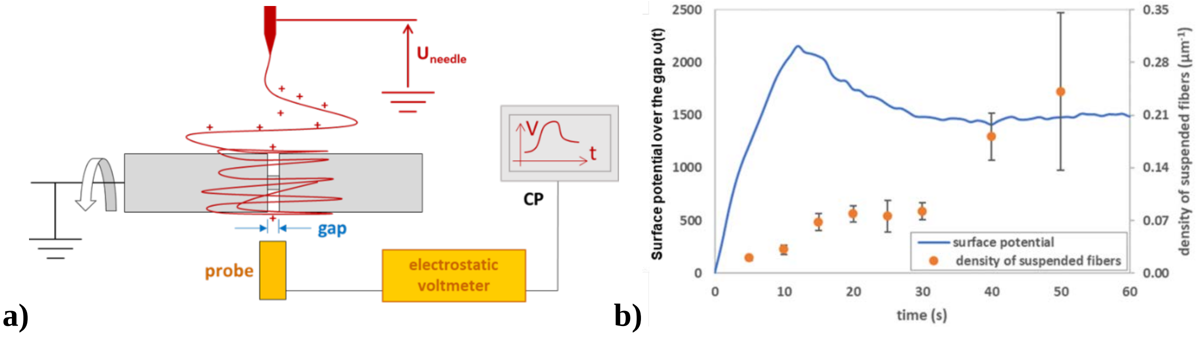

Figure 2 : *a) Montage permettant la mesure du potentiel de surface au-dessus des segments de fibres suspendus au-dessus d’un de largeur ajustable. b) Evolution du potentiel de surface et de longueur de segments de nanofibre de PLA suspendus au-dessus du gap.*

a. Analyse du potentiel de surface et cinétique de décharge de fibres suspendues

Les charges portées par les portions de fibres suspendues jouent le rôle principal pour l’élaboration des scaffolds 3D structurés. L’étude de la formation du « template électrostatique » et de la cinétique de sa décharge est donc primordiale pour mieux comprendre les phénomènes mis en jeu et de pouvoir *in fine* assurer un meilleur contrôle de la structuration 3D des scaffolds et ce, sur des épaisseurs encore plus importantes. Nous avons donc étudié le « template électrostatique » pour l’electrospinning du PLA en solution dans un système diméthyle formamide/dichlorométhane (DMF/DCM), d’une part, et du PEO en solution dans l’eau. Un collecteur cylindrique a été spécialement fabriqué pour l’étude (Fig. 1a), il a permis la mesure en continu de l’évolution du potentiel à la surface de fibres suspendues au-dessus d’un gap simple localisé sur une circonférence du collecteur et de largeur ajustable entre 0 et 10 mm.

Nous avons montré que l’évolution du potentiel de surface au cours du dépôt par electrospinning se décompose en trois phases (Fig. 1b). Dans les premiers instants, pendant environ une dizaine de secondes, le potentiel augmente quasi-proportionnellement avec le temps. Ce comportement s’explique par l’augmentation proportionnelle du nombre de segments de fibres suspendus, mesuré par observations MEB, au-dessus du gap (Fig. 1b). Il est à noter aussi que les segments sont parallèles entre eux et perpendiculaire au gap ce qui est dû aux forces d’interactions électrostatiques. La quantité de charges étant proportionnelle à la densité de charge linéique le long de la nanofibre, il s’en suit une augmentation du potentiel de surface. Dans une deuxième phase, on observe de manière étonnante une diminution du potentiel de surface. Les images MEB montrent des défauts de parallélisme des segments de fibres et résultent à la formation de « circuits fibreux fermés » (Fig. 2a) interconnectés aux points de contact fibre-fibre. Ces circuits présentent une distribution de charges hétérogène et peuvent être caractérisé par un circuit $R_{loop}C_{loop}$ formé d'une résistance et d'un condensateur en parallèle. L'association des circuits $R_{loop}C_{loop}$ forme une membrane fine suspendue uniformément chargée au-dessus du gap et qui elle aussi peut être modélisée par un circuit électrique équivalent caractérisé par un temps caractéristique de décharge $\tau = R(t)C_{gap}$ (Fig. 2a). Le temps τ diminue probablement avec la taille du « circuit fibreux fermé ». Il apparaît que le temps caractéristique τ résulte d'une part des propriétés d'interconnexion et de résistivité des nanofibres caractérisées par la résistance R(t) et de la capacité C_{gap} qui elle, est fonction de la géométrie du gap. Alors que C_{gap} est constant, la résistance R(t), quant à elle, diminue au cours du temps à cause de la densification des réseaux fibreux améliorant ainsi l'interconnexion des fibres et donc la décharge de la membrane suspendue. Ainsi, la diminution du potentiel de surface pendant la deuxième phase est expliquée par la décharge des segments suspendus attribués à la décharge des « circuits fibreux fermés » par la circulation des charges localisée à la surface des fibres. Lors de la troisième phase, l'apport des charges par la fibre en cours de dépôt est parfaitement compensé par la dissipation des charges. Dans cette troisième et dernière phase, des charges sont à la fois apportées par de nouveaux segments de fibre alors que d'autres charges sont dissipées d'autant plus efficacement que la taille des « circuits fibreux fermés » diminue jusqu'à une valeur limite de l'ordre de quelques µm expliquant ainsi la quasi-stabilité du potentiel de surface. L'évolution du potentiel de surface généré au-dessus des fibres suspendues a ensuite été étudiée en fonction de la taille du gap et de différents paramètres de procédé. Par ailleurs, le potentiel de surface généré dans le cas des fibres de PEO est bien plus faible que pour les fibres de PLA. Ceci est probablement dû à une conductivité plus élevée des fibres de PEO à cause de la présence probable d'eau résiduelle favorisant la dissipation des charges.

La cinétique de décharge du tapis fibreux suspendus au-dessus du gap a ensuite été étudiée à partir de l'instant t_{spin} pour lequel le potentiel à l'aiguille d'electrospinning est mis à la masse correspondant ainsi à l'arrêt de production de fibres (Fig. 2b). A partir de l'instant t_{spin}, aucune nouvelle charge électrique n'est apportée et la morphologie du tapis fibreux ne change plus. Dans les deux cas, pour le PLA et pour le PEO, une cinétique de décharge du potentiel ω à la surface du tapis fibreux a pu être modélisée par deux temps de relaxation, un temps court τ_s et un temps long τ_l environ 10 fois plus élevé que le temps court :

$$V(t) = A_s e^{-\left(\frac{t-t_{spin}}{\tau_s}\right)} + A_l e^{-\left(\frac{t-t_{spin}}{\tau_l}\right)}$$

Il a été observé qu'une augmentation de la durée de production t_{spin} se traduit par une augmentation du temps court τ_s et une diminution du temps long τ_l (Fig. 2c). Ce comportement opposé pourrait s'expliquer par l'origine physique des deux phénomènes de relaxation : le temps court τ_s, pourrait être attribué à la recombinaison de charges avec des ions présents dans l'air alors que le temps long τ_l pourrait être attribué à la décharge des « circuits fibreux fermés». En effet, aux temps de production t_{spin} court, le nombre de segments de fibres du tapis fibreux localisés au-dessus du gap est faible, réduisant ainsi le nombre de charges en contact avec les ions libres de l'air. Par ailleurs, lorsque t_{spin} augmente, la taille des « circuits fibreux fermés» (Fig. 2a) diminue conduisant alors à la diminution de leur temps caractéristique RC dont la valeur moyenne pourrait correspondre au temps de relaxation τ_l. En conclusion, le « template électrostatique » induit par les segments suspendus de nanofibres est beaucoup plus stable pour des dépôts faiblement denses en fibres et donc pour des temps de production t_{spin} courts.

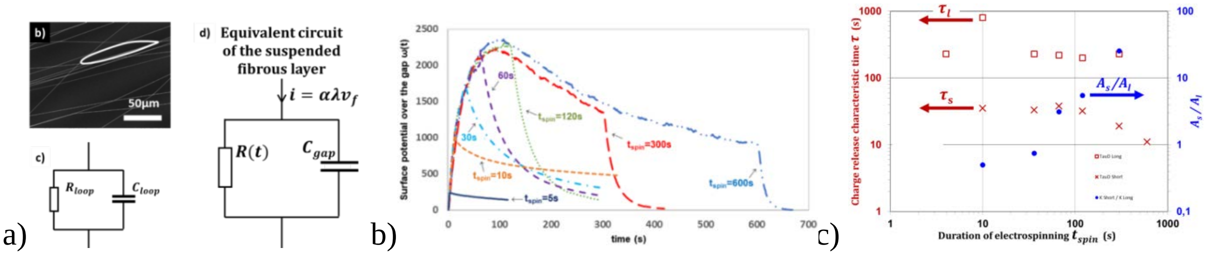

Figure 3 : a) Image MEB de segments de nanofibres suspendus. En blanc un « circuits fibreux fermés » et dessous le circuit électrique équivalent. b) Evolution du potentiel de surface en fonction du temps avant et après t_{spin} et pour différentes valeurs de t_{spin} dans le cas de l'electrospinning de PEO. c) Evolution des temps de relaxation court τ_s et long τ_l et du rapport A_s/A_l en fonction de t_{spin} dans le cas de l'electrospinning de PEO.

b. Electrospraying de particules par « dépôt assisté par template électrostatique » DATE

L'effet de «template électrostatique » a ensuite été appliqué pour guider le dépôt de microparticules par electrospraying. Pour ce faire, un collecteur cylindrique présentant des stries parallèles en circonférence et espacées de 500 microns a été spécialement fabriqué. Cette géométrie a permis d'extrapoler les analyses effectuées avec le collecteur cylindrique à simple gap ajustable. Dans une première étape, des nanofibres de PLA ou de PEO ont été déposées sur le collecteur pour différents temps de production t_{spin}. Puis, dans une deuxième étape, le « dépôt assisté par template électrostatique » (DATE) de microparticules de PCL a été effectué pour différentes durées t_{spray}. Les expériences ont montré l'amélioration de la qualité du contrôle du DATE avec la diminution du temps d'electrospinning t_{spin}. En effet, il s'agit de la situation pour laquelle le « template électrostatique » est plus stable pendant la production de microparticules par electrospraying.

c. Structures 3D élaborées par DATE.

Des scaffolds composites ont été élaborés par electrospinning de PLA et electrospraying de PCL en utilisant des collecteurs structurés afin d'obtenir des structures 3D multicouches via la stratégie DATE par dépôt successif de bicouches nanofibres-microparticules. L'organisation de chaque bicouche ainsi que le potentiel de surface ont été étudiés et discutés tout au long du procédé d'élaboration et en fonction de la durée et de l'arrangement des séquences des dépôts (Fig. 4 and 5).

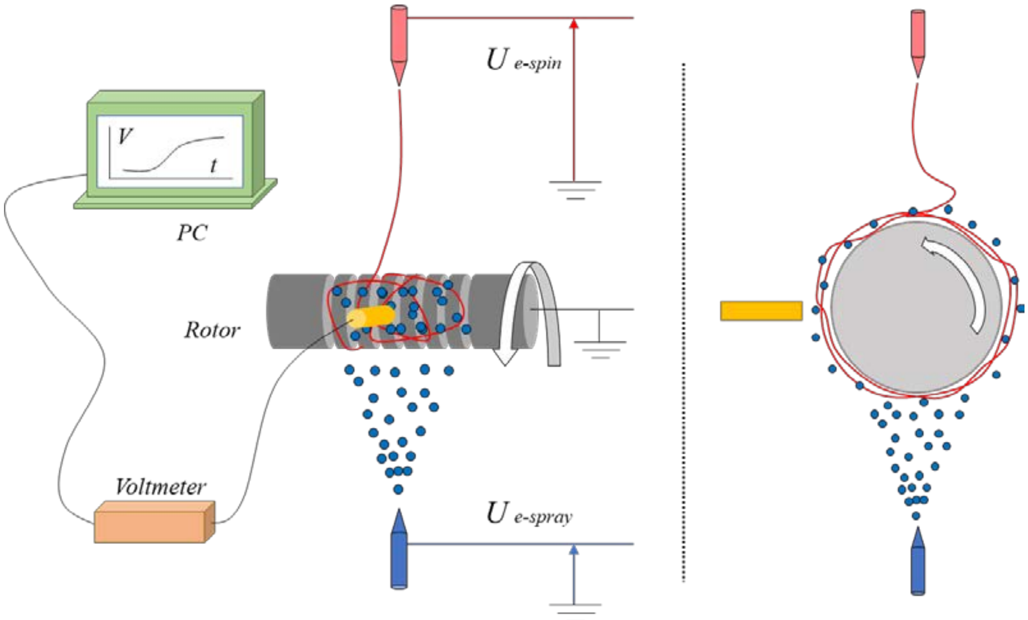

Figure 4 : *Principe de l'expérience permettant de produire des membranes par le procédé DATE et de mesure online du potentiel de surface.*

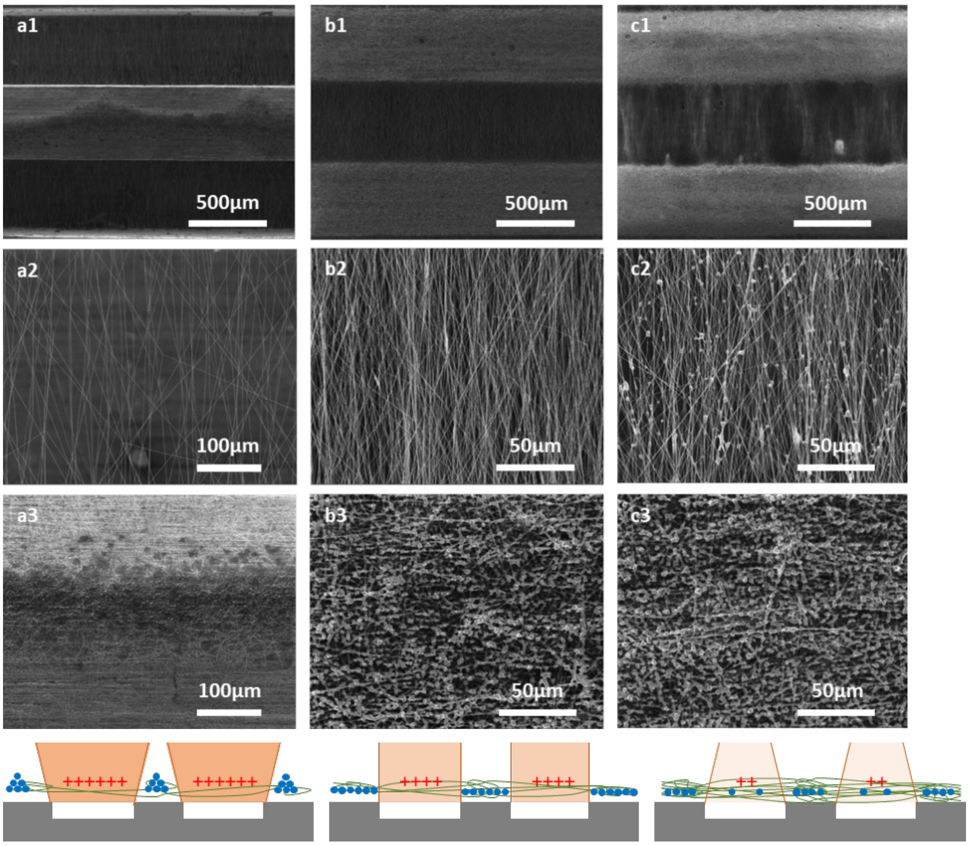

Figure 5 : *Bicouches formés par une couche de nanofibres recouverte d'une couche de microparticules obtenus pour différents temps d'electrospinning* $t_{spin} = 15s$ *(a1, a2, a3), 3min (b1, b2, b3) et 5min (c1, c2, c3). a1, b1 et c1 montrent des images MEB des nanofibres et microparticules localisés au-dessus d'un gap et d'un mur d'une strie. a2, b2 et c2 montrent le bicouche au-dessus d'un gap et a3, b3 et c3 au-dessus d'un mur d'une strie. Les dessins dessous schématisent l'organisation des particules.*

General introduction

General context:

After two decades of development, electrospinning, as a powerful technique to produce nanofibers with a diameter in the range from tens of nanometer to micrometers, has gained a great attention to produce fibrous membranes applied in wound healing, drug delivery, tissue engineering, air filtration, sensor, etc [1]–[5]. Now, some products have been developed at industrial scale in several fields. Although electrospinning is well-known to produce non-woven mats, it has been discovered that the deposition of the nanofiber can be controlled in order to obtain structured scaffolds with specific patterns paving the way for novel applications and specifically in tissue engineering in order to mimic the structures and biological functions of the extracellular matrix and enhance the cell immigration and proliferation providing a route for researchers to develop new products for the treatment of patients and for the society to save a huge economic burden. For example, for only cardiovascular patients, the total health care was estimated at $108 billion in 2012 [6]. Besides the high value in tissue engineering, fibrous mats with high specific surface area and small pores can filtrate the impurities efficiently, it was reported that PM 2.5 causes around 3.2 million deaths in 2010 which becomes the major threaten to the survival of human beings [7], thus electropsun scaffolds facilitates modern people to manage the challenges from the air pollution.

During the production of fibrous mats, fibers can be transformed into particles by simply decreasing polymer chain entanglements, the process is called electrospraying and already widely used in drug delivery. Moreover, former researches developed in our group demonstrated that by combining the processes of electrospraying and electrospinning, 3D structured composite mats can be obtained and furthermore with enhanced thickness. It was shown that the successfull fabrication of a structured nanofibrous mat relies on the control of the charges carried by the nanofibers during their deposition.

Thus, the main goal of this PhD is to understand the effect of electric charges on the morphology of the resulting material and on the building of structured scaffolds generated by coupling fibers and particles. A precisely selective deposition of particles is obtained resulting from falling particles undergoing an efficient electrostatic template effect controlled by the surface potential remaining on the fibers. Hence, studying the surface potential of electrospun fibers to understand the formation mechanism of electrostatic template effect is necessary for better controlling the building of thick composite scaffolds with spatial structures.

Methodology:

In this study, PLA and PEO are chosen as the basic polymer materials to generate electrospun fibers. For electrospraying, PCL having either a molar mass of 14 kg/mol or 80 kg/mol are used to prepare particles in different sizes. When nanofibers are electrospun on a patterned collector made of protuberances, a surface potential can be generated by the fiber strands suspended between the protuberances. The resulting electrostatic template is thus able to modify the trajectory of particles allowing their deposition on selective areas. In order to study the interaction between fibers and particles, the amount of charges brought by jets, the accumulation and dissipation of charges remaining on fibrous mats and suspended fibers are deeply studied. Finally, 3D structured scaffolds are generated by the alternate deposition of electrospun PLA fibers and electrosprayed PCL particles on patterned collectors.

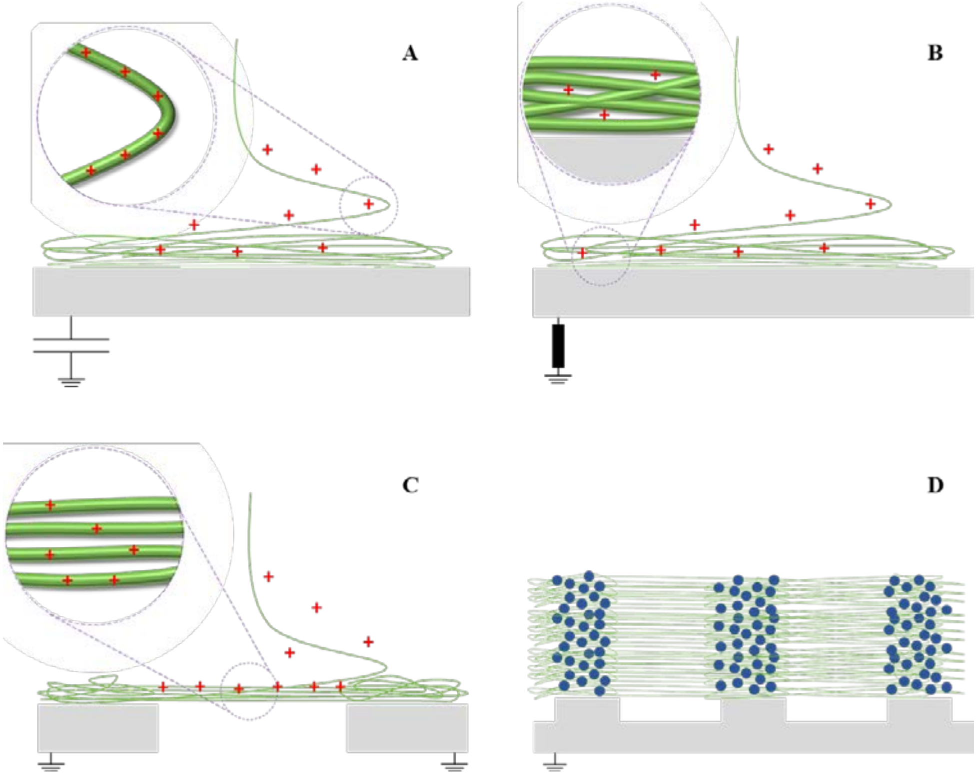

Fig. 1 The different steps of the PhD: A) Charges induced by a single electrospun jet: measurement and impact of processing parameters. B) Charge accumulation and dissipation in a fibrous mat produced on a flat collector: characterization and relationship with the porous morphology of the mat. C) Surface potential formation and decay on suspended fibers: a model experiment. D) Preparation of structured scaffolds by coupling electrospun fibers and electrosprayed particles on patterned collectors (D)

The goals of this PhD were to investigate, at both nanofiber and mat length scales, the relationships between the charges carried by the deposited nanofibers and the morphology of the produced mat. The several stages of this PhD are presented in Fig. 1.

Chapter 1 presents a state of the art in the topic of the PhD. Electrospinning and electrospraying will be introduced briefly then, the latest studies dealing with the measurement and the characterization of the electrical charges carried by the nanofibers and the resulting surface potential of the produced mat will be presented. In **chapter 2**, we focused at the nanofiber lengthscale. The charge density of PLA fibers is precisely studied by a novel approach which also provides more details on the effects of various processing conditions (polymer concentration, applied voltage, conductivity, ambient humidity and flow rate) on the rate of charge accumulation and the formation velocity of fibers. The amount of charges carried by PEO, PEO/Alginate fibers and PCL particles is measured as well.

Chapter 3deals with the measurement of charges and surface potential during electrospinning of PLA fibers deposited on a flat and grounded collector. The effect of polymer concentrations, applied voltages and ambient humidity on the mat surface potential is studied. Furthermore, a model is proposed to get more insight into the formation and the decay kinetic of the surface potential and its relationship with the porous structure of the produced mat.

In order to understand how the surface potential is generated on suspended fibers, a specific collector with an adjustable gap in size was designed (**the 1st section of chapter 4**). Here, PLA and PEO are electrospun onto the single gap to examine the effect of of the type of the processed polymer on the storage of surface potential. Additionally, the intensity of the surface potential on suspended fibers is studied as a function of the gap size and the processing time. A model is also developed in order to understand the mechanisms of the formation kinetic of the surface potential generated by suspended fibers.

Finally, the combination of electrospun fibers and electrosprayed particles deposited on patterned collectors is studied in the **2nd section of chapter 4**. First, PCL particles are electrosprayed on either PLA or PEO electrospun fibers deposited on a striated collector. Such regular collector geometry allows to extend the results obtained in the previous section. Then, a grid collector with smaller gaps and grooves than the striated collector is used to improve the efficiency to produce 3D multilayer samples. The results indicate that the selective deposition of PCL particles is constant after preparing few layers of PLA fibers and

PCL particles alternately. Thus, multilayer samples with spatial structures, combining PLA fibers and PCL particles, are eventually obtained.

[1] A. Podgórski, A. Bałazy, and L. Gradoń, “Application of nanofibers to improve the filtration efficiency of the most penetrating aerosol particles in fibrous filters,” *Chemical Engineering Science*, vol. 61, no. 20, pp. 6804–6815, Oct. 2006, doi: 10.1016/j.ces.2006.07.022.

[2] H. Liu, J. Kameoka, D. A. Czaplewski, and H. G. Craighead, “Polymeric Nanowire Chemical Sensor,” *Nano Letters*, vol. 4, no. 4, pp. 671–675, Apr. 2004, doi: 10.1021/nl049826f.

[3] A. Melaiye *et al.*, “Silver(I)−Imidazole Cyclophane *gem* -Diol Complexes Encapsulated by Electrospun Tecophilic Nanofibers: Formation of Nanosilver Particles and Antimicrobial Activity,” *Journal of the American Chemical Society*, vol. 127, no. 7, pp. 2285–2291, Feb. 2005, doi: 10.1021/ja040226s.

[4] H. Yoshimoto, Y. M. Shin, H. Terai, and J. P. Vacanti, “A biodegradable nanofiber scaffold by electrospinning and its potential for bone tissue engineering,” *Biomaterials*, vol. 24, no. 12, pp. 2077–2082, May 2003, doi: 10.1016/S0142-9612(02)00635-X.

[5] L. Chen, L. Bromberg, T. A. Hatton, and G. C. Rutledge, “Catalytic hydrolysis of p-nitrophenyl acetate by electrospun polyacrylamidoxime nanofibers,” *Polymer*, vol. 48, no. 16, pp. 4675–4682, Jul. 2007, doi: 10.1016/j.polymer.2007.05.084.

[6] C. Cook, G. Cole, P. Asaria, R. Jabbour, and D. P. Francis, “The annual global economic burden of heart failure,” *International Journal of Cardiology*, vol. 171, no. 3, pp. 368–376, Feb. 2014, doi: 10.1016/j.ijcard.2013.12.028.

[7] J. S. Apte, J. D. Marshall, A. J. Cohen, and M. Brauer, “Addressing Global Mortality from Ambient PM $_{2.5}$,” *Environ. Sci. Technol.*, vol. 49, no. 13, pp. 8057–8066, Jul. 2015, doi: 10.1021/acs.est.5b01236.

Chapter 1 State of the art: accumulation and dissipation of electric charges during electrospinning - application to the fabrication of 3D structured nanofibrous scaffolds

This chapter presents a state of the art. First, the processes of electrospinning and electrospraying, allowing the fabrication of nanofibrous scaffolds and microparticles respectively, will be presented. Then, we will study more deeply how the surface potential develops on the top surface of the scaffolds during its production by electrospinning. In the third part, we will show how the surface potential decreases with time. Such property is of prime importance for electret applications and also for the fabrication of 3D structured fibrous constructs thanks to the help of electrostatic interactions which will be studied in the final part.

1.1 The processes of electrospinning and electrospraying

1.1.1 Electrospinning

Electrospinning is a process allowing the fabrication of nanofibers by subjecting a polymer solution to a high electric field. The original idea of electrospinning dates back to early twenty century [1]–[4]. Based on its simplicity, versatility and low cost, electrospinning already becomes one of the most representative and efficient approach generating nano-structured materials in the past decades [5]. Until now, it is not only available to prepare nanofibers with a wide range of raw materials in terms of natural polymers [6], synthetic polymers [7], polymer blends [8] as well as organic and inorganic complexes [9]. The controllability of the morphology and the diameter of fibers can be tuned to control the mechanical properties, the porosity and the surface-to-volume ratio of the resulting electrospun nanofibrous mats. Due to its numerous advantages, electrospinning has been applied in various fields including filters [10]–[12], sensors [13], [14], drug delivery [15]–[17], tissue engineering [18]–[20], catalysts [21]–[23], and energy conversion [24], [25].

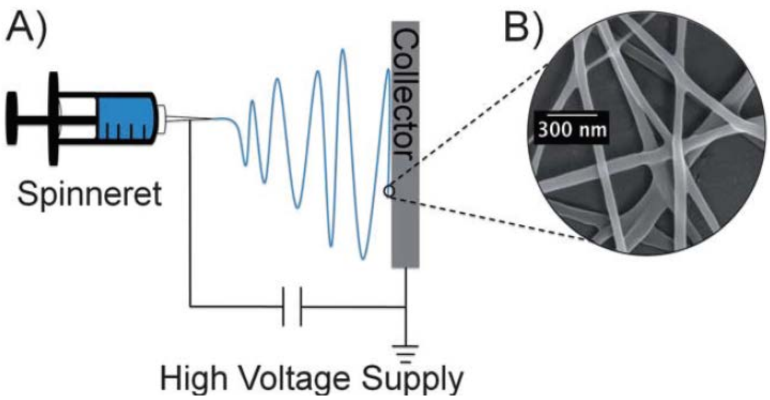

Fig. 1.1 (A) Illustration of the setup of electrospinning. (B) Scanning electron micrograph displaying the nanofiber morphology of an electrospun non-woven mat
Reprinted with the permission from [26]

Electrospinning uses a high electric field to form nanofibers from a polymer solution [27], [28]. As shown in Fig. 1.1, the typical setup is made of three main parts: (i) a voltage power supply, (ii) an emitter electrode connected to a high voltage from which the polymer solution is ejected and (iii) a collector connected to the ground. In the process of electrospinning, a syringe delivering the polymer solution is pushed by a syringe pump to dispense the liquid to the emitter, generally a stainless needle. When the voltage is applied at the needle, electrical charges accumulate at the surface of the droplets exiting the needle. If the voltage is enough high, it deforms in the shape of a cone called the Taylor cone. When the electric force overcomes the surface tension of the droplet, a jet of the polymer solution is propelled from the apex of the Taylor cone towards the collector. Before hitting the collector, the charged jet experiences whipping movements favoring the decrease of the fiber diameter and the solvent evaporation. In the end, a solidified fiber is randomly deposited on the collector in the form of a non-woven mat also called scaffold or membrane.

The polymer chain entanglements in the processed solution play an important role to form a continuous jet under the action of the electric field. The density of chain entanglements is a function of the polymer molar mass and its concentration in the solution, it can be characterized by the viscosity of the solution[29]. The viscoelastic force increases as well to counterbalance the stretching force allowing to the jet to not split into offspring particles [30]. If the viscosity decreases to a certain level, the jet breaks into particles and the process is called electrospraying [31]. As shown in Fig. 1.2, Lavielle et al. studied the relationship between the fiber diameter and the product of the polymer concentration C in the solution with the molar mass, represented by the intrinsic viscosity [η] [32]. Similarly, to [η]C, the ratio C/C^* can be used, where C^* represents the critical chain-overlap concentration [33]. When [η]C is located in the domain 4, the viscosity of the solution is too high and the jet cannot be efficiently stretched avoiding the formation of the Taylor cone and thus, avoiding electrospinning. When decreasing the concentration to domain 3, an ideal balance between the electric force and the surface tension of the droplet allows the efficient production of an electrospun jet resulting in the production of uniform fibers (Fig. 1.2c). It is shown that the diameter of fibers decreases with the decrease of the polymer concentration. If the concentration is decreased in the domain 2, beaded fibers are formed (Fig. 1.2b) due to hydrodynamic instabilities caused by the forces acting at the surface of the jet which favor the decease the jet surface area. Finally, when the concentration is still decreased in domain 1, only electrosprayed particles are collected (Fig. 1.2a). Because of the low polymer concentration in the solution, chain entanglements are not sufficient to avoid the breaking of the jet resulting in the deposition of microparticles [34]. The process of electrospraying [35] will be presented more precisely later.

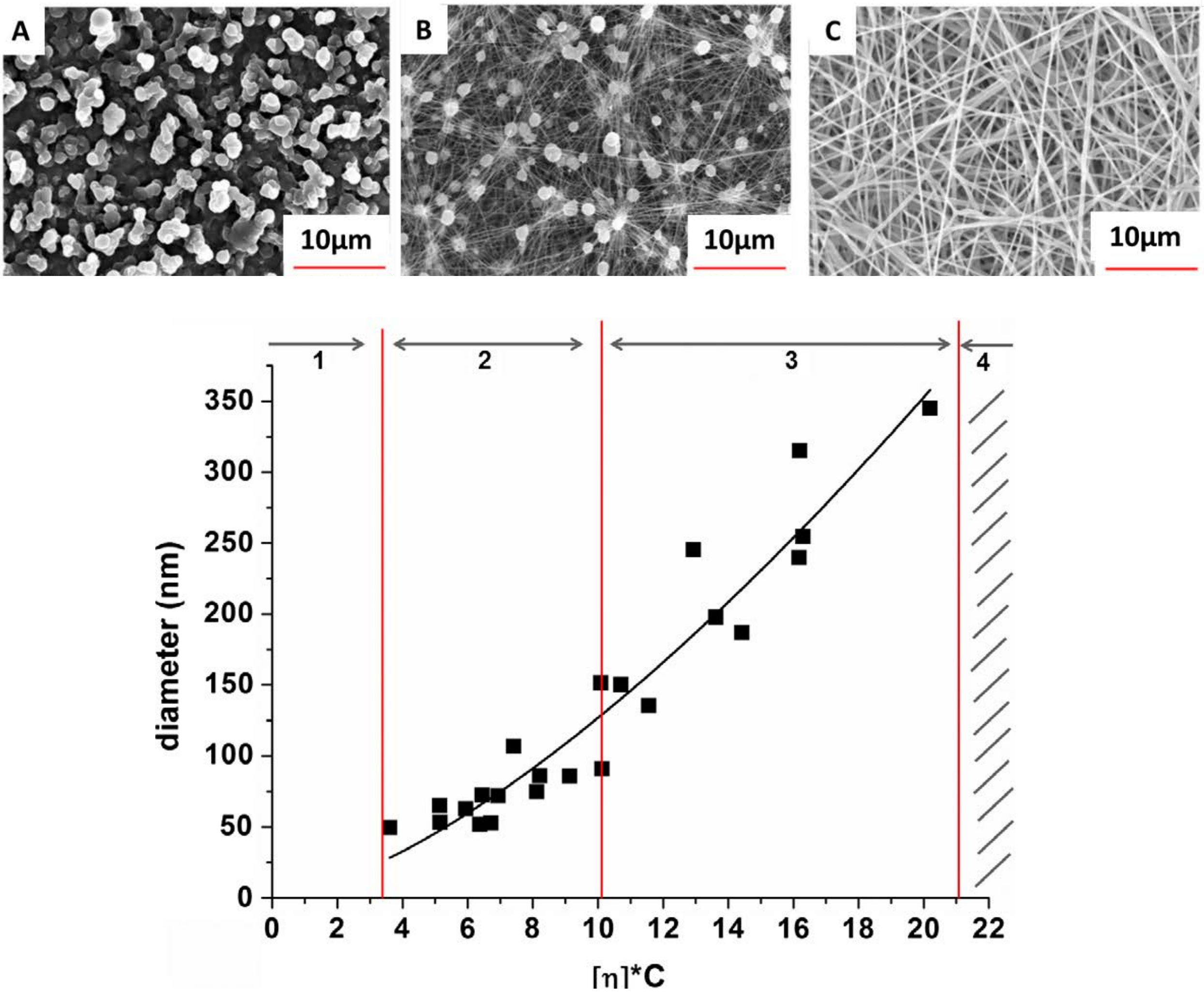

Fig. 1.2 SEM images of electrosprayed PCL particles (a), beaded PCL fibers (b), electrospun PCL fibers (c) and variation of fibers average diameter with [η]C (d): 1: electrospraying, 2: beaded electrospun fibers, 3: bead-free electrospun fibers and zone 4: no electrospinning Reprinted with the permission from [32]

Besides the intrinsic viscosity and surface tension, the main factors affecting the morphology of the fibers include the conductivity of the solution, the applied voltage, the polymer solution flow rate, the needle-to-collector distance and the ambient humidity and temperature.

Regarding the study of the effect of the parameters on the fiber morphology, studies have shown that the conductivity affects significantly the fibers diameter. When, thanks to high conductivity, the electrospun jet has the capability to transport a large amount of charges, the jet undergoes a stronger stretching force under the electric field resulting in the decrease of the fiber diameter. However, some articles reported the inverse situation showing that the fiber diameter can increase with the amount of salt added within the solution [36], [37]. Supaphol et al. analyzed that the jet containing more salts experienced simultaneously an increasing strength in the electrostatic and Coulombic repulsion forces. Whereas the former factor speeds up the flowing rate enlarging the diameter, the latter force enhances the repulsive power stretching the jets [38]. Additionally, changing the type of salt (in terms of compositions and molar mass) in the solution induces different effects on the fiber diameter which might be attributed to various physical-chemical interactions [37].

The applied voltage has to reach a critical value to overcome the surface tension of the droplet in order to eject the jet from the tip of the Taylor cone, leading to the deposition of a continuous fiber. In most cases, the increase of the voltage, inducing the amount of charge density carried by the jet, leads to the decrease of the fiber diameter [39]. However, some articles reported the inverse tendency. Indeed, the enlargement of charge density due to a higher applied voltage results in larger whipping movements experienced by the electrospun jet. Thus, in the same time, the jet is subjected to an increase of the elongation force (favoring the decrease of the diameter) as well as an increase of the rate of solvent evaporation (favoring the increase of the diameter). Thus, some reports found that by increasing the voltage, the faster evaporation avoids the efficient stretching resulting in fibers with larger diameter [40], [41].

For a given set of parameters, a polymer solution system has its own lowest critical flow rate to maintain the generation of continuous jets. Actually, a flow rate which is too low contributes to a rapid solvent evaporation resulting in less fusion formed in the fiber-fiber contact domains and furthermore few beads can appear on the fibrous mesh [42]. The increase of flow rate leads to the increase of the diameter of fibers. Furthermore, when the flow rate is high, the insufficient evaporation of solvents happens resulting in the fusion of the fiber-fiber contact domains in the mat, flat ribbons instead of cylindrical fibers might be produced [42], [43]. Such morphology has an important impact on the final mechanical properties of the mat.

The influence of ambient humidity on the morphology of fibers depends mainly on the polymer-solvent hydrophily or hydrophobicity and the solvent volatility. In the process of electrospinning, a hydrophilic jet can absorb the water molecules of air causing a plasticizing effect. Thus, a slow solidification occurs leading to the efficient jet stretching for a longer time resulting in the generation of thinner fibers. Pelipenko et al. investigated the effect of relative humidity on the morphology of fibers prepared from hydrophilic polymers, such as

PEO and PVA fibers, showing the decrease of the fiber diameter with the increase of the ambient humidity [44]. Other studies reported the same phenomenon [45]–[47]. In the case of hydrophobic polymers, an opposite trend is observed. Indeed, in the case of high humidity, a growing number of water molecules around the jets facilitate the electrostatic discharge and also the precipitation of the polymer resulting in weaker whipping movements and a less deformable jet. Therefore, thick fibers are fabricated after increasing the relative humidity [48]–[52].

The temperature experienced during the process of electrospinning plays also an important role on the final fibrous morphology. Indeed, the viscosity of the polymer solution decreases with increasing the temperature due to higher polymer chain mobility. Thus, a jet of lower viscosity is more deformable and consequently more stretched under the Columbic force: thinner fibers are produced [40], [46], [53]–[55]. De Vrieze et al. found that there are two opposing effects when the temperature is modified. Indeed, although increasing the temperature reduces the viscosity, it also favors the solvent evaporation which has an opposite effect on the final fiber diameter. Such phenomenon was shown for the electrospinning of poly(vinylpyrrolidone) (PVP) for which smaller diameters were measured for the lowest air temperatures. This effect was attributed to the weak volatilization rate extending the period for jet to solidify. The jet is consequently elongated in a longer length leading to thinner produced fibers [46]. Bipul et al. also observed that for non-hydrosoluble polymers low temperatures, as also high air humidity, facilitate the appearance of surface irregularities due to phase separation [51].

The emitter-to-collector distance affects the average electric field between the emitter and the collector. However, such effect is negligible. The main property which is mainly affects by the emitter-to-collector distance is the time of jet flight allowing more or less time for the solvent to evaporate. Indeed, the morphology of fibers can change remarkably as a function of the emitter-to-collector distance. Ki et al. proved that there is a minimum distance allowing enough time for the solvent to evaporate efficiently otherwise a liquid film is formed at the surface of the collector. At intermediate emitter-to-collector distance the presence of residual solvent leads to the fusion of fibers at their contact points modifying the overall mechanical properties of the mat. [56]. Doshi et al. observed that the amount of fibers generated on the collector drops down remarkably when the needle-to-collector are too large [57].

1.1.2 Electrospraying

As mentioned previously, the morphology can be varied from regular nanofibers to microparticles by simply decreasing the density of polymer chain entanglements in the processed solution. In this case, the process is named electrospraying. Nowadays, a wide range of polymers can be used for the fabrication of electroprayed particles, including PLA, PCL, PGA, PLGA, PS,…[58]–[62]. Such fabricated microparticles are of great interest for various biomedical and drug encapsulation applications [63], [64].

Bock et al. shows the effect of the polymer concentration and viscosity on the morphology of the produced electrosprayed particles (see also Fig. 1.2) [33], [65]. They found that there is a critical chain overlap concentration C_{ov} for which the particles can be produced by electrospraying and that the particle morphology is related to C_{ov} [33]. Figure 1.3 shows that no overlap occurs among the polymer chains when the concentration C is smaller than C_{ov}, it is called the dilute regime, the droplets are deposited into the form of film or flat particles. By increasing the concentration to the semi-dilute unentangled regime, some portions of polymer chains are entangled leading to the deposition of irregular and fused particles on the collector as shown in Fig. 1.3b. By increasing even more the concentration over the critical value C_{ent}, the state of the polymer solution system enters from semi-dilute unentangled regime to semi-dilute entangled regime, for which isolated and solid particles with spherical morphology are obtained. When the concentration is larger than $3C_{ov}$, the chain entanglement is too high and beaded fibers are obtained: particles are interconnected by a network of thin nanofibers as shown in Fig. 1.3d.

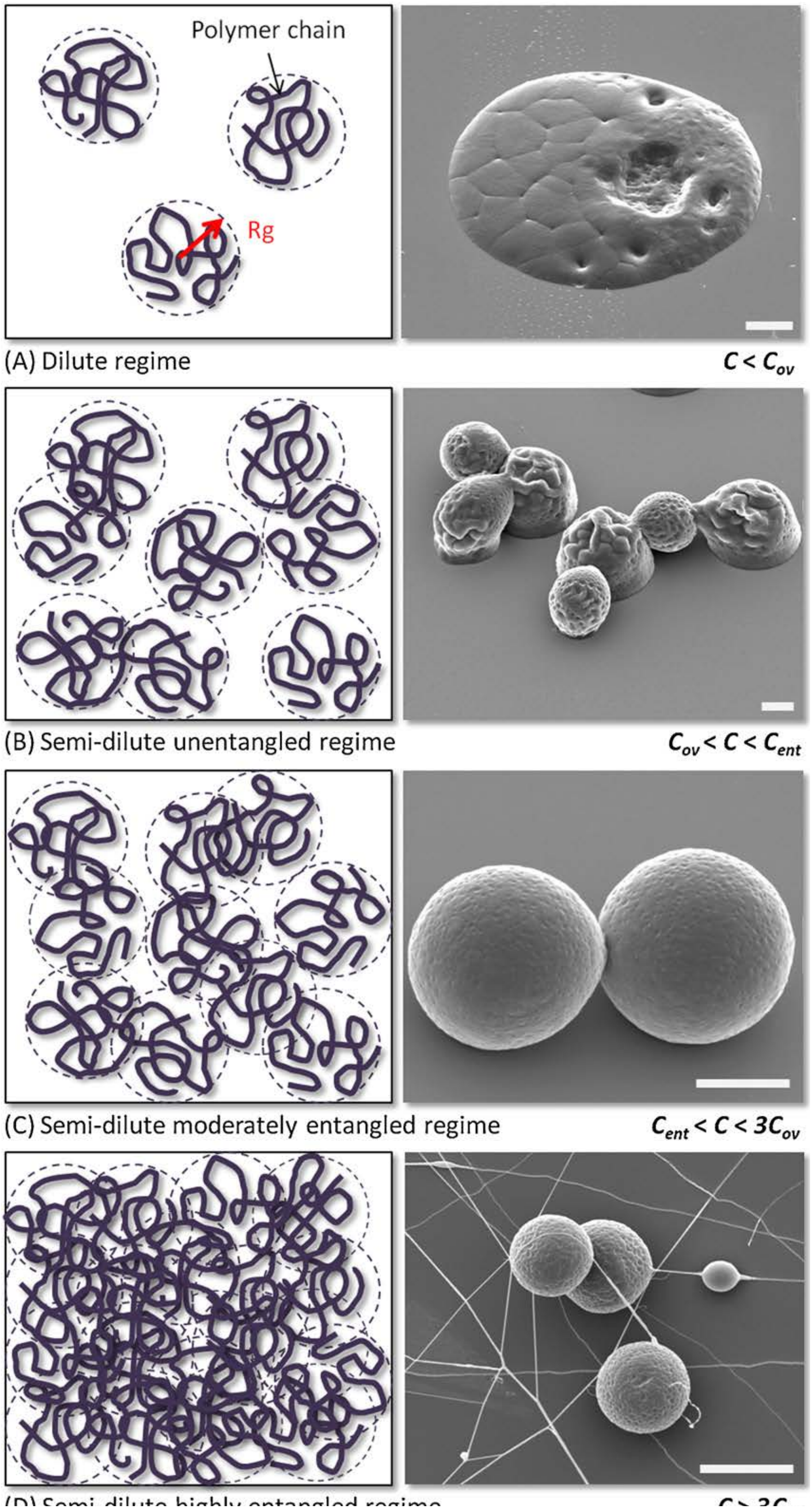

Fig. 1.3 Left side: physical representation of entanglement regimes achieved in different polymer concentrations. Right side: SEM images of corresponding PCL particles Reprinted with the permission from [33]

The morphology of the particles is mostly affected by the rate of solvent evaporation. An efficient and homogeneous evaporation leads to the fabrication of isolated round microparticles. When evaporation is incomplete, particles are flat. Furthermore, when the solidification occurs very rapidly at the surface of the particle during its flight, the solid surface shrinks leading to the deposition of rough particles [66]–[68].

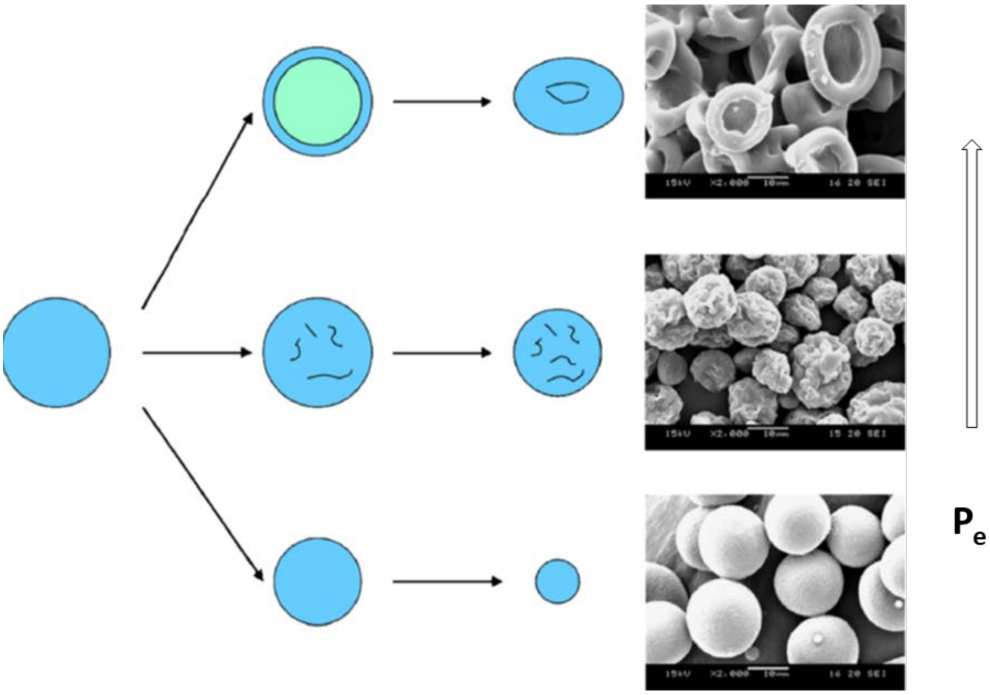

Fig. 1.4 Variation of particle morphology with increasing Pe
Reprinted with the permission from [69]

Yao et al. [69] correlated the morphology of electrosprayed particles with a modified Peclet number (P_e). As shown below, P_e reflects the relation between the shrinking rate of the droplet surface and the polymer diffusion coefficient in the droplets, which represents the solvent volatilization rate and polymer diffusion rate, respectively.

$$P_e = \frac{r_d \cdot \frac{dr_d}{d_t}}{D_{AB}} \tag{1.1}$$

dr_d/d_t is the shrinking rate of droplets, r_d is the diameter of the droplet and D_{AB} represents the diffusion rate of the polymer in the droplets.

When P_e has a large value meaning that the diffusion rate is slow, the generation of a solidified surface can happen quickly resulting from the rapid solvent evaporation on the surface of droplets. The hysteretic evaporation of solvent inside the droplets leads to a solvent-rich domain which causes a hollow structure in the particles after the complete solvent evaporation. Depending on the thickness and the mechanical strength of the shell of particles, portions of particles may perform a concave or fragmented morphology.

By increasing the diffusion rate, polymers can move rapidly from the core region to the surface where fast solvent evaporation occurs, thus no hollow sphere is generated. However, the rate of diffusion is still large enough to remove all solvent-rich domains in the droplets, as a result, porous and corrugated topography appears on the surface of particles.

By increasing even more the diffusion rate to reach a critical value, the polymer fills homogeneously all the volume of the electrosprayed droplets evenly and instantly before the evaporation of solvent happening from the surface, thus dry particles with smooth surface are formed in the end.

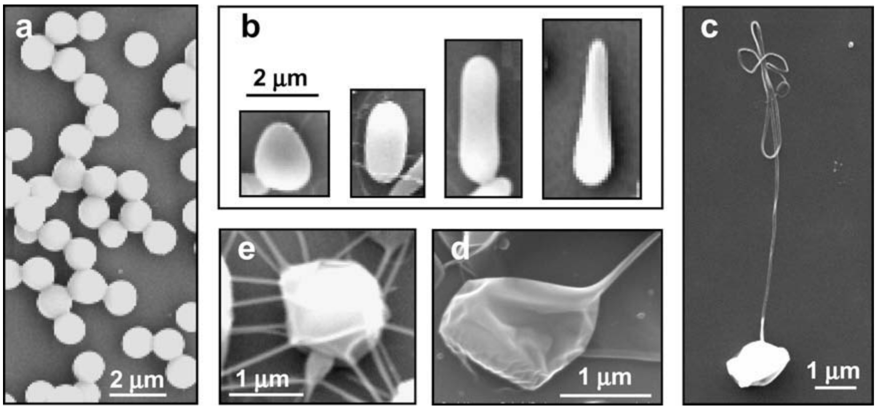

Fig. 1.5 Diverse morphologies of PLGA particles

Reprinted with the permission from [70]

Besides the effects of solvent volatilization and polymer diffusion, Almeria et al. analyzed the effects of chain entanglements and Coulomb fission during the process of electrospraying on the morphology of PLGA particles [70]. When the charge density of particles reaches the Rayleigh limit [71], the electric force induced by Coulomb fission overcomes the surface tension of droplets resulting to the disintegration of the droplets into small offsprings. As shown in Fig. 1.5, particles interconnected with very thin nanofibers are generated when entanglements between the polymer chains occur before reaching the Rayleigh limit (Fig. 1.5c). In contrast, the disruption of droplets occurs when the intensity of

Coulomb fission was enough large. Depending on the solvent evaporation rate, spherical morphology are obtained (Fig. 1.5a) whereas for rapid solvent evaporation, if the solidification and the fission progresses simultaneously, it results in particles with irregular morphologies, such as elongated particles (Fig. 1.5b).

Other researchers used a water bath to collect the generated electrosprayed particles with controlled porous structures. Such process allowed also to functionalize and encapsulate a drug for drug delivery and release applications [72], [73]. When non-water soluble polymers are electrosprayed in a water bath, it was shown that the presence of water around the particles leads to phase separation and solvents exchange, resulting in the formation of pores at the particle surface which affects the drug release properties.

1.2 Electric current produced during electrospinning

After applying the voltage on the electrospinning emitter, charges of same sign than the emitter's polarity move to the surface of the droplet exiting the emitter resulting to a high surface charge density. If the surface charge density is high enough, the hemispherical droplet deforms into the Taylor cone. Once the electric force overcomes the surface tension, the ejection of a jet occurs at the apex of the cone, removing the excess of charges on the drop. Thus, the resulting electrospun jet carried a high amount of charges and after its flight and solvent evaporation, a charged solid nanofiber is deposited on the collector. When the collector is a conducting metal, the charges can be released in an efficient manner towards the ground [74].

As mentioned previously, the initial charges in the droplet of the polymer solution are distributed on the surface of the droplet resulting in the formation of the Taylor cone by a stretching force. The droplet is undergoing a capillary pressure originated from the surface tension, $\Delta P_c = 2\sigma/(D/2)$, as well as a pressure originated from the Coulombic electrical pressure, $\Delta P_e = -e^2/(32\pi^2\varepsilon_0(D/2)^4$. The electric pressure dominates the capillary pressure for a small droplet. Thus, taking into account both equation, a droplet of a given diameter D can withstand a maximum charge per unit mass which is given by $\Delta P_c + \Delta P_e = 0$ [75] :

$$\frac{e}{M} = \sqrt{\frac{288\varepsilon_0\sigma}{\rho^2 D^3}} \tag{1.2}$$

Where σ is the surface tension, ε_0 is the vacuum permittivity, e is the total charge carried by the droplet and M is the mass of the droplet and ρ its density. In this condition, there is no consideration about any external interference. Eq. 1.2, called the Rayleigh criterion, shows that the maximum charge amount decreases with the increase of the size of the droplet [75]. Here, Eq. 1.2 does not take into account the evaporation which occurs at the saturation pressure. Moreover, the conductivity and the viscosity of the solution play also a role in the shape of the Taylor cone but with a less significant manner.

The amount of charges carried by the electrospun jet can be estimated by the measurement of the current during the process. By installing a resistor between the collector and the ground, the measurement of the difference of potential through the resistor allows to calculate the electrospinning current thanks to the Ohm's law (Fig. 1.6 a). The volume charge density ρ and surface charge density q are calculated by the following equations:

$$\rho = \frac{I}{Q} \tag{1.3}$$

$$q = \frac{\rho d}{4} \tag{1.4}$$

Where I represent the current, Q is the flow rate, d is the diameter of the jet at the tip of Taylor cone, q is the surface charge density.

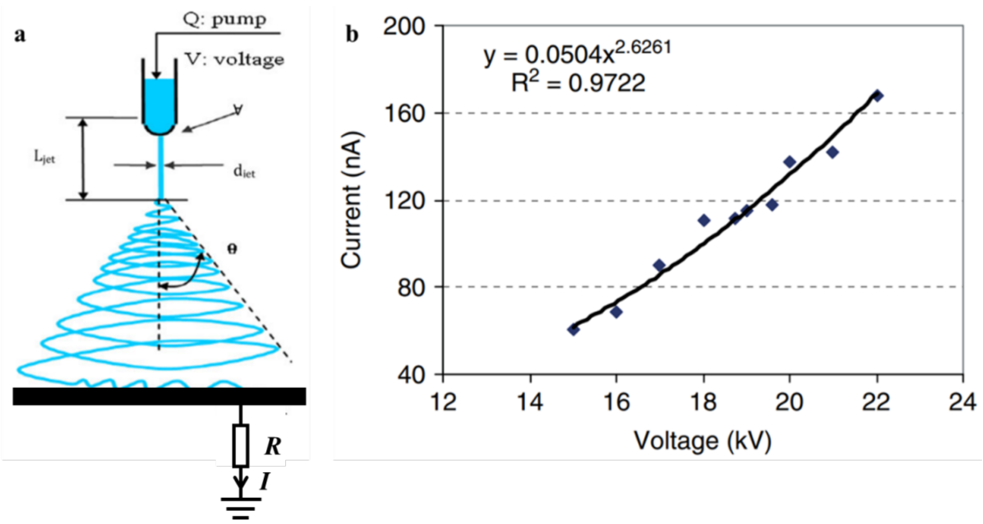

Fig. 1.6 (a) Measurable process parameters; (b) Effect of applied voltage on jet current. The curve shows the power-law fitting the experimental data. The fitted equation and R2 value are shown

Reprinted with the permission from [76], [77]

Fig. 1.6 b presents, during the process of electrospinning a polyacrylonitrile solution, a power-law dependence between the electric current and the voltage with an exponent of 2.62. This behavior was attributed to a growing amount of charges injected into the solution or melt from the increasing voltage. Thus, the jets formed under the highest voltage transports an increased amount of charges. A similar exponents of 2.7 to 3 was measured in other reports [78], [79]. However, Shin et al. obtained a linear relation between the current and the applied voltage in the condition of lower flow rates [80].

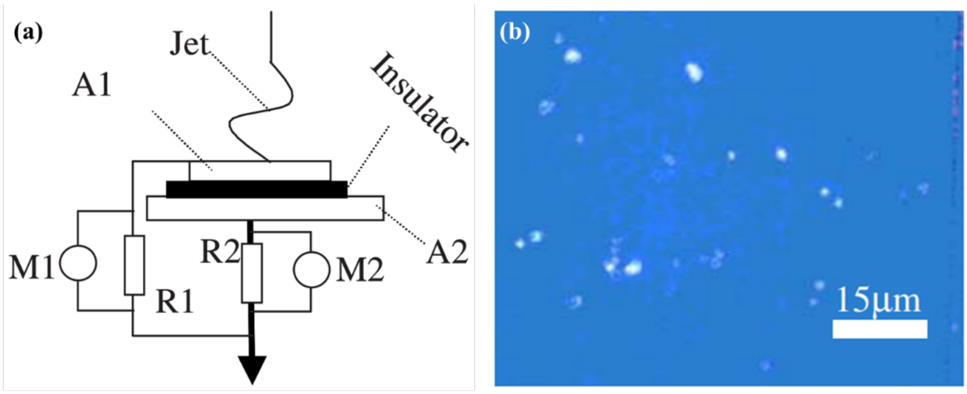

Fig. 1.7 (a) Schematic of the modified setup for the measurement of the currents passing R1 and R2, respectively. The collector plate is divided into two parts A1 and A2, which are separated from each other by a thin insulator film. Current on the plates is determined using the voltage drops across 1 MΩ resistors (R1 and R2) measured by multimeters (M1 and M2); (b) fluorescent clusters of electrosprayed traces of solvent seen on the glass slide Reprinted with the permission from [81]

Some reports have shown in some cases that there might be two types of currents composing the total current during electrospinning. As shown in Fig. 1.7a, the main current is formed by the flowing jets deposited on A1, which varies with the electric field. Another type of current recorded on A2 is due to the generation of electrosprayed solvent droplets from the surface of the jet (Fig. 1.7 b), which is independent of the electric field, but related with the flow rate and the conductivity of the polymer solution. The origin of a current due to electrosprayed droplets might be attributed to the uneven distribution of polymers in the solution. Thus solvent-rich domains lead to the emission of droplets out of the jet during the whipping movements [81]. Yarin et al. found that the stability of the surface of the jet can change with the modification of the electric field, resulting in secondary jets emitted from the surface of the main jet [82]. Furthermore, the redistribution of charges on the jet resulting from the whipping movements is a factor to account for the formation of secondary jets [83].

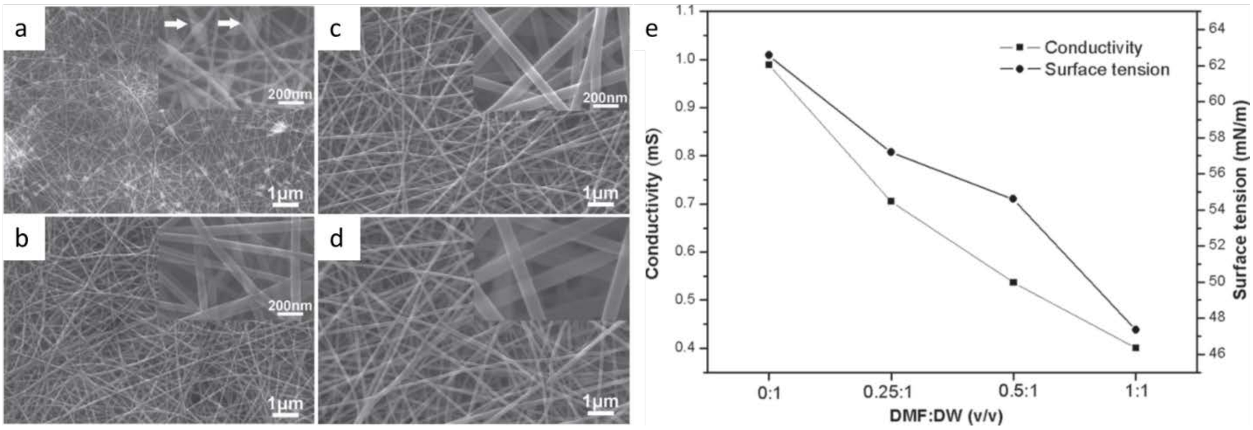

Fig. 1.8 SEM images of eletrospun 0.75% (w/v) HA nanofibers at different volume ratio of DMF to deionized water (DW): (a) DMF/DW= 0:1, (b) DMF/DW= 0.25:1, (c) DMF/DW= 0.5:1, (d) DMF/DW= 1:1; Conductivity and surface tension of 0.75% (w/v) HA solutions with different solvent. 0:1, 0.25:1, 0.5:1, and 1:1 represent the volume ratio of DMF to DW Reprinted with the permission from [84]

It has been widely accepted that the solvent properties affect the electrospinnability of the polymer solution and control the morphology of the deposited fiber. Among these properties, the nature of the solvent affects the amounts of charges carried by the jet. As shown in Fig. 1.8, the increase of the amount of DMF in the DMF/DW solvent mixture leads to the decrease of the surface tension as well as the solution conductivity which balance both forces responsible to the formation of the Taylor and thus the generation of the electrospun jet. When the conductivity of the polymer solution decreases gradually it results in fewer charges carried by the jet. Thus, the intensity of the electric force imposed on the jet is weaker favoring the enlargement of the diameter of the jet. Therefore, the diameter of fibers increases with the increasing DMF content [84]. Other researchers report similar results about the modification of the mixing ratio of solvents on the electrospinnability of the polymer solution and thus, on the morphology of the fibers [85], [86].

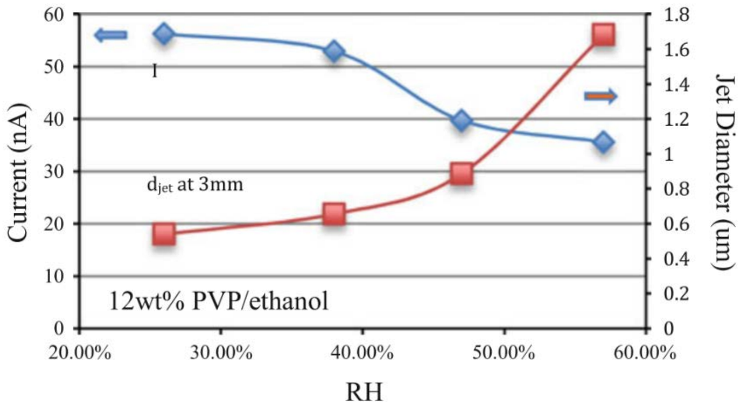

Fig. 1.9 Impact of RH on measurable parameters for 12 wt% PVP/ ethanol solutions. (a) Jet diameter and current versus RH. Diamonds: current (I), squares: jet diameter (djet) Reprinted with the permission from [76]

Fig. 1.9 shows the correlation of the electric current and the jet diameter with the ambient humidity during electrospinning of PVP in solution in ethanol, a hygroscopic polymer mixture. It is shown that, in this case, the electric current decreases gradually with the increase of the ambient humidity, while the humidity increases the jet diameter. At high humidity, the high amount of water molecules leads to the significant weakening of the surface charge density carried by the jet which was attributed to the polarization of water molecules: the charges located at the jet surface are neutralized by the surrounded water molecules resulting in the decrease of the current. Furthermore, at high humidity, the electrospun jet is thus subjected to low whipping movements (which are favored by the repulsive charges carried by the jet) resulting in the increase of the fiber diameter [87], [88]. For hydrophobic polymer-solvent mixtures the situation may be different.

In conclusion, the high electric field allows the production of charges at the surface of the droplet exiting the emitter and leading to the formation of the jet. The charges are transported by the flying jet. Depending on the processing conditions, a fraction of the total amount of charges produced at the emitter are lost along the jet by various phenomena (corona discharge, charge removal by humidity, solvent evaporation and secondary solvent electrospraying) while the rest of charges is deposited when the fiber enters in contact with the collector resulting in the electrospinning current flowing towards the ground (Fig. 1.10) [29].

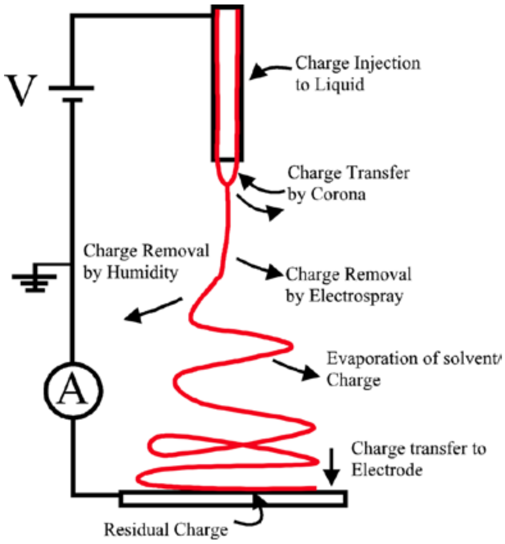

Fig. 1.10 Schematic diagram of a typical electrospinning experiment showing all the mechanisms of charge transports. Reprinted with the permission from [29]

1.3 Surface potential on a fibrous mat: in-situ charging during electrospinning and charge release

1.3.1 In-situ charging by electrospinning - development of the surface potential

As discussed in the former section, the charges are produced thanks to the high imposed electric field. The charges are then transported by the electrospun jet and in the end, when the solidified fiber hits the metallic collector, the charges are released towards the ground. The resulting continuous transfer of charges to the ground is thus responsible of an electrical current. Actually, the deposited fibers, which are in most cases dielectric materials, can maintain residual charges over a long period of time that can produce an external electric field oppositely to the electric field imposed by the power supply. For long times of deposition, charges accumulate in the deposited fibrous mat leading to the formation of a surface potential limiting the deposition of the incoming electrospun fiber.

The capacity of the charge storage of the fibrous mat is related with the nature and the structure of the fibers and the mat. The inner structure, such as impurities, crystallinities and polymer defects, plays also an important role by offering traps which can remain the charges on the surface or the core of the fibers and the mat. Former studies reported that surface traps might result from additives, impurities and broken polymer chains [29], [89]. The traps are located at the interface of different phases or crystalline regions. In fact, the existence of traps in the fibers decreases the charge release resulting in a growing number of charges stored on fibrous mats during electrospinning [90].

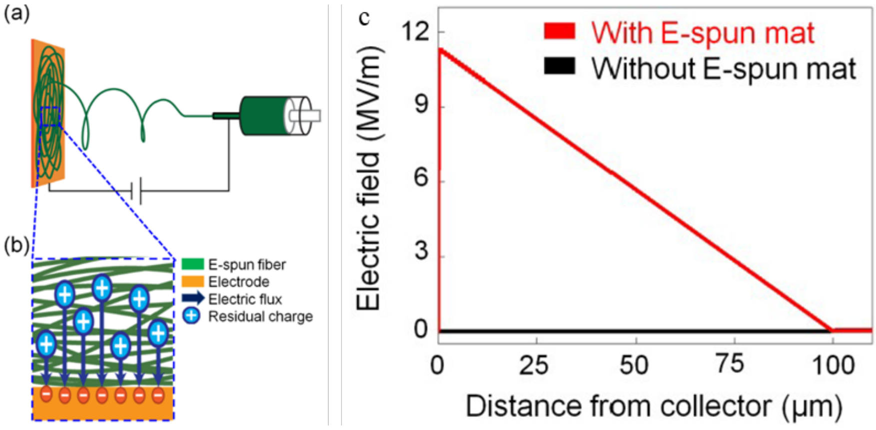

Fig. 1.11 (a) Schemes of the far-field electrospinning process. (b) Poly (vinylidene fluoride–co–trifluoroethylene) (PVDF–TrFE) is oriented with the direction of the electric field and the local electric field is generated by residual charges. (c) Simulation results of the local electric field by residual charge with or without electrospun mat

Reprinted with the permission from [91]

Regarding the accumulated residual charges on the fibrous mat during electrospinning, Choi et al. [91] have shown that a local electric field between the nanofibers and the electrode develops during the processing time. This effect is due to the fact that dielectric fibers are deposited on the collector and form an insulating porous layer limiting the charge release towards the ground (Fig. 1.11). The residual charges generate thus a local electric field related with the intensity of the volume charge density and the thickness of the fibrous mesh. The equation is presented as followed:

$$E = \frac{\rho t}{\varepsilon_r \varepsilon_0} \tag{1.5}$$

Where ρ is the volume charge density, t is the thickness of fibrous mesh, ε_r is the relative permittivity of the studied PVDF–TrFE polymer and ε_0 is the permittivity of vacuum. It indicates that the strength of the local electric field enhances with the increase of the thickness of the fibrous mat. However, such too simplistic model does not take into account the fact that the mat is a composite porous material made of polymer and air. Furthermore, the authors calculated an electric field higher than 11 MV/m which is much greater than electric discharge induced by the corona effect.

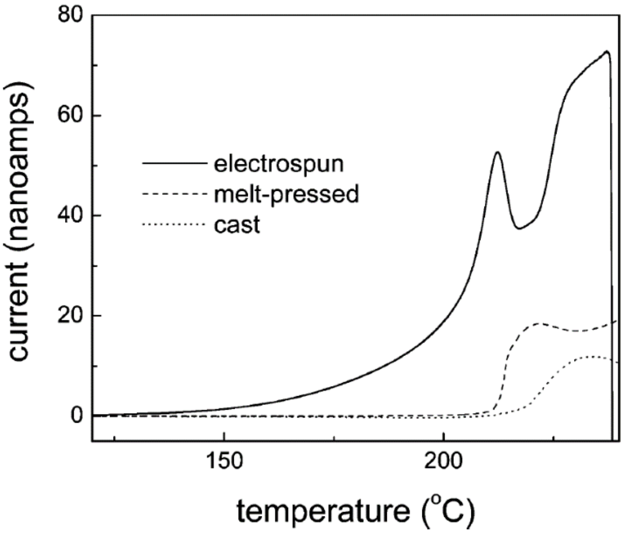

Fig. 1.12 Thermally stimulated relaxation spectra of PBT near melting

Reprinted with the permission from [90]

It is expected that during electrospinning dipole orientation and space charge separation occur in the fibrous mat and that injection of charges into the fibers is also possible[92]. Trapped charges in a dielectric can be measured thanks to the thermally stimulated current (TSC) technique. By increasing the temperature over the glass transition (T_g) for amorphous phase or over the melting point (T_m) for semi-crystalline polymers, charges trapped in the amorphous bulk or the amorphous-crystalline interface can be released and the intensity of this measured current is related to the amount of charges. In the case of PET mat [93] as well as poly(butylene terephthalate) (PBT),[90] it was shown by TSC that also for nanofibers charges are trapped inside the mats after electrospinning (Fig. 1.12). The charge storage was attributed to dipole orientation and space charge separation in the mat and charge injection into the fibers. In the case of PBT, a continuous charge release was observed from the T_g of PBT below its T_m indicating a dipole relaxation process which was not observed for PBT films prepared either by melt pressed or solvent casting processes. Around the T_m, a peak is observed being the signature of the release of charges trapped at amorphous-crystalline interfaces. [94], [95].

A mat having residual charges forms thus an electret which can be used in applications. Indeed, it was shown that the residual charges can enhance the filtration efficiency [96] [97] or improve cell spreading and proliferation on the nanofibrous scaffolds for biomedical applications [98]. Furthermore, measuring the surface potential continuously could be an interesting way to have an online control of the process of electrospinning during the time of production.

1.3.2 Charge release and surface potential decay of charged fibrous mats

Although the fundamental understanding is currently not completely achieved, it is well-known that different mechanisms are responsible for the decrease of the surface potential of a charged dielectric. First, the charges trapped on the surface of the material can be neutralized by opposite ions present in the atmosphere giving rise to a quick decline in the initial stage of the charge release. The charges trapped in the volume hold a much slower dissipation rate than surface decay. Indeed, the charges in the volume of the fibers must first diffuse from the core of the fibers to the surface of fibers before being released from the surface.

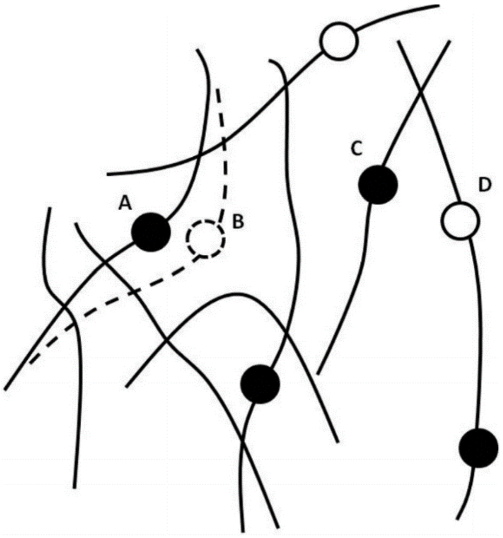

Fig. 1.13 Figurative representation of “trapped” changes (A, C…) and empty sites (B, D …) in an amorphous linear polymer. Reprinted with the permission from [92]

Furthermore, when a polymer material is subjected to a constant electric field, a current is produced, originated from two main mechanisms: an “absorption” current due to a gradual change in the polarization of the polymer and a "conducting" current attributed to charges hopping from trap to trap (Fig. 1.13) [92]. Furthermore, as an RC circuit in series, the total current decreases with time but without a simple exponential decay due to a wide distribution of relaxation times. It is worth noting that the charge transport is favored in loose network of amorphous polymer phase [92].

1.3.3 Surface potential decay of fibrous mat charged by corona effect

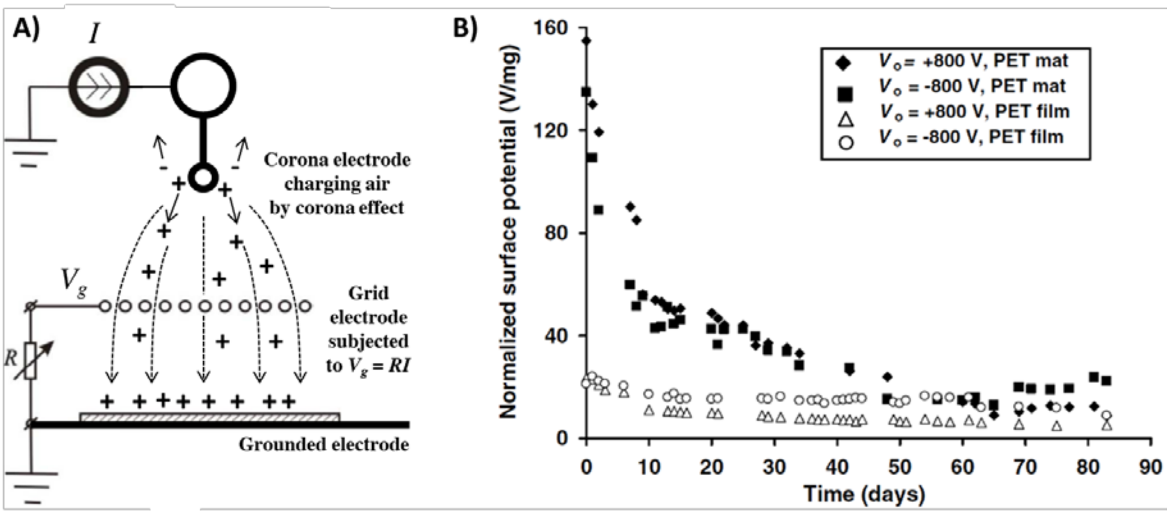

Fig. 1.14 A) Example of a triode-type electrode arrangement for the charging by corona effect of a dielectric material deposited on the grounded electrode adapted from [99]. B) Dependences of the surface potential normalized to unit mass on storage time at 25 ℃ and RH = (38–40) %[93]

Tabti et al. studied the charge storage and release of PP non-woven mats for electret applications [99]. The mats were initially charged by corona effect. Such technique consists in applying a high voltage to a thin needle or wire corona electrode inducing a high local electric field leading to the production of ions in the air. The ions travel then towards the dielectric material which is deposited on a grounded electrode. In a triode-type arrangement (Fig. 1.14), a supplementary grid electrode is placed over the material to be charged. In this case, the grid is connected to the ground through a resistor *R* whereas the corona electrode is connected to a power supply delivering an imposed current *I*. This configuration is interesting because the production of ions is controlled thanks to the fact that the grid is subjected to a controlled potential V_g = RI driving the charge carriers through the grid and towards the dielectric sample. The potential generated at the surface of the sample is limited by either the potential of the grid or by the partial discharge voltage of the sample [99]. Furthermore, the authors observed that the charge release was faster at higher applied voltage. Ignatova et al. studied the charge release of PET materials in the forms of films and electrospun mats for electret applications [93]. The materials were also initially charged by corona effect. It was shown that the initial surface potential per unit mass was higher for the mats than for the films thanks to their high specific area subjected to the corona effect. Furthermore, a surface potential decay was observed in the case of the mat whereas low constant voltage was measured in the case of films. The discharge observed in the case of the mats was attributed to several effects such as relaxation of the separated space charges and dipole disorientation or injected charges within the bulk of the fibers[93], [100]. Thakur et al [101] studied the charge decay of electrets formed by fibrous mesh obtained from the meltblown process. The meshes were charged by corona effect. It was shown that the surface potential decay follows a double exponential decay [101] (Fig. 1.15):

$$\xi(t) = a_s e^{-t/\tau_s} + a_l e^{-t/\tau_l} \tag{1.6}$$

Where $\xi(t)$ represents the normalized surface potential, τ_s and τ_l the two relaxation times characteristic of a short time and a long time decay respectively. Compared with the poor fitting by the single exponential function, the double exponential function allowed an accurate fitting with the experimental data proving the presence of two mechanisms of charge release. The short time decay was attributed to charges located onto the surface of the fibers whereas long time decay was allotted to the release of bulk charges produced by polarization during corona charging. Each parameters of the double exponential decay were studied as a function of the parameters (applied voltage, electrode distance and charging time) used during corona charging process. In all cases, the double exponential model allows a perfect fitting of the experimental data. Nevertheless, the characteristic data obtained from the model were not related to the structure of the mat complicating the analysis of the results.

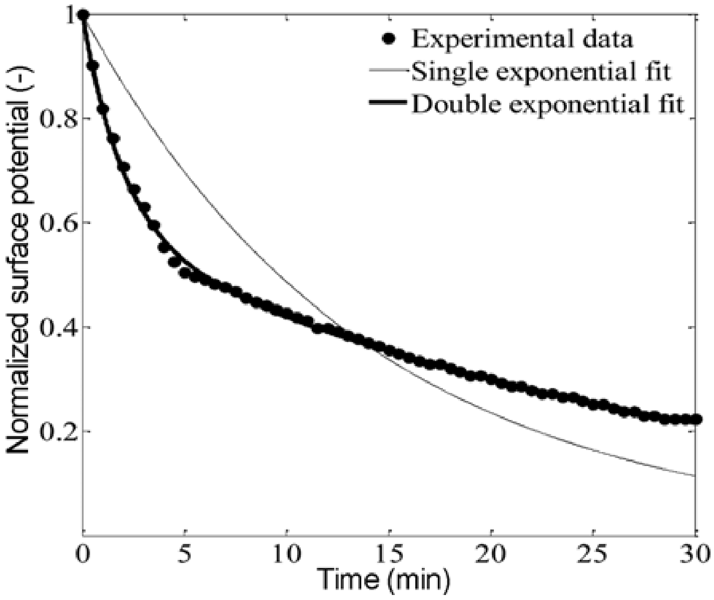

Fig. 1.15 Comparison between single and double exponential functions of charge decay in fibrous electrets

Reprinted with the permission from [101]

1.3.4 Surface potential decay of fibrous mat charged by in-situ electrospinning

The process of electrospinning can be seen as an in-situ charging process during the elaboration of the fibrous material. Thus, the distribution and the amount of every kinds of charges should be different between a mat prepared from electrospinning and the same fibrous structure charged by corona effect. Indeed, it is expected higher charge injection in the bulk of the fibers and higher surface charge density in the case of electrospinning. After stopping the process of electrospinning, no more charges are brought from the jet. However, starting from this point, the mat releases its charges. The kinetic of charge release, which is directly related with the mat surface potential decay, depends on the morphological and the material properties of the mat as shown for mats charged by corona effect. Furthermore, parameters such as ambient temperature and humidity may also influence the surface potential decay. Indeed, high temperature could offer more energy for the trapped charges to bring enough mobility for a fast dissipation. The moisture in the surrounding air could induce a water-adsorption layer increasing the charge distribution on the surface of polymer materials and thus favoring the surface conductivity [102]. Furthermore, it is expected that in the case of electrospinning, fibers made of amorphous polymer with moreover, residual solvent, should favor the charge release.

Ignatova et al [93] compared both in-situ charging by electrospinning and corona charging method, unfortunately they didn't comment how the electrospun mats were stored and no information was given concerning the duration between the elaboration of the mats and the characterization of the surface potential decay. Thus, no conclusion can be drawn. Tong et al. studied the effect of the charges stored in PLA electrospun mats for biomedical applications [98]. The mats were produced by applying a positive or a negative voltage on the emitter. They observed that negatively charged mats retained the charges for a longer period but such mechanism was not explained.

1.4 The role of surface potential on the building of structured scaffolds and applications of 3D structured scaffolds

Former sections have shown that electrospinning leads to the production of fibrous materials with embedding charges located both at the surface and in the bulk. The charge release towards the grounded collector is favored by the fact the collector is generally a perfect conducting metal plate or cylinder. However, if an insulating electrode is used as a collector instead of a conducting one, charges cannot be efficiently released leading to a high amount of stored charges leading to the formation of an electric field which is opposed to the deposition of the incoming electrospun fiber. If a patterned collector formed by conducting as well as dielectric areas is used, the way the charges are released is much more complex. It is expected that the dielectric patterns of the collector avoid the efficient charge release of the portion of the mat directly deposited on it. Thus, such mat portions should be subjected to a high repulsive surface potential compared to the mat portions directly deposited on the conducting patterns. In the next sections it will be shown the different kinds of structures (1D, 2D, 3D, with electrospun fibers only or with electrospun fibers and electrosprayed particles) which can be obtained by playing with the geometry of the patterned collector. Then, the mechanism of structuration favored by an electrostatic template will be explained.

1.4.1 1D aligned fibers

When a patterned collector with conducting and insulating areas is used, it was shown that it affects the way the electrospun fiber is deposited by modifying the electric field at the vicinity of the top surface of the mat under fabrication. For example, it was found that aligned fibers can be obtained using a collector with parallel rectangular conducting electrodes separated by a dielectric material or more simply by an air gap [103]–[105]. As shown in Fig 1.16, when landing on the collector, the fiber is subjected to two kinds of electrostatic forces: a force F1 induced by the external electric field and a coulombic repulsive force F2 between the landing jet and the collector or the already deposited nanofibres[106], [103]. The fiber follows first the direction of the electric field lines towards the parallel electrodes and then lands across the gap. The suspended fiber strand can retain its charges inducing a positively charged electrostatic template and image charges created at the surface of the grounded electrode. Thus, the conducting patterns generate a coulombic attractive force stretching the fiber across the gap with perpendicular orientation. Furthermore, because the electrostatic template remains highly positively charged, it induces repulsive coulombic forces with the incoming electrospun jet enhancing the fiber alignment. Thus, such configuration leads to the production of poorly dense aligned fibers crossing the gap and a highly dense non-woven fibrous structure covering the conducting parallel electrodes. Furthermore, Liu et al. found that alignments of suspended fibers improved substantially with increasing the gap size [107]. This can be probably explained by the fact that the repulsive resultant force induced by the electrostatic template is higher for the largest gap.

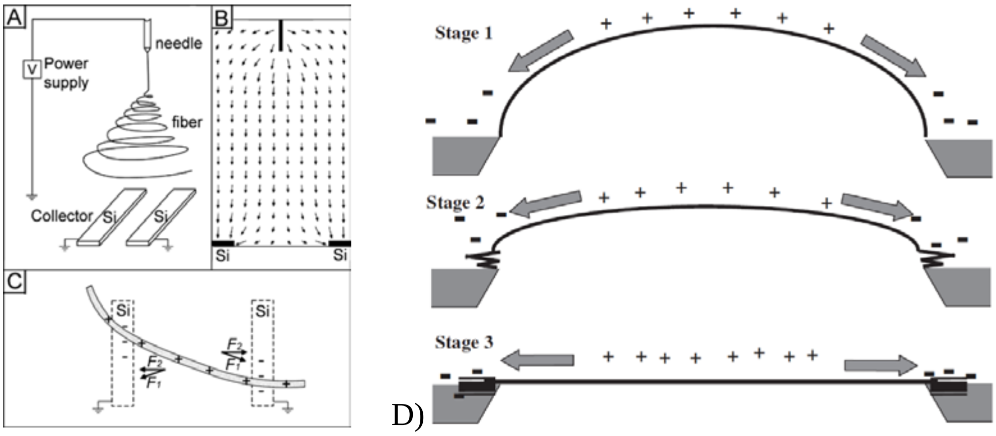

Fig. 1.16 (A) Schematic illustration of the electrospinning setup to generate uniaxially aligned nanofibers. The collector contained two pieces of conductive silicon stripes separated by a gap. (B) Calculated electric field strength vectors in the region between the needle and the collector. The arrows denote the direction of the electrostatic field lines. (C) Electrostatic force analysis of a charged nanofiber spanning across the gap. The electrostatic force (F1) resulted from the electric field and the Coulomb interactions (F2) between the positive charges on the nanofiber and the negative image charges on the two grounded electrodes. Reprinted with the permission from [103]. D) Principle of fiber alignment. Stage 1: electrospun fiber with residual positive charges is attracted to the negatively charged steel blade. Stage 2: electrostatic force pulls the fiber towards the tip of the steel blades under the direction of electric field lines. Stage 3: fiber is fully stretched across the gap between the steel blades. Reprinted with the permission from [106]

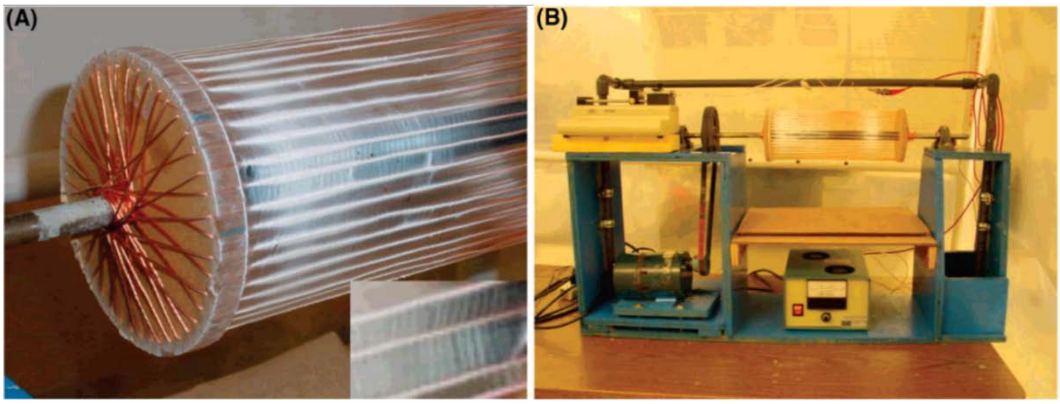

Fig. 1.17 (A) Plexiglas disk with copper wires. Electrospun nylon nanofibers are collected on the copper wires. The nanofiber mat shows stratified layering in the magnified image. (B) Apparatus for rotating the copper wire drum during electrospinning

Reprinted with the permission from [108]

A wire drum collector was used by Katta et al [108] in order to prepare a high amount of aligned nylon-6 nanofibers. It is shown (Fig. 1.17) that such configuration allows an efficient fiber alignment perpendicularly to the axis of the wires. By fabricating electrospun fibers with different times of production (from 5min to 2.5h), the authors found that the fiber alignment disappears gradually with time. A good alignment was obtained for time of production lower than 15 min whereas highly random mats were obtained over all the surface of the collector for the largest times of production. This result is of prime importance, because it seems that the electrostatic template effect disappears after a certain time of production. To the best of our knowledge, this mechanism was not studied.

1.4.2 An electrostatic template for the fabrication of 2D fibrous structures

The electrostatic template effect used for the 1D fiber alignment was expended for the building of various 2D structures. Instead of parallel conducting electrodes, it is possible to use different kinds of collector geometries leading to the fabrication of various fibrous 2D structures.

For example, it was proposed a collector using two pairs of electrodes which were grounded alternately during electrospinning (Fig. 1.18). In such a way, aligned fibers were only deposited between the grounded electrodes allowing the fabrication aligned multi-layer structures with several principal directions perpendicular to the grounded electrodes [109]. However, this method is limited. First, the fiber alignment is lost very rapidly leading to random deposition. Second, there was a limitation in the area of the resulted assembly: an increasing number of fibers lost the parallel alignment with overlapping fibers in the case of large intersecting areas.

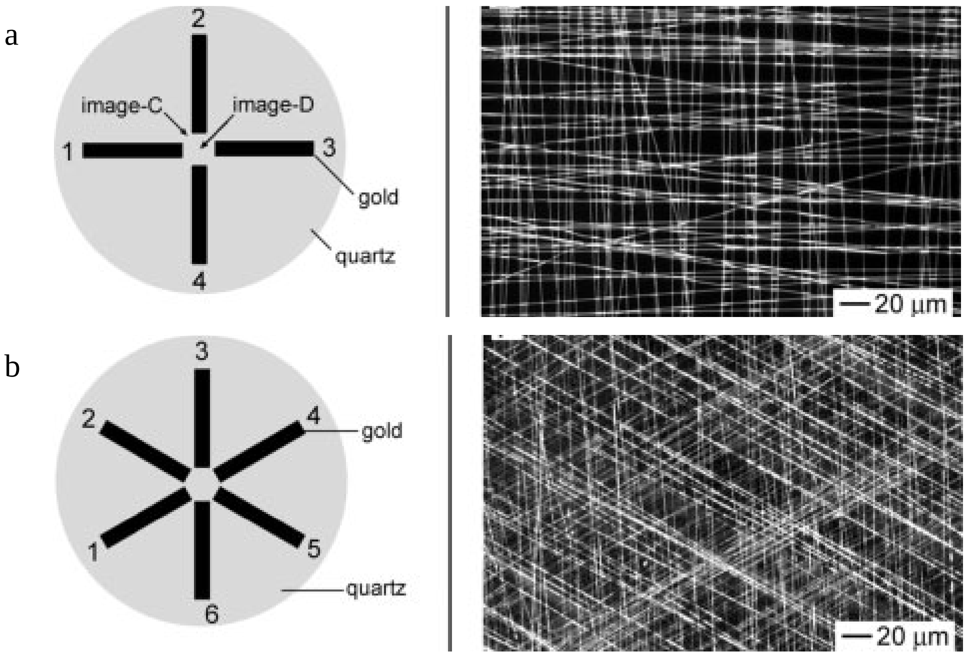

Fig. 1.18 Gold electrodes patterned on a quartz substrate. (a) The opposite electrodes were grounded sequentially every 5s to achieve aligned fibers distributing in 2 directions with an intersection angle of 90°; (b) The opposite electrodes were grounded sequentially every 5s to achieve aligned fibers distributing in 3 directions with an intersection angle of 60°
Reprinted with the permission from [109]

Several authors studied deposition of electrospun nanofibers on complex micropatterned collectors in order to achieve various kinds of structures [110], [111]. For example, Lavielle, et al [112] used different micro-patterned collectors made of conducting or dielectric protrusions as shown in Fig 1.19. The controlled deposition was both influenced by the geometry and the electrical properties of the patterns. Multiple "micro spider-webs" or perpendicularly interconnected microgrids were obtained using a collector made of a matrix of conducting protrusions. When dielectric protrusions where used aligned fibers were observed between the dielectric blocks along the thin conducting paths formed at the bottom of the collector (Fig 1.19 Bc). In the case of patterns made of dielectric micro-holes having a conductive bottom can be filled by the nanofiber.

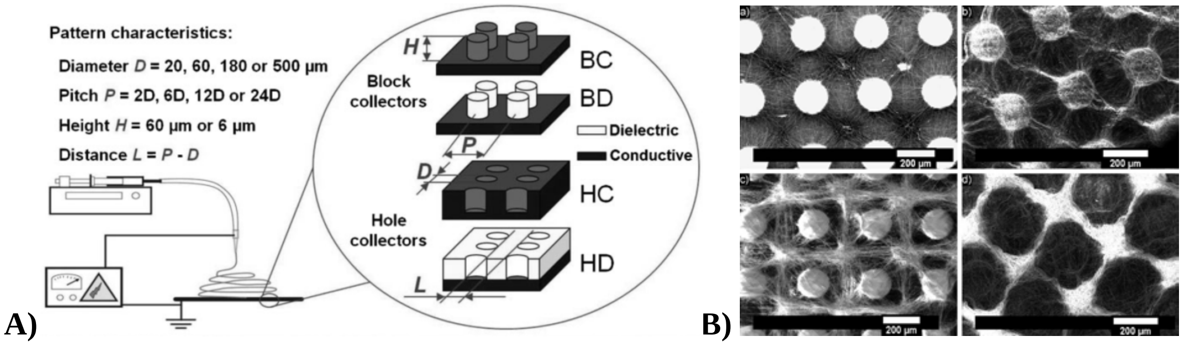

Fig. 1.19 A) Electrospinning on micropatterned collectors with different characteristic sizes and electrical properties. B) Nanofibrous membranes obtained with Blocks of D=180µm, H=60µm and L=3H=360µm. BC collector: (a) Topside view and (b) downside view. BD collector: (c) topside view and (d) downside view. Reprinted with the permission from [112]

Similarly, Zhao et al [113] electrospun nanofibers on a metal grid and a gauze collector to generate nanofibrous patterns with different topographies. Numerical simulation allowed the estimation of the electric field over the patterns in these cases. The authors found that the electric field lines were concentrated on the convex parts of the metal collector grid. The authors explained the favorable deposition on these areas instead over the holes of the grid. However, it is worth noting that such numerical simulation did not take into account the repulsive charges which should play an important role. Indeed, the specific observed fibrous structure may not be due only by the electric field induced by the geometry of the collector: it should be a combined effect between the electric field imposed by the electrode geometry and the one induced by the charges carried by the suspended fibers. In the same manner, electrospinning was carried out on knit patterns obtained from a fabric mesh coated with a conducting gold layer [114]. In agreement with the previous results, most of the fibers are deposited on the conducting mesh whereas aligned fibers were observed in between.

The charges remaining on the surface of fiber portion suspended in the air or deposited on the dielectric portions of patterned collectors should play an important role on the way the fibers are deposited in the form of 2D fibrous structure. Such effect was clarified by Nedjari et al [115]. Indeed, the authors proposed to fabricate 2D fibrous composite structures made of a thin layer of electrospun PLA nanofibers coated by a layer of electrosprayed calcium phosphate microparticles as shown in Fig. 1.20 a and b. In this manner, a highly selective deposition of the particles over the wall of the collector was observed. Patterns of characteristic sizes as small as 40 μm were reproduced by the particles when only a very thin layer of fibers was previously deposited. When electrosprayed particles were deposited without the presence of the layer of electrospun fibers, it was shown that particles covered the pattern walls but also covered the bottom of the pattern holes (Fig. 1.20 g). Thus, the electric field generated by the geometry of the collector alone doesn't allow guiding the controlled deposition of particles. The presence of the suspended fiber strands forming an electrostatic template being the replication of the geometry of the pattern holes is thus a necessary condition to drive the deposition of the particles. The force induced by this repulsive electric field is high enough to guide the particles and should also impact the way the fibers are deposited during electrospinning explaining that more fibers are deposited on the pattern walls instead over the pattern holes.

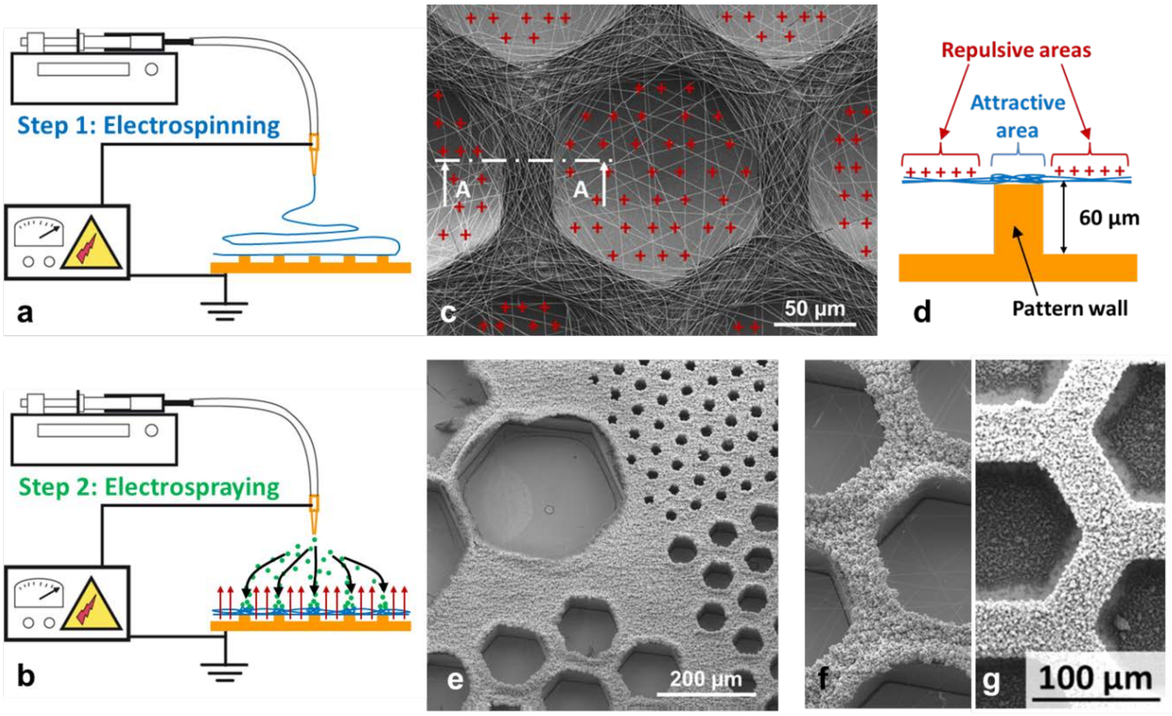

Fig. 1.20 Principle of the Electrostatic Template-Assisted Deposition of electrosprayed microparticles on electrospun nanofibers. a) Step 1 of the process: electrospinning on a micropatterned collector. b) SEM picture showing electrospun PCL fibers deposited on a honeycomb pattern, the suspended fiber portions are positively charged. c) Cross-section A-A of a pattern wall showing the repulsive suspended electrospun fibers and the attractive area located above the wall. d) Step 2 of the process: electrospraying on the electrostatic template formed by the thin layer of fibers. e) HA electrosprayed particles on a thin layer of PCL fibers obtained after only te = 45s of electrospinning, a highly selective deposition is observed over honeycomb patterns with a wall width of Ltop = 20 µm an internal diameter ranging from Lbot = 40 to 360 µm. f) Detail of the previous picture for honeycomb patterns of internal diameter of 160 µm. g) HA electrosprayed particles on a patterned collector without the presence of the layer of electrospun fibers: no selective deposition is observed. Reprinted with the permission from [115]

1.4.3 3D fibrous structures

The 2D electrospinning/electrospraying process was expended in 3D. It was reported that the simultaneous electrospinning of PLA fibers and electrospraying PEO particles on a honeycomb patterned collector (Fig. 1.21 a) leads to the generation of 3D structured scaffolds with pores having the diameter of the honeycomb patterns of the collector [116]. The build-up process was studied by observing the construction after the first 3min of deposition (Fig. 1.21 b) by electrospinning and electrospraying and for longer time of production (Fig. 1.2 c). It is shown that after 3 min of deposition that most of electrospun fibers and particles are deposited on the wall of the patterned collector in the form of bundles with aligned fibers interconnected with the particles. Over the hole of the honeycomb patterns, only few stretched fibers are suspending and no particles were detected proving that the electrostatic template effect was very efficient. The suspended fibers form the honeycomb electrostatic template leading to the selective deposition of particles. Moreover, numerical simulations were carried out taking into account the external field imposed by the emitter-collector electrodes as well as by the suspended fibers (Fig. 1.21 e). The calculation of the vertical component of the electric field shows that (i) highly repulsive areas are formed over the honeycomb walls (in red) and (ii) a highly attractive areas are formed over the walls (in blue). Finally, the particles play a pivotal role in the 3D structuration. Indeed, the particles insure the electric interconnection of the fibrous bundles located over the walls of the patterns maintaining the honeycomb shape of the electrostatic template during long time of production. This was evidenced when electrospinning was carried out without electrospraying: in such situation no 3D structuration was achieved as shown in Fig. 1.21 d. A similar process was used to fabricate 3D constructs made of PLA fibers and phosphate calcium particles by alternating the deposition of fibers and particles layers (Fig.1.22) proving that the process can be expended for a wide range of materials for various applications.

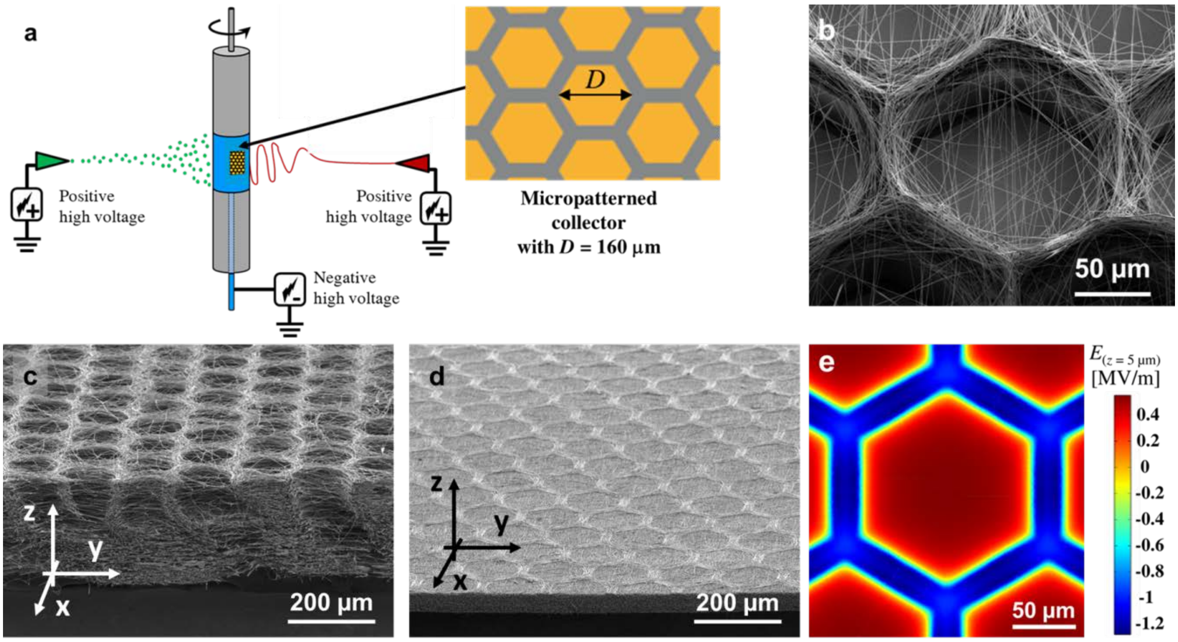

Fig. 1.21 (a) Schematic of the process to produce composite scaffolds by coupling fibers and particles. The diameter D of the honeycombs was 160 µm. The width and the height of honeycombwalls were respectively 20 µm and 60 µm; (b) SEM picture obtained after 3 min of electrospinning and electrospraying on a honeycomb collector with D = 160 µm; (c) 3D columnar structures obtained for D = 160 µm after 1 h of production; (d) Fibrous structure obtained with the same operating conditions and time of production than for (b) but without electrospraying; (e) Simulation of the vertical component of the electric field 5 µm above a charged fibrous layer deposited on the top of a honeycomb pattern of D = 160 µm. Reprinted with the permission from [116]

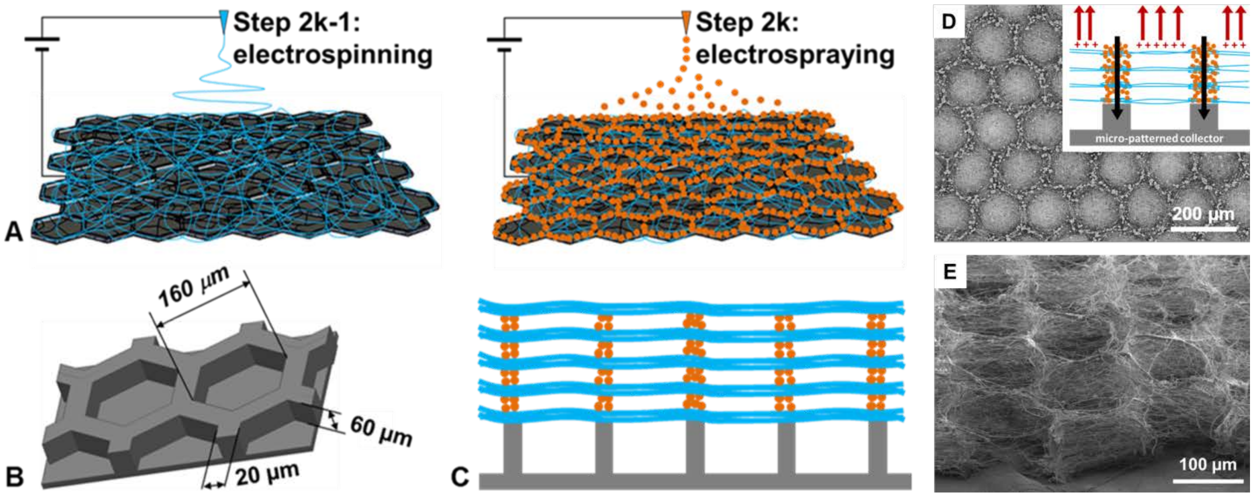

Fig. 1.22 (a) Design of the honeycomb-like scaffolds. (A) Odd steps: electrospinning process. Even steps: electrospraying process; (B) Geometry of the honeycomb collector; (C) Both steps were repeated to achieve the production of a 3D multilayer scaffold with HA microparticles mainly located over the wall of the honeycomb collector thanks to the electrostatic template effect; (D) Top view of a PCL-HA 3D scaffolds obtained from deposits of four bilayers of PCL fibers and HA particles. The inset shows a schematic view of the cross section of this type of scaffold. The black arrows represent the conductive paths formed by the aggregated fibers and particles in contact with the walls of the collector patterns. The red arrows represent the repulsive areas due to the suspended charged fiber segments; (E) Cross-section of a PCL-HA 3D scaffold showing the 3D microcavities sparsely filled by PCL fibers. Reprinted with the permission from [117]

In agreement with what is was observed for electrospinning/electrospraying on patterned collectors, if 3D structures are expected with only electrospun fibers (i.e. without electrosprayed particles), only fibers showing a bimodal distribution of the fiber diameter can achieve good results. Indeed, as shown in Fig. 1.21 d and Fig. 1.23 b, only flat fibrous mats are obtained when PLA fibers having a narrow distribution of the fiber diameter are electrospun with patterned collectors. In this case, the fiber structuration was only achieved at the very first time of electrospinning. For longer times of deposition, the structuration rapidly disappeared and no 3D structuration is obtained. When PCL fibers are electrospun with patterned collectors, the situation is very different and a 3D structuration is achieved (Fig. 1.23 c and d [118]). Indeed, in this case, the fibers present a bimodal distribution of the diameter and in such situation, the thick portions of the electrospun fiber played the same role as the particles in the electrospinning/electrospraying technique. As shown in Fig. 1.23 e and f the thick fiber portions are more charged, because less elongated, than the thin portions. Thus, they are more influenced by the electrostatic template formed by the thin fiber portions. Furthermore, the thick fiber portions insure a good electric contact between the fibrous bundles covering the pattern walls maintaining the electrostatic template over long time of production necessary for a 3D structuration.

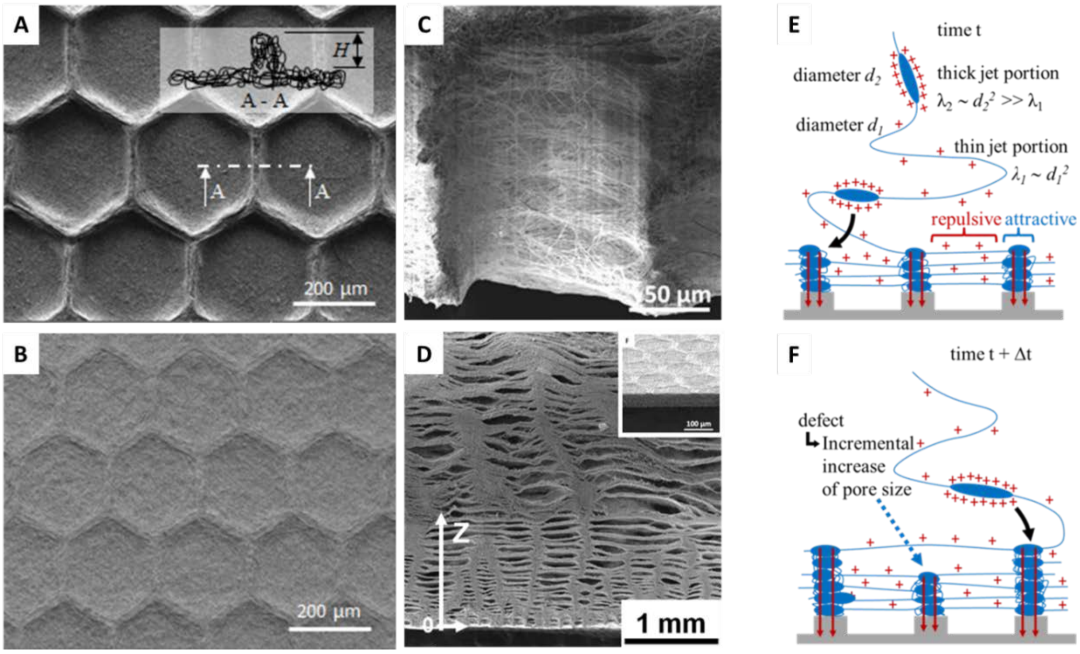

Fig. 1.23 (a) SEM image of a PCL honeycomb scaffold obtained with D_p = 360µm; (b) SEM image of a PLA honeycomb scaffold obtained with D_p = 360µm; (c) SEM image of a porous column with controlled pore size (D =160 µm) in a PCL scaffold; (d) Proposed mechanism for the construction of porous columns with controlled pores size; (e)Proposed mechanism for the merging of two columns; (f) SEM image of the cross-section of a PCL scaffold (1h, D = 160 µm). Reprinted with the permission from [118], [119]

1.4.4 The case of nanofiber self-assembling during electrospinning

In the previous sections it was shown how 2D and 3D structuration can be obtained when patterned collectors are used. In fact, simple electrospinning using a simple flat collector can also lead to the fabrication of 3D fibrous structures thanks to a self-assembling approach. Such technique could be interesting because of its low-cost. Deitzel et al [120] found that mats produced from PEO fibers having a wide distribution in diameter have a 3D honeycomb-like structure. It has also been reported that beaded fibers obtained from low polymer concentration solutions led to the formation of honeycomb-like structures [104], [121]. Ahirwal et al [122] studied the electrospinning of bimodal PCL fibers on flat collectors. At the very first times of electrospinning, a pseudo-random deposition of the fiber is achieved. However, due to the bimodal distribution of the diameter, only the thick portions are touching the flat collector whereas the thin ones are suspended (Fig 1.24 c). Monte Carlo simulations demonstrated that a random deposition of bimodal fibers leads to the formation of a heterogeneous fibrous surface with bundles formed by the aggregation of the thick fiber portions linked by a network of thin suspended fiber portions. The thin suspended membrane suspended in the air remains charged: an electrostatic template is thus formed engaging the 3D structuration. Furthermore, the repulsive initial areas formed by the suspended fibers are not uniform in size. Thus, a heterogeneous surface charge density is achieved explaining that non-regular 3D structures are generally obtained by fiber self-assembling [122], [123]. In few cases, regular 3D structures can however be obtained as demonstrated by Yan et al (Fig. 1.24 f-i) [121]. Finally, the self-assembling process can also be achieved in a similar manner by simultaneous electrospinning / electrospraying on flat collectors as observed by Lavielle et al [32].

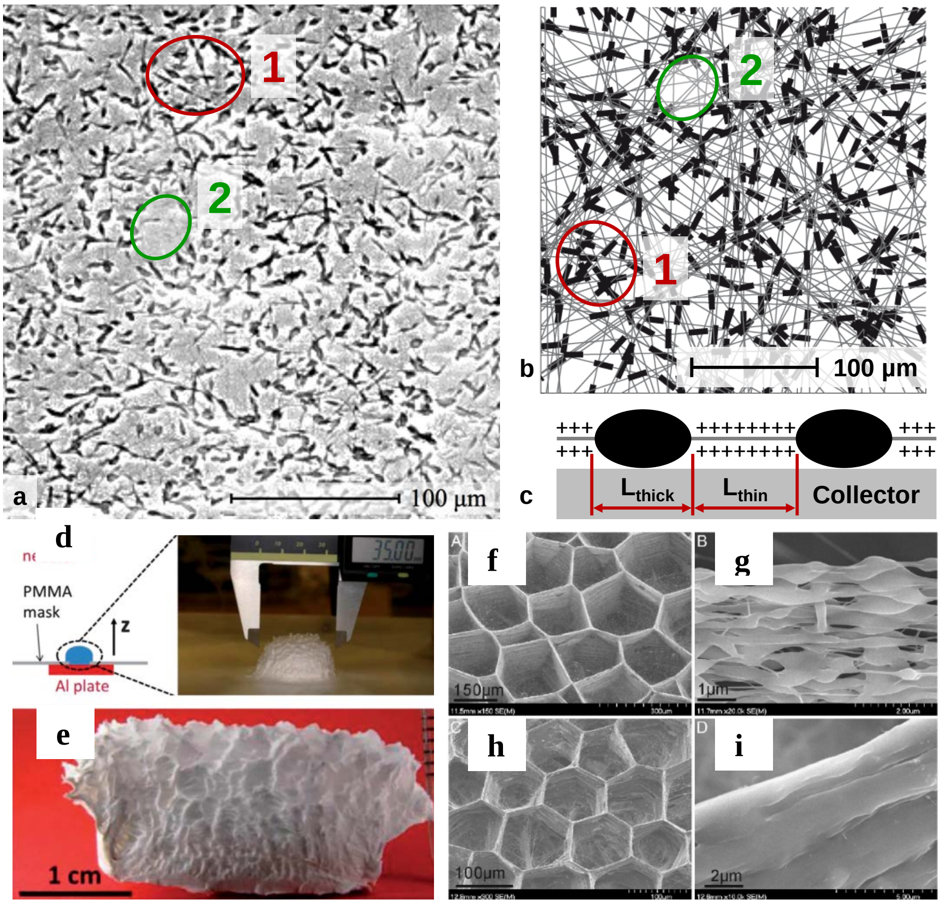

Fig. 1.24 (a) SEM image showing the very first moments (10 s) of the deposition of irregular beaded electrospun nanofibers. Region 1 shows the aggregation of thick fiber domains, whereas only thin fibers cover region 2; (b) Monte Carlo simulations of the previous image showing the aggregation of thick fiber domains after a random deposition of 150 fibers with characteristic length Lthick = 15 μm and Lthin = 100 μm.; (c) Schematic section of a heterogeneous fiber deposited on the collector; (d) Thick scaffolds obtained by focusing the electrospun jet through a PMMA mask; (e) Cross-section of a 15mm thick scaffold; SEM images showing the surface morphology and wall structure of the HNFSs of PVA and PEO electrospun at different conditions: (f, g) PVA, concentration 6%, 22kV, on plastic film; (h, i) PEO, concentration 16%, 22kV, on Al substrates

Reprinted with the permission from [121] and [122]

1.4.5 Recent applications of structured fibrous structures

Besides the remarkable features of electrospun fibers mimicking the extracellular matrix (ECM) of tissues such as skin, bone or muscles. The high porosity and large specific surface area endow such fibrous mats for great potential of applications in filtration, tissue engineering or drug delivery. [124]–[126]. The 3D fibrous structures obtained when using patterned collectors render electrospinning more attractive for targeted applications. Some recent applications of such 3D structures are shown in this section.

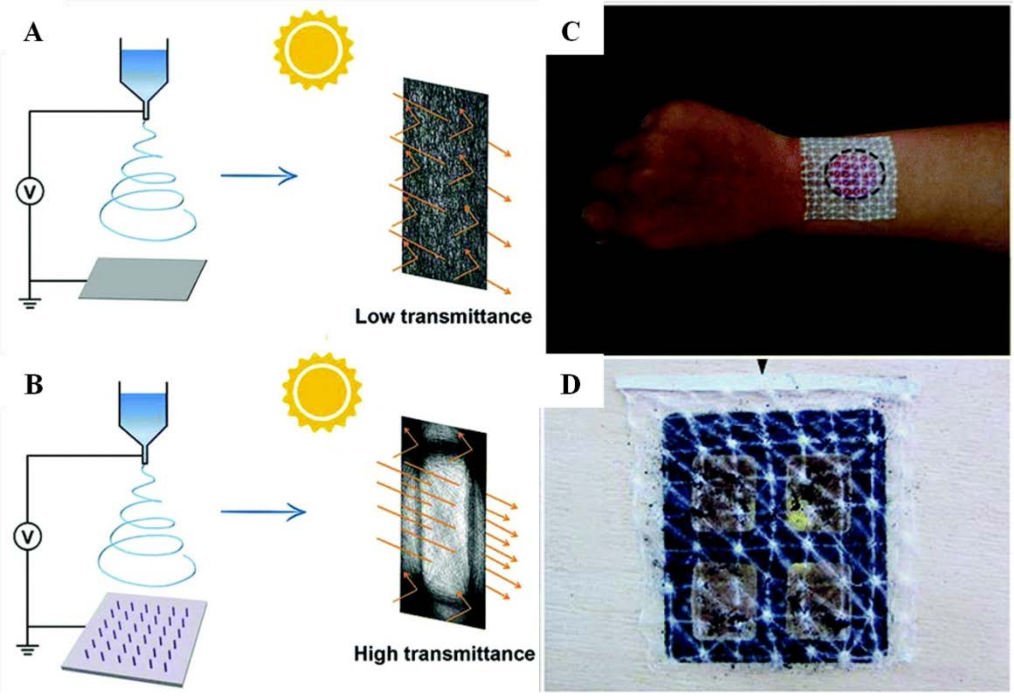

Fig. 1.25 (A) mechanism of the light passing through the isotropous mat; (B) mechanism of the light passing through the anisotropous mat; (C) visually monitoring the wound healing (red circle on the student's aim was to mimic the wound); (D) the black dust was filtered on the mat with flowing time at 3min.

Reprinted with the permission from [127]

According to previous reports on electrospinning, the high transparency of the nanofibrous scaffolds is a key parameter for various specific applications. Fig. 1.25 a and b present the difference in the mechanisms of light penetrating between the isotropic and anisotropic mats. Whereas strong light scattering occurred when isotropic random mats are used leading to a low light transmittance. In the case of mats having an anisotropic fiber orientation, an improved light transmittance was observed. This property might be interesting for wound dressing applications for which anisotropic transparent dressings allow the doctors to detect the wound status visually [127], [128]. Anisotropic mats can also found applications for air quality control allowing the detection of the dust blocked on the fibrous mesh filter decreasing the overall transparency [129]–[133]. In the case of solar cells application, patterned fibrous scaffolds exhibited improved optical properties enhancing the electrical conversion efficiency [134], [135].

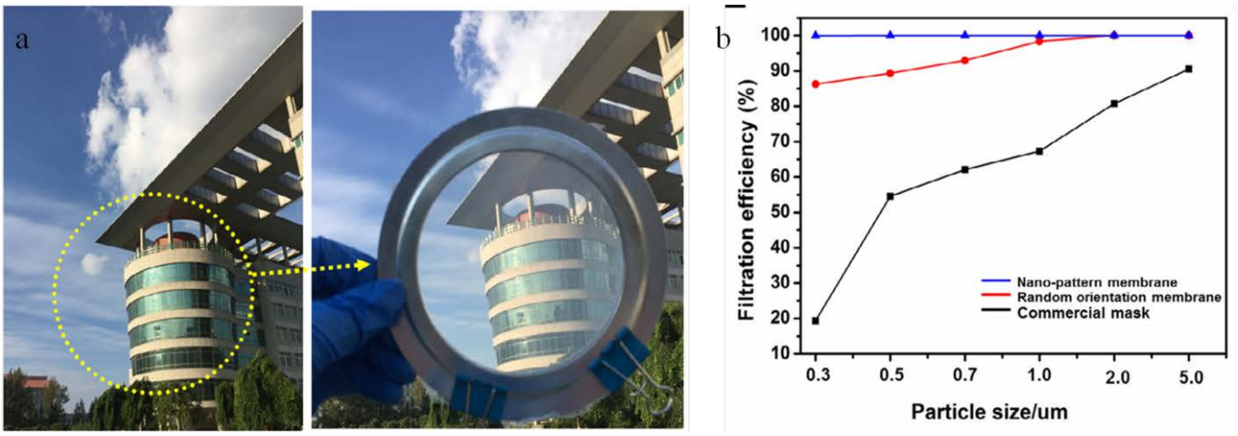

Fig. 1.26 (A) Photographs of a typical transparent electrospun nanofiber membranes with optical transmittance; (B) Comparison of filtration efficiency of the three samples for various PM particle sizes. The insets are the corresponding pictures for the membranes. Reprinted with the permission from [136]

Similar research was developed by Cheng et al [136]. In Fig. 1.26, the scenery spot was clearly observed through the freestanding nanofiber membrane with high transparency. Regarding the filtration efficiency, Polyamide 66 transparent nano-pattern window screen can filter almost 100% of the particles in the size ranging from 0.3µm to 5µm which was much higher than those tested with the randomly orientated mats. The high filtration efficiency of the tailored membrane offers a new route for people to conquer the threat of PM2.5 in modern time.

Former studies already demonstrated that mimicking the micro/nanostructure of tissues plays an important role for applications using bioengineered scaffolds [26], [137], [138]. Aiming to promote the cell ingrowth and differentiation in the structured scaffolds, the optimal pore size should be located between 100µm and 400µm by providing guidance cues to supply oxygen and nutrient for cell migration and tissue regeneration [139]. 3D structured scaffolds fabricated with patterned collector exhibit a stimulatory impact on the cell attachment, growth and differentiation, favoring thus the re-epithelialization of wound healing [140]–[143]. Combined with the addition of active inorganic ions, such as Ca, Si, Mg, etc, structured scaffolds can have positive effects by accelerating the skin wound healing in a short time [144]–[148] or bone regeneration [117].

Fig. 1.27 shows the comparison of the morphologies of a traditional fibrous mat, a self-assembled nanofiber/microparticles scaffold and a patterned nanofiber/microparticles 3D scaffold. For the traditional fibrous mat, the pores formed by the intersection of fibers were not large enough for cell ingrowth resulting in cell only adhering on the surface of the mesh. The self-assembled nanofiber/microparticles scaffold contained spherical pores in micro size in favor of the migration of cell within the scaffold. However, most of pores were isolated inhibiting the application in the cell culture. Due to the controllable deposition of fibers and particles on the metal grid, sufficiently large and regular pores were generated in the patterned nanofiber/microparticles 3D scaffolds facilitating the cell proliferation more efficiently. These scaffolds are good candidates to support cell proliferation for bone tissue regeneration [149]. Zaiss et al. and Liu et al. achieved the similar result regarding the application of structured scaffolds on bone tissue engineering [150], [151].

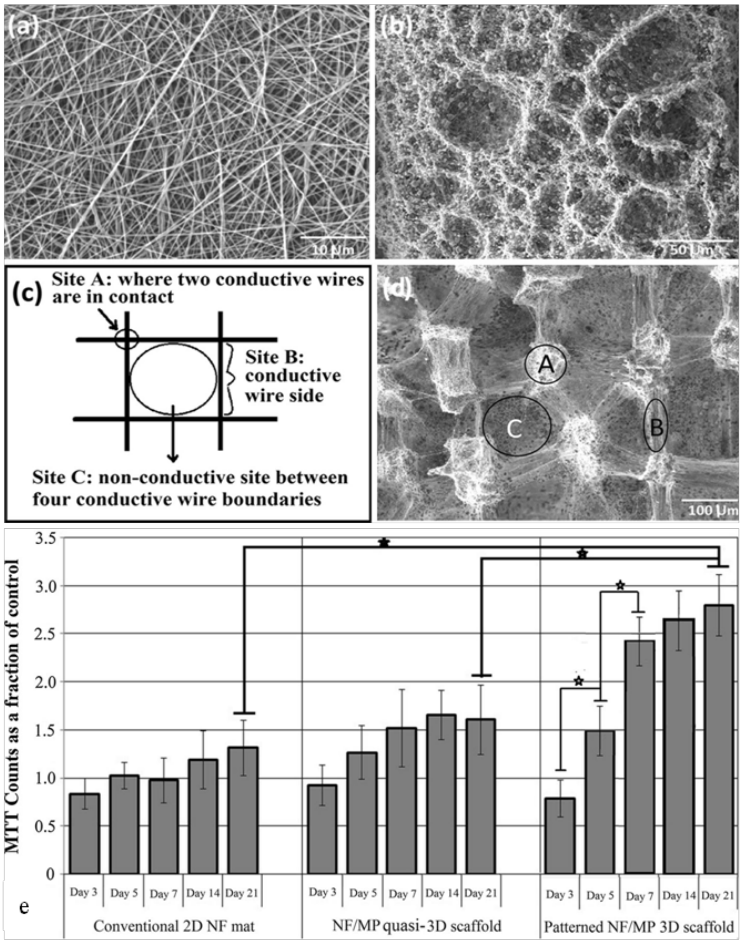

Fig. 1.27 SEM images of (a) conventional nanofiber PCL mat, (b) nanofiber/microparticle quasi-3D scaffold, (c) Schematic illustration of different regions in the conductive metal mesh, (d) Patterned nanofiber/microparticle 3D scaffold, (e) MG-63 cell proliferation on the prepared 2D & 3D scaffolds at different time points. Significant difference of investigated groups is denoted as (*$P < 0.05$). Error bars represent the standard deviation of three independent measurements

Reprinted with the permission from [149]

1.5 Conclusion

In this chapter, the principles of electrospinning and electrospraying were presented briefly in the beginning. Then, the generation of charges by electrospinning and the mechanism of charge release and time dependence of surface potential on fibrous mats were introduced. Finally, it was presented the important role of the surface potential generated by suspended fibers deposited on patterned collectors for the building of 2D and 3D structured scaffolds. It was shown that suspended charged fibers form an electrostatic template which plays the pivotal role in the controlled deposition of the jet allowing the fabrication of 2D and 3D structured fibrous mats.

Electrospinning can thus be treated as an in-situ charging process. In order to get more insight into the process, it is important to measure the charges carried by the jet as a function of the processing conditions: this will be the subject of chapter 2 in which a new method is proposed.

The process of electrospinning is thus an interesting way for the direct fabrication of electret filters. It is worth noting that, compared to the corona charging process, in-situ charging by electrospinning should be more efficient to inject charges in the bulk of the fibers. This feature is important for electret applications knowing that the bulk charges are released for the longest times. Indeed, the charge release of such electrets is expected to follow a double exponential decay having one short time mainly allotted to the surface charge release and a long characteristic time devoted to the release of bulk charges. The few articles dealing with this subject studied only polymer materials dedicated for electret filtering applications. The link between the internal porous structure of mats produced by simple electrospinning and the in-situ charging kinetic by electrospinning as well as the charge release kinetic will be studied deeply in chapter 3.

Furthermore, it will be shown in chapter 4 that charges remaining during the process of electrospinning may be used for the elaboration of 3D structured mats thanks to favorable electrostatic interactions and with various polymers. Thus, the understanding of the kinetic of formation of the surface potential by in-situ electrospinning charging and the kinetic of surface potential decay are important to control the overall structuration of electrospun mats.

References

[1] A. Formhals, “Process and Apparatus for Preparing Artificial Threads,” 1975504, 1934.

[2] A. Formhals, “Method and apparatus for spinning,” 2160962, 1939.

[3] A. Formhals, “Production of artificial fibers,” 2077373, 1937.

[4] A. Formhals, “Method and apparatus for the production of artificial fibers,” 2158416, 1939.

[5] X. Lu, C. Wang, and Y. Wei, “One-Dimensional Composite Nanomaterials: Synthesis by Electrospinning and Their Applications,” *Small*, vol. 5, no. 21, pp. 2349–2370, Nov. 2009, doi: 10.1002/smll.200900445.

[6] Y. Ji *et al.*, “Electrospun three-dimensional hyaluronic acid nanofibrous scaffolds,” *Biomaterials*, vol. 27, no. 20, pp. 3782–3792, Jul. 2006, doi: 10.1016/j.biomaterials.2006.02.037.

[7] K. Kim *et al.*, “Control of degradation rate and hydrophilicity in electrospun non-woven poly(d,l-lactide) nanofiber scaffolds for biomedical applications,” *Biomaterials*, vol. 24, no. 27, pp. 4977–4985, Dec. 2003, doi: 10.1016/S0142-9612(03)00407-1.

[8] E.-R. Kenawy *et al.*, “Release of tetracycline hydrochloride from electrospun poly(ethylene-co-vinylacetate), poly(lactic acid), and a blend,” *Journal of Controlled Release*, vol. 81, no. 1–2, pp. 57–64, May 2002, doi: 10.1016/S0168-3659(02)00041-X.

[9] F. Ko *et al.*, “Electrospinning of Continuous Carbon Nanotube-Filled Nanofiber Yarns,” *Advanced Materials*, vol. 15, no. 14, pp. 1161–1165, Jul. 2003, doi: 10.1002/adma.200304955.

[10] A. Podgórski, A. Bałazy, and L. Gradoń, “Application of nanofibers to improve the filtration efficiency of the most penetrating aerosol particles in fibrous filters,” *Chemical Engineering Science*, vol. 61, no. 20, pp. 6804–6815, Oct. 2006, doi: 10.1016/j.ces.2006.07.022.

[11] V. G. Pol, E. Koren, and A. Zaban, “Fabrication of Continuous Conducting Gold Wires by Electrospinning,” *Chemistry of Materials*, vol. 20, no. 9, pp. 3055–3062, May 2008, doi: 10.1021/cm7036958.

[12] N. A. M. Barakat, K.-D. Woo, M. A. Kanjwal, K. E. Choi, M. S. Khil, and H. Y. Kim, “Surface Plasmon Resonances, Optical Properties, and Electrical Conductivity Thermal

Hystersis of Silver Nanofibers Produced by the Electrospinning Technique," *Langmuir*, vol. 24, no. 20, pp. 11982–11987, Oct. 2008, doi: 10.1021/la802084h.

[13] H. Liu, J. Kameoka, D. A. Czaplewski, and H. G. Craighead, "Polymeric Nanowire Chemical Sensor," *Nano Letters*, vol. 4, no. 4, pp. 671–675, Apr. 2004, doi: 10.1021/nl049826f.

[14] S.-H. Choi *et al.*, "Hollow ZnO Nanofibers Fabricated Using Electrospun Polymer Templates and Their Electronic Transport Properties," *ACS Nano*, vol. 3, no. 9, pp. 2623–2631, Sep. 2009, doi: 10.1021/nn900126k.

[15] A. Melaiye *et al.*, "Silver(I)−Imidazole Cyclophane *gem* -Diol Complexes Encapsulated by Electrospun Tecophilic Nanofibers: Formation of Nanosilver Particles and Antimicrobial Activity," *Journal of the American Chemical Society*, vol. 127, no. 7, pp. 2285–2291, Feb. 2005, doi: 10.1021/ja040226s.

[16] Y. K. Luu, K. Kim, B. S. Hsiao, B. Chu, and M. Hadjiargyrou, "Development of a nanostructured DNA delivery scaffold via electrospinning of PLGA and PLA–PEG block copolymers," *Journal of Controlled Release*, vol. 89, no. 2, pp. 341–353, Apr. 2003, doi: 10.1016/S0168-3659(03)00097-X.

[17] S. Lakshmi, D. S. Katti, and C. T. Laurencin, "Biodegradable polyphosphazenes for drug delivery applications," *Advanced Drug Delivery Reviews*, vol. 55, no. 4, pp. 467–482, Apr. 2003, doi: 10.1016/S0169-409X(03)00039-5.

[18] H. Yoshimoto, Y. M. Shin, H. Terai, and J. P. Vacanti, "A biodegradable nanofiber scaffold by electrospinning and its potential for bone tissue engineering," *Biomaterials*, vol. 24, no. 12, pp. 2077–2082, May 2003, doi: 10.1016/S0142-9612(02)00635-X.

[19] T. Courtney, M. Sacks, J. Stankus, J. Guan, and W. Wagner, "Design and analysis of tissue engineering scaffolds that mimic soft tissue mechanical anisotropy," *Biomaterials*, Mar. 2006, doi: 10.1016/j.biomaterials.2006.02.024.

[20] J. A. Matthews, G. E. Wnek, D. G. Simpson, and G. L. Bowlin, "Electrospinning of Collagen Nanofibers," *Biomacromolecules*, vol. 3, no. 2, pp. 232–238, Mar. 2002, doi: 10.1021/bm015533u.

[21] L. Chen, L. Bromberg, T. A. Hatton, and G. C. Rutledge, "Catalytic hydrolysis of p-nitrophenyl acetate by electrospun polyacrylamidoxime nanofibers," *Polymer*, vol. 48, no. 16, pp. 4675–4682, Jul. 2007, doi: 10.1016/j.polymer.2007.05.084.

[22] E. Formo, Z. Peng, E. Lee, X. Lu, H. Yang, and Y. Xia, "Direct Oxidation of Methanol on Pt Nanostructures Supported on Electrospun Nanofibers of Anatase," *The*

Journal of Physical Chemistry C, vol. 112, no. 27, pp. 9970–9975, Jul. 2008, doi: 10.1021/jp803763q.

[23] H.-S. Shim *et al.*, “Efficient photovoltaic device fashioned of highly aligned multilayers of electrospun TiO2 nanowire array with conjugated polymer,” *Applied Physics Letters*, vol. 92, no. 18, p. 183107, May 2008, doi: 10.1063/1.2919800.

[24] A. R. S. Priya, A. Subramania, Y.-S. Jung, and K.-J. Kim, “High-Performance Quasi-Solid-State Dye-Sensitized Solar Cell Based on an Electrospun PVdF−HFP Membrane Electrolyte,” *Langmuir*, vol. 24, no. 17, pp. 9816–9819, Sep. 2008, doi: 10.1021/la801375s.

[25] Y. R. Ahn, C. R. Park, S. M. Jo, and D. Y. Kim, “Enhanced charge-discharge characteristics of RuO2 supercapacitors on heat-treated TiO2 nanorods,” *Applied Physics Letters*, vol. 90, no. 12, p. 122106, Mar. 2007, doi: 10.1063/1.2715038.

[26] K. A. Rieger, N. P. Birch, and J. D. Schiffman, “Designing electrospun nanofiber mats to promote wound healing – a review,” *Journal of Materials Chemistry B*, vol. 1, no. 36, p. 4531, 2013, doi: 10.1039/c3tb20795a.

[27] Z.-M. Huang, Y.-Z. Zhang, M. Kotaki, and S. Ramakrishna, “A review on polymer nanofibers by electrospinning and their applications in nanocomposites,” *Composites Science and Technology*, vol. 63, no. 15, pp. 2223–2253, Nov. 2003, doi: 10.1016/S0266-3538(03)00178-7.

[28] A. Greiner and J. H. Wendorff, “Electrospinning: A Fascinating Method for the Preparation of Ultrathin Fibers,” *Angewandte Chemie International Edition*, vol. 46, no. 30, pp. 5670–5703, Jul. 2007, doi: 10.1002/anie.200604646.

[29] G. Collins, J. Federici, Y. Imura, and L. H. Catalani, “Charge generation, charge transport, and residual charge in the electrospinning of polymers: A review of issues and complications,” *Journal of Applied Physics*, vol. 111, no. 4, p. 044701, Feb. 2012, doi: 10.1063/1.3682464.

[30] X. Zong, K. Kim, D. Fang, S. Ran, B. S. Hsiao, and B. Chu, “Structure and process relationship of electrospun bioabsorbable nanofiber membranes,” *Polymer*, vol. 43, no. 16, pp. 4403–4412, Jul. 2002, doi: 10.1016/S0032-3861(02)00275-6.

[31] H. Fong, I. Chun, and D. H. Reneker, “Beaded nanofibers formed during electrospinning,” *Polymer*, vol. 40, no. 16, pp. 4585–4592, Jul. 1999, doi: 10.1016/S0032-3861(99)00068-3.

[32] N. Lavielle *et al.*, “Controlled formation of poly(ε-caprolactone) ultrathin electrospun nanofibers in a hydrolytic degradation-assisted process,” *European Polymer Journal*, vol. 49, no. 6, pp. 1331–1336, Jun. 2013, doi: 10.1016/j.eurpolymj.2013.02.038.

[33] P. Gupta, C. Elkins, T. E. Long, and G. L. Wilkes, “Electrospinning of linear homopolymers of poly(methyl methacrylate): exploring relationships between fiber formation, viscosity, molecular weight and concentration in a good solvent,” *Polymer*, vol. 46, no. 13, pp. 4799–4810, Jun. 2005, doi: 10.1016/j.polymer.2005.04.021.

[34] G. Riboux, Á. G. Marín, I. G. Loscertales, and A. Barrero, “Whipping instability characterization of an electrified visco-capillary jet,” *Journal of Fluid Mechanics*, vol. 671, pp. 226–253, Mar. 2011, doi: 10.1017/S0022112010005586.

[35] D. Fantini, M. Zanetti, and L. Costa, “Polystyrene Microspheres and Nanospheres Produced by Electrospray,” *Macromolecular Rapid Communications*, vol. 27, no. 23, pp. 2038–2042, Dec. 2006, doi: 10.1002/marc.200600532.

[36] P. Heikkilä and A. Harlin, “Parameter study of electrospinning of polyamide-6,” *European Polymer Journal*, vol. 44, no. 10, pp. 3067–3079, Oct. 2008, doi: 10.1016/j.eurpolymj.2008.06.032.

[37] J. Zeng *et al.*, “Ultrafine fibers electrospun from biodegradable polymers,” *Journal of Applied Polymer Science*, vol. 89, no. 4, pp. 1085–1092, 2003, doi: 10.1002/app.12260.

[38] P. Supaphol, C. Mit -Uppatham,
polyamide-6 fibers: Effect of emitting electrode polarity on morphology and average fiber diameter,” *Journal of Polymer Science Part B: Polymer Physics*, vol. 43, no. 24, pp. 3699–3712, 2005, doi: 10.1002/polb.20671.

[39] D. S. Katti, K. W. Robinson, F. K. Ko, and C. T. Laurencin, “Bioresorbable nanofiber-based systems for wound healing and drug delivery: Optimization of fabrication parameters,” *Journal of Biomedical Materials Research Part B: Applied Biomaterials*, vol. 70B, no. 2, pp. 286–296, 2004, doi: 10.1002/jbm.b.30041.

[40] M. M. Demir, I. Yilgor, E. Yilgor, and B. Erman, “Electrospinning of polyurethane ®bers,” p. 7, 2002.

[41] C. Zhang, X. Yuan, L. Wu, Y. Han, and J. Sheng, “Study on morphology of electrospun poly(vinyl alcohol) mats,” *European Polymer Journal*, vol. 41, no. 3, pp. 423–432, Mar. 2005, doi: 10.1016/j.eurpolymj.2004.10.027.

[42] X. Yuan, Y. Zhang, C. Dong, and J. Sheng, “Morphology of ultrafine polysulfone fibers prepared by electrospinning,” *Polymer International*, vol. 53, no. 11, pp. 1704–1710, 2004, doi: 10.1002/pi.1538.

[43] S. Megelski, J. S. Stephens, D. B. Chase, and J. F. Rabolt, “Micro- and Nanostructured Surface Morphology on Electrospun Polymer Fibers,” *Macromolecules*, vol. 35, no. 22, pp. 8456–8466, Oct. 2002, doi: 10.1021/ma020444a.

[44] J. Pelipenko, J. Kristl, B. Janković, S. Baumgartner, and P. Kocbek, “The impact of relative humidity during electrospinning on the morphology and mechanical properties of nanofibers,” *International Journal of Pharmaceutics*, vol. 456, no. 1, pp. 125–134, Nov. 2013, doi: 10.1016/j.ijpharm.2013.07.078.

[45] B. De Schoenmaker *et al.*, “Effect of the relative humidity on the fibre morphology of polyamide 4.6 and polyamide 6.9 nanofibres,” *Journal of Materials Science*, vol. 48, no. 4, pp. 1746–1754, Feb. 2013, doi: 10.1007/s10853-012-6934-9.

[46] S. De Vrieze, T. Van Camp, A. Nelvig, B. Hagström, P. Westbroek, and K. De Clerck, “The effect of temperature and humidity on electrospinning,” *Journal of Materials Science*, vol. 44, no. 5, pp. 1357–1362, Mar. 2009, doi: 10.1007/s10853-008-3010-6.

[47] E. S. Medeiros *et al.*, “Electrospun Nanofibers of Poly(vinyl alcohol) Reinforced with Cellulose Nanofibrils,” *Journal of Biobased Materials and Bioenergy*, vol. 2, no. 3, pp. 231–242, Sep. 2008, doi: 10.1166/jbmb.2008.411.

[48] R. M. Nezarati, M. B. Eifert, and E. Cosgriff-Hernandez, “Effects of Humidity and Solution Viscosity on Electrospun Fiber Morphology,” *Tissue Engineering Part C: Methods*, vol. 19, no. 10, pp. 810–819, Oct. 2013, doi: 10.1089/ten.tec.2012.0671.

[49] E. S. Medeiros, L. H. C. Mattoso, R. D. Offeman, D. F. Wood, and W. J. Orts, “Effect of relative humidity on the morphology of electrospun polymer fibers,” *Canadian Journal of Chemistry*, vol. 86, no. 6, pp. 590–599, Jun. 2008, doi: 10.1139/v08-029.

[50] G.-T. Kim *et al.*, “Investigation of pore formation for polystyrene electrospun fiber: Effect of relative humidity,” *Korean Journal of Chemical Engineering*, vol. 22, no. 5, pp. 783–788, Sep. 2005, doi: 10.1007/BF02705799.

[51] B. Barua and M. C. Saha, “Influence of humidity, temperature, and annealing on microstructure and tensile properties of electrospun polyacrylonitrile nanofibers,” *Polymer Engineering & Science*, vol. 58, no. 6, pp. 998–1009, 2018, doi: 10.1002/pen.24657.

[52] S. Yao, X. Wang, X. Liu, R. Wang, C. Deng, and F. Cui, “Effects of Ambient Relative Humidity and Solvent Properties on the Electrospinning of Pure Hyaluronic Acid

Nanofibers," *Journal of Nanoscience and Nanotechnology*, vol. 13, no. 7, pp. 4752–4758, Jul. 2013, doi: 10.1166/jnn.2013.7197.

[53] C. Wang, C.-H. Hsu, and J.-H. Lin, "Scaling Laws in Electrospinning of Polystyrene Solutions," *Macromolecules*, vol. 39, no. 22, pp. 7662–7672, Oct. 2006, doi: 10.1021/ma060866a.

[54] O. Hardick, B. Stevens, and D. G. Bracewell, "Nanofibre fabrication in a temperature and humidity controlled environment for improved fibre consistency," *Journal of Materials Science*, vol. 46, no. 11, pp. 3890–3898, Jun. 2011, doi: 10.1007/s10853-011-5310-5.

[55] C. Mit-uppatham, M. Nithitanakul, and P. Supaphol, "Ultrafine Electrospun Polyamide-6 Fibers: Effect of Solution Conditions on Morphology and Average Fiber Diameter," *Macromolecular Chemistry and Physics*, vol. 205, no. 17, pp. 2327–2338, Nov. 2004, doi: 10.1002/macp.200400225.

[56] C. S. Ki, D. H. Baek, K. D. Gang, K. H. Lee, I. C. Um, and Y. H. Park, "Characterization of gelatin nanofiber prepared from gelatin–formic acid solution," *Polymer*, vol. 46, no. 14, pp. 5094–5102, Jun. 2005, doi: 10.1016/j.polymer.2005.04.040.

[57] "Electrospinning of Polyacrylonitrile Solutions at Elevated Temperatures | Macromolecules." [Online]. Available: https://pubs-acs-org.scd-rproxy.u-strasbg.fr/doi/full/10.1021/ma070508n. [Accessed: 04-Dec-2019].

[58] C. H. Park and J. Lee, "Electrosprayed polymer particles: Effect of the solvent properties," *Journal of Applied Polymer Science*, vol. 114, no. 1, pp. 430–437, 2009, doi: 10.1002/app.30498.

[59] X. Huang, J. Gao, W. Li, H. Xue, R. K. Y. Li, and Y.-W. Mai, "Preparation of poly(ε-caprolactone) microspheres and fibers with controllable surface morphology," *Materials & Design*, vol. 117, pp. 298–304, Mar. 2017, doi: 10.1016/j.matdes.2016.12.096.

[60] M. L. Hans and A. M. Lowman, "Biodegradable nanoparticles for drug delivery and targeting," *Current Opinion in Solid State and Materials Science*, p. 9, 2002.

[61] T. M. Fahmy, P. M. Fong, A. Goyal, and W. M. Saltzman, "Targeted for drug delivery," *Materials Today*, vol. 8, no. 8, pp. 18–26, Aug. 2005, doi: 10.1016/S1369-7021(05)71033-6.

[62] R. Mainardes and L. Silva, "Drug Delivery Systems: Past, Present, and Future," *Current Drug Targets*, vol. 5, no. 5, pp. 449–455, Jul. 2004, doi: 10.2174/1389450043345407.

[63] H. Takeuchi, H. Yamamoto, and Y. Kawashima, “Mucoadhesive nanoparticulate systems for peptide drug delivery,” *Advanced Drug Delivery Reviews*, vol. 47, no. 1, pp. 39–54, Mar. 2001, doi: 10.1016/S0169-409X(00)00120-4.

[64] O. C. Farokhzad *et al.*, “Targeted nanoparticle-aptamer bioconjugates for cancer chemotherapy in vivo,” *Proceedings of the National Academy of Sciences*, vol. 103, no. 16, pp. 6315–6320, Apr. 2006, doi: 10.1073/pnas.0601755103.

[65] N. Bock, T. R. Dargaville, and M. A. Woodruff, “Electrospraying of polymers with therapeutic molecules: State of the art,” *Progress in Polymer Science*, vol. 37, no. 11, pp. 1510–1551, Nov. 2012, doi: 10.1016/j.progpolymsci.2012.03.002.

[66] Y. Hong, Y. Li, Y. Yin, D. Li, and G. Zou, “Electrohydrodynamic atomization of quasi-monodisperse drug-loaded spherical/wrinkled microparticles,” *Journal of Aerosol Science*, vol. 39, no. 6, pp. 525–536, Jun. 2008, doi: 10.1016/j.jaerosci.2008.02.004.

[67] I. W. Lenggoro, T. Hata, F. Iskandar, M. M. Lunden, and K. Okuyama, “An experimental and modeling investigation of particle production by spray pyrolysis using a laminar flow aerosol reactor,” *Journal of Materials Research*, vol. 15, no. 3, pp. 733–743, Mar. 2000, doi: 10.1557/JMR.2000.0106.

[68] C. H. Park and J. Lee, “Electrosprayed polymer particles: Effect of the solvent properties,” *Journal of Applied Polymer Science*, vol. 114, no. 1, pp. 430–437, 2009, doi: 10.1002/app.30498.

[69] J. Yao, L. Kuang Lim, J. Xie, J. Hua, and C.-H. Wang, “Characterization of electrospraying process for polymeric particle fabrication,” *Journal of Aerosol Science*, vol. 39, no. 11, pp. 987–1002, Nov. 2008, doi: 10.1016/j.jaerosci.2008.07.003.

[70] B. Almería, W. Deng, T. M. Fahmy, and A. Gomez, “Controlling the morphology of electrospray-generated PLGA microparticles for drug delivery,” *Journal of Colloid and Interface Science*, vol. 343, no. 1, pp. 125–133, Mar. 2010, doi: 10.1016/j.jcis.2009.10.002.

[71] Lord Rayleigh, “XX. *On the equilibrium of liquid conducting masses charged with electricity*,” *The London, Edinburgh, and Dublin Philosophical Magazine and Journal of Science*, vol. 14, no. 87, pp. 184–186, Sep. 1882, doi: 10.1080/14786448208628425.

[72] Y. Xu and M. Hanna, “Electrospray encapsulation of water-soluble protein with polylactide☆Effects of formulations on morphology, encapsulation efficiency and release profile of particles,” *International Journal of Pharmaceutics*, vol. 320, no. 1–2, pp. 30–36, Aug. 2006, doi: 10.1016/j.ijpharm.2006.03.046.

[73] Y. Wu and R. L. Clark, “Controllable porous polymer particles generated by electrospraying,” *Journal of Colloid and Interface Science*, vol. 310, no. 2, pp. 529–535, Jun. 2007, doi: 10.1016/j.jcis.2007.02.023.

[74] I. Marginean, L. Parvin, L. Heffernan, and A. Vertes, “Flexing the Electrified Meniscus: The Birth of a Jet in Electrosprays,” *Analytical Chemistry*, vol. 76, no. 14, pp. 4202–4207, Jul. 2004, doi: 10.1021/ac049817r.

[75] D. R. Salem, “Electrospinning of nanofibers and the charge injection method,” in *Nanofibers and Nanotechnology in Textiles*, Elsevier, 2007, pp. 3–21.

[76] Y. Cai and M. Gevelber, “The effect of relative humidity and evaporation rate on electrospinning: fiber diameter and measurement for control implications,” *Journal of Materials Science*, vol. 48, no. 22, pp. 7812–7826, Nov. 2013, doi: 10.1007/s10853-013-7544-x.

[77] D. Fallahi, M. Rafizadeh, N. Mohammadi, and B. Vahidi, “Effect of applied voltage on jet electric current and flow rate in electrospinning of polyacrylonitrile solutions,” *Polymer International*, vol. 57, no. 12, pp. 1363–1368, Dec. 2008, doi: 10.1002/pi.2482.

[78] M. M. Demir, I. Yilgor, E. Yilgor, and B. Erman, “Electrospinning of polyurethane fibers,” *Polymer*, vol. 43, no. 11, pp. 3303–3309, May 2002, doi: 10.1016/S0032-3861(02)00136-2.

[79] X.-H. Qin, Y.-Q. Wan, J.-H. He, J. Zhang, J.-Y. Yu, and S.-Y. Wang, “Effect of LiCl on electrospinning of PAN polymer solution: theoretical analysis and experimental verification,” *Polymer*, vol. 45, no. 18, pp. 6409–6413, Aug. 2004, doi: 10.1016/j.polymer.2004.06.031.

[80] Y. M. Shin, M. M. Hohman, M. P. Brenner, and G. C. Rutledge, “Experimental characterization of electrospinning: the electrically forced jet and instabilities,” *Polymer*, vol. 42, no. 25, pp. 09955–09967, Dec. 2001, doi: 10.1016/S0032-3861(01)00540-7.

[81] P. K. Bhattacharjee, T. M. Schneider, M. P. Brenner, G. H. McKinley, and G. C. Rutledge, “On the measured current in electrospinning,” *Journal of Applied Physics*, vol. 107, no. 4, p. 044306, Feb. 2010, doi: 10.1063/1.3277018.

[82] A. L. Yarin, W. Kataphinan, and D. H. Reneker, “Branching in electrospinning of nanofibers,” *Journal of Applied Physics*, vol. 98, no. 6, p. 064501, Sep. 2005, doi: 10.1063/1.2060928.

[83] M. M. Hohman, M. Shin, G. Rutledge, and M. P. Brenner, “Electrospinning and electrically forced jets. I. Stability theory,” *Physics of Fluids*, vol. 13, no. 8, pp. 2201–2220, Aug. 2001, doi: 10.1063/1.1383791.

[84] S. Yao, X. Wang, X. Liu, R. Wang, C. Deng, and F. Cui, “Effects of Ambient Relative Humidity and Solvent Properties on the Electrospinning of Pure Hyaluronic Acid Nanofibers,” *j. nanosci. nanotech.*, vol. 13, no. 7, pp. 4752–4758, Jul. 2013, doi: 10.1166/jnn.2013.7197.

[85] G.-T. Kim *et al.*, “Investigation of pore formation for polystyrene electrospun fiber: Effect of relative humidity,” *Korean Journal of Chemical Engineering*, vol. 22, no. 5, pp. 783–788, Sep. 2005, doi: 10.1007/BF02705799.

[86] H. Fashandi and M. Karimi, “Comparative Studies on the Solvent Quality and Atmosphere Humidity for Electrospinning of Nanoporous Polyetherimide Fibers,” *Industrial & Engineering Chemistry Research*, vol. 53, no. 1, pp. 235–245, Jan. 2014, doi: 10.1021/ie4028846.

[87] L. Huang, N.-N. Bui, S. S. Manickam, and J. R. McCutcheon, “Controlling electrospun nanofiber morphology and mechanical properties using humidity,” *Journal of Polymer Science Part B: Polymer Physics*, vol. 49, no. 24, pp. 1734–1744, Dec. 2011, doi: 10.1002/polb.22371.

[88] E. S. Medeiros, L. H. C. Mattoso, R. D. Offeman, D. F. Wood, and W. J. Orts, “Effect of relative humidity on the morphology of electrospun polymer fibers,” *Canadian Journal of Chemistry*, vol. 86, no. 6, pp. 590–599, Jun. 2008, doi: 10.1139/v08-029.

[89] N. Mohmeyer *et al.*, “Additives to improve the electret properties of isotactic polypropylene,” *Polymer*, vol. 48, no. 6, pp. 1612–1619, Mar. 2007, doi: 10.1016/j.polymer.2006.08.001.

[90] L. H. Catalani, G. Collins, and M. Jaffe, “Evidence for Molecular Orientation and Residual Charge in the Electrospinning of Poly(butylene terephthalate) Nanofibers,” *Macromolecules*, vol. 40, no. 5, pp. 1693–1697, Mar. 2007, doi: 10.1021/ma061342d.

[91] A. Y. Choi, H. J. Sim, M. K. Shin, S. J. Kim, and Y. T. Kim, “Residual Charges during Electrospinning Assist in Formation of Piezoelectricity in Poly(Vinylidene Fluoride-co-Trifluoroethylene) Nanofibers,” *Journal of Nano Research*, vol. 37, pp. 13–19, Dec. 2015, doi: 10.4028/www.scientific.net/JNanoR.37.13.

[92] J. Lowell, “Absorption and conduction currents in polymers: a unified model,” *Journal of Physics D: Applied Physics*, vol. 23, no. 2, pp. 205–210, Feb. 1990, doi: 10.1088/0022-3727/23/2/011.

[93] M. Ignatova, T. Yovcheva, A. Viraneva, G. Mekishev, N. Manolova, and I. Rashkov, “Study of charge storage in the nanofibrous poly(ethylene terephthalate) electrets prepared by electrospinning or by corona discharge method,” *European Polymer Journal*, vol. 44, no. 7, pp. 1962–1967, Jul. 2008, doi: 10.1016/j.eurpolymj.2008.04.027.

[94] T. Yamashita and K. Ikezaki, “A method for correlating charge traps of polypropylene to its morphology,” *Journal of Electrostatics*, vol. 63, no. 6–10, pp. 559–564, Jun. 2005, doi: 10.1016/j.elstat.2005.03.016.

[95] Y. Arita, S. Sha Shiratori, and K. Ikezaki, “A method for detection and visualization of charge trapping sites in amorphous parts in crystalline polymers,” *Journal of Electrostatics*, vol. 57, no. 3–4, pp. 263–271, Mar. 2003, doi: 10.1016/S0304-3886(02)00166-3.

[96] B. M. Cho, Y. S. Nam, J. Y. Cheon, and W. H. Park, “Residual charge and filtration efficiency of polycarbonate fibrous membranes prepared by electrospinning,” *Journal of Applied Polymer Science*, vol. 132, no. 1, Jan. 2015, doi: 10.1002/app.41340.

[97] S. Wang, X. Zhao, X. Yin, J. Yu, and B. Ding, “Electret Polyvinylidene Fluoride Nanofibers Hybridized by Polytetrafluoroethylene Nanoparticles for High-Efficiency Air Filtration,” *ACS Applied Materials & Interfaces*, vol. 8, no. 36, pp. 23985–23994, Sep. 2016, doi: 10.1021/acsami.6b08262.

[98] H.-W. Tong, M. Wang, and W. W. Lu, “Enhancing the biological performance of osteoconductive nanocomposite scaffolds through negative voltage electrospinning,” *Nanomedicine*, vol. 8, no. 4, pp. 577–589, Apr. 2013, doi: 10.2217/nnm.13.51.

[99] B. Tabti, M. R. Mekideche, M.-C. Plopeanu, L. M. Dumitran, L. Herous, and L. Dascalescu, “Corona-Charging and Charge-Decay Characteristics of Nonwoven Filter Media,” *IEEE Transactions on Industry Applications*, vol. 46, no. 2, pp. 634–640, Mar. 2010, doi: 10.1109/TIA.2010.2041090.

[100] C. Gonzalez, “Charge-Storage mechanisms in polymer electrets,” p. 117.

[101] R. Thakur, D. Das, and A. Das, “Study of charge decay in corona-charged fibrous electrets,” *Fibers and Polymers*, vol. 15, no. 7, pp. 1436–1443, Jul. 2014, doi: 10.1007/s12221-014-1436-9.

[102] E. Németh, V. Albrecht, G. Schubert, and F. Simon, “Polymer tribo-electric charging: dependence on thermodynamic surface properties and relative humidity,” *Journal of Electrostatics*, vol. 58, no. 1–2, pp. 3–16, May 2003, doi: 10.1016/S0304-3886(02)00137-7.

[103] D. Li, Y. Wang, and Y. Xia, “Electrospinning of Polymeric and Ceramic Nanofibers as Uniaxially Aligned Arrays,” *Nano Letters*, vol. 3, no. 8, pp. 1167–1171, Aug. 2003, doi: 10.1021/nl0344256.

[104] H. Yan, L. Liu, and Z. Zhang, “Alignment of electrospun nanofibers using dielectric materials,” *Applied Physics Letters*, vol. 95, no. 14, p. 143114, Oct. 2009, doi: 10.1063/1.3242378.

[105] V. Chaurey, P.-C. Chiang, C. Polanco, Y.-H. Su, C.-F. Chou, and N. S. Swami, “Interplay of Electrical Forces for Alignment of Sub-100 nm Electrospun Nanofibers on Insulator Gap Collectors,” *Langmuir*, vol. 26, no. 24, pp. 19022–19026, Dec. 2010, doi: 10.1021/la102209q.

[106] W. E. Teo and S. Ramakrishna, “Electrospun fibre bundle made of aligned nanofibres over two fixed points,” *Nanotechnology*, vol. 16, no. 9, pp. 1878–1884, Sep. 2005, doi: 10.1088/0957-4484/16/9/077.

[107] L. Liu and Y. A. Dzenis, “Analysis of the effects of the residual charge and gap size on electrospun nanofiber alignment in a gap method,” *Nanotechnology*, vol. 19, no. 35, p. 355307, Sep. 2008, doi: 10.1088/0957-4484/19/35/355307.

[108] P. Katta, M. Alessandro, R. D. Ramsier, and G. G. Chase, “Continuous Electrospinning of Aligned Polymer Nanofibers onto a Wire Drum Collector,” *Nano Letters*, vol. 4, no. 11, pp. 2215–2218, Nov. 2004, doi: 10.1021/nl0486158.

[109] D. Li, Y. Wang, and Y. Xia, “Electrospinning Nanofibers as Uniaxially Aligned Arrays and Layer-by-Layer Stacked Films,” *Advanced Materials*, vol. 16, no. 4, pp. 361–366, Feb. 2004, doi: 10.1002/adma.200306226.

[110] S. J. Cho, B. Kim, T. An, and G. Lim, “Replicable Multilayered Nanofibrous Patterns on a Flexible Film,” *Langmuir*, vol. 26, no. 18, pp. 14395–14399, Sep. 2010, doi: 10.1021/la102467u.

[111] Z. Ding, A. Salim, and B. Ziaie, “Selective Nanofiber Deposition through Field-Enhanced Electrospinning,” *Langmuir*, vol. 25, no. 17, pp. 9648–9652, Sep. 2009, doi: 10.1021/la901924z.

[112] N. Lavielle, A. Hébraud, C. Mendoza-Palomares, A. Ferrand, N. Benkirane-Jessel, and G. Schlatter, “Structuring and Molding of Electrospun Nanofibers: Effect of Electrical

and Topographical Local Properties of Micro-Patterned Collectors,” *Macromolecular Materials and Engineering*, vol. 297, no. 10, pp. 958–968, Oct. 2012, doi: 10.1002/mame.201100327.

[113] S. Zhao, Q. Zhou, Y.-Z. Long, G.-H. Sun, and Y. Zhang, “Nanofibrous patterns by direct electrospinning of nanofibers onto topographically structured non-conductive substrates,” *Nanoscale*, vol. 5, no. 11, p. 4993, 2013, doi: 10.1039/c3nr00676j.

[114] Y. Ner, C. Asemota, J. R. Olson, and G. A. Sotzing, “Nanofiber Alignment on a Flexible Substrate: Hierarchical Order from Macro to Nano,” *ACS Applied Materials & Interfaces*, vol. 1, no. 10, pp. 2093–2097, Oct. 2009, doi: 10.1021/am900382f.

[115] S. Nedjari *et al.*, “Electrostatic template-assisted deposition of microparticles on electrospun nanofibers: towards microstructured functional biochips for screening applications,” *RSC Advances*, vol. 5, no. 102, pp. 83600–83607, 2015, doi: 10.1039/C5RA15931H.

[116] C. R. Wittmer, A. Hébraud, S. Nedjari, and G. Schlatter, “Well-organized 3D nanofibrous composite constructs using cooperative effects between electrospinning and electrospraying,” *Polymer*, vol. 55, no. 22, pp. 5781–5787, Oct. 2014, doi: 10.1016/j.polymer.2014.08.044.

[117] A. Garcia Garcia *et al.*, “Poly(ε-caprolactone)/Hydroxyapatite 3D Honeycomb Scaffolds for a Cellular Microenvironment Adapted to Maxillofacial Bone Reconstruction,” *ACS Biomaterials Science & Engineering*, vol. 4, no. 9, pp. 3317–3326, Sep. 2018, doi: 10.1021/acsbiomaterials.8b00521.

[118] S. Nedjari, G. Schlatter, and A. Hébraud, “Thick electrospun honeycomb scaffolds with controlled pore size,” *Materials Letters*, vol. 142, pp. 180–183, Mar. 2015, doi: 10.1016/j.matlet.2014.11.118.

[119] S. Nedjari, S. Eap, A. Hébraud, C. R. Wittmer, N. Benkirane-Jessel, and G. Schlatter, “Electrospun Honeycomb as Nests for Controlled Osteoblast Spatial Organization: Electrospun Honeycomb as Nests for Controlled …,” *Macromolecular Bioscience*, vol. 14, no. 11, pp. 1580–1589, Nov. 2014, doi: 10.1002/mabi.201400226.

[120] J. M. Deitzel, J. Kleinmeyer, D. Harris, and N. C. Beck Tan, “The effect of processing variables on the morphology of electrospun nanofibers and textiles,” *Polymer*, vol. 42, no. 1, pp. 261–272, Jan. 2001, doi: 10.1016/S0032-3861(00)00250-0.

[121] G. Yan *et al.*, “Self-Assembly of Electrospun Polymer Nanofibers: A General Phenomenon Generating Honeycomb-Patterned Nanofibrous Structures,” *Langmuir*, vol. 27, no. 8, pp. 4285–4289, Apr. 2011, doi: 10.1021/la1047936.

[122] D. Ahirwal, A. Hébraud, R. Kádár, M. Wilhelm, and G. Schlatter, “From self-assembly of electrospun nanofibers to 3D cm thick hierarchical foams,” *Soft Matter*, vol. 9, no. 11, p. 3164, 2013, doi: 10.1039/c2sm27543k.

[123] T. Yao, H. Chen, P. Samal, S. Giselbrecht, M. B. Baker, and L. Moroni, “Self-assembly of electrospun nanofibers into gradient honeycomb structures,” *Materials & Design*, vol. 168, p. 107614, Apr. 2019, doi: 10.1016/j.matdes.2019.107614.

[124] T. J. Sill and H. A. von Recum, “Electrospinning: Applications in drug delivery and tissue engineering,” *Biomaterials*, vol. 29, no. 13, pp. 1989–2006, May 2008, doi: 10.1016/j.biomaterials.2008.01.011.

[125] A. Haider, S. Haider, and I.-K. Kang, “A comprehensive review summarizing the effect of electrospinning parameters and potential applications of nanofibers in biomedical and biotechnology,” *Arabian Journal of Chemistry*, vol. 11, no. 8, pp. 1165–1188, Dec. 2018, doi: 10.1016/j.arabjc.2015.11.015.

[126] S. Peng *et al.*, “Electronic and Defective Engineering of Electrospun $CaMnO_3$ Nanotubes for Enhanced Oxygen Electrocatalysis in Rechargeable Zinc-Air Batteries,” *Advanced Energy Materials*, vol. 8, no. 22, p. 1800612, Aug. 2018, doi: 10.1002/aenm.201800612.

[127] N. Pan, J. Qin, P. Feng, and B. Song, “Window screen inspired fibrous materials with anisotropic thickness gradients for improving light transmittance,” *Nanoscale*, vol. 11, no. 28, pp. 13521–13531, 2019, doi: 10.1039/C9NR02810B.

[128] K. Tonsomboon and M. L. Oyen, “Composite electrospun gelatin fiber-alginate gel scaffolds for mechanically robust tissue engineered cornea,” *Journal of the Mechanical Behavior of Biomedical Materials*, vol. 21, pp. 185–194, May 2013, doi: 10.1016/j.jmbbm.2013.03.001.

[129] R. Zhang *et al.*, “Nanofiber Air Filters with High-Temperature Stability for Efficient $PM_{2.5}$ Removal from the Pollution Sources,” *Nano Letters*, vol. 16, no. 6, pp. 3642–3649, Jun. 2016, doi: 10.1021/acs.nanolett.6b00771.

[130] J. Xu *et al.*, “Roll-to-Roll Transfer of Electrospun Nanofiber Film for High-Efficiency Transparent Air Filter,” *Nano Letters*, vol. 16, no. 2, pp. 1270–1275, Feb. 2016, doi: 10.1021/acs.nanolett.5b04596.

[131] R. Chen *et al.*, “Transparent thermoplastic polyurethane air filters for efficient electrostatic capture of particulate matter pollutants,” *Nanotechnology*, vol. 30, no. 1, p. 015703, Jan. 2019, doi: 10.1088/1361-6528/aae611.

[132] M. Sofiev *et al.*, “Cleaner fuels for ships provide public health benefits with climate tradeoffs,” *Nature Communications*, vol. 9, no. 1, Dec. 2018, doi: 10.1038/s41467-017-02774-9.

[133] R.-J. Huang *et al.*, “High secondary aerosol contribution to particulate pollution during haze events in China,” *Nature*, vol. 514, no. 7521, pp. 218–222, Oct. 2014, doi: 10.1038/nature13774.

[134] S. An *et al.*, “Oxidation-resistant metallized nanofibers as transparent conducting films and heaters,” *Acta Materialia*, vol. 143, pp. 174–180, Jan. 2018, doi: 10.1016/j.actamat.2017.09.068.

[135] K. Hong *et al.*, “Continuous 1D-Metallic Microfibers Web for Flexible Organic Solar Cells,” *ACS Applied Materials & Interfaces*, vol. 7, no. 49, pp. 27397–27404, Dec. 2015, doi: 10.1021/acsami.5b09060.

[136] Z. Cheng, J. Cao, L. Kang, Y. Luo, T. Li, and W. Liu, “Novel transparent nano-pattern window screen for effective air filtration by electrospinning,” *Materials Letters*, vol. 221, pp. 157–160, Jun. 2018, doi: 10.1016/j.matlet.2018.03.110.

[137] W. Zhong, M. M. Q. Xing, and H. I. Maibach, “Nanofibrous materials for wound care,” *Cutaneous and Ocular Toxicology*, vol. 29, no. 3, pp. 143–152, Sep. 2010, doi: 10.3109/15569527.2010.489307.

[138] W.-X. He, A. K. Rajasekharan, A. R. Tehrani-Bagha, and M. Andersson, “Mesoscopically Ordered Bone-Mimetic Nanocomposites,” *Advanced Materials*, vol. 27, no. 13, pp. 2260–2264, Apr. 2015, doi: 10.1002/adma.201404926.

[139] A. Gautieri, S. Vesentini, A. Redaelli, and M. J. Buehler, “Hierarchical Structure and Nanomechanics of Collagen Microfibrils from the Atomistic Scale Up,” *Nano Letters*, vol. 11, no. 2, pp. 757–766, Feb. 2011, doi: 10.1021/nl103943u.

[140] P. A. George, K. Quinn, and J. J. Cooper-White, “Hierarchical scaffolds via combined macro- and micro-phase separation,” *Biomaterials*, vol. 31, no. 4, pp. 641–647, Feb. 2010, doi: 10.1016/j.biomaterials.2009.09.094.

[141] J. Xie, W. Liu, M. R. MacEwan, Y.-C. Yeh, S. Thomopoulos, and Y. Xia, “Nanofiber Membranes with Controllable Microwells and Structural Cues and Their Use in Forming Cell

Microarrays and Neuronal Networks,” *Small*, vol. 7, no. 3, pp. 293–297, Feb. 2011, doi: 10.1002/smll.201001446.

[142] J. Xie, M. R. MacEwan, W. Z. Ray, W. Liu, D. Y. Siewe, and Y. Xia, “Radially Aligned, Electrospun Nanofibers as Dural Substitutes for Wound Closure and Tissue Regeneration Applications,” *ACS Nano*, vol. 4, no. 9, pp. 5027–5036, Sep. 2010, doi: 10.1021/nn101554u.

[143] L. Bacakova, E. Filova, M. Parizek, T. Ruml, and V. Svorcik, “Modulation of cell adhesion, proliferation and differentiation on materials designed for body implants,” *Biotechnology Advances*, vol. 29, no. 6, pp. 739–767, Nov. 2011, doi: 10.1016/j.biotechadv.2011.06.004.

[144] W. Zhai *et al.*, “Silicate bioceramics induce angiogenesis during bone regeneration,” *Acta Biomaterialia*, vol. 8, no. 1, pp. 341–349, Jan. 2012, doi: 10.1016/j.actbio.2011.09.008.

[145] W. Zhai *et al.*, “Stimulatory effects of the ionic products from Ca–Mg–Si bioceramics on both osteogenesis and angiogenesis in vitro,” *Acta Biomaterialia*, vol. 9, no. 8, pp. 8004–8014, Aug. 2013, doi: 10.1016/j.actbio.2013.04.024.

[146] K. Kawai *et al.*, “Calcium-Based Nanoparticles Accelerate Skin Wound Healing,” *PLoS ONE*, vol. 6, no. 11, p. e27106, Nov. 2011, doi: 10.1371/journal.pone.0027106.

[147] A. B. G. Lansdown, “Calcium: a potential central regulator in wound healing in the skin,” *Wound Repair and Regeneration*, vol. 10, no. 5, pp. 271–285, Sep. 2002, doi: 10.1046/j.1524-475X.2002.10502.x.

[148] H. Xu *et al.*, “Hierarchically micro-patterned nanofibrous scaffolds with a nanosized bio-glass surface for accelerating wound healing,” *Nanoscale*, vol. 7, no. 44, pp. 18446–18452, 2015, doi: 10.1039/C5NR04802H.

[149] F. Hejazi and H. Mirzadeh, “Novel 3D scaffold with enhanced physical and cell response properties for bone tissue regeneration, fabricated by patterned electrospinning/electrospraying,” *Journal of Materials Science: Materials in Medicine*, vol. 27, no. 9, Sep. 2016, doi: 10.1007/s10856-016-5748-8.

[150] S. Zaiss, T. Brown, J. Reichert, and A. Berner, “Poly(ε-caprolactone) Scaffolds Fabricated by Melt Electrospinning for Bone Tissue Engineering,” *Materials*, vol. 9, no. 4, p. 232, Mar. 2016, doi: 10.3390/ma9040232.

[151] H. Liu, S. Mukherjee, Y. Liu, and S. Ramakrishna, “Recent studies on electrospinning preparation of patterned, core-shell, and aligned scaffolds: REVIEW,” *Journal of Applied Polymer Science*, vol. 135, no. 31, p. 46570, Aug. 2018, doi: 10.1002/app.46570.

Chapter 2 Direct measurement of the surface charge density on an electrospun fiber and on an individual electrosprayed particle: effects of processing parameters

2.1 Introduction

As mentioned in the first chapter, electrospinning is a simple method allowing the fabrication mats with a fiber diameter in the range of tens of nanometer to few micrometers. The process is used in various fields such as filtration, drug delivery, tissue engineering, batteries and sensors, etc.[1]–[7]. In certain applications, it is reported that the charges carried on the fibers play an important role for example by the enhancement of the filtration efficiency [5], for the building of structured scaffolds with suitable pore size[8] and to improve cell attachment and proliferation on fibrous scaffolds for tissue repair[9]. Furthermore, the amount of charges carried by the jet influences the fiber diameter [10]. Hence, measuring precisely the charge density carried by the electrospun fiber becomes a valuable issue.

The charge density of the fiber can be related with the intensity of the electrospun jet current and can be expressed as [11]:

$$I = \lambda v + \pi r^2 KE \tag{2.1}$$

Where λ is the linear charge density, v the jet velocity, E the electric field and K the electrical conductivity. In fact, in electrospinning the advection λv dominates the conductive component because due to the small jet radius [11]. Thus, the current should have a linear behavior with the flow rate as following:

$$I = \lambda v = 2\sigma Q/r \tag{2.2}$$

Where σ is the surface charge density and Q the jet flow rate [12]. It is worth noting that the linear behavior of the electrospinning current with the flow rate differs with the electrospraying process for which the current scales with $Q^{0.5}$ [11]. It was shown that the jet current is significantly by solution parameters (concentration, conductivity, surface tension...) [13]–[15] and processing factors (voltage, processing distance, feeding rate...) [16]–[18]. Theron et al. highlighted that, even for the process of electrospinning, the current does not scale linearly with Q [19]. Indeed, the current is not measured at the emitter but rather at the fiber landing area, i.e. at the collector, by applying the Ohm's law after measuring the difference of potential across a resistor located in series between the collector and the ground [20]. Thus, the measured current reflects the amount of charges carried by the solid fiber during its deposition and does not take into account charge release which can happen during the flying of the jet in the air. The velocity which must then be taken into account in Eqs. 2.1 and 2.2 is the velocity of the fiber v_f. Collins et al. reported that before the landing of the jet on the collector, charges release may occur by corona discharge near the emitter, charge removal by humidity, charge removal by electrospraying solvent-rich droplets from the surface of the electrospun jet and finally charge removal due to solvent evaporation [21]. For example, in the case when charge removal by secondary electrospraying of solvent-rich droplets occurs, it was shown that the current scales as [11]:

$$I = EQ^{0.5}K^{0.4} \tag{2.3}$$

The corona discharge, which is the local breakdown of the air surrounding the Taylor cone, generally happens under high humidity and voltage and renders the process of electrospinning unstable; when possible, it can thus be avoided by decreasing the electric field and humidity. Siavash et al. discussed the situations when splitting and swinging of jets occurs reflecting an unstable character of the process [22]. They showed that in such cases, the current is also unstable and has an intermittent status. Ravikant et al. observed four types of jets which were (1) fluctuating jet, (2) stable jet, (3) stable jet with drops dripping down intermittently, (4) multiple jets. They correlated these jets types with the current and proved that only stable jet induces a stable current which varies in a narrow range, other three types induce a current fluctuation [23].

Our attempt was to have a direct measure of all the charges carried by the fiber landing on the collector. However, the measurement of the current reflects only the amount of charges flowing towards the collector[24], [25]. Thus, the calculation of the surface charge density from the measurement of the current underestimates the total charges carried by the fiber at its landing. Here, we propose an original method allowing the measurement of all charge carriers. A capacitor was placed in series between a collector and the ground. Once electrospinning has reached a steady state regime, the fiber is deposited for few seconds on a rotating collector connected to a capacitor in series with the ground. At the same time, the voltage is measured at the top surface of the collector. In this case, the voltage, which results from the charging of the known capacitor, is due to the total amount of charges carried by the fiber. When the capacitor is short-circuited, the resulting voltage is then an image of the residual charges. For all these experiments we measured the fiber average diameter. Because only few fibers are deposited during the short time of electrospinning on the rotating collector, it was also possible to estimate the average length of fiber deposited on the collector. Thus, the linear as well as the surface charge density were also obtained. To show the potential of this method, we studied the effects of various parameters (polymer concentration in the solution, voltage applied on the electrospinning emitter, feeding rate, ambient humidity and presence of salt in the solution) on the resulting charge density either for PLA or PEO electrospinning. We also applied this method to measure the charges carried by an individual electrosprayed particle which was never done before. Here, two kinds of PCL particles were prepared and studied in terms of morphology, formation mechanism and charge density.

2.2 Materials and methods

Materials

PLA (Mw=180k, Natureworks), PEO (Mw=400k), TEBAC, alginate (4-12 cP, 1 % in H_2O at 25 °C) and deionized water were used as received. PCL (Mw=14k and 80k), DMAC, chloroform, Dichloromethane (DCM) and N, N-Dimethylformamide (DMF) were purchased from Sigma-Aldrich.

Preparation of the solutions

Pure PLA solutions for electrospinning were prepared by dissolving different amounts of PLA in DMF/DCM (50:50 v/v) to get the polymer weight concentration at 7%, 9% 11% and 13% (w/w). TEBAC (0.5% w/w) was added to 9% PLA solution for PLA/TEBAC solution. For the fabrication of the solution, PLA or PLA+TEBAC were added in DMF/DCM in a glass bottle with stirring magnetically overnight at room temperature.

With the same method, 5% w/w PEO in deionized water was stirred 24h prior to electrospinning. PEO/alginate solution was produced by adding 1% w/w alginate in PEO solution.

For the solutions dedicated to electrospraying, PCL14k solution of 5% in DMAC (w/w) was prepared by heating the solution at 60 °C during agitation 5 h before electrospraying. PCL80k solution was achieved through dissolving PCL80k in chloroform at 2% w/w concentration and stirred overnight.

Electrospinning process

The governing parameters of electrospinning PLA fibers were shown in Tab. 2.1. Fig. 2.1 presents the experimental setup of electrospinning. The solution in the syringe was pushed by a pump (Fischer scientific) and passed through the plastic tube connecting the syringe to a stainless steel needle with an inner diameter of 0.5 mm. The needle was connected to a high voltage DC power supply (Spellman SL10). An aluminum cylinder, called the collector, (external diameter De = 110 mm, Width = 30 mm) was mounted around a rotor (diameter Dr = 60 mm) connected to the ground. The collector was mechanically linked to the rotor by a thick insulating ring of Teflon. A capacitor (C = 1 nF) was electrically connected between the collector and the rotor. The distance from the nozzle and the top surface of the collector was set at 15 cm. The rotation rate was set at 120 rpm.

Table 2.1 Parameters for electrospinning

Sample name	Parameters				
	Concentration	Voltage	TEBAC	Feeding rate	Humidity
PLA-1	7%	25kV	-	1ml/h	38%±2%
PLA-2	9%	25kV	-	1ml/h	38%±2%
PLA-3	11%	25kV	-	1ml/h	38%±2%
PLA-4	13%	25kV	-	1ml/h	38%±2%
PLA-5	9%	15kV	-	1ml/h	38%±2%
PLA-6	9%	20kV	-	1ml/h	38%±2%
PLA-7	9%	30kV	-	1ml/h	38%±2%
PLA-8	9%	25kV	0.1%	1ml/h	38%±2%
PLA-9	9%	25kV	0.5%	1ml/h	38%±2%
PLA-10	9%	25kV	-	1ml/h	28%±2%
PLA-11	9%	25kV	-	1ml/h	48%±2%
PLA-12	9%	25kV	-	1ml/h	58%±2%
PLA-13	9%	25kV	-	2ml/h	38%±2%
PLA-14	9%	25kV	-	3ml/h	38%±2%
PLA-15	9%	25kV	-	4ml/h	38%±2%
PEO	5%	25kV	-	1ml/h	38%±2%
PEO-ALG	5% PEO + 1% Alginate	25kV	-	1ml/h	38%±2%

For the electrospinning of PEO and PEO/Alginate the same setup was used. The distance between the needle and the collector was 15cm and the experiment was operated at the room temperature.

Electrospraying process

For the electrospraying of PCL14k particles, the solution was delivered with a feeding rate of 0.6 ml/h. Experiments were performed with a potential at 30 kV and a needle-collector distance of 15cm. The value of capacitor was 1nF.

For the electrospraying of PCL80k particles, the solution was delivered at a feeding rate of 0.8 ml/h. The distance was 15 cm from the needle to the collector and the voltage was at 12kV. In order to get accurate measurements, the capacitor used for electospraying PCL80k particles was C = 100 pF.

SEM measurements

The morphology of fibers and particles was studied by scanning electron microscope (SEM) (Vega-3, Tescan). The samples were gold coated (sputter Quorum Q 150 RS, Quorum Technologies) for 2 min before SEM characterization.

Voltage acquisition, calculation of length of fiber and charge density of fibers and particles

First, electrospinning (or electrospraying) was carried out on a shutter connected to the ground and which was placed just over the top surface of the collector below the emitter. When, stable process was observed, at least 2 min after starting electrospinning (or electrospraying), the shutter was rapidly removed offering the free surface of the collector available for the deposition of the fiber (or the particles). When reaching a surface voltage of ~ 2500 V, the shutter was rapidly placed over the collector in order to stop the deposition of fiber and thus stop the increase of voltage. For each given electrospinning (or electrospraying) set of parameters, at least 5 measurements were carried out.

To measure the surface potential, a non-contacting electrostatic voltmeter ESVM (Trek Model 347-3-H-CE) connected to a computer for data acquisition was used. The measurement is based on a field-nulling technique for non-contacting voltage measurement achieving direct current stability and high accuracy, with no need for fixed probe-to-surface spacing. The technique allows an accurate measurement of the surface potential of stationary or moving surfaces. The measurement range is 0 to ± 3 kV with accuracy of 0.1% of the full range. The probe of the voltmeter (end-view probe model 6000B-7C with a speed of response of 4.5 ms for 1 kV step) having a disc surface of 11.2 mm diameter was placed 2 mm below the surface of the collector as shown in Fig 2.1. An acquisition rate of 30 measurements/s was chosen.

The time t_{spin}, corresponding to the time the fiber is deposited on the rotating collector, can be easily obtained from the voltage acquired during the measurement. Indeed, during the time of collection on the rotating collector, the voltage rises sharply until the shutter is manually placed between the emitter and the collector, at which point the voltage remains constant. Thus, from the acquisition file giving the voltage as a function of time, it was possible to get t_{spin}.

Characterization of electrospun fibers:

In order to get the average length of fiber L_f deposited on the whole surface S_c of the collector during the time of electrospinning t_{spin}, SEM images were taken from the aluminium foil which covered the collector. For a given electrospinning experiment, at least 10 SEM images were taken from the center and the border of the collector. From the SEM images having a surface S_{SEM}, the average fiber diameter ϕ_f and the length L_{SEM} of the fiber were determined using ImageJ software. L_f was then calculated by:

$$L_f = L_{SEM} \frac{S_c}{S_{SEM}} \tag{2.4}$$

It was then also possible to estimate the fiber velocity as well as the fiber flow rate:

$$v_f = \frac{L_f}{t_{spin}} \tag{2.5}$$

$$Q_f = \pi \phi_f^2 v_f \tag{2.6}$$

Characterization of electrosprayed particles:

In the case of PCL80k, the voltage increased very slowly, thus the electrospraying was stopped when the surface potential reached around 1400 V instead of 2500 V for all other experiments. In order to get the average number of particles N_p deposited on the whole surface S_c of the collector during the time of electrospraying t_{spray}, SEM images were taken from the aluminium foil which covered the collector. For a given electrospraying experiment, at least 10 SEM images were taken from the center and the border of the collector. For each SEM image of given surface S_{SEM}, the average particle diameter ϕ_p and the number N_{SEM} of particles were determined. N_p was then calculated by:

$$N_p = N_{SEM} \frac{S_c}{S_{SEM}} \tag{2.7}$$

It was then also possible to estimate the production rate and the flow rate of particles respectively:

$$\xi_p = \frac{N_p}{t_{spray}} \tag{2.8}$$

$$Q_p = \frac{\pi}{6}\phi_p^3\xi_p \tag{2.9}$$

Measuring the initial slope $k = \left[\frac{dV}{dt}\right]_{t=0}$ of the surface potential, the number of charges per particle and the surface charge density are respectively given by:

$$q_p = \frac{Ck}{\xi_p} \tag{2.10}$$

$$\sigma_p = \frac{4q_p}{\pi\phi_p^2} \tag{2.11}$$

Where C is the capacitance value of the capacitor placed between the collector and the ground (1 nF for PCL14k particles and 100 pF for PCL80k particles).

2.3 A method allowing the measurement of the charges carried by the jet

An original method allowing the measurement of all charges carried by the deposited fiber is proposed (see Fig. 2.1). Once electrospinning has reached a steady state regime on a grounded shutter, it is removed offering thus the surface of a rotating collector placed just below and connected to a capacitor C in series with the ground. During this time t_{spin} of electrospinning, the voltage is measured at the top surface of the rotating collector. This surface potential results from the charging of the capacitor due to the incoming fiber. Fig. 2.2 shows an example of such curves in the cases of PLA (experimental parameters of PLA-2 as seen in Table 2.1) and PEO electrospinning. It is shown that in the case of PLA, the voltage increases linearly with the time, proving that the charge flow rate and thus the fiber flow rate was constant during t_{spin}. This was always the case for all experiments carried out with pure PLA (i.e. without any addition of salt). In the case of PEO, it can be seen that the slope dV/dt decreases with t meaning that the rate of deposited fiber decreases at little bit during the acquisition.

When the shutter was placed below the emitter and the power supply was switched-off, a slow voltage decay was observed which was attributed to weak charge release from the surface of collector to the atmosphere. Then, when the capacitor was short-circuited, the surface potential decreases very rapidly to a value resulting from residual charges remaining on the top surface of the fiber. It is shown that in the case of PEO no significant voltage was recorded: all charges were transferred from the fiber to the collector. However, in the case of PLA, a residual voltage of 10 V remained without transferring in the ground or in the air.

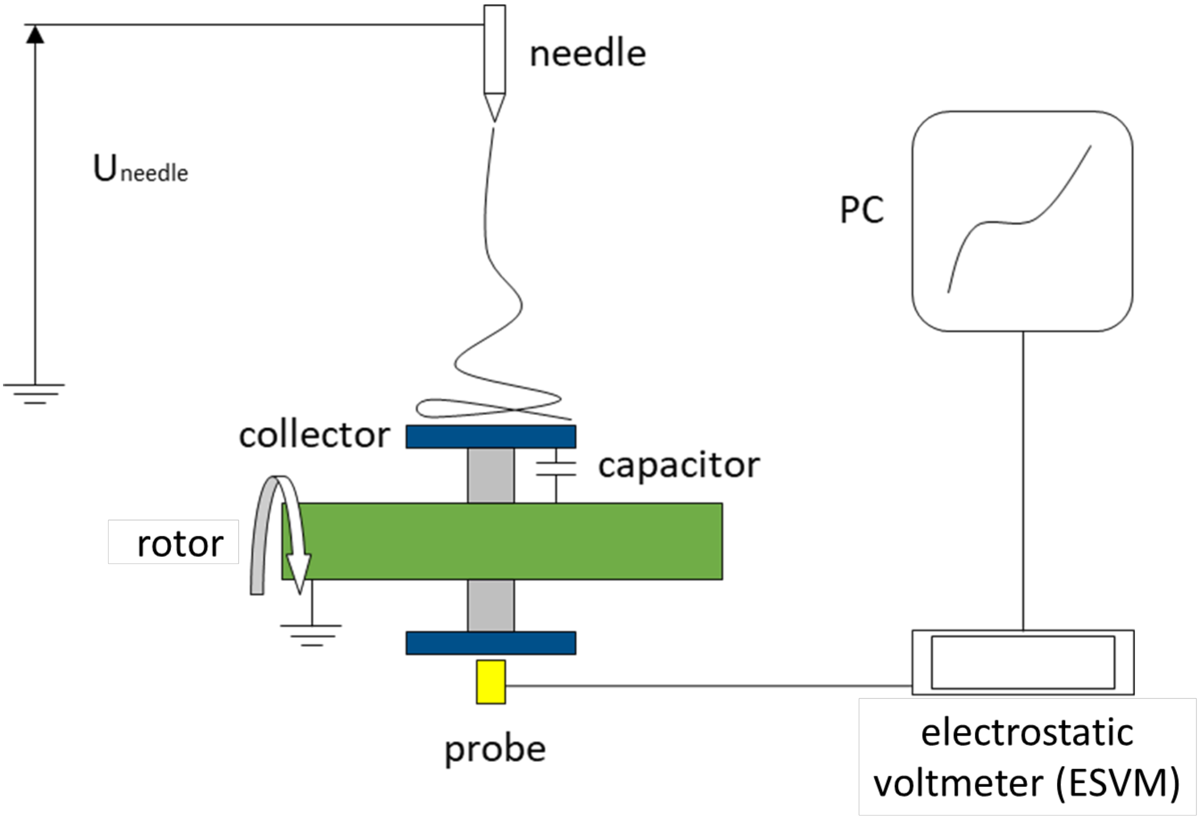

Fig. 2.1 Sketch of the experimental setup for the measurement of the surface potential

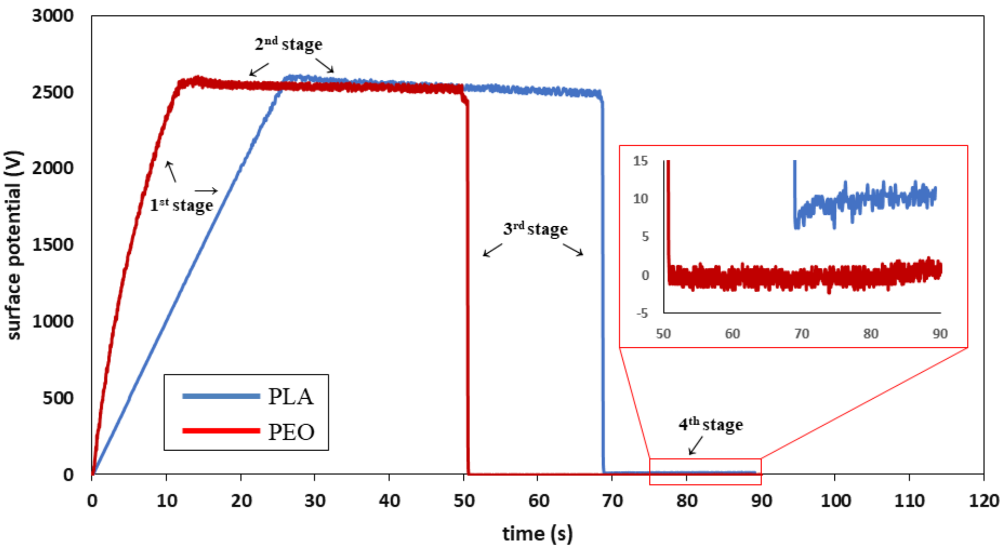

Fig. 2.2 Example of the evolution of the surface potential as a function of time in the case of PLA-2 parameters (see Table 1). 1st stage: accumulation of surface potential during electrospinning; 2nd stage: slow dissipation of surface potential after stopping the power; 3rd stage: sharp decline of surface potential by discharging the charges accumulated on the collector to the ground; 4th stage: stable stage of surface potential induced by residual charges remaining the on the fiber)

The fact that charges remain after having short-circuited the capacitor demonstrate that during the deposition of the fiber a fraction α of charges remain on the fiber and that only a fraction $(1-\alpha)$ are transferred on the surface of the collector resulting in the distribution of the charges as shown in Fig. 2.3a. Thus, during electrospinning, if a total amount of charge Q is deposited, the probe of the electrostatic voltmeter (ESVM) measures a voltage U_{ESVM} induced by the voltage U_C on the capacitor C with a charge $(1-\alpha)Q$ uniformly distributed on the collector, on one hand, and a voltage originated from the charge αQ through the thickness of the fiber, on the other hand. If s_f is the fraction of the surface of the collector which is covered by the fiber, at first approximation, the voltage recorded by the probe can be seen as the following average:

$$U_{ESVM} = s_f U_f + U_C \tag{2.12}$$

Where U_C is given by:

$$U_C = \frac{(1-\alpha)Q}{C} \tag{2.13}$$

U_f is the difference of potential between the top surface of the deposited fiber and its bottom in perfect contact with the collector (see Fig. 2.3a). Considering that the charges are located on the fiber surface and that the deposited fiber behaves as a capacitor of surface $\phi_f L_f$ and thickness ϕ_f, the corresponding capacitance of the deposited fiber can be given by:

$$C_f = \frac{\varepsilon_0 \varepsilon_r}{\phi_f} \phi_f L_f = \varepsilon_0 \varepsilon_r L_f \qquad (2.14)$$

Where ε_0 is the permittivity of vacuum and ε_r is the relative permittivity of the fiber. Thus, U_f can be estimated assuming a difference of charges between the upper and the lower surfaces of the fiber (see Fig. 2.3a):

$$C_f U_f = \big(\alpha - (1-\alpha)s_f\big)Q \qquad (2.15)$$

Knowing that Q can be calculated from the total linear charge density λ carried by the fiber just before landing on the collector:

$$Q = \lambda L_f \qquad (2.16)$$

U_f can thus be estimated by:

$$U_f = \frac{\big(\alpha-(1-\alpha)s_f\big)Q}{\varepsilon_0 \varepsilon_r L_f} = \frac{\big(\alpha-(1-\alpha)s_f\big)\lambda}{\varepsilon_0 \varepsilon_r} \qquad (2.17)$$

Using Eqns. 2.12, 2.13, 2.16 and 2.17, the voltage seen by the ESVM can be approximated by:

$$U_{ESVM} = s_f \frac{\big(\alpha-(1-\alpha)s_f\big)\lambda}{\varepsilon_0 \varepsilon_r} + \frac{(1-\alpha)\lambda L_f}{C} \qquad (2.18)$$

However, the first term in Eqn. 2.18 can be neglected compared to the second. Indeed, from the experiment with the conditions PLA-2 taken in Table 2.1 and Fig. 2.2, $L_f = 5400\ m$ at $t_{spin} = 27\ s$ $\varepsilon_0 = 8{,}8 \times 10^{-12}$ and for PLA $\varepsilon_r = 2{,}7$ [26] and $C = 10^{-9}\ F$, it can thus easily seen that:

$$\frac{\big(\alpha - (1-\alpha)s_f\big)}{\varepsilon_0 \varepsilon_r} \ll \frac{(1-\alpha)L_f}{C}$$

Simplifying the notation $V = U_{ESVM}$, the ESVM see the following voltage:

$$V = U_{ESVM} \approx \frac{(1-\alpha)\lambda L_f}{C} \qquad (2.19)$$

Measuring the slope $\frac{dV}{dt}$ of the surface potential, the fraction of the linear and the surface charge densities which are deposited on the collector are respectively given by:

$$(1-\alpha)\lambda = \frac{kC}{v_f} \qquad (2.20)$$

$$(1-\alpha)\sigma = \frac{(1-\alpha)\lambda}{\pi \phi_f} \qquad (2.21)$$

With:

$$k = \frac{dV}{dt} \tag{2.22}$$

SEM allows the measurement of ϕ_f, the fiber diameter and v_f, the fiber velocity as proposed in the experimental part:

$$v_f = \frac{dL_f}{dt} = \frac{L_f}{t_{spin}} \tag{2.23}$$

Furthermore, the accumulation rate of charges J which are deposited on the collector can be seen as a current:

$$J = kC = (1-\alpha)\lambda v_f \tag{2.24}$$

Fig. 2.3b shows a scheme of what it is measured by the ESVM probe once the collector is connected to the ground, i.e. when the capacitor is short-circuited. Under this condition:

$$U_{ESVM} \approx s_f U_{fsc} = \frac{\alpha\lambda}{\varepsilon_0\varepsilon_r} \tag{2.25}$$

$$s_f \approx \frac{\phi_f L_f}{S_{collector}} \tag{2.26}$$

The experimental conditions of experiment PLA-2 shows that $s_f \approx 0{,}2$ after a time of electrospinning of 27 s. Using 2.20 and 2.25 it is possible to estimate the total linear charge carried by the fiber just before its landing:

$$\lambda = (1-\alpha)\lambda + \alpha\lambda = \frac{kC}{v_f} + s_f U_{fsc}\varepsilon_0\varepsilon_r \tag{2.27}$$

The fraction of charges remaining on the fiber can then be estimated as follows:

$$\alpha = \frac{s_f U_{fsc}\varepsilon_0\varepsilon_r}{\frac{kC}{v_f} + s_f U_{fsc}\varepsilon_0\varepsilon_r} = \frac{1}{1+\frac{kC}{v_f s_f U_{fsc}\varepsilon_0\varepsilon_r}} \tag{2.28}$$

Using the average data taken from the PLA-2 set of experiments, one obtains a fraction of charges $\alpha_{PLA-2} = 0{,}7$. Although we did several assumptions for this estimation, for example we assumed that all charges remaining on the fiber are located on its surface, it is shown that more charges remain on the fiber than charges being released on the collector surface! Nevertheless, the capacitor was not always short-circuited and, in the following, only the released fraction of charges has been calculated from eqn. 2.20: $(1-\alpha)\lambda = \frac{kC}{v_f}$. In the next section, the effects of different parameters and the nature of polymer on the charge density of fibers and the accumulation rate in electrospinning is discussed deeply.

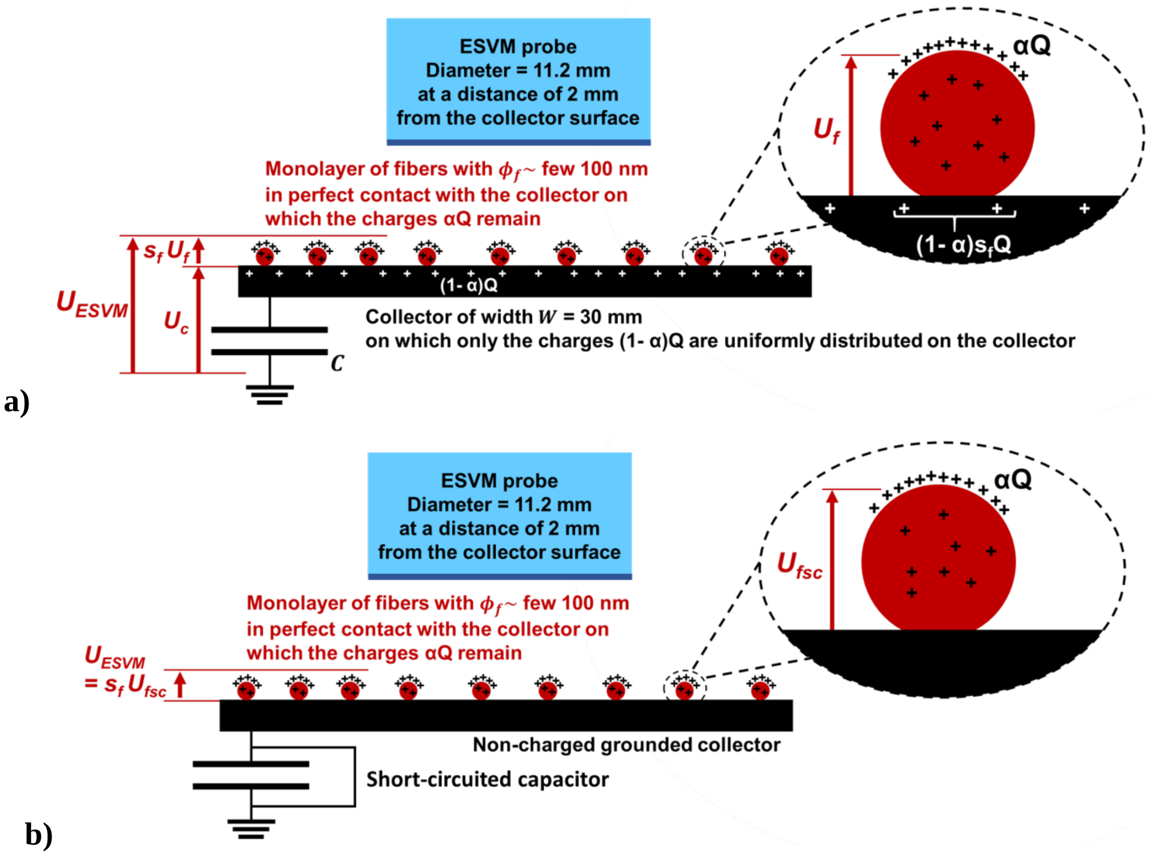

Fig. 2.3 Scheme highlighting the difference in scales between the collector, the ESVM probe and the collector and showing also the voltage measured by the ESVM probe a) during electrospinning and b) after having short circuited the capacitor

2.4 Effect of processing parameters on the linear and surface charge densities in the case of PLA electrospinning

2.4.1 Effect of the polymer concentration in the solution

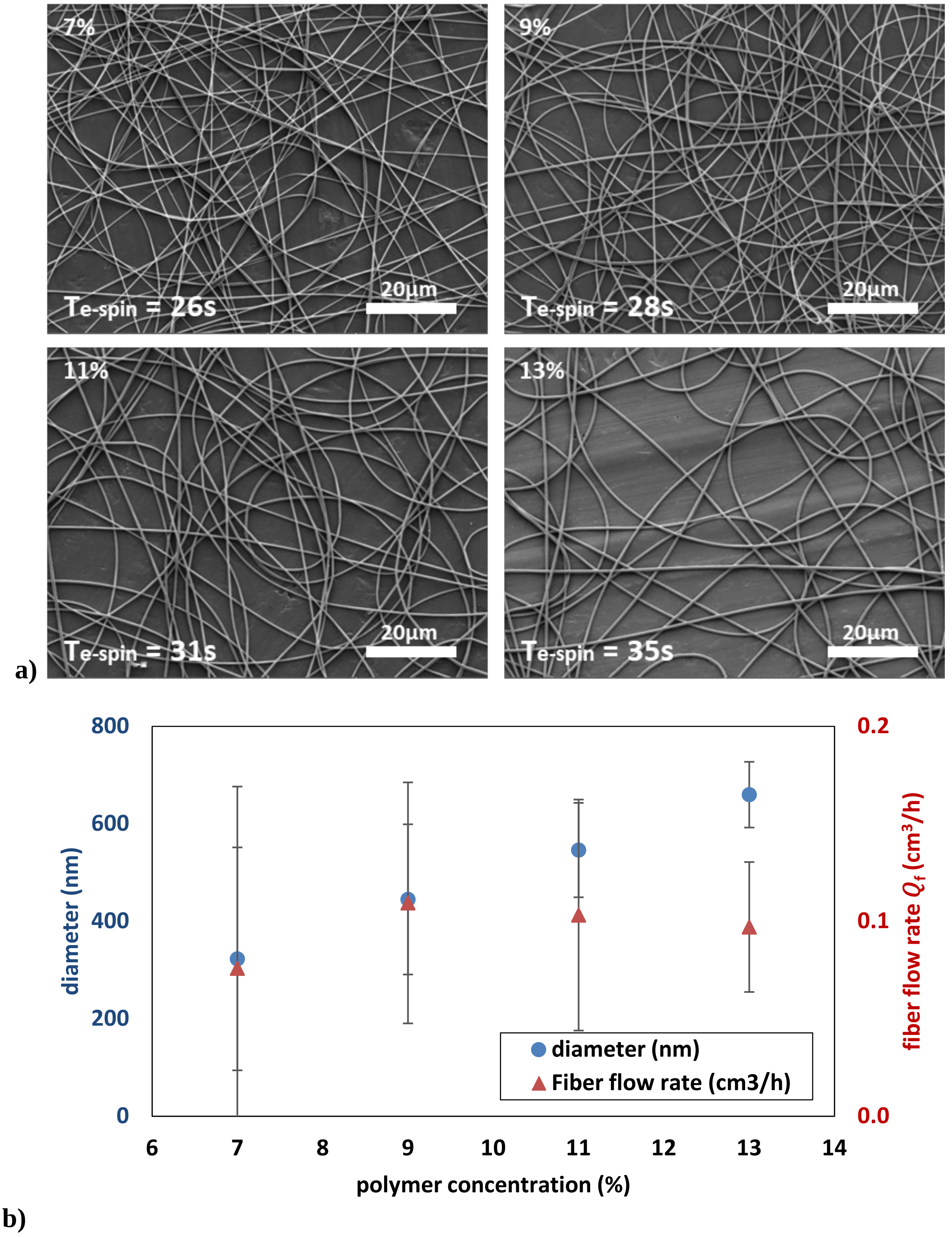

Fig. 2.4 a) morphology and b) diameter and fiber flow rate Q_f of PLA fibers prepared from the polymer solution at the concentration of 7%, 9%, 11% and 13%

Fig. 2.4 presents SEM images of fibers and the graph of PLA fiber diameter and fiber flow rate as a function of PLA concentration. Keeping all other parameters constant, fibers generated at a concentration of 7% have the lowest average diameter (i.e. 322nm). It is shown that in the studied range of concentration the average diameter increases linearly with concentration with a maximum value of 659 nm at a weight concentration of 13%. This well-known effect is attributed to the increase of the solution viscosity with the concentration due to enhanced polymer chains entanglement. Indeed, a high viscosity reduces the deformations (i.e. the whipping movements) of the flying jet which are responsible for the increasing jet diameter [27], [28].

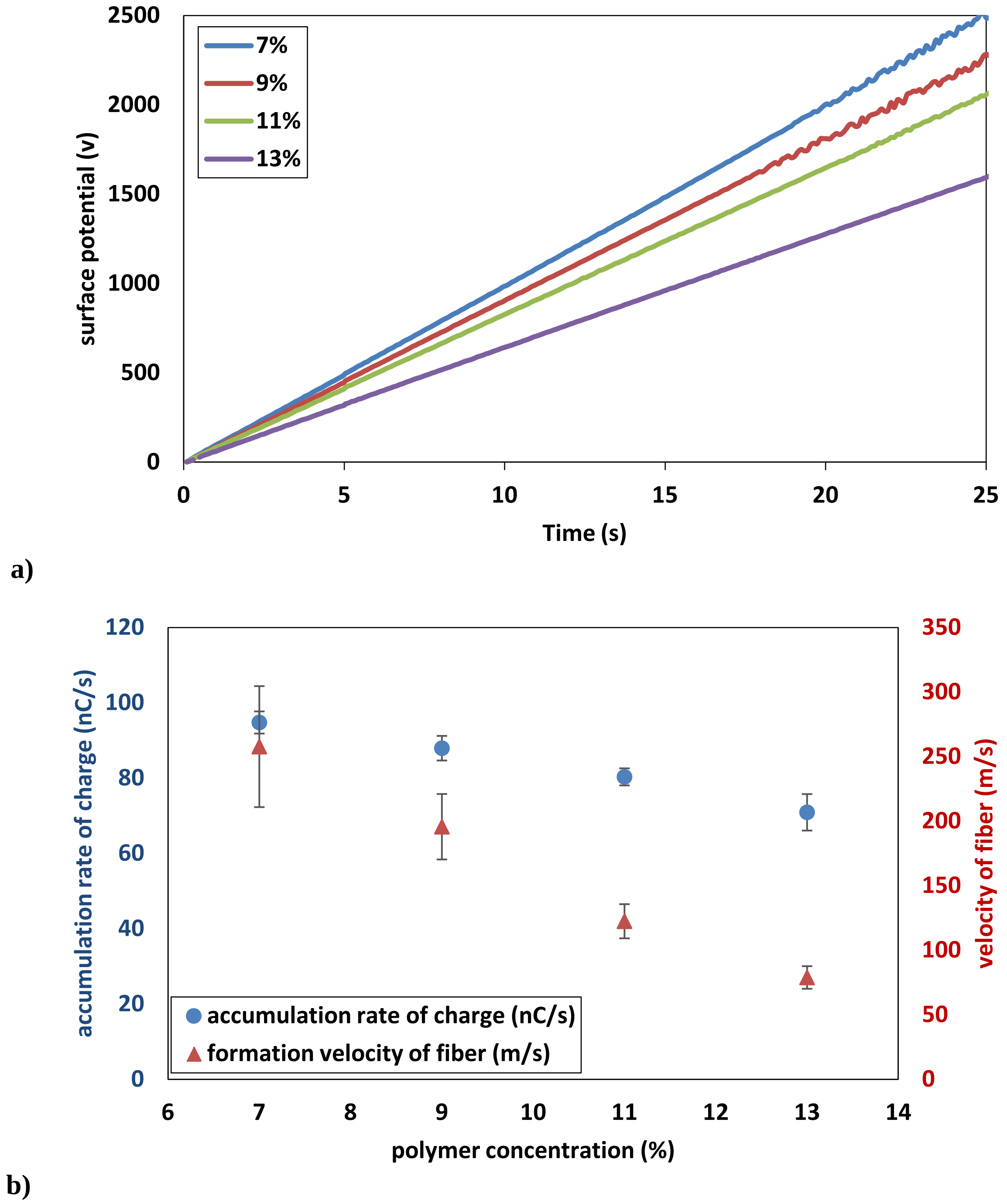

Fig. 2.5 a) Example of acquired curves giving the surface potential of PLA fibers as a function of time for the concentrations of 7%, 9%, 11% and 13%. b) Accumulation rate of charges J and fiber velocity v_f

Fig. 2.5 presents the effect of polymer concentration on the accumulation rate of charges J and the fiber velocity v_f. It clearly appears that both accumulation rate and fiber velocity decreases with increasing PLA concentration. The decrease of v_f is due to the increase of the solution viscosity with the increasing concentration. Thus, for a given production time t_{spin} a longer fiber length is produced at lower concentration as depicted in Fig. 2.6.

The effect of the concentration on J is more complex. It is worth noting that in these experiments, solution feed rate was fixed at 1 mL/h. Thus, in a first assumption, regarding the polymer alone when the dry fiber lands the collector, increasing the concentration should lead to the increase of the polymer flow rate and thus also the total amount of accumulated charges represented by J. Nevertheless, as shown in Fig. 2.4, the fiber flow rate Q_f is almost constant. In fact, the fiber flow rate is a complex function resulting from the feeding rate of the pump and from the electrostatic ejection force at the Taylor cone. Regarding the feeding rate, because the solution rate was fixed at 1 mL/h, an increase of the concentration would lead to an increase of the polymer fiber flow rate. However, regarding the effect of coulombic forces responsible of the production of fiber, an increase of the concentration should lead to a decrease of the fiber flow rate due to the enhancement of the solution viscosity. Nevertheless, it must be mentioned that the estimation of Q_f from Eqn 2.6 leads to wide error bars. Furthermore, the modification of the polymer concentration has also an effect on the amount of solvents which is a 50/50 mixture of DCM and DMF as seen in Fig. 2.6. Thus, an increase of the polymer concentration leads also to a decrease of the amount of DMF which is known to have beneficial effect on the fiber electrospinninability due to its high dielectric constant and high conductivity compared to DCM[29]–[31]. Thus, in conclusion, it appears that increasing the concentration may have a predominant effect on (i) the viscosity decreasing the fiber production and (ii) on the decrease of the amount of DMF lowering the electrospinninability explaining the evolution of the accumulation rate J as a function of the concentration.

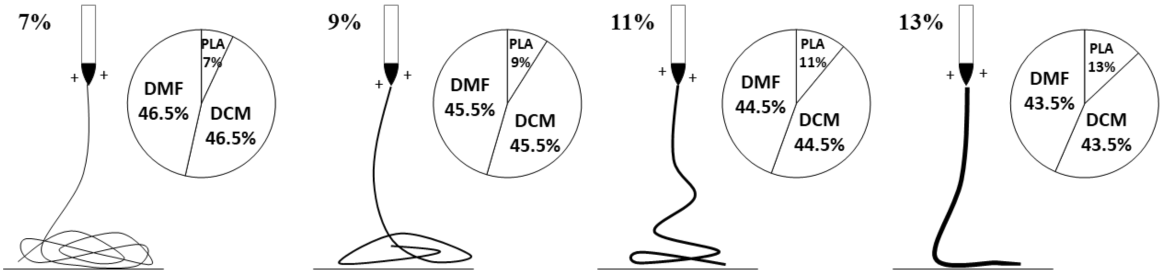

Fig. 2.6 illustration of the charged status of the droplets of PLA solution at the concentration of 7%, 9%, 11% and 13%

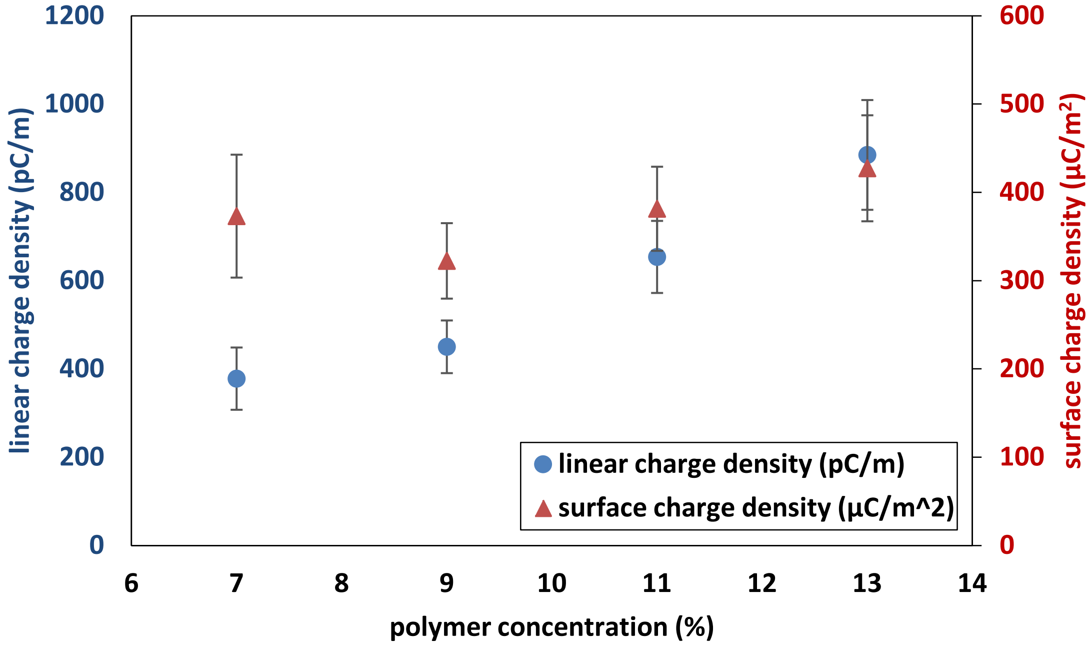

Fig. 2.7 linear and surface charge densities of PLA fibers as a function of the polymer concentration

Fig. 2.7 shows that the linear charge density λ increases with the concentration. As shown in Eqn. 2.12, λ is proportional with J and inversely with v_f. Although J and v_f decrease with the concentration, it appears that the decrease of v_f dominates and explains the increase of the linear charge density. The evolution of the surface charge density is more complex due to its dependence on the fiber diameter and no significant trend can be drawn.

2.4.2 Effect of the solution conductivity: addition of a salt TEBAC

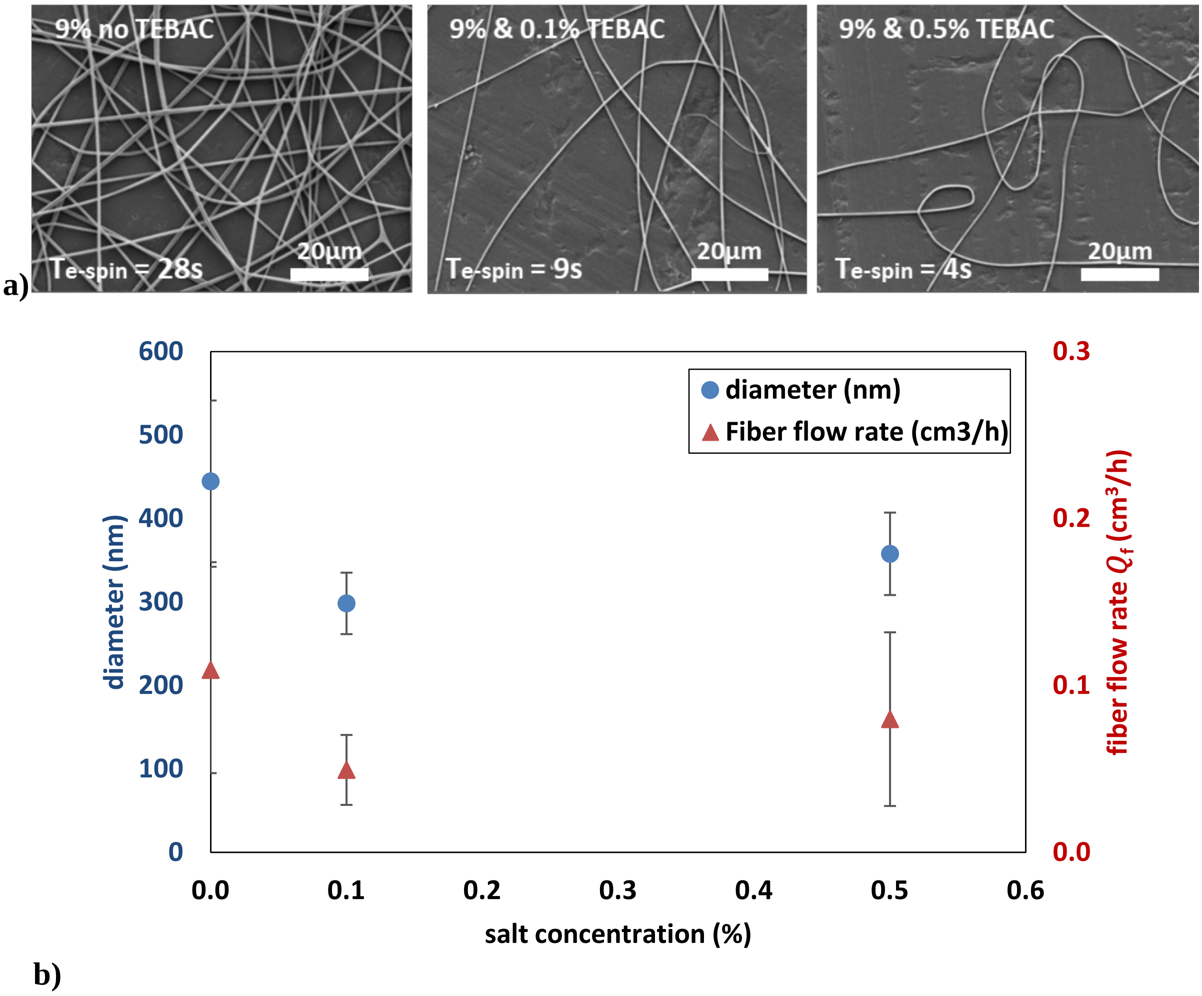

Fig. 2.8 a) Morphology and b) diameter and fiber flow rate Q_f of PLA fibers prepared from the polymer solutions mixed with TEBAC salt at various contents

Fig. 2.8 shows no significant effect of the salt content on the fiber flow rate. When adding a small amount of TEBAC salt (0.1%) in the solution, a decrease of the fiber diameter can be observed in Fig. 2.8. Indeed, it is generally admitted that adding a salt can increases sharply the solution conductivity leading to stronger elongating force provided during the stretching of the jet [32]–[34]. However, for a much higher salt content no significant evolution of the fiber diameter is observed which might be explained by the reaching of a critical value as mentioned in several other reports [35]–[37].

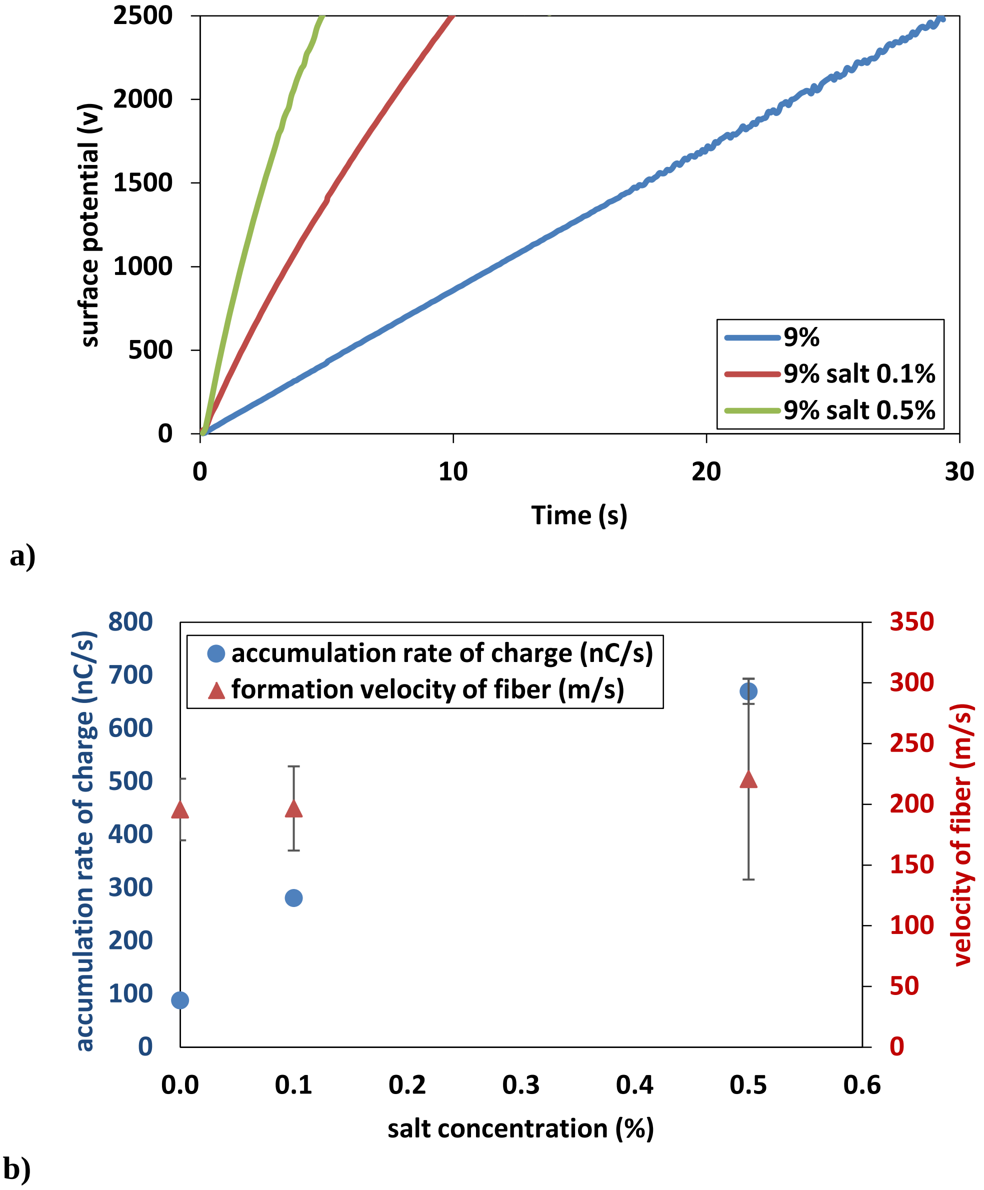

Fig. 2.9 a) Examples of curves of surface potential as a function time for PLA fibers prepared from various TEBAC salt contents. b) Accumulation rate of charges J and fiber velocity v_f as a function of the salt content

Tab. 2.2 Conductivity of the solutions as a function of TEBAC salt content

Salt content (%) in a 9% PLA solution in 50/50 DCM/DMF	Conductivity (µS/cm)
0	3.08
0.1	304
0.5	1049

Fig. 2.9b showed that the accumulation rate of charge J increases very significantly with the salt content even at the highest values. The increase of the salt content induces obviously a sharp increase of the solution conductivity as shown in Table 2.2 explaining that increasing the amount of TEBAC ions in the solutions enhances directly the accumulation rate of charges on the collector. Moreover, as shown in Fig. 2.9a, when electrospinning the PLA solutions with salt, the slope dV/dt decreases with time. This effect is probably due to the fact that a small amount of fiber is deposited outside the collector surface due to repulsion effect. Indeed, the high amount of charges located on the collector surface, characterized by the high J value, induces a repulsive electric field which may prevent the efficient deposition of the incoming fiber on the collector surface. Surprisingly, the high level of charges measured in the cases of salted solutions has a poor effect on the jet velocity and on the average fiber diameter. However, it is seen that the polydispersity of the fiber velocity increases significantly with the addition of salt proving that the introduction of TEBAC changes the stability of jet remarkably. In this case, during the whipping movement of the jet, the highly charged jet produces repulsive forces causing the fiber to swing more violently and fall in a larger beyond the collector surface. Thus, the measured fiber velocity may also be underestimated in these cases. In agreement with these observations, both the linear and the surface charge densities increase sharply with the addition of TEBAC salt (see Fig. 2.10).

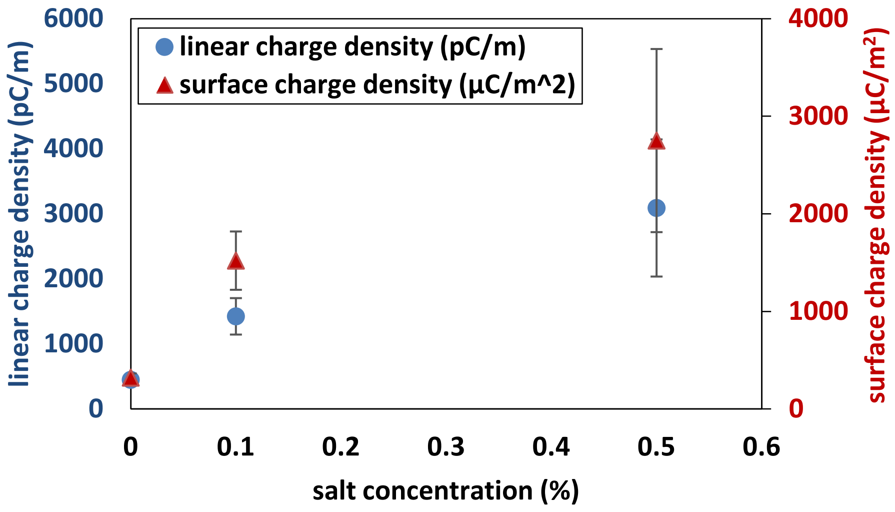

Fig. 2.10 Linear and surface charge densities of PLA fibers prepared with various TEBAC salt contents

2.4.3 Effect of the applied voltage

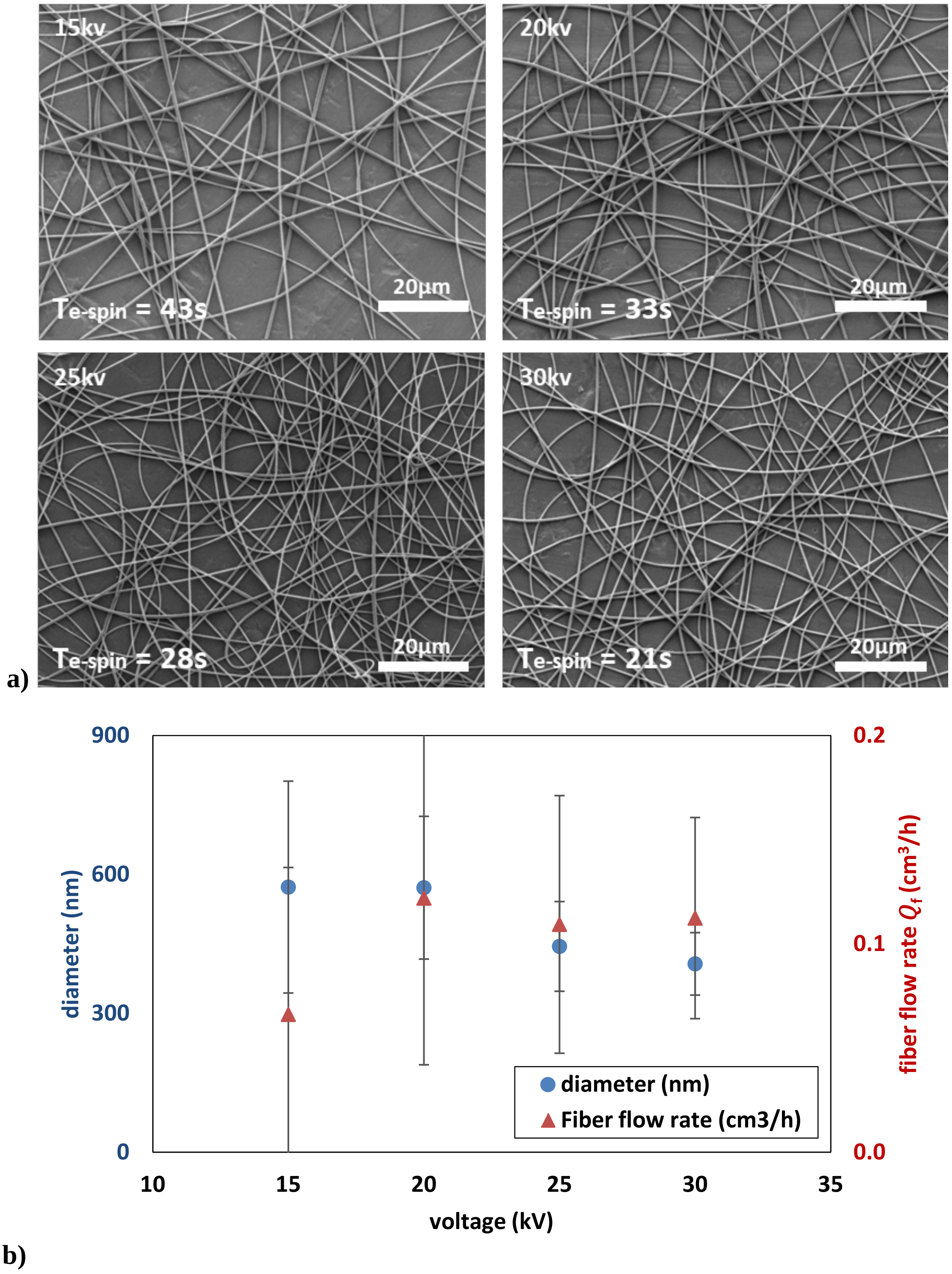

Fig. 2.11 a) Morphology and b) diameter and fiber flow rate Q_f of PLA fibers prepared under various applied voltages

Fig. 2.11 shows the SEM images of PLA fibers generated from electrospinning at different voltages and the corresponded values of fiber diameter and fiber flow rate. Although the wide error bars, a small decrease of the fiber diameter happens from voltage higher than 20 kV. In the process of electrospinning, a sufficient applied voltage is required to form an electric field which overcomes the surface tension allowing the jet ejection from the apex of the Taylor cone. A more intense electric field at the surface of the Taylor cone provides thus more charges to the jet resulting to stronger whipping movements and jet stretching. Consequently, the fibers formed under the highest voltage have the smallest fiber diameter as observed by many authors [38], [39]. However, in our case, this effect was not pronounced. Fig. 2.11 shows also that the error bars decrease gradually with enlarging the voltage, inducing that the distribution of fiber diameters is narrower for the highest voltage. During electrospinning under high voltage, the resulting strong electric field leads to a coulombic strength allowing efficiently overcoming the surface tension at the Taylor cone and stretching the jet, resulting in a fiber with a narrow diameter distribution.

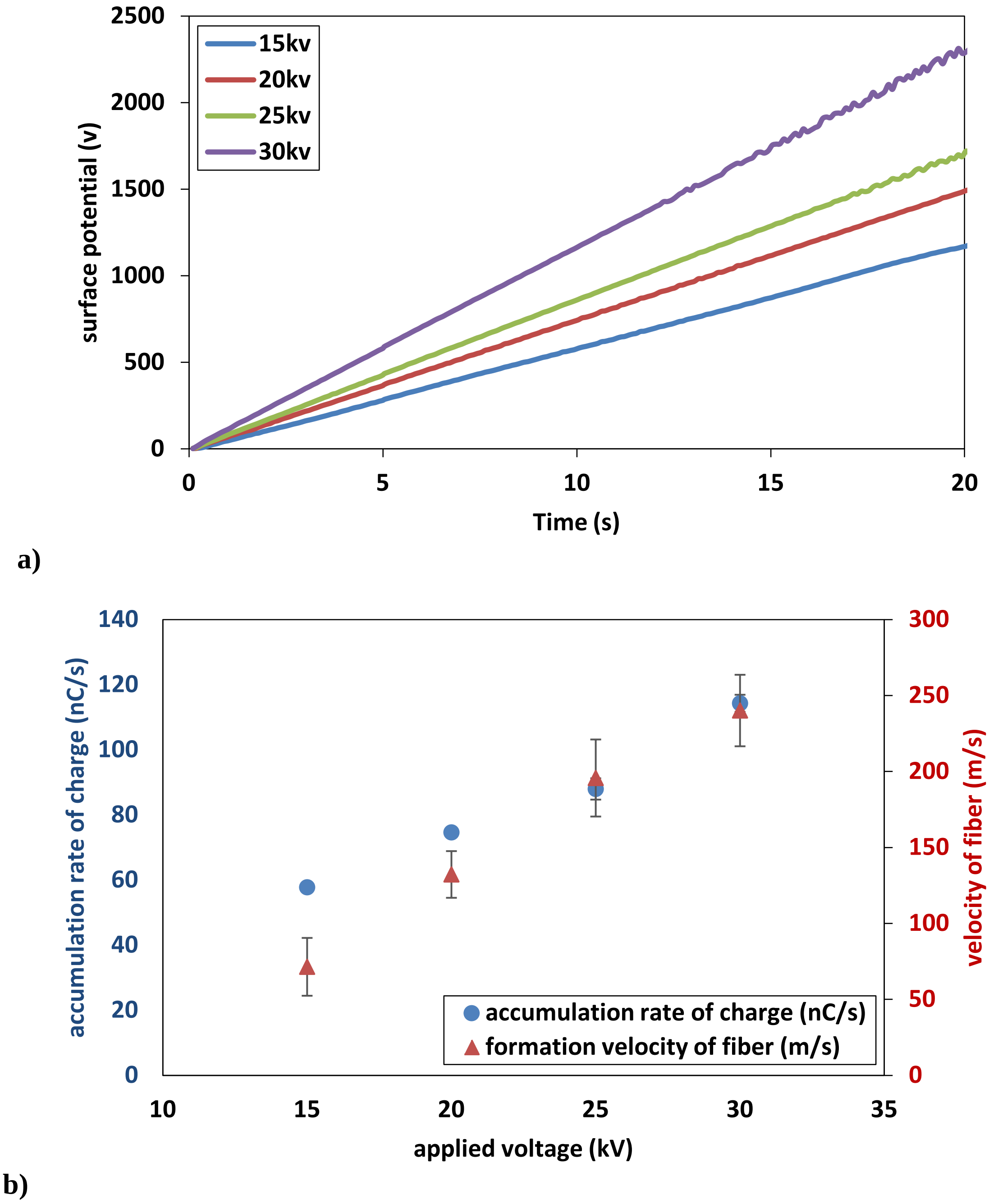

Fig. 2.12 a) Examples of curves of surface potential versus time for the electrospinning of PLA under various applied voltages. b) Accumulation rate of charges J and fiber velocity v_f as a function of the applied voltage

As expected, Fig. 2.12 shows that the accumulation rate of charges increases linearly with the applied voltage which appears as an intuitive result. Thus, it is clearly proven that the total amount of charges brought by the deposited fiber is directly linked with the applied voltage. Similarly, the fiber velocity evolves with the same trend: increasing the voltage, ensures higher jet stretching and thus a higher fiber velocity.

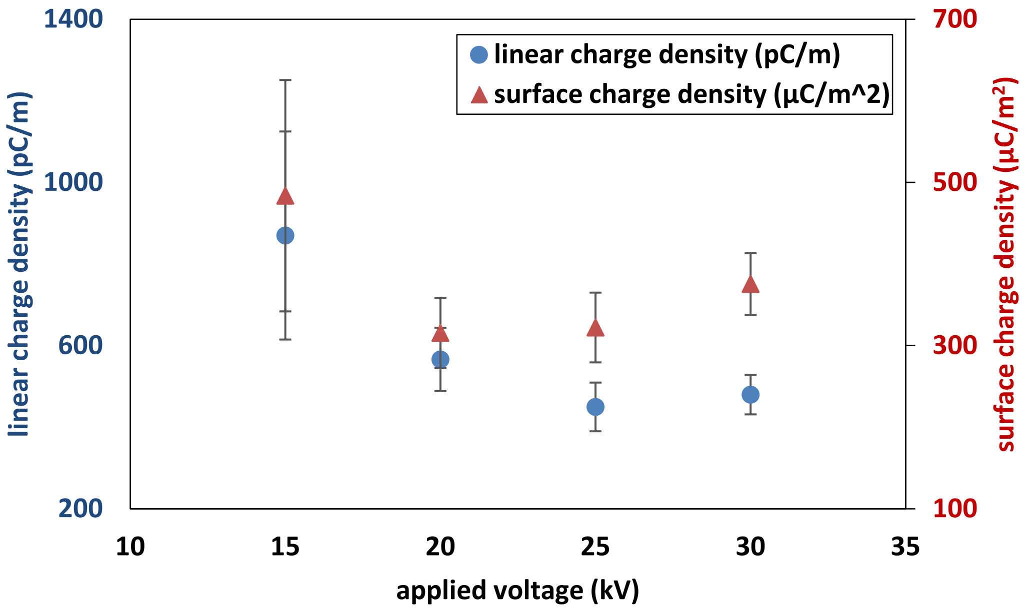

Fig. 2.13 Linear and surface charge densities of PLA fibers generated under various applied voltages

The evolution of the linear as well as the surface charge density with the applied voltage is not obvious due to their dependence with several factors. Because v_f increases more rapidly than J, it results from Eqn. 2.14 a decrease of the linear charge density with the applied voltage. The fact that the surface charge density depends also on the fiber diameter, a minimum σ_f is observed for an intermediate voltage ranging between 20 kV and 25 kV.

2.4.4 Effect of ambient humidity

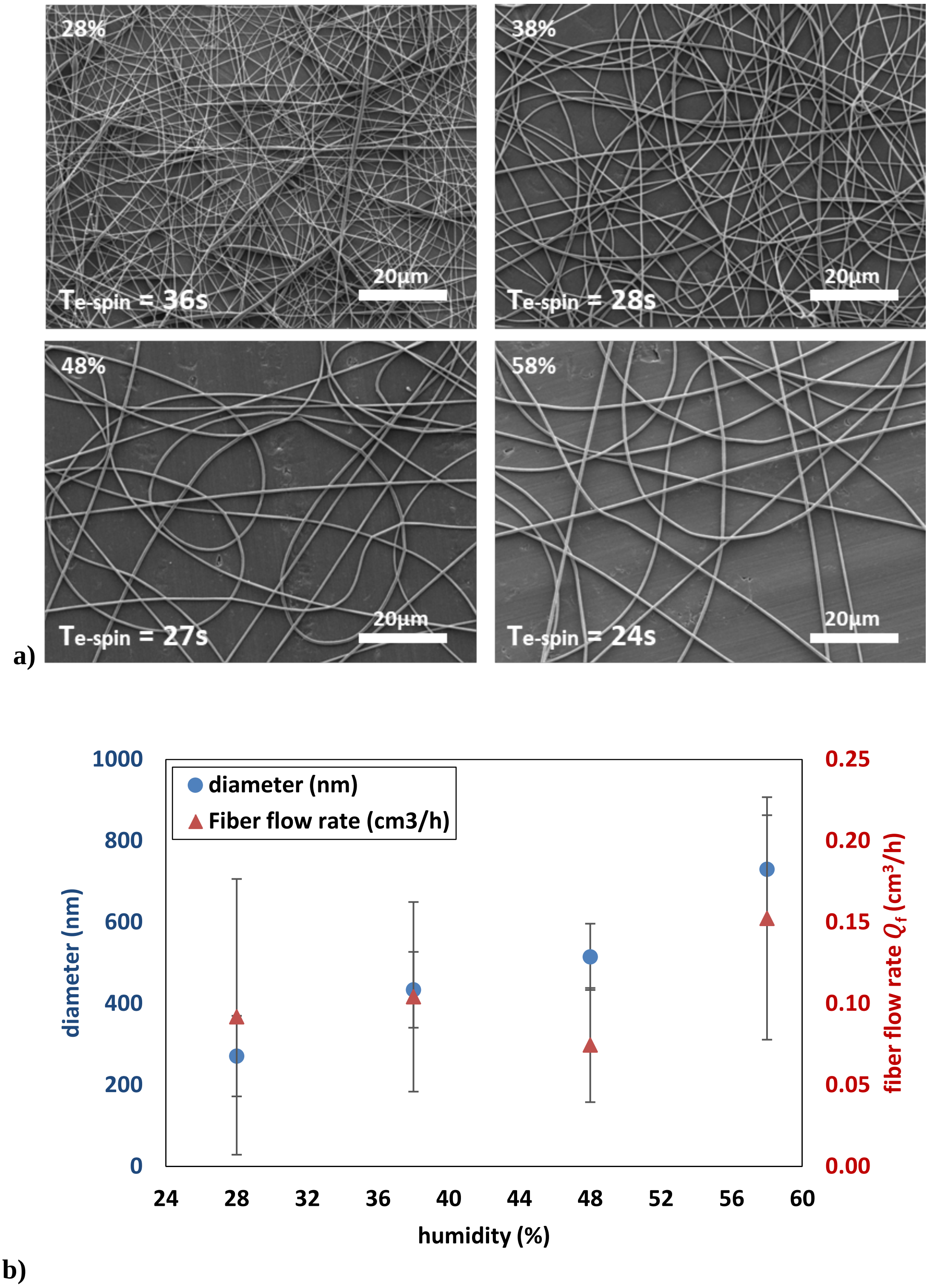

Fig. 2.14 a) SEM pictures showing the morphology and b) diameter and fiber flow rate Q_f of PLA fibers produced under various conditions of ambient humidity

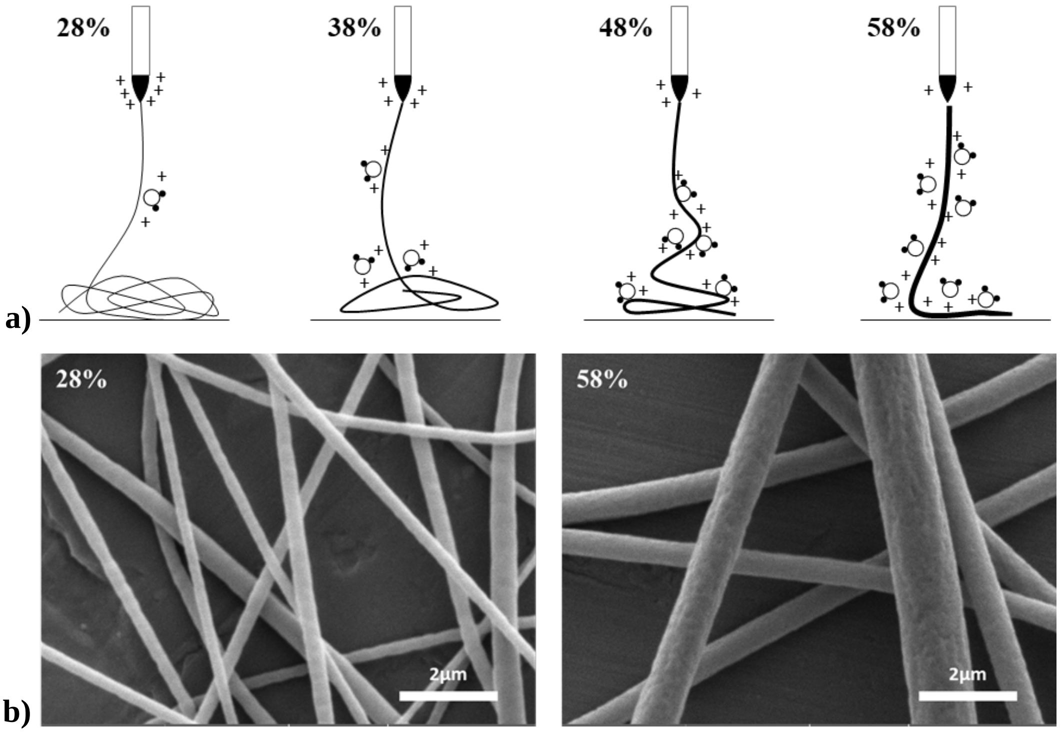

Fig. 2.15 a) Illustration of the absorption of water molecules on the surface of the PLA jet with increasing relative humidity. b) Comparison of the morphology of PLA fibers obtained at *RH* = 28% and *RH* = 58%

Fig. 2.14 shows SEM images of PLA fibers prepared under different ambient humidity and the corresponding fiber diameters. It clearly appears a strong linear increase of ϕ_f with the relative humidity (*RH*) which was already reported [40], [41]. This trend may be explained by two effects: (i) charge release by molecular polarization and (ii) fast PLA precipitation. Indeed, due to the large dielectric constant of water molecules, it could be expected that at high *RH*, the jet may be subjected to a high level of charge release by molecular polarization explaining thus less efficient whipping movements leading to larger diameters. At low *RH,* thin fibers are observed which could be attributed to more electrostatic charges kept on the jet due to less charge release by molecular polarization. Thus, a high density of electrostatic charges is expected at low *RH* increasing the jet stretching and thinning [42]–[44]. Furthermore, SEM pictures show that fibers elaborated at high *RH* held pores on their surface. The appearance of such porous structure is attributed to the condensation of water vapor at the jet surface resulting in phase separation in the PLA/DCM/DMF system (Fig. 2.15). Indeed, DMF is miscible in water which allows the water molecules to flow into the jet. However, as a hydrophobic polymer, PLA moves out of the solution as water molecules are absorbed by DMF resulting in two phases: one PLA-rich phase and one solvent-rich phase containing water molecules. Hence, the solvent-rich portions of the jet induce the formation of pores after the final evaporation [41], [43], [45]. Furthermore, the presence of absorbed water in the jet at high *RH* may lead to rapid precipitation of PLA when the jet is thick explaining also the increase of ϕ_f with *RH*.

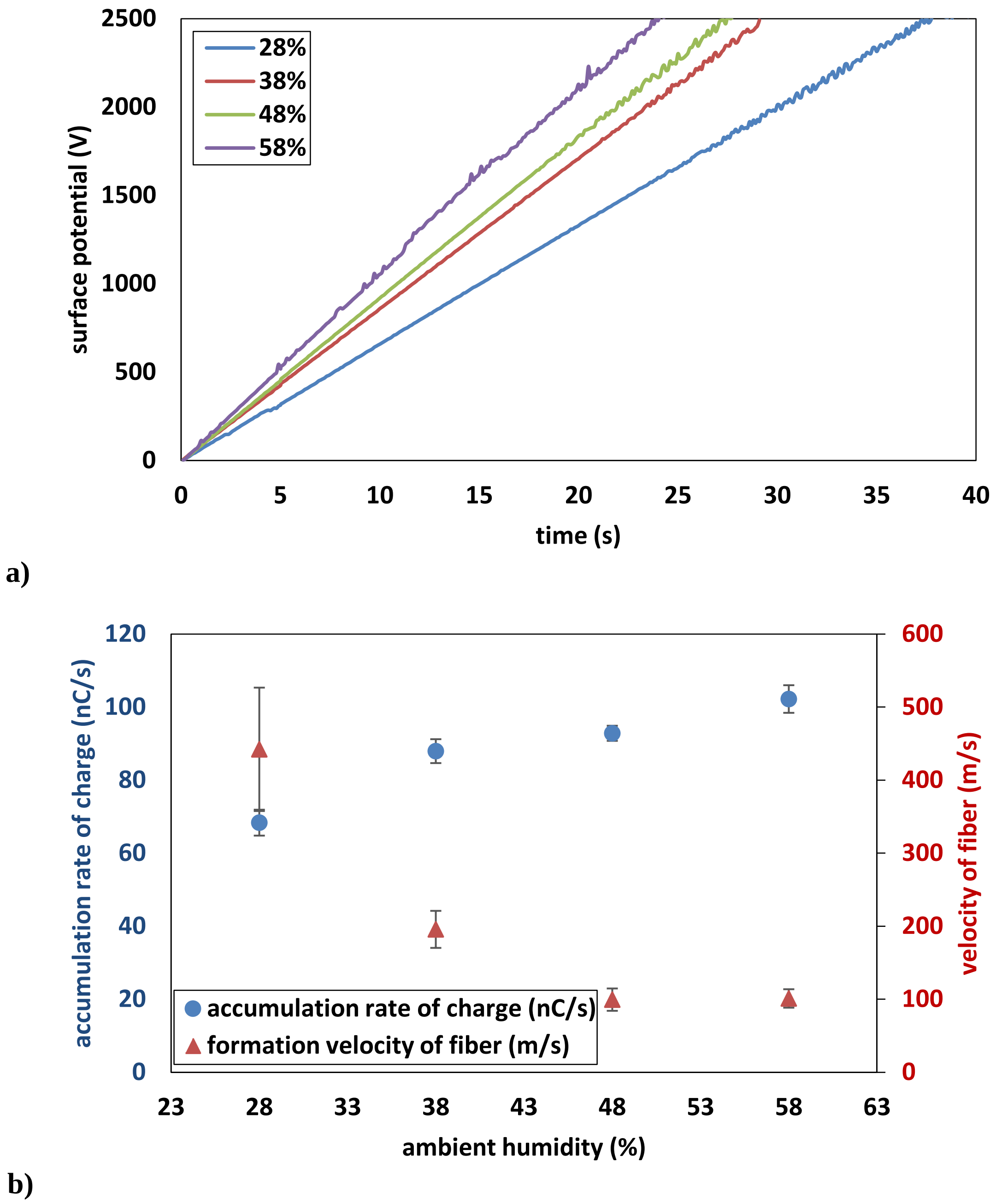

Fig. 2.16 a) Examples of curves of the surface potential as a function of time for various *RH*. b) Accumulation rate of charges J and fiber velocity v_f as a function of *RH*

Fig. 2.16b shows surprisingly that the accumulation rate of charges J increases with *RH* whereas the fiber velocity v_f decreases sharply. Pure electrostatic effects would explain an increase of v_f with J, however the opposite trend is observed. Thus, another phenomenon must account for the decrease of the fiber velocity with *RH*. As discussed before, the increase of the fiber diameter might be explained by two phenomena: (i) charge release by molecular polarization and (ii) PLA precipitation. Because J increases with *RH*, charge release by molecular polarization cannot be responsible for the decrease of the fiber velocity. Thus, the predominant phenomenon explaining both the decrease of v_f and the increase of ϕ_f with RH is the fast PLA precipitation induced by absorption of water molecules. Indeed, a fast precipitation induces the solidification of the jet when it is thick. Meanwhile, the whipping movements have poor stretching effects on a jet which is thick and solid. Consequently, it is observed a huge increase of the linear and the surface charge densities, especially from *RH* = 28 % to 48 % as shown in Fig. 2.17.

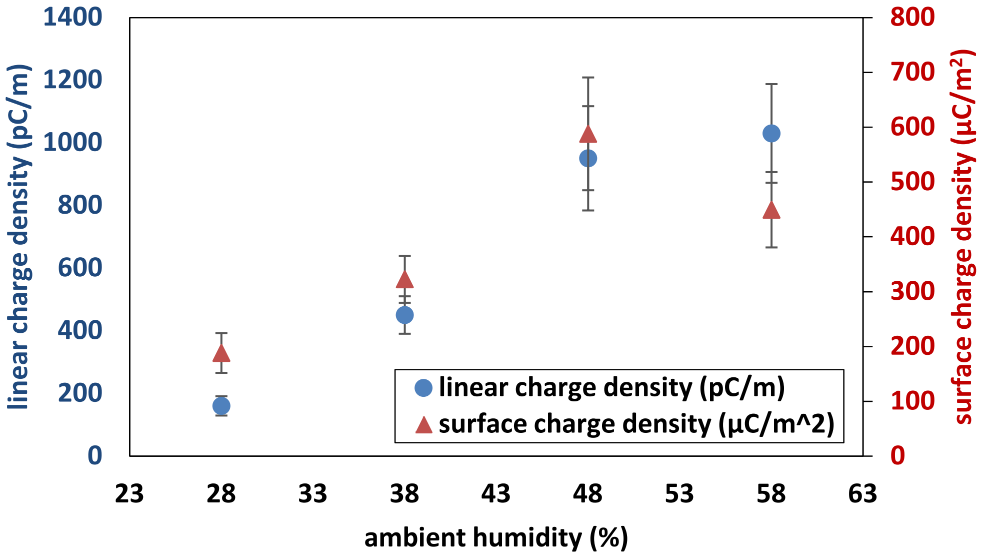

Fig. 2.17 Linear and surface charge densities of PLA fibers produced under various *RH*

2.4.5 Effect of the feeding rate

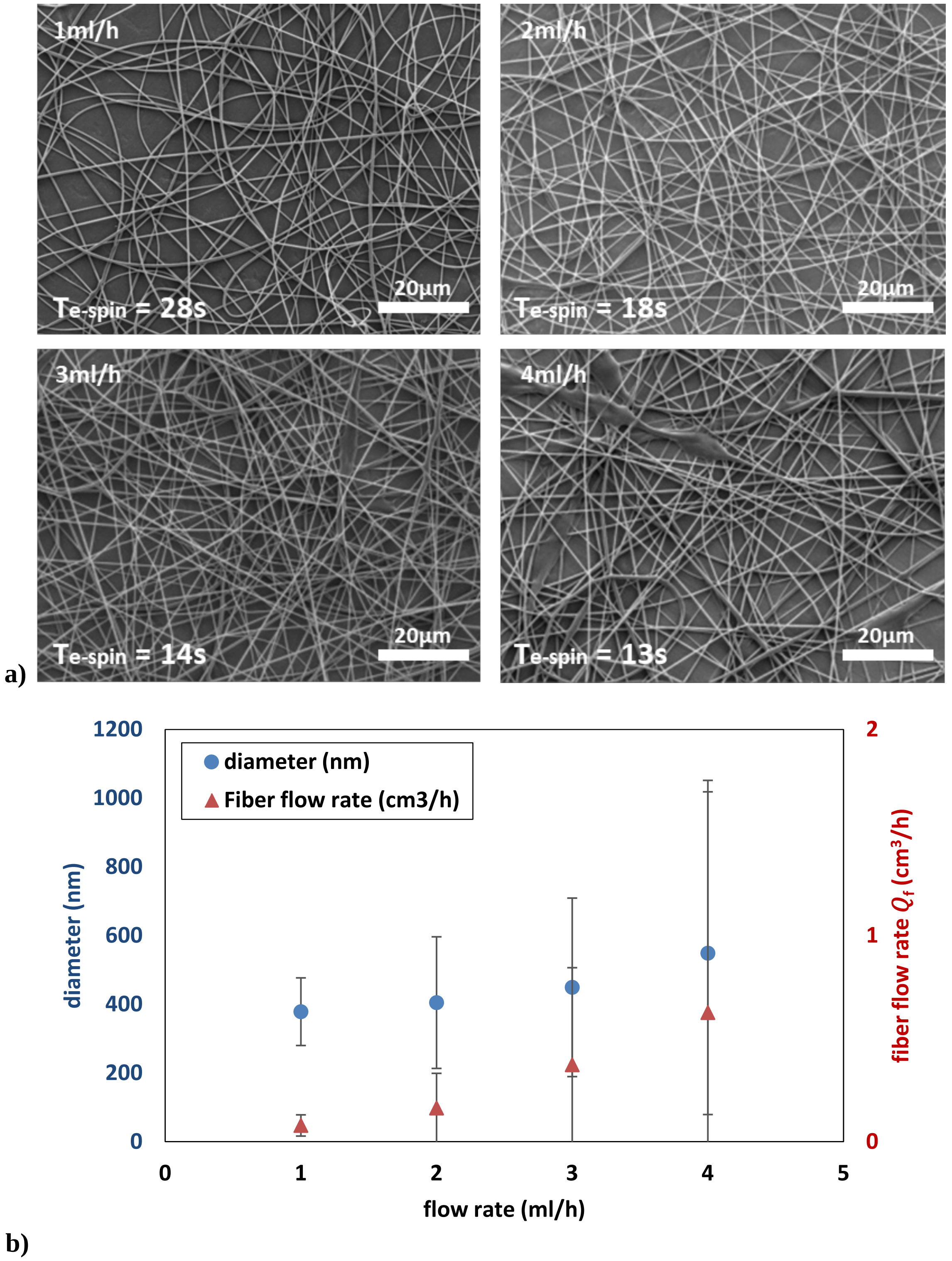

Fig. 2.18 a) SEM pictures of PLA fibers and b) diameter and fiber flow rate Q_f as a function of the solution feeding rate

In the whole process of electrospinning, an optimal intensity of the electric field around the emitter is required for the stable formation of the jet for a given solution feeding rate. Similarly, some reports mention that an optimal solution feeding rate is necessary to insure a steady cone-jet [45], [46]. In the previous sections, we have seen that a steady process was achieved for a solution feeding rate of 1mL/h. Starting from this condition, the flow rate was increased gradually to prepare PLA fibers for flow rate rising to 4 mL/h.

Fig. 2.18 shows that the solution feeding rate has no significant effect on the average fiber diameter although a small increase may be seen. In fact, the increase of the feeding rate enlarges the distribution of the fiber diameter remarkably. This phenomenon is shown on SEM images where large and thick fiber portions can be observed in the case of the highest feeding rate. Moreover, fusion at the fiber-fiber contact points is also observed for the highest feeding rate, which phenomenon is attributed to insufficient evaporation.

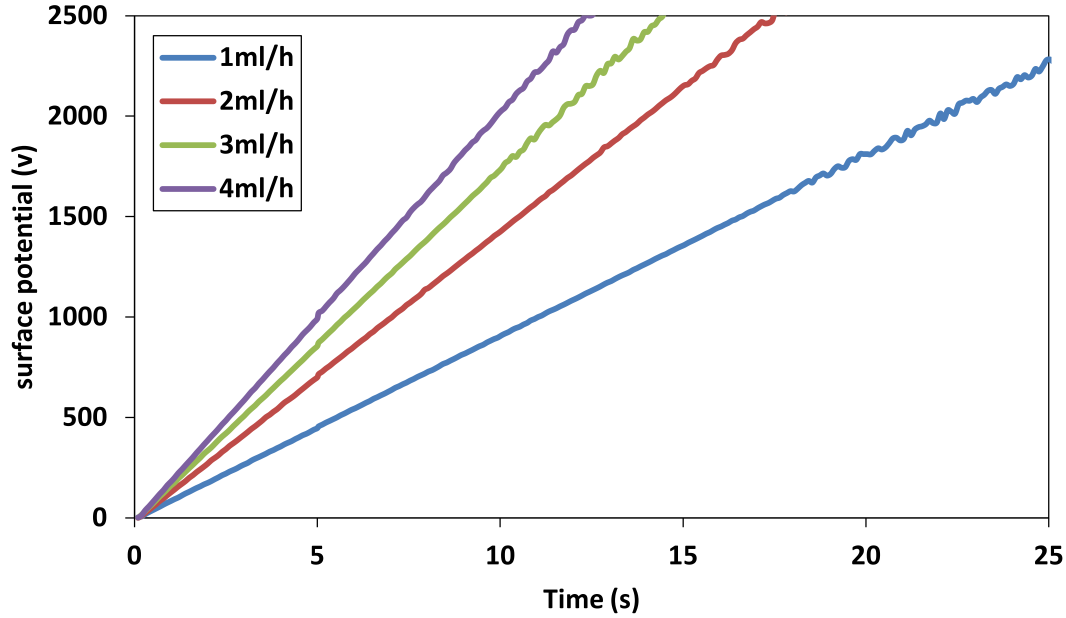

a)

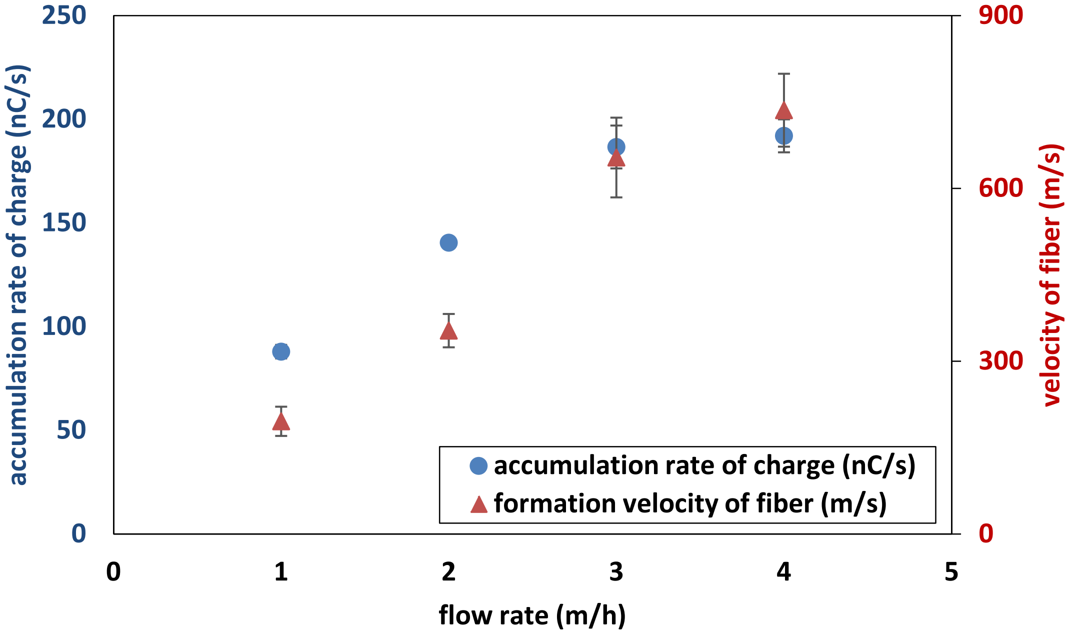

b)

Fig. 2.19 a) Examples of curves showing the evolution of the surface potential as function of time for various solution feeding rates. b) Accumulation rate of charges J and fiber velocity v_f as a function of the solution feeding rate

Fig. 2.19 shows the variation of the accumulation rate of charges J and the fiber velocity with the solution feeding rate. Increasing the feeding rate has a direct consequence on J as the charges are transported more rapidly. The same trend is observed for the fiber velocity which increases very significantly with the solution feeding rate.

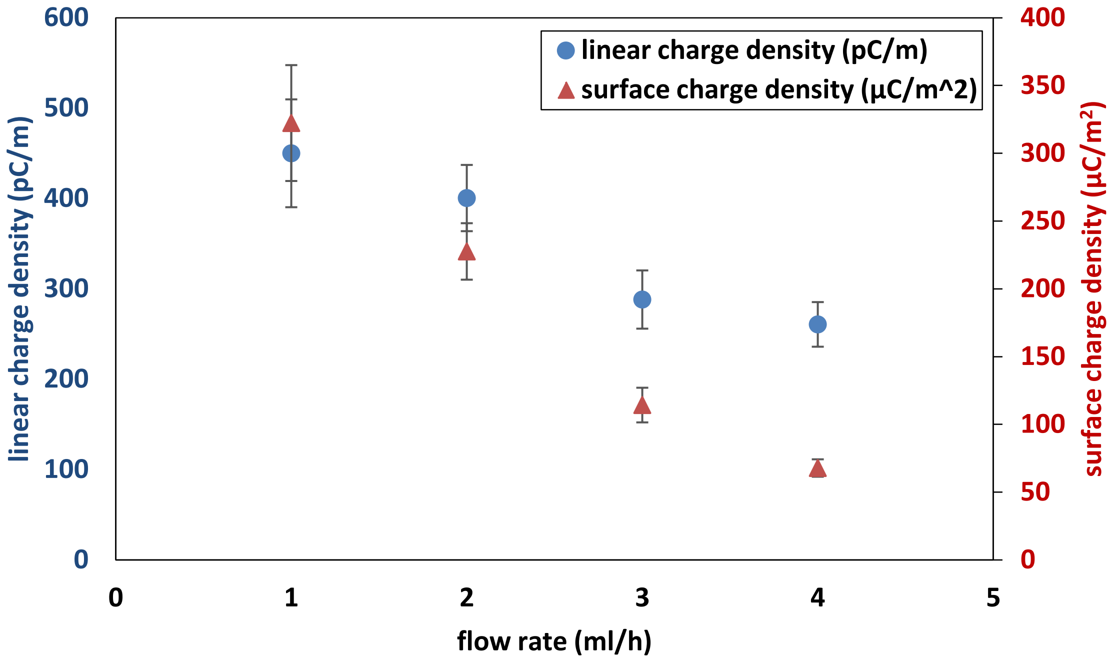

Fig. 2.20 Linear and surface charge densities of PLA fibers fabricated from various feeding rates

Because the increase of the fiber velocity with the feeding rate is much more pronounced than the increase of J, a sharp decrease of the linear and the surface charge densities is consequently observed (Fig. 2.20).

2.5 Effect of the nature of the processed polymer on the linear and surface charge densities

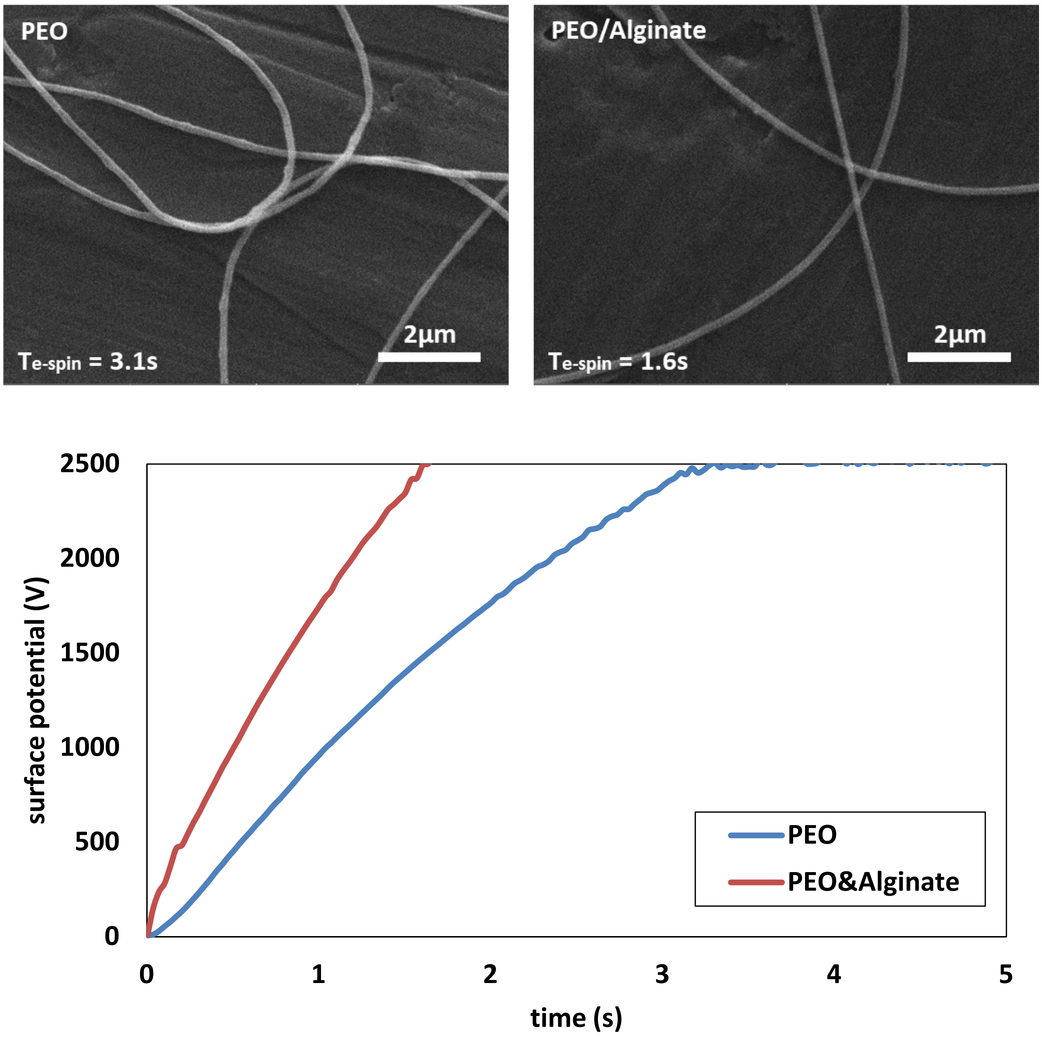

Fig. 2.21 SEM images of PEO fibers and PEO/Alginate fibers and corresponding curves of surface potential

Tab. 2.3 Diameter, velocity and accumulation rate of charges for PEO/Alginate and PEO fibers. Values are given as mean ± standard deviation

	PEO/Alginate	PEO
Diameter (nm)	151.75 ± 25.40	169.10 ± 22.06
Fiber velocity (m/s)	162.05 ± 14.99	162.15 ± 50.22
Accumulation rate of charge (µC/s)	1.64 ± 0.05	1.02 ± 0.03
Linear charge density (nC/m)	4.8	2.7
Surface charge density (mC/m^2)	10	5

Compared to the previous sections, here aqueous polymer solutions having a much higher conductivity were electrospun. Fig. 2.21 shows the morphologies of PEO and PEO/Alginate fibers. Tab. 2.3 shows that the diameter as well as the fiber velocity do not evolve significantly with the addition of alginate. However, the addition of alginate leads to the increase of the accumulation rate of charges which is attributed to the polyelectrolyte nature of alginate enhancing the number of ions in the solution. Such effect on J and ϕ_f clearly explains the increase of the linear and the surface charge densities with the incorporation of alginate.

Tab. 2.4 conductivity of PEO/Alginate, PEO, PLA/TEBAC and PLA solutions and the fibers produced in corresponding solutions, values were given as means ± standard error of the mean

	conductivity (µs/cm)	linear charge density (nC/m)
PEO/Alginate	12150	4.76 ± 0.10
PEO	17.26	2.68 ± 0.19
PLA/TEBAC	1049	3.09 ± 1.05
PLA	3.08	0.45 ± 0.05

2.6 Charge density carried by individual electrosprayed particles

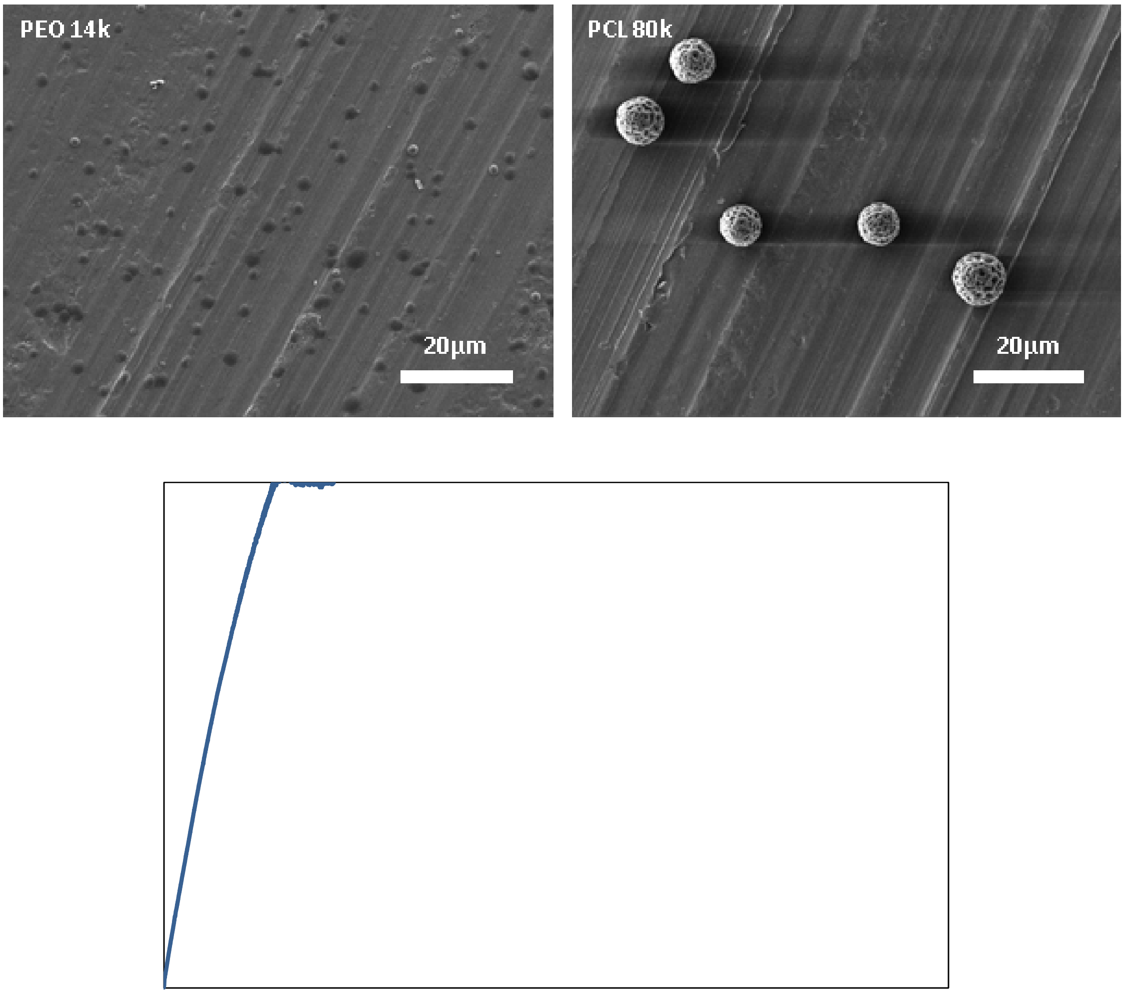

Fig. 2.22 SEM images of PCL 14k particles and PCL 80k particles and corresponding curves of surface potential

As shown in Fig. 2.22, flattened morphology was achieved when the PCL14k of low molar mass (M_w=14k) was electrosprayed. The flattened morphology is due to the fact that the solvent did not volatilize fully when the particles hit the collector, which is attributed to the high boiling point of DMAC (166.1 °C). Thus, when the emitter-to-collector distance is insufficient for a full evaporation, semi-solid particles containing residual solvent are deformed during their deposition. In the case of PCL 80k particles, a spherical morphology is obtained. The boiling point of chloroform (61.3 °C), used in this case, ensured a full volatilization, favoring the deposition of non-deformable dry particles. In the case of PCL80k, the particles are much larger and show a rough surface. The rough surface can be explained by the rapid evaporation of chloroform from the surface of the particles. This rapid evaporation leads to the formation of a solid polymer shell embedding a solvent-rich core. During the evaporation of the solvent contained in the core, a rough surface is obtained through the shrinking of the solid shell [47]–[50].

Tab. 2.4 Diameter, production rate, charge density of per particle and surface charge density of PCL 14k and 80k particles, values were given as means ± standard error of the mean

	PCL 14k	PCL 80k
Diameter (µm)	1.9 ± 0.6	8.8 ± 1.0
Production rate (Number of particles/s)	$5.1\times10^6 \pm 42\times10^4$	$1.2\times10^4 \pm 5\times10^3$
Charge density per particle (pC)	0.01 ± 0.001	0.70 ± 0.03
Surface charge density (mC/m^2)	4.8 ± 0.4	2.90 ± 0.2

As shown in Table 2.4, PCL80k particles are much larger than those produced from PCL14k. In the process of electrospraying, the voltage is set at 30kV for electrospraying PCL14k particles which was much higher than 15kV for PCL80k particles. Indeed, larger voltage induces a stronger force allowing the enhanced breaking and pulverization of electrosprayed droplets. In addition, the difference in diameter is also related to the dielectric constant of solvents. Dielectric constants of DMAC and chloroform are 37.8 and 4.8, respectively. Thus, a solvent, such as DMAC, having a high dielectric constant allows an efficient polarization favoring the breaking and pulverization of electrosprayed droplets in small particles. In contrast, the use of chloroform, having a low dielectric constant, induces a bad pulverization and thus larger particles.

From Tab. 2.4, it is obvious that the production rate of PCL14k particles is significantly higher than the one measured for PCL80k particles. Besides the small size causes the increasing number of PCL14k particles, high voltage and fast feeding rate are two other crucial factors enlarging the number of produced particles. Due to the low size and the high production rate of PCL14k, the amount of charges is much lower than in the case of PCL80k. However, the surface charge densities are in the same range although a little bit higher for the smallest PCL14k particles.

2.7 Conclusion

The electrostatic template, which is affected by the intensity of charges carried by fibers and particles, is the main responsible for the construction of structured scaffolds. Thus, the accurate measurement of the charge density carried by a single electrospun nanofiber and an individual electrosprayed microparticle is of prime importance. In this chapter, we developed a new approach for the direct measurement of all charges carried either by the fibers or the particles landing on the collector, in order to get complementary information than what it is generally obtained through the measurement of the current. Here, in the setup, a capacitor is connected between the collector and the ground to keep all the charges of the deposited nanofiber on the surface of the collector. Knowing the value of the capacitor, the measurement of the potential detected at the top surface of the collector allows the estimation of the of the charges carried by the deposited fibers. Additionally, the length of fibers and the number of particles deposited on the collector is measured by SEM. Thus, the charge density of fibers and particles are also obtained. After having short-circuited the capacitor, the remained potential can give an estimation on the ratio between the charges instantaneously transferred to the ground and the charges remaining in the bulk or on the top surface of the fiber or particle.

For electrospinning, PLA fibers was chosen as an example. It was shown that a significant amount of charges remains in or on the fiber after having short-circuited the capacitor. It proves that PLA is a good candidate for the production of structured mat as a significant amount of residual charges may be used to form an efficient electrostatic template. In addition, it is shown that the linear charge density of a single PLA fiber is enhanced by increasing the polymer concentration, the solution conductivity and the ambient relative humidity and by decreasing the applied voltage and the solution feeding rate. Thus, the electrostatic template might be more effective in these conditions for a better building of structured scaffolds. Unlike PLA fibers, although a high linear charge density is measured on PEO fibers, almost no residual charges can be stored after their deposition. This discharging might lead to form a poor electrostatic template which might negatively affect the use of PEO fibers for the building of structured scaffolds. This part will be studied in next chapter.

For electrospraying, due to the difference in the processing and solution parameters, PCL14k particles hold a flattened morphology with a diameter around 2 µm, while PCL80k particles show a spherical morphology with a large average diameter of 9 µm. Furthermore, the low molar mass of PCL14k combined with the high applied voltage necessary for an efficient electrospraying led to a high production rate (in number of produced particles per unit time) and a relatively large surface charge density. These two features are advantageous for particles that have to be subjected to an electrostatic template for the efficient building of structured 3D scaffolds. This aspect will be discussed in Chapter 4.

References

[1] H. Yoshimoto, Y. M. Shin, H. Terai, and J. P. Vacanti, “A biodegradable nanofiber scaffold by electrospinning and its potential for bone tissue engineering,” *Biomaterials*, vol. 24, no. 12, pp. 2077–2082, May 2003, doi: 10.1016/S0142-9612(02)00635-X.

[2] P. Taepaiboon, U. Rungsardthong, and P. Supaphol, “Drug-loaded electrospun mats of poly(vinyl alcohol) fibres and their release characteristics of four model drugs,” *Nanotechnology*, vol. 17, no. 9, pp. 2317–2329, May 2006, doi: 10.1088/0957-4484/17/9/041.

[3] J. Wang *et al.*, “Electrospinning Synthesis of Porous $NiCoO_2$ Nanofibers as High Performance Anode for Lithium Ion Batteries,” *Particle & Particle Systems Characterization*, vol. 36, no. 7, p. 1900109, Jul. 2019, doi: 10.1002/ppsc.201900109.

[4] D. H. Reneker, A. L. Yarin, H. Fong, and S. Koombhongse, “Bending instability of electrically charged liquid jets of polymer solutions in electrospinning,” *Journal of Applied Physics*, vol. 87, no. 9, pp. 4531–4547, May 2000, doi: 10.1063/1.373532.

[5] B. M. Cho, Y. S. Nam, J. Y. Cheon, and W. H. Park, “Residual charge and filtration efficiency of polycarbonate fibrous membranes prepared by electrospinning,” *Journal of Applied Polymer Science*, vol. 132, no. 1, Jan. 2015, doi: 10.1002/app.41340.

[6] Q. Chen *et al.*, “Enhanced acetone sensor based on Au functionalized In-doped ZnSnO3 nanofibers synthesized by electrospinning method,” *Journal of Colloid and Interface Science*, vol. 543, pp. 285–299, May 2019, doi: 10.1016/j.jcis.2019.02.055.

[7] M. Bognitzki *et al.*, “Nanostructured Fibers via Electrospinning,” *Advanced Materials*, vol. 13, no. 1, pp. 70–72, Jan. 2001, doi: 10.1002/1521-4095(200101)13:1<70::AID-ADMA70>3.0.CO;2-H.

[8] S. Nedjari, G. Schlatter, and A. Hébraud, “Thick electrospun honeycomb scaffolds with controlled pore size,” *Materials Letters*, vol. 142, pp. 180–183, Mar. 2015, doi: 10.1016/j.matlet.2014.11.118.

[9] P. K. Szewczyk *et al.*, “Surface-Potential-Controlled Cell Proliferation and Collagen Mineralization on Electrospun Polyvinylidene Fluoride (PVDF) Fiber Scaffolds for Bone Regeneration,” *ACS Biomaterials Science & Engineering*, vol. 5, no. 2, pp. 582–593, Feb. 2019, doi: 10.1021/acsbiomaterials.8b01108.

[10] S. V. Fridrikh, J. H. Yu, M. P. Brenner, and G. C. Rutledge, “Controlling the Fiber Diameter during Electrospinning,” *Physical Review Letters*, vol. 90, no. 14, Apr. 2003, doi: 10.1103/PhysRevLett.90.144502.

[11] P. K. Bhattacharjee, T. M. Schneider, M. P. Brenner, G. H. McKinley, and G. C. Rutledge, “On the measured current in electrospinning,” *Journal of Applied Physics*, vol. 107, no. 4, p. 044306, Feb. 2010, doi: 10.1063/1.3277018.

[12] D. Fallahi, M. Rafizadeh, N. Mohammadi, and B. Vahidi, “Effect of applied voltage on surface and volume charge density of the jet in electrospinning of polyacrylonitrile solutions,” *Polymer Engineering & Science*, vol. 50, no. 7, pp. 1372–1376, Jul. 2010, doi: 10.1002/pen.21677.

[13] S. G. Kumbar, S. P. Nukavarapu, R. James, L. S. Nair, and C. T. Laurencin, “Electrospun poly(lactic acid-co-glycolic acid) scaffolds for skin tissue engineering,” *Biomaterials*, vol. 29, no. 30, pp. 4100–4107, Oct. 2008, doi: 10.1016/j.biomaterials.2008.06.028.

[14] H. Fong, I. Chun, and D. H. Reneker, “Beaded nanofibers formed during electrospinning,” *Polymer*, vol. 40, no. 16, pp. 4585–4592, Jul. 1999, doi: 10.1016/S0032-3861(99)00068-3.

[15] N. Bhardwaj and S. C. Kundu, “Electrospinning: A fascinating fiber fabrication technique,” *Biotechnology Advances*, vol. 28, no. 3, pp. 325–347, May 2010, doi: 10.1016/j.biotechadv.2010.01.004.

[16] M. M. Demir, I. Yilgor, E. Yilgor, and B. Erman, “Electrospinning of polyurethane fibers,” *Polymer*, vol. 43, no. 11, pp. 3303–3309, May 2002, doi: 10.1016/S0032-3861(02)00136-2.

[17] C. S. Ki, D. H. Baek, K. D. Gang, K. H. Lee, I. C. Um, and Y. H. Park, “Characterization of gelatin nanofiber prepared from gelatin–formic acid solution,” *Polymer*, vol. 46, no. 14, pp. 5094–5102, Jun. 2005, doi: 10.1016/j.polymer.2005.04.040.

[18] X. Yuan, Y. Zhang, C. Dong, and J. Sheng, “Morphology of ultrafine polysulfone fibers prepared by electrospinning,” *Polymer International*, vol. 53, no. 11, pp. 1704–1710, Nov. 2004, doi: 10.1002/pi.1538.

[19] S. A. Theron, E. Zussman, and A. L. Yarin, “Experimental investigation of the governing parameters in the electrospinning of polymer solutions,” *Polymer*, vol. 45, no. 6, pp. 2017–2030, Mar. 2004, doi: 10.1016/j.polymer.2004.01.024.

[20] F. Yalçinkaya, “EFFECT OF CURRENT ON POLYMER JET IN ELECTROSPINNING PROCESS,” *Tekstil ve Konfeksiyon*, vol. 25, no. 3, pp. 201–206, Dec. 2015.

[21] G. Collins, J. Federici, Y. Imura, and L. H. Catalani, “Charge generation, charge transport, and residual charge in the electrospinning of polymers: A review of issues and complications,” *Journal of Applied Physics*, vol. 111, no. 4, p. 044701, Feb. 2012, doi: 10.1063/1.3682464.

[22] S. Sarabi-Mianeji, J. Scott, and D. J. Y. S. Pagé, “Impact of electrospinning process parameters on the measured current and fiber diameter,” *Polymer Engineering & Science*, vol. 55, no. 11, pp. 2576–2582, Nov. 2015, doi: 10.1002/pen.24150.

[23] R. Samatham and K. J. Kim, “Electric current as a control variable in the electrospinning process,” *Polymer Engineering & Science*, vol. 46, no. 7, pp. 954–959, Jul. 2006, doi: 10.1002/pen.20565.

[24] D. Lovera, C. Bilbao, P. Schreier, L. Kador, H.-W. Schmidt, and V. Altstädt, “Charge storage of electrospun fiber mats of poly(phenylene ether)/polystyrene blends,” *Polymer Engineering & Science*, vol. 49, no. 12, pp. 2430–2439, Dec. 2009, doi: 10.1002/pen.21493.

[25] L. H. Catalani, G. Collins, and M. Jaffe, “Evidence for Molecular Orientation and Residual Charge in the Electrospinning of Poly(butylene terephthalate) Nanofibers,” *Macromolecules*, vol. 40, no. 5, pp. 1693–1697, Mar. 2007, doi: 10.1021/ma061342d.

[26] C. Dichtl, P. Sippel, and S. Krohns, “Dielectric Properties of 3D Printed Polylactic Acid,” *Advances in Materials Science and Engineering*, vol. 2017, pp. 1–10, 2017, doi: 10.1155/2017/6913835.

[27] R. Casasola, N. L. Thomas, and S. Georgiadou, “Electrospinning of poly(lactic acid): Theoretical approach for the solvent selection to produce defect-free nanofibers,” *Journal of Polymer Science Part B: Polymer Physics*, vol. 54, no. 15, pp. 1483–1498, Aug. 2016, doi: 10.1002/polb.24042.

[28] R. Casasola, N. L. Thomas, A. Trybala, and S. Georgiadou, “Electrospun poly lactic acid (PLA) fibres: Effect of different solvent systems on fibre morphology and diameter,” *Polymer*, vol. 55, no. 18, pp. 4728–4737, Sep. 2014, doi: 10.1016/j.polymer.2014.06.032.

[29] A. Bandegi and M. R. Moghbeli, “Effect of solvent quality and humidity on the porous formation and oil absorbency of SAN electrospun nanofibers: ARTICLE,” *Journal of Applied Polymer Science*, vol. 135, no. 1, p. 45586, Jan. 2018, doi: 10.1002/app.45586.

[30] H. Fashandi and M. Karimi, “Comparative Studies on the Solvent Quality and Atmosphere Humidity for Electrospinning of Nanoporous Polyetherimide Fibers,” *Industrial & Engineering Chemistry Research*, vol. 53, no. 1, pp. 235–245, Jan. 2014, doi: 10.1021/ie4028846.

[31] S. Yao, X. Wang, X. Liu, R. Wang, C. Deng, and F. Cui, “Effects of Ambient Relative Humidity and Solvent Properties on the Electrospinning of Pure Hyaluronic Acid Nanofibers,” *Journal of Nanoscience and Nanotechnology*, vol. 13, no. 7, pp. 4752–4758, Jul. 2013, doi: 10.1166/jnn.2013.7197.

[32] F. Topuz, B. Satilmis, and T. Uyar, “Electrospinning of uniform nanofibers of Polymers of Intrinsic Microporosity (PIM-1): The influence of solution conductivity and relative humidity,” *Polymer*, vol. 178, p. 121610, Sep. 2019, doi: 10.1016/j.polymer.2019.121610.

[33] S. J. Kim, C. K. Lee, and S. I. Kim, “Effect of ionic salts on the processing of poly(2-acrylamido-2-methyl-1-propane sulfonic acid) nanofibers,” *Journal of Applied Polymer Science*, vol. 96, no. 4, pp. 1388–1393, May 2005, doi: 10.1002/app.21567.

[34] Y. You, S. J. Lee, B.-M. Min, and W. H. Park, “Effect of solution properties on nanofibrous structure of electrospun poly(lactic-co-glycolic acid),” *Journal of Applied Polymer Science*, vol. 99, no. 3, pp. 1214–1221, Feb. 2006, doi: 10.1002/app.22602.

[35] D.-G. Yu, K. White, J.-H. Yang, X. Wang, W. qian, and Y. Li, “PVP nanofibers prepared using co-axial electrospinning with salt solution as sheath fluid,” *Materials Letters*, vol. 67, no. 1, pp. 78–80, Jan. 2012, doi: 10.1016/j.matlet.2011.09.035.

[36] J. M. Seo, G. K. Arumugam, S. Khan, and P. A. Heiden, “Comparison of the Effects of an Ionic Liquid and Triethylbenzylammonium Chloride on the Properties of Electrospun Fibers, 1 - Poly(lactic acid),” *Macromolecular Materials and Engineering*, vol. 294, no. 1, pp. 35–44, Jan. 2009, doi: 10.1002/mame.200800198.

[37] J. S. Choi *et al.*, “Effect of organosoluble salts on the nanofibrous structure of electrospun poly(3-hydroxybutyrate-co-3-hydroxyvalerate),” *International Journal of Biological Macromolecules*, vol. 34, no. 4, pp. 249–256, Aug. 2004, doi: 10.1016/j.ijbiomac.2004.06.001.

[38] C. J. Buchko, L. C. Chen, Y. Shen, and D. C. Martin, “Processing and microstructural characterization of porous biocompatible protein polymer thin films,” *Polymer*, vol. 40, no. 26, pp. 7397–7407, Dec. 1999, doi: 10.1016/S0032-3861(98)00866-0.

[39] C. Wang, W. Zhang, Z. H. Huang, E. Y. Yan, and Y. H. Su, “Effect of concentration, voltage, take over distance and diameter of pinhead on precursor poly(phenylene vinylene) electrospinning,” *Pigment & Resin Technology*, vol. 35, no. 5, pp. 278–283, Sep. 2006, doi: 10.1108/03699420610692887.

[40] E. S. Medeiros, L. H. C. Mattoso, R. D. Offeman, D. F. Wood, and W. J. Orts, “Effect of relative humidity on the morphology of electrospun polymer fibers,” *Canadian Journal of Chemistry*, vol. 86, no. 6, pp. 590–599, Jun. 2008, doi: 10.1139/v08-029.

[41] C. L. Casper, J. S. Stephens, N. G. Tassi, D. B. Chase, and J. F. Rabolt, “Controlling Surface Morphology of Electrospun Polystyrene Fibers: Effect of Humidity and Molecular Weight in the Electrospinning Process,” *Macromolecules*, vol. 37, no. 2, pp. 573–578, Jan. 2004, doi: 10.1021/ma0351975.

[42] R. M. Nezarati, M. B. Eifert, and E. Cosgriff-Hernandez, “Effects of Humidity and Solution Viscosity on Electrospun Fiber Morphology,” *Tissue Engineering Part C: Methods*, vol. 19, no. 10, pp. 810–819, Oct. 2013, doi: 10.1089/ten.tec.2012.0671.

[43] L. Huang, N.-N. Bui, S. S. Manickam, and J. R. McCutcheon, “Controlling electrospun nanofiber morphology and mechanical properties using humidity,” *Journal of Polymer Science Part B: Polymer Physics*, vol. 49, no. 24, pp. 1734–1744, Dec. 2011, doi: 10.1002/polb.22371.

[44] G.-T. Kim *et al.*, “Investigation of pore formation for polystyrene electrospun fiber: Effect of relative humidity,” *Korean Journal of Chemical Engineering*, vol. 22, no. 5, pp. 783–788, Sep. 2005, doi: 10.1007/BF02705799.

[45] S. Megelski, J. S. Stephens, D. B. Chase, and J. F. Rabolt, “Micro- and Nanostructured Surface Morphology on Electrospun Polymer Fibers,” *Macromolecules*, vol. 35, no. 22, pp. 8456–8466, Oct. 2002, doi: 10.1021/ma020444a.

[46] X. Zong, K. Kim, D. Fang, S. Ran, B. S. Hsiao, and B. Chu, “Structure and process relationship of electrospun bioabsorbable nanofiber membranes,” *Polymer*, vol. 43, no. 16, pp. 4403–4412, Jul. 2002, doi: 10.1016/S0032-3861(02)00275-6.

[47] J. Yao, L. Kuang Lim, J. Xie, J. Hua, and C.-H. Wang, “Characterization of electrospraying process for polymeric particle fabrication,” *Journal of Aerosol Science*, vol. 39, no. 11, pp. 987–1002, Nov. 2008, doi: 10.1016/j.jaerosci.2008.07.003.

[48] B. Almería, W. Deng, T. M. Fahmy, and A. Gomez, “Controlling the morphology of electrospray-generated PLGA microparticles for drug delivery,” *Journal of Colloid and Interface Science*, vol. 343, no. 1, pp. 125–133, Mar. 2010, doi: 10.1016/j.jcis.2009.10.002.

[49] F.-L. Zhou, P. L. Hubbard Cristinacce, S. J. Eichhorn, and G. J. M. Parker, “Preparation and characterization of polycaprolactone microspheres by electrospraying,” *Aerosol Science and Technology*, vol. 50, no. 11, pp. 1201–1215, Nov. 2016, doi: 10.1080/02786826.2016.1234707.

[50] N. Bock, M. A. Woodruff, D. W. Hutmacher, and T. R. Dargaville, “Electrospraying, a Reproducible Method for Production of Polymeric Microspheres for Biomedical Applications,” *Polymers*, vol. 3, no. 1, pp. 131–149, Jan. 2011, doi: 10.3390/polym3010131.

Chapter 3 In-situ charging during simple electrospinning and surface potential decay: modeling and experimental study

3.1 Introduction

Electrospinning is a widespread technology enabling the fabrication of nanofibrous scaffolds with most of the polymers available on the market and for a wide range of applications such as filtration [1], tissue engineering [2], and biomedical applications [3]–[5]. The principle of the process consists in subjecting a polymer solution droplet to a high electric field in the order of 1 kV/cm which induces the emission of a liquid jet toward a grounded counter-electrode, the so-called collector, located about 10-20 cm away from the jet emission. During its flight in the air, the electrified and charged jet is experiencing whipping movements allowing an efficient stretching and the solvent evaporation. A continuous fiber having a diameter in the range of 100-1000 nm is pseudo-randomly deposited in the form of a non-woven mat. By playing with the material properties (polymer molar mass, concentration, nature of the solvents…) as well as the processing parameters (applied voltage, solution flow rate, jet emission-to-collector distance, collector geometry, air temperature and humidity…), scaffolds with various morphological and physical properties (fiber diameter, scaffold pore size, polymer crystallinity, mechanical properties…) can be elaborated rendering the process of electrospinning successful and versatile for a wide range of applications.

Several articles deals with the effect of parameters such as the solution and processing parameters on the current reflecting the amount of charges carried by the electrospun jet[6]–[8]. Such a method is easy to implement, indeed by installing a resistor between the collector and the ground, the measurement of the difference of potential through the resistor allows calculating the electrospinning current thanks to the Ohm’s law. Nevertheless, the current is not related to the amount of charges remaining in the mat during and after electrospinning and it don’t give any information about the internal structure of the fibrous mat. Researchers also highlighted that residual charges remaining on the deposited fiber may represent an important amount of the total charges carried by the fiber just before its landing on the collector [9]**.** In electrospinning charges are present due to dipole orientation, space charge separation and direct injection of charges into the fibers [10]–[12].

Understanding, how charges accumulate on the mat during its fabrication and how charges dissipate through its thickness are of prime importance for various reasons. Indeed, we have seen that the current and the amount of charges are directly linked with the processing conditions. Thus, a measure of the charge accumulation can be an efficient way to control the process of fabrication. Such control could help (i) to fine tune the processing conditions which can fluctuate during the time of production and (ii) to have an immediate action on the process when these fluctuations occur. Because electrospinning is currently emerging in the industry: simple and efficient quality controls are needed online the process. Another application for which residual charges can play an important role is filtration for air cleaning in a variety of industries [1]. Indeed, in addition to the well-known specific properties of nanofibrous masts (i.e. small diameter, high specific surface area and tortuous porous structures) adapted for filtration applications, electrostatic forces may also play an important role on the air filtration performance thanks to the presence of charged fibers enhancing the efficiency to adsorb or repel the dust [1], [13]–[16]. For biomedical applications, electrets may also be interesting as they improve cell spreading and proliferation [17]. Moreover, it was reported that charge transfer and accumulation through the mat as well as charge dissipation occur in the process of electrospinning may impact the morphology of fibers and the inner structure of the mat [18]–[23]. More precisely, it was shown that residual charges carried by the fibers may form an electrostatic template [24] guiding the deposition of the incoming electrospun jet allowing the fabrication of mats with various morphologies through self-assembling processes [25], [26] or with the help of patterned collectors [27], [28].

In this chapter, *in-situ* charging during electrospinning and the kinetic of the mat surface potential during electrospinning and after stopping electrospinning are studied as a function of various parameters (polymer concentration, applied voltage and ambient relative humidity). An original model of the *in-situ* charging is proposed and shows the correlation between the characteristic features surface potential kinetic with the porous morphology of the fabricated mat. The study of the surface potential decay measured after stopping electrospinning is also discussed with the help of a double exponential model. The results demonstrate that the online measurement of the surface potential could be an efficient way to monitor the process of electrospinning regarding the final morphology of the nanofibrous mat and its building during processing.

3.2 Materials and methods

Materials and solution preparation

PLA (Mw=180k, Natureworks) was used as received, Dichloromethane (DCM), N, N-Dimethylformamide (DMF) and polyethylene oxide (PEO Mw=400k, 600k, 900k) were purchased from Sigma-Aldrich. PLA/DCM/DMF solution was prepared by dissolving PLA in DMF/DCM (50:50 v/v) with stirring 24h prior to electrospinning. In the same way, 5% w/w PEO in different polymer weights was dissolved in deionized water, respectively, overnight to obtain the spinning solution. The governing parameters to electrospinning PLA and PEO fibers were shown in Tab. 3.1 and Tab. 3.2.

Tab. 3.1 preparation parameters of PLA fibers

Samples	Parameters						
	Concentration (w/w)	Voltage	Processing time	Processing distance	Decay time	Flow rate	Humidity
PLA-S1	7%	25kV	300 s	15cm	150s	1ml/h	38%±2%
PLA-S2	9%	25kV	300 s	15cm	150s	1ml/h	38%±2%
PLA-S3	11%	25kV	300 s	15cm	150s	1ml/h	38%±2%
PLA-S4	13%	25kV	300 s	15cm	150s	1ml/h	38%±2%
PLA-S5	9%	15kV	300 s	15cm	150s	1ml/h	38%±2%
PLA-S6	9%	20kV	300 s	15cm	150s	1ml/h	38%±2%
PLA-S7	9%	30kV	300 s	15cm	150s	1ml/h	38%±2%
PLA-S8	9%	25kV	300 s	15cm	150s	1ml/h	28%±2%
PLA-S9	9%	25kV	300 s	15cm	150s	1ml/h	48%±2%
PLA-S10	9%	25kV	300 s	15cm	150s	1ml/h	58%±2%

Tab. 3.2 preparation parameters of PEO fibers

Samples	Parameters						
	Molar mass	Concentration (w/w)	Voltage	Processing time	Processing distance	Flow rate	Humidity
PEO-S1	400k	5%	25kV	300 s	15cm	1ml/h	38%±2%
PEO-S2	400k	5%	25kV	300 s	20cm	1ml/h	38%±2%
PEO-S3	400k	5%	25kV	300 s	25cm	1ml/h	38%±2%
PEO-S4	600k	5%	25kV	300 s	15cm	1ml/h	38%±2%
PEO-S5	600k	5%	25kV	300 s	20cm	1ml/h	38%±2%
PEO-S6	600k	5%	25kV	300 s	25cm	1ml/h	38%±2%
PEO-S7	900k	5%	25kV	300 s	15cm	1ml/h	38%±2%
PEO-S8	900k	5%	25kV	300 s	20cm	1ml/h	28%±2%
PEO-S9	900k	5%	25kV	300 s	25cm	1ml/h	38%±2%

Electrospinning process

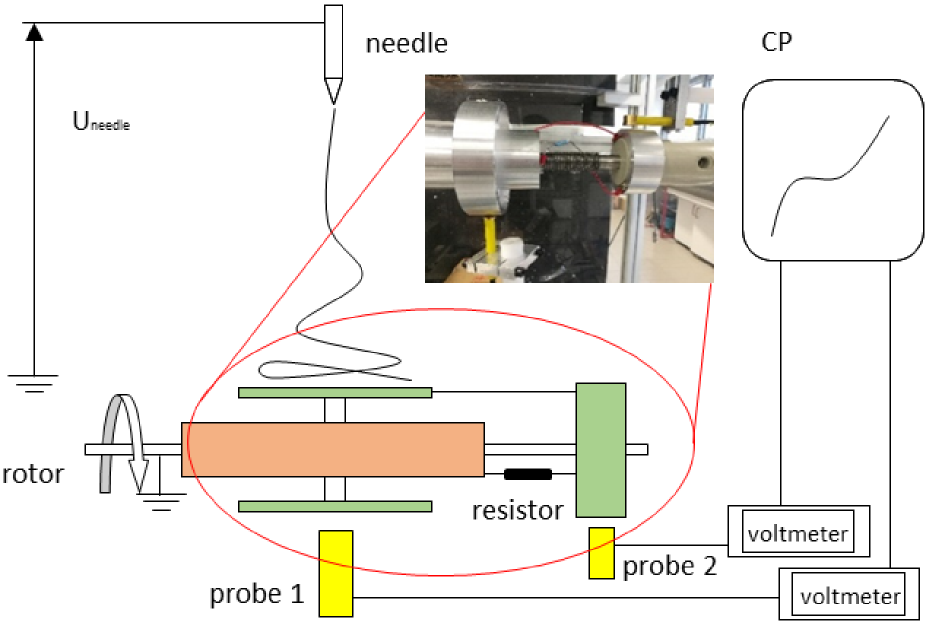

Fig. 3.1 sketch of the experimental setup allowing the measurement of the mat surface potential (Probe 1) and the potential at the bottom of the mat (Probe 2).

Fig. 3.1 presents the sketch of the experimental setup of electrospinning. The polymer solutions were fed by a syringe pump (Fischer scientific) with a stainless steel needle in an inner diameter of 0.5 mm. The needle was electrically connected to the positive terminal of a high voltage DC power supply (Spellman SL10). The cylindrical collector (Diameter = 110 mm and Width = 30 mm) was mounted around the rotor connected to the ground, an insulating Teflon ring was fixed between the collector and the rotor to avoid any charge transfer directly from the collector to the rotor. The collector was electrically connected to a metallic ring at a distance of 20cm from the collector to avoid any fibers deposition on this ring. The metallic ring was mechanically linked to the rotor by a thick insulating ring of Teflon. A resistor was installed between the ring and the rotor connected to the ground allowing the measurement of the potential at the bottom of the electrospun mat and allowing also the calculation of the electrospinning current thanks to the Ohm's law. The resistor value was 500 MΩ for PLA fibers and 10 MΩ for PEO fibers. The velocity of rotation of the rotor was set at 120 rpm.

To measure the surface potential at the top surface of the mat, a non-contacting electrostatic voltmeter ESVM (Trek Model 347-3-H-CE) connected to a computer for data acquisition was used. The measurement is based on a field-nulling technique for non-contacting voltage measurement achieving direct current stability and high accuracy, with no need for fixed probe-to-surface spacing. The technique allows an accurate measurement of the surface potential of stationary or moving surfaces. The measurement range is 0 to ± 3 kV with an accuracy of 0.1% of the full range. The probe (Probe 1) of the voltmeter (probe model 6000B-7C with a speed of response of 4.5 ms for 1 kV step) having a disc surface of 11.2 mm diameter was placed 2 mm below the surface of the collector as shown in Fig 3.1. An acquisition rate of 30 measurements/s was chosen.

To measure the potential at the bottom of the mat, a non-contacting electrostatic voltmeter ESVM (Trek Model 323-H-CE) connected to a computer for data acquisition was used. The measurement is based on a field-nulling technique for non-contacting voltage measurement achieving direct current stability and high accuracy, with no need for fixed probe-to-surface spacing. The technique allows an accurate measurement of the surface potential of stationary or moving surfaces. The measurement range is 0 to ± 100 V with an accuracy of 0.05% of the full range. The probe (Probe 2) of the voltmeter (probe model 6000B-16 with a speed of response of 300 ms for 100 V step) having a square surface of

9.5×9.5 mm^2 mm was placed 2 mm below the surface of the supplementary ring as shown in Fig 3.1. An acquisition rate of 30 measurements/s was chosen.

SEM measurements

The morphology of fibers and particles was studied by scanning electron microscope (SEM) (Vega-3, Tescan). The samples were gold coated (sputter Quorum Q 150 RS, Quorum Technologies) for 2 min before SEM characterization.

3.3 In-situ charging during electrospinning

3.3.1 Evolution of the mat surface potential during electrospinning: a model

Fig. 3.2 shows the potential of the collector and the surface potential over the mat recorded during 300 s of electrospinning PLA in the case of PLA-S2 conditions (see Table 3.1) and after stopping electrospinning (time > 300 s). The measurement of the potential of the collector, i.e. the potential below the mat, corresponds to the difference of potential through the resistor and allows the calculation of the current due to the flow of charges through the mat thanks to the Ohm’s law. It is shown that the current is constant during the time of electrospinning due to the electrospun jet bringing a constant amount of charges per unit time. However, it is shown that the surface potential increases along the time of production due to residual charges accumulating in the mat. During the first time of electrospinning, $t \leq 15$ s, the surface potential is almost constant. It is only after a certain time that the surface potential starts to increase significantly and linearly as a function of time. In order to get more insight into the experimental results, a model allowing the prediction of the evolution of the surface potential of a scaffold during electrospinning is proposed.

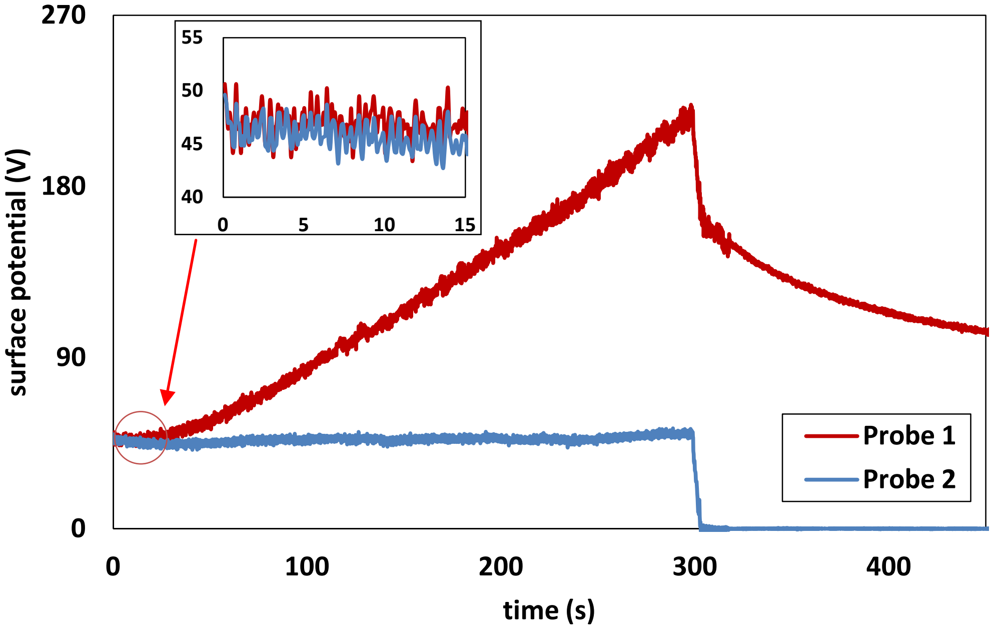

Fig. 3.2 Example of the evolution of the potential on the collector (probe 2 in blue) and the surface potential on the mat (probe 1 in red) during electrospinning of PLA in case of PLA-S2 conditions.

3.3.1.1 Behavior of a single pore of the scaffold

Electrospinning can be treated as a process allowing the layer by layer building of a porous scaffold. The electric behavior is depicted in Fig. 3.3. At time t, when the jet, having a linear charge density λ, enters in contact with the top surface of the scaffold, it starts to release its charges towards the ground along the electrical circuit formed by the interconnected fibers. The elementary domain of this interconnected circuit is the pore which is a small volume of air dV_p surrounded by fiber segments which are heterogeneously charged. Consequently, one pore can be treated as a parallel resistor-capacitor circuit having a characteristic time $\tau = R_p C_p$. The capacitance C_p may be linked with the pore size whereas the resistance R_p may be linked with the intrinsic resistivity of the fiber, the quality of the fiber-fiber contact points and the number of contact points per unit volume of mat. During the deposition process, the electrospun jet brings a constant amount of charges per unit time, thus the elementary current i_p flowing through the $R_p C_p$ circuit is constant during time t. If the $R_p C_p$ circuit is formed at time t', it is subjected to the following difference of potential $du_{(t)}$:

$$du_{(t)} = \left(1 - e^{-(t-t')/\tau}\right) i_p R_p \tag{3.1}$$

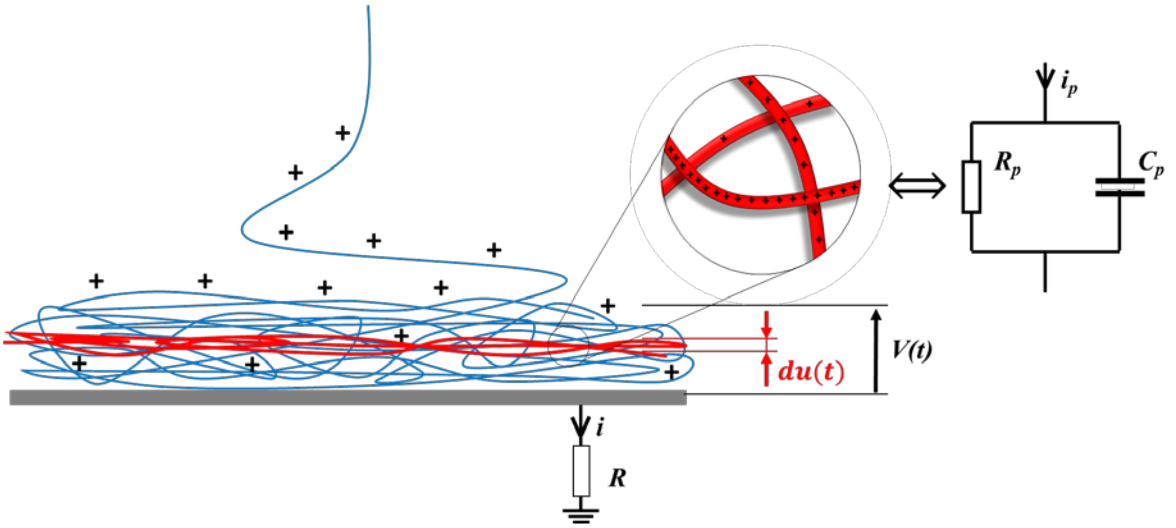

Fig. 3.3 Charge accumulation during electrospinning. The detail shows that charges are heterogeneously distributed on the fibers due to the fiber strands were not deposited on the same time

3.3.1.2 Evolution of the surface potential of the scaffold during electrospinning

Assuming that the scaffold have an electrical resistance R_m and a surface S_m, an average of $P = S_m/D_p^2$ pores of diameter D_p forms an elementary porous layer of scaffold made of $P\ R_pC_p$ circuits in parallel. The equivalent resistance of such elementary porous layer is thus $dR_m = R_p/P$ and the equivalent capacitance is $dC_m = PC_p$. The elementary layer of pores has the same difference of potential $du_{(t)}$ as a single pore as well as the same characteristic time $\tau = dR_m dC_m = R_pC_p$. Furthermore, the current flowing the elementary layer of pores corresponds to the total electrospinning current i. Thus, a porous layer of thickness dy at position y and formed at time t', is subjected to the following difference of potential at time t:

$$du_{(t)} = \left(1 - e^{-(t-t')/\tau}\right) i dR_m \tag{3.2}$$

The surface potential at time t of the scaffolds having a thickness $h(t)$ is the sum of the potential $du_{(t)}$ of all elementary layers and the difference of potential through the resistor R used for the measurement of the current:

$$V(t) = Ri + \int_0^{h(t)} du_{(t)} = Ri + \int_0^{t} \left(1 - e^{-(t-t')/\tau}\right) i \frac{dR_m}{dt'} dt' \tag{3.3}$$

It is assumed that the rate of resistance $\dot{R}_m = \frac{dR_m}{dt'}$ and the characteristic time τ are constant. Thus, the surface potential can be expressed as:

$$V(t) = Ri + \left[t - \tau\left(1 - e^{-t/\tau}\right)\right] i\dot{R}_m \tag{3.4}$$

Fig. 3.4 shows the trend of V as a function of t and how the parameters i, τ and $\dot{R}_m$ can be graphically obtained. It is seen that:

$$V(t = 0) = V(y = 0) = V_0 = Ri \tag{3.5}$$

V_0 corresponds to the potential at the collector-scaffold interface (i.e. at the position y = 0) and can be easily measured in order to get the current i.

When $t < \tau$, the surface potential is almost constant. Indeed, the characteristic time can be treated as the time it takes to completely charge a layer of characteristic thickness h_τ. When $t \gg \tau$, all the layers located below the upper layer of fibers of characteristic thickness h_τ are completely charged and are equivalent to a resistive layer of interconnected fibers having a thickness of $h(t) - h_\tau$. Under this condition, the surface potential evolves linearly with time:

$$V(t \gg \tau) \sim Ri + [t - \tau] i\dot{R}_m \tag{3.6}$$

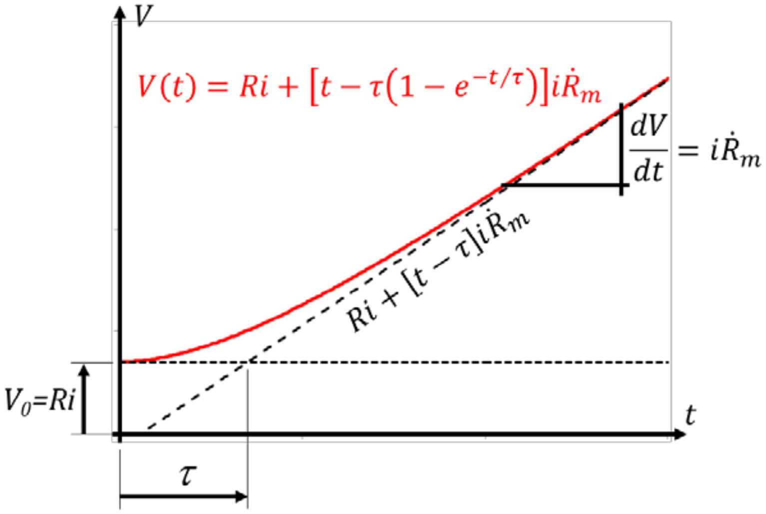

Fig. 3.4 Theoretical evolution of the scaffold surface potential as a function of the time and the characteristic parameters V_0, i, τ and $\dot{R}_m$ of the curve.

3.3.2 Effect of processing parameters on the current and surface potential

3.3.2.1 Effect of applied voltage

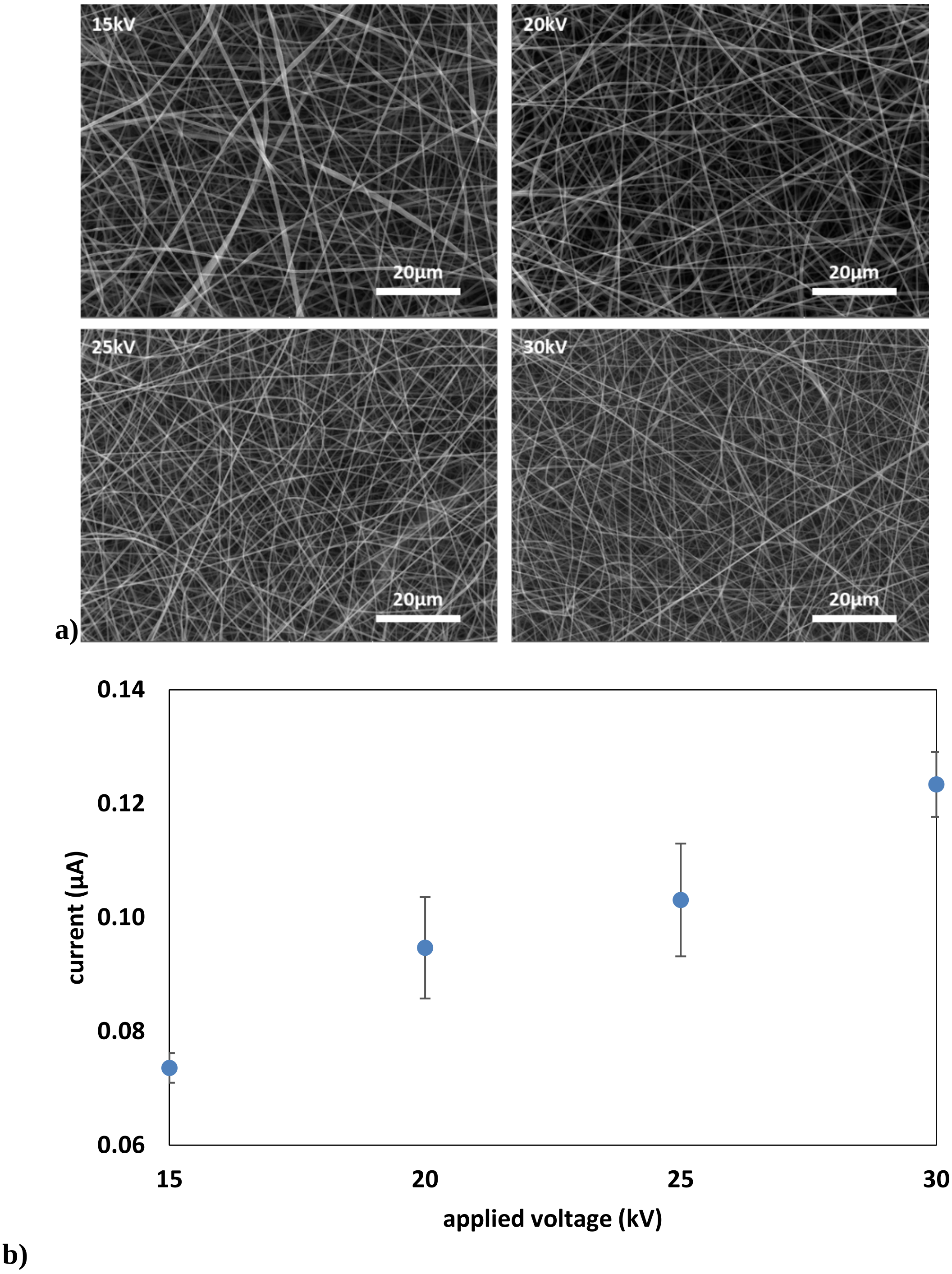

Fig. 3.5 a) SEM images of PLA fibers obtained under various voltages. b) Evolution of the current as a function of applied voltage

Fig. 3.5 shows that currents increases significantly with the enlargement of applied voltage. This result can be compared with the accumulation rate of charges discussed in the previous chapter (see also Fig. 2.12). It is shown that similar results are obtained with the same trend. Thus, the current, corresponding to the amount of charges brought by the jet per unit time, increases with the applied voltage.

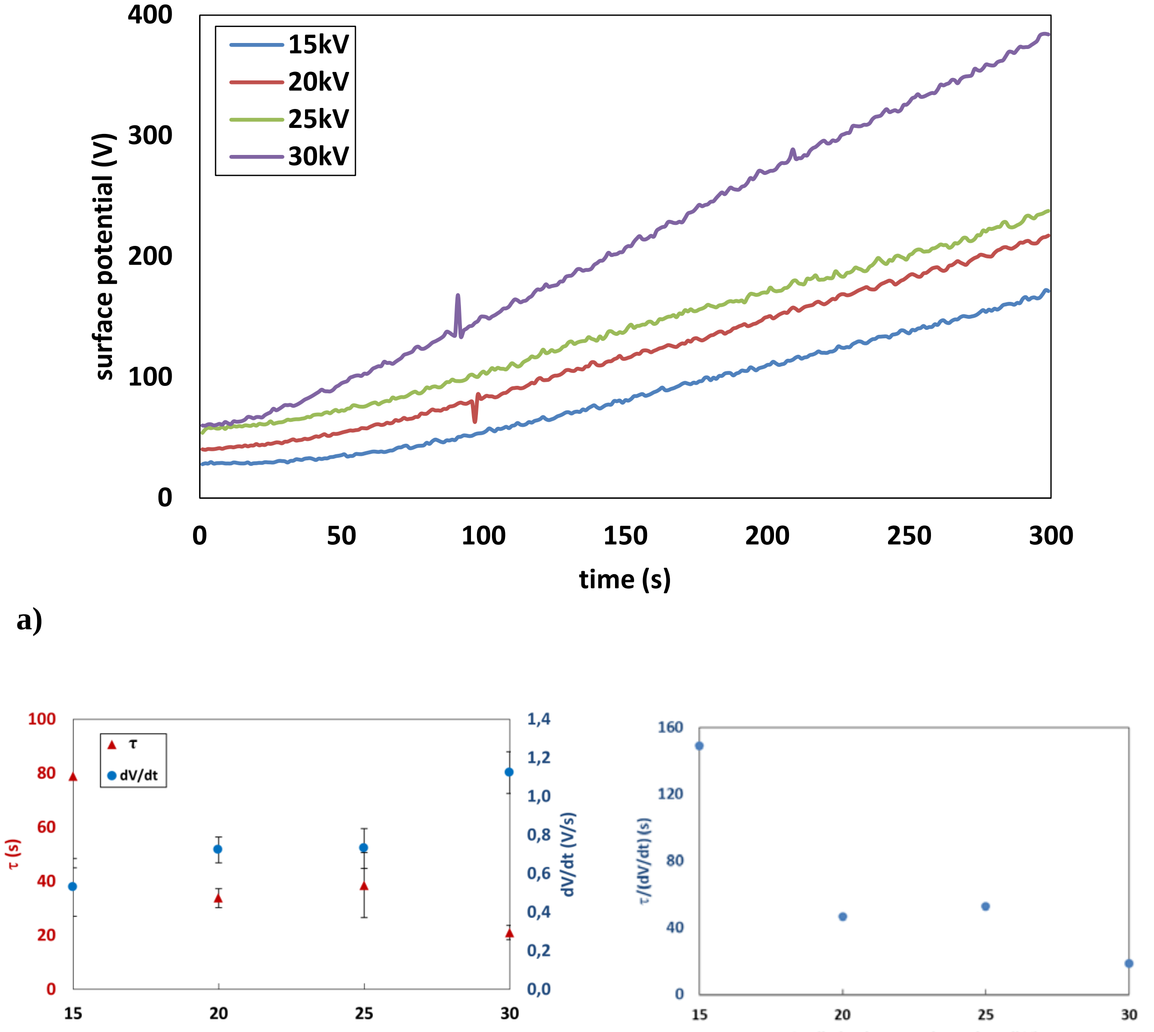

a)

b) **c)**

Fig. 3.6 a) Examples of experimental curves of the surface potential as a function of time for various applied voltages. b) Characteristic time τ and slope $\frac{dV}{dt} = i\dot{R}_m$ and c) $\tau/\left(\frac{dV}{dt}\right)$ ratio as a function of the applied voltage.

From Fig. 3.6, it is shown that τ decreases gradually with the increase of the voltage, the value changed from 79s to 21s when increasing the applied voltage at the emitter from 15kV to 30kV. The final slope of the surface potential corresponding to $i\dot{R}_m$ is almost constant from 15 kV to 25 kV. An increase of $i\dot{R}_m$ is observed for the highest voltage of 30 kV which means that for this condition the resistance of the mat increases faster than in the other cases. It was observed by SEM that when the voltage increases continuously, higher electrostatic force acted on the jet resulting in thinner fibers as well as more efficient solvent evaporation as shown in Fig. 3.7. Indeed, for the lowest applied voltage, fusion among fibers was observed resulting in lower mat electrical resistance. As shown in the previous section, the characteristic time relies on the average behavior of one pore having a capacitance directly correlated with the pore size. It is well known that thicker fibers results in larger pores [29], increasing thus enough the capacitance C_p leading to a higher characteristic time.

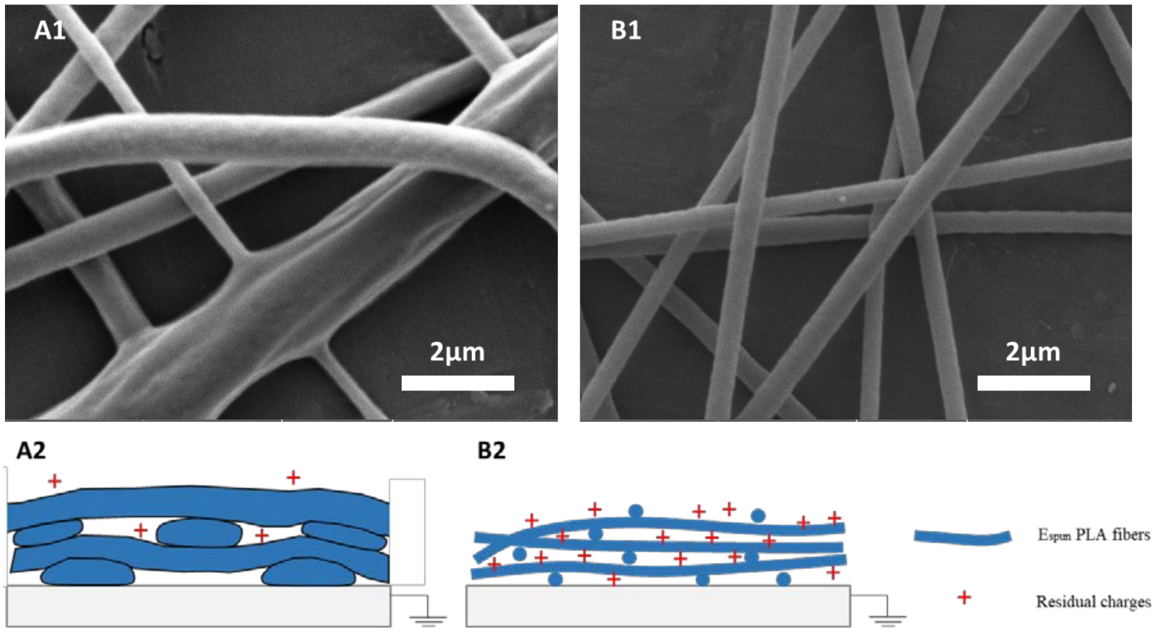

Fig. 3.7 SEM images and schemes of corresponding deposited fibers electrospun at 15kV (A1 and A2) and 30kV (B1 and B2)

3.3.2.2 Effect of polymer concentration

As shown in Fig. 3.8, the polymer concentration in the solution dose not impact the current significantly with a distribution from 0.09 µA to 0.13 µA when changing the concentration from 7% to 13%. This result is not in agreement with the previous chapter in which a slow decrease of the production rate of charge was observed with the increase of concentration, although the measured currents are in the same range. However, the current is the consequence of complex mechanisms. Indeed, regarding the polymer alone, at constant solution feeding rate (i.e. 1 mL/h), an increase of the polymer concentration results in the increase of the fiber flow rate enhancing thus the rate of charges landing the collector leading to the increase of the current. Concurrently, increasing the concentration induces the enlargement of the solution viscosity decreasing thus the fiber production and consequently, the current. In our case, these two phenomena being in competition resulted in a current which is almost constant with the concentration.

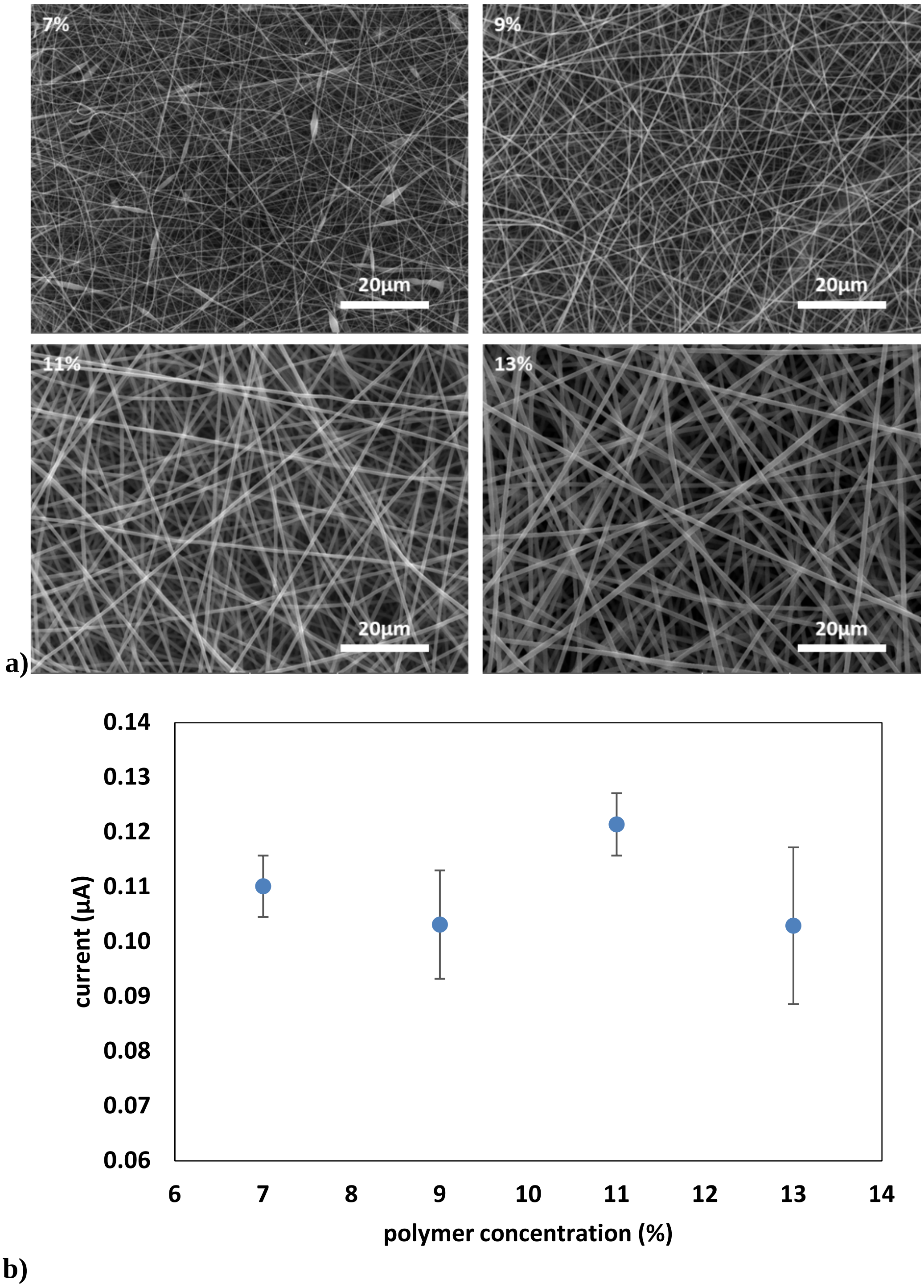

Fig. 3.8 a) SEM images of PLA fibers fabricated from polymer solutions at various concentrations. b) Evolution of the current as a function of the polymer concentration.

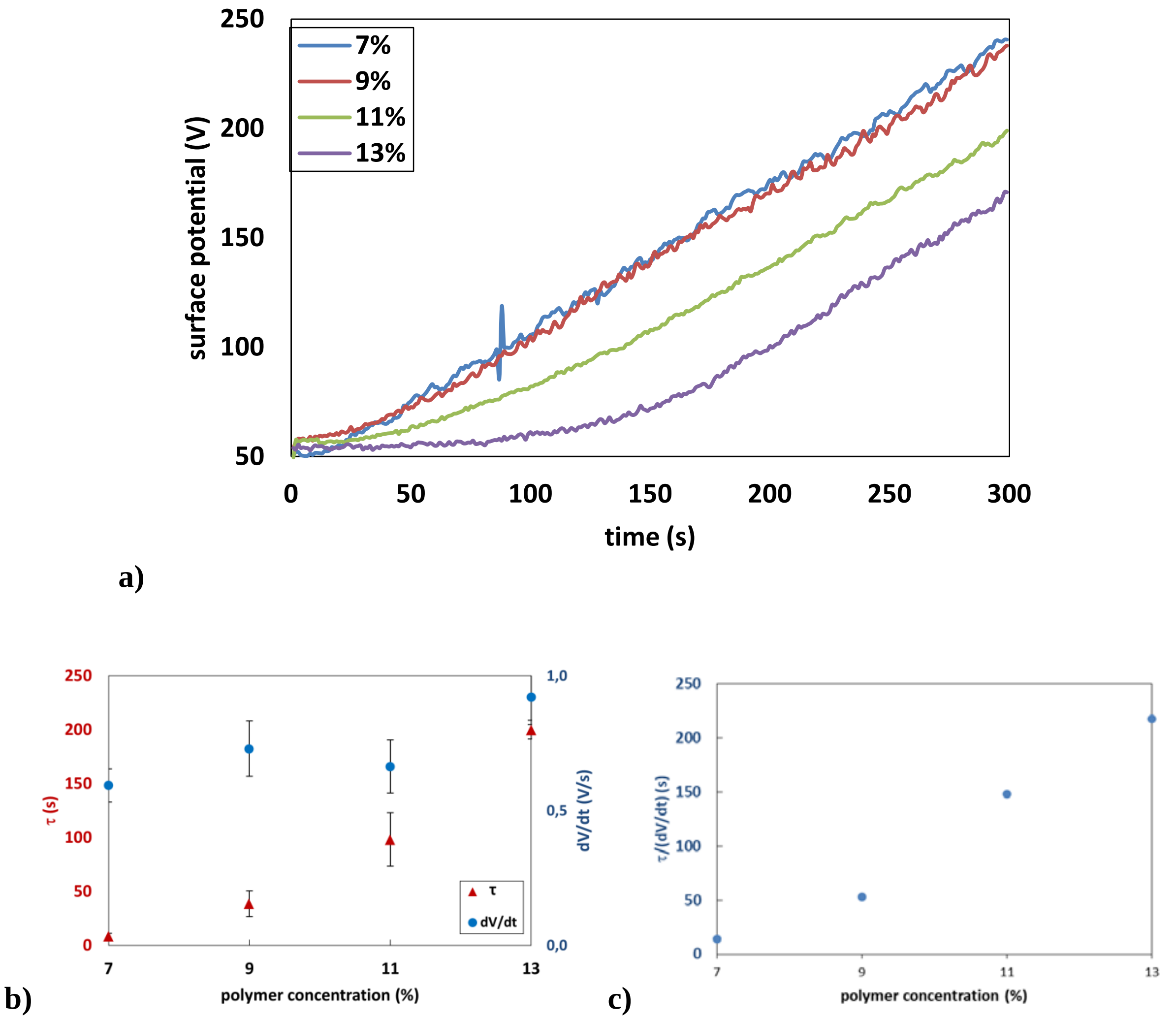

Fig. 3.9 a) Examples of experimental curves of the surface potential as a function of the polymer concentration. b) Characteristic time τ and slope $\frac{dV}{dt} = i\dot{R}_m$ and c) $\tau/\left(\frac{dV}{dt}\right)$ ratio as a function of the polymer concentration.

As shown in Fig. 3.9, τ increases gradually from 8 s to 200 s when the concentration increases from 7% to 13% whereas the slope $i\dot{R}_m$ is almost constant with, however, a small increase observed for the highest studied concentration. Once again, the characteristic time seems to be in good correlation with the size of the pores being proportional with the fiber diameter (see Fig. 3.10). Thus, increasing the polymer concentration induces the enlargement of the fiber diameter due to high solution viscosities and thus leads to remarkable increase of τ. It is also worth noting that for the highest concentration C = 13%, a lag time was used to fit adequately the experimental curve of the surface potential. The presence of this lag time could be explained that at high concentration solvent can remain in the fiber when it lands on the collector. This residual solvent could enhance the electrical contact between the first layer of fibers and the collector. Thus, this first fibrous layer could have a very low resistance inducing no rise of the surface potential during this lag time.

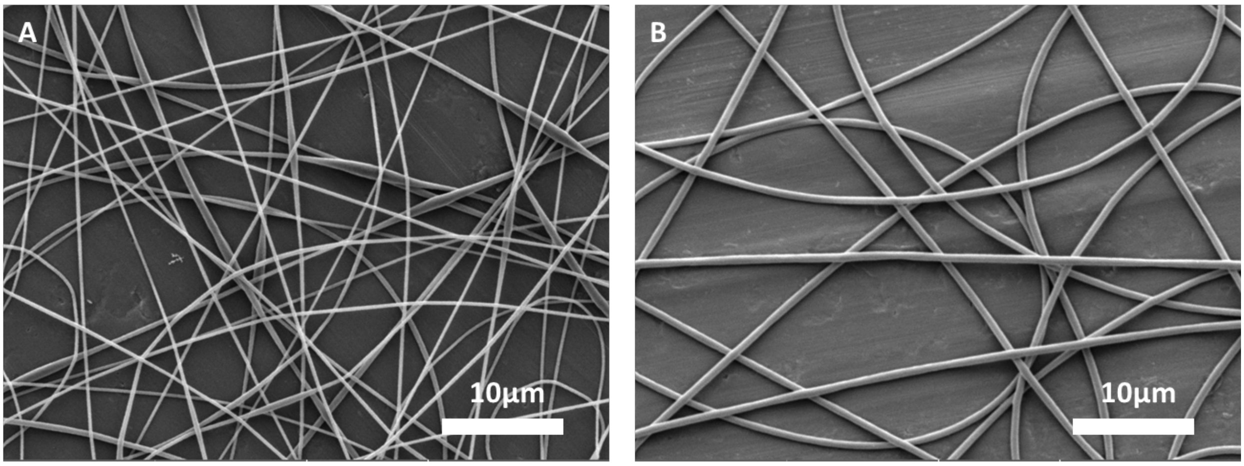

Fig. 3.10 SEM images of PLA fibers fabricated from polymer solutions at a concentration of 7% (A) and 13% (B) after a short time of electrospinning.

3.3.2.3 Effect of ambient relative humidity

No significant effect of the ambient relative humidity (RH) on the current was observed (Fig. 3.11) as opposed to the slow increase of the accumulation rate of charges observed in the previous chapter. The current being influenced by many parameters, it is complex to draw any conclusion. In contrary, the two main parameters, τ and $i\dot{R}_m$, describing the surface potential model evolve significantly with RH (see Fig. 3.12). First, a gradual increase of τ was observed. Once more, it can be noticed that τ increases with the pore size of the mat. Indeed, as observed on SEM (Fig. 3.13), the fiber diameter increases sharply with RH resulting in the formation of larger pores [29]. It was also observed an effect of RH on the slope $i\dot{R}_m$ of the curves representing the surface potential as a function of time. A significant decrease of $i\dot{R}_m$ is firstly observed a relative humidity increasing from 28% to 48%. Then, the slope is rising sharply when increasing RH from 48% to 58%. The slope is mainly related to the rate of the mat electrical resistance $\dot{R}_m$, the current being indeed almost constant with RH. The resistance should be linked with the resistivity of the polymer, here PLA, the quality of the fiber-fiber contact points and the number of contact points per unit volume of mat. As shown in Fig. 3.13, all these features seem to change as a function of RH explaining thus the complex trend of $i\dot{R}_m$.

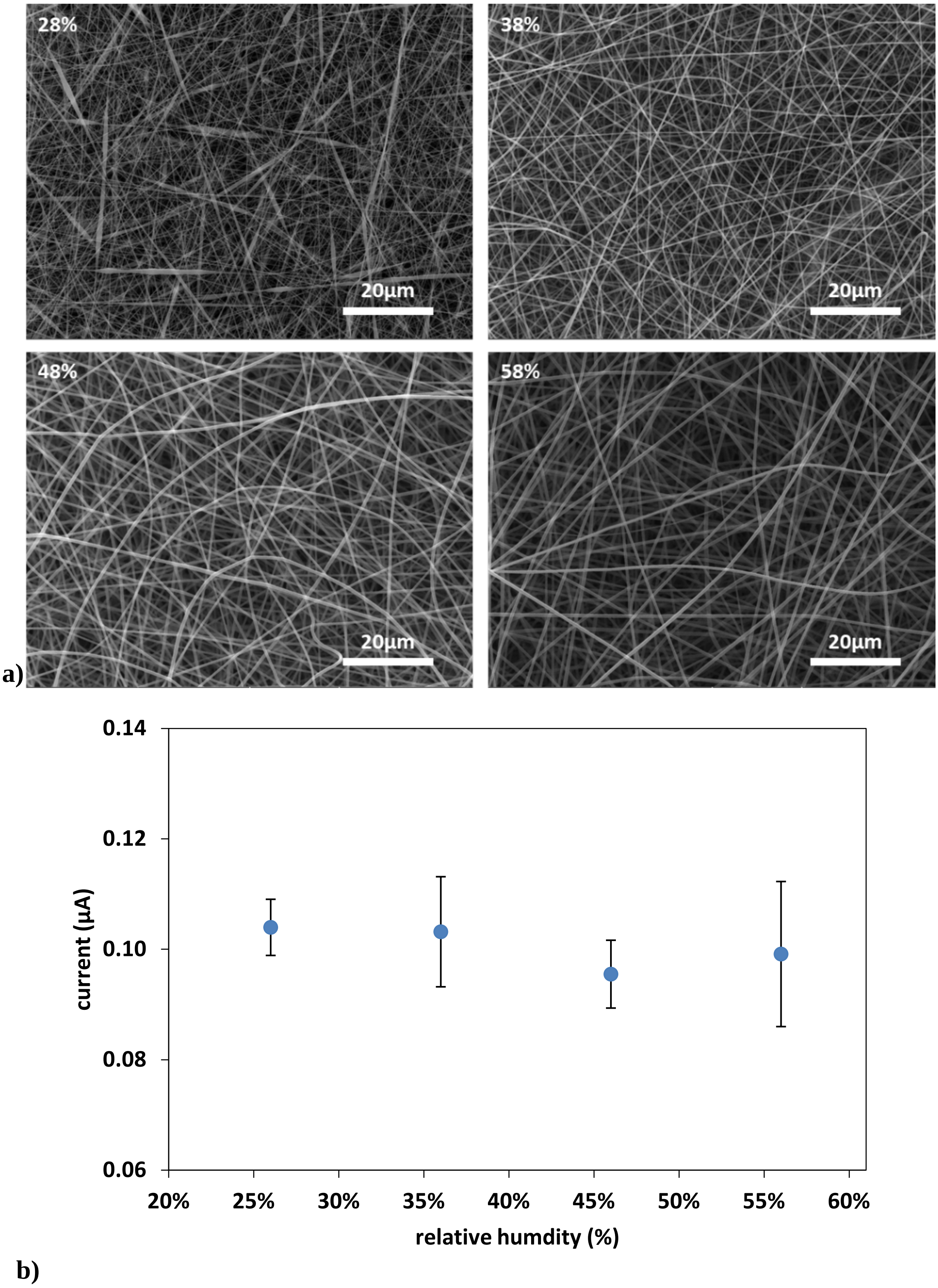

Fig. 3.11 a) SEM images of PLA fibers fabricated from various ambient relative humidity. b) Evolution of the current as a function of the relative humidity

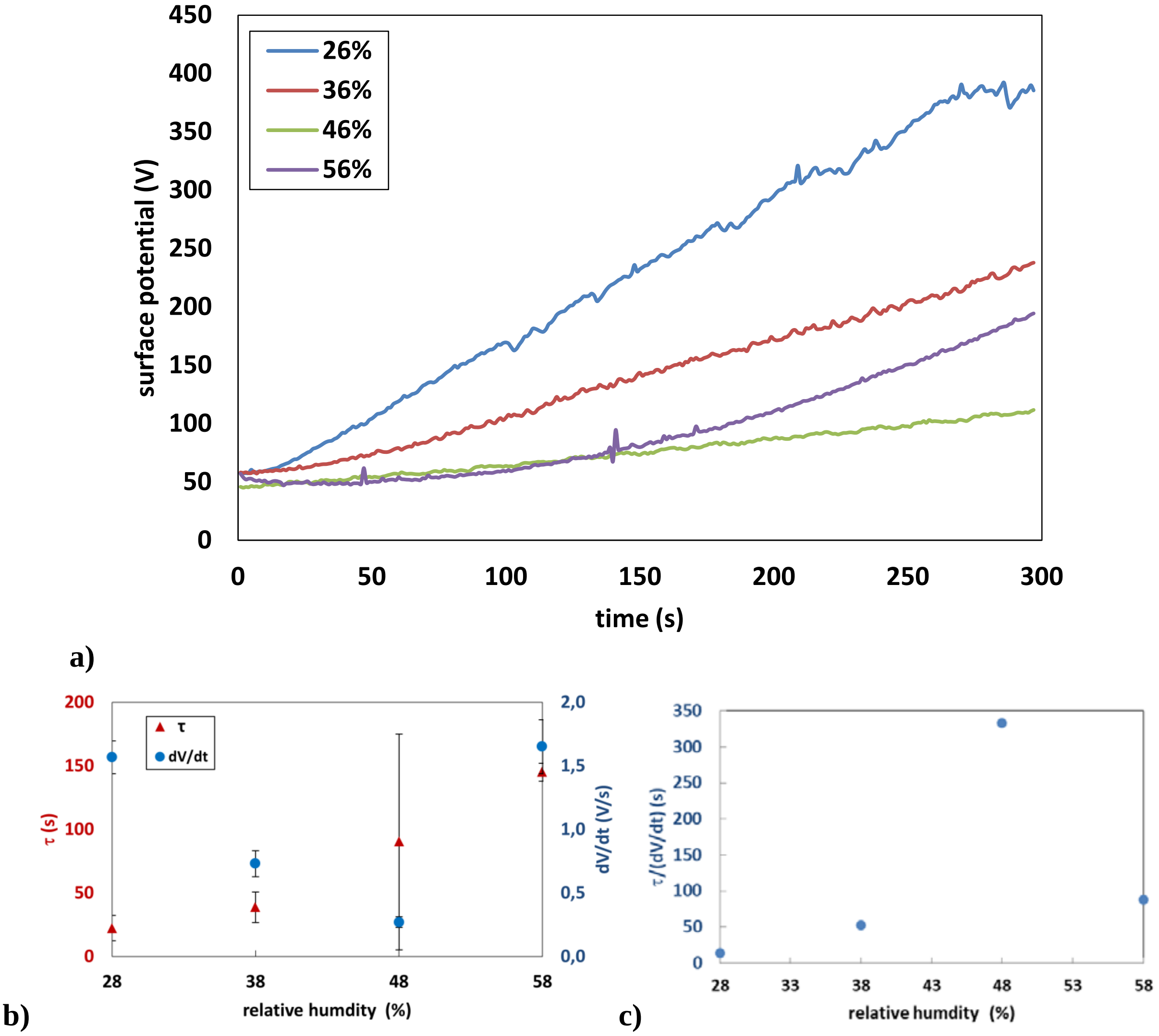

Fig. 3.12 a) Examples of experimental curves of the surface potential as a function of the ambient relative humidity. b) Characteristic time τ and slope $\frac{dV}{dt} = i\dot{R}_m$ and c) $\tau/\left(\frac{dV}{dt}\right)$ ratio as a function of the relative humidity.

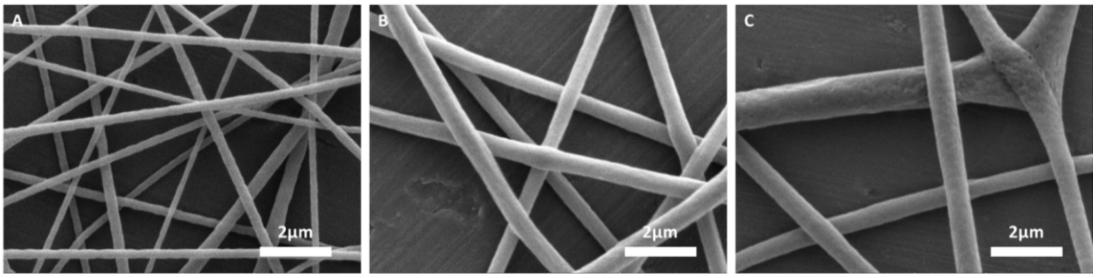

Fig. 3.13 SEM images of PLA fibers fabricated from different ambient relative humidities (A-D: 28%; B: 48%; C: 58%)

3.4 Decay of the surface potential of the mat after stopping the fiber production – mechanism of residual charges dissipation

3.4.1 Surface potential decay: a model

In this section, we will study how the stored charges release during time after stopping electrospinning. When the power supply connected to the emitter is switched-off, the jet is no more produced, the current is thus zero and no more charges are deposited. Since the current is zero, no charges are released to the ground. However, it is observed a decrease of the surface potential over time as shown in Fig. 3.14. Several mechanisms of charge release can explain the surface potential decay. First, charges located at the topmost surface of the mat are subjected to ion neutralization with air. This charge release phenomenon may occur at short times, characterized by a time denoted τ_s. Second, charges mostly located at the surface of the fibers, but inside the porosity of the mat, should release their charges within each pore having already participated to the kinetic of in-situ charging by electrospinning. It is thus expected that this second characteristic time of decay, denoted τ_m, is in the same order than the characteristic time τ measured during in-situ charging. This medium characteristic time τ_m is expected to be higher than τ_s. Third, in-situ electrospinning may lead the production of charges efficiently trapped in the bulk of the fibers. Indeed, although electrospinning of PLA leads to the fabrication of fibers with low crystallinity [27], charges may be trapped inside the fibers between amorphous and crystalline domains. This charge release phenomenon may occur at long times characterized by a time denoted τ_l. Thus, although a double exponential fitting was proposed in the literature for fibrous mats charged by corona effect [30], it is expected that the normalized surface potential decay may be modeled by the sum of three exponential functions as follows:

$$V(t) = A_s e^{-\left(\frac{t-t_{spin}}{\tau_s}\right)} + A_m e^{-\left(\frac{t-t_{spin}}{\tau_m}\right)} + A_l e^{-\left(\frac{t-t_{spin}}{\tau_l}\right)} \tag{3.7}$$

Fig. 3.14 shows the surface potential decay obtained after stopping electrospinning carried out under the conditions of PLA-S2 with a long time of acquisition of 2000 s. It is shown that the model described by Eqn 3.7 fits perfectly the experimental data. After fitting by a least square method, the obtained times were respectively τ_s =11 s, τ_m =104 s and τ_l =2183 s. A double exponential model was tested in order to compare the fitting quality:

$$V(t) = A_1 e^{-\left(\frac{t-t_{spin}}{\tau_1}\right)} + A_2 e^{-\left(\frac{t-t_{spin}}{\tau_2}\right)} \tag{3.8}$$

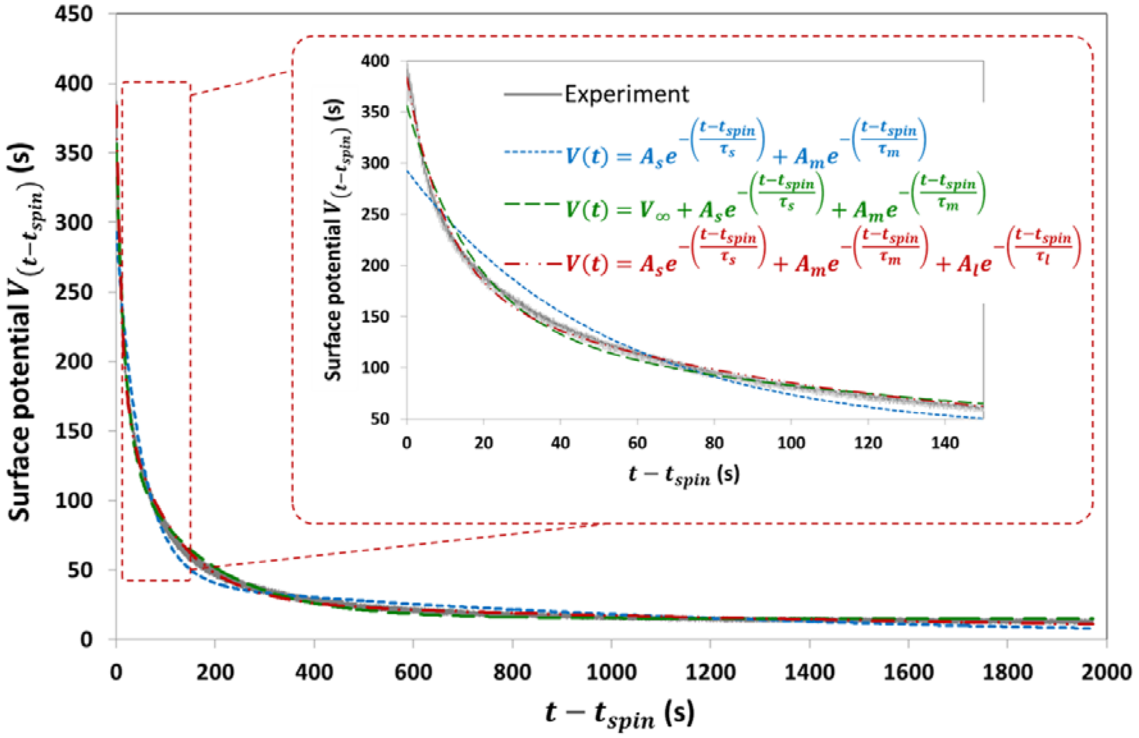

Fig. 3.14 Surface potential decay after stopping electrospinning carried out under the conditions of PLA-S2 (see Table 3.1). Experimental data (grey line), model with two characteristic times only (short dashed blue line), model with 2 characteristic times and one asymptote (dashed green line), model with three characteristic times only (dashed-point red line).

Using Eqn. 3.8, one characteristic time is obviously lost, leading to bad fitting as shown in Fig. 3.14. In this case, the obtained characteristic times were $\tau_1 = 51$ s and $\tau_2 = 1187$ s. Another model can be proposed, using also two characteristic times but introducing an asymptote V_∞ instead of the long time as introduced in the model described by Eqn 3.7. The model is the following:

$$V(t) = V_\infty + A_s e^{-\left(\frac{t-t_{spin}}{\tau_s}\right)} + A_m e^{-\left(\frac{t-t_{spin}}{\tau_m}\right)} \tag{3.9}$$

It is shown that Eqn. 3.9 allows also a good fitting of the experimental data as V_∞ can better take into account the behavior at long times whereas τ_s and τ_m play the same role as in the model using three characteristic times. Using Eqn. 3.9, the least square method gave the corresponding characteristic times: $\tau_s = 17$ s and $\tau_m = 166$ s. Because in the next part, all measurements of the surface potential decay were carried out during a time of 150 s, the three exponential model didn't allow a good estimation of the long time τ_l. Thus, the model using two characteristic times with an asymptote V_∞ (Eqn. 3.9) was chosen to fit the experimental data and only the behavior at short and medium times was studied. Furthermore, the following normalized weight factors were also studied as a function of the processing conditions:

$$A_s\% = \frac{100\,A_s}{V_\infty + A_s + A_m} \tag{3.10}$$

$$A_m\% = \frac{100\,A_m}{V_\infty + A_s + A_m} \tag{3.11}$$

$$V_\infty\% = \frac{100\,V_\infty}{V_\infty + A_s + A_m} \tag{3.12}$$

3.4.2 Effect of processing parameters on the surface potential

3.4.2.1 Effect of applied voltage

Fig. 3.15 presents both τ_s and τ_m obtained from eqn. 3.9 to fit the surface potential decay measured for various applied voltage on the emitter. It should be mentioned that the two exponentials are needed to fit all experimental data. The normalized weight factors are not influenced by applied voltage whereas the medium decay process is preponderant compared to the short one. The discharged of the top surface, characterized by the short time τ_s being in the order of 10 s, is a little bit faster for the mats produced for the highest voltage. Indeed, the highest applied voltage led to the production of mats with the thinnest fibers and consequently having the largest surface area offered to the ions of the air for a quick decay. It is also shown that the short time decay is around ten times faster than the medium one. A slow decrease of the medium time with applied voltage is observed. Moreover, τ_m is of the same order of magnitude than the characteristic time τ determined for the modeling of the surface potential during in-situ charging by electrospinning. These features seem to show that τ_m and τ have the same physical originating from the effect of the pores of the mat on the kinetic of the surface potential. However, the effect of applied voltage on τ_m is weaker than what it was observed for τ during electrospinning. Although efficient charge injection is expected in the bulk of the fibers produced for the highest applied voltage, $V_\infty\%$, characterizing the amount of bulk charges, is surprisingly constant with applied voltage. However, such result must be taken with caution because the measurements were carried out along short period, i.e.150 s that don’t allow a precise description of the kinetic at long times.

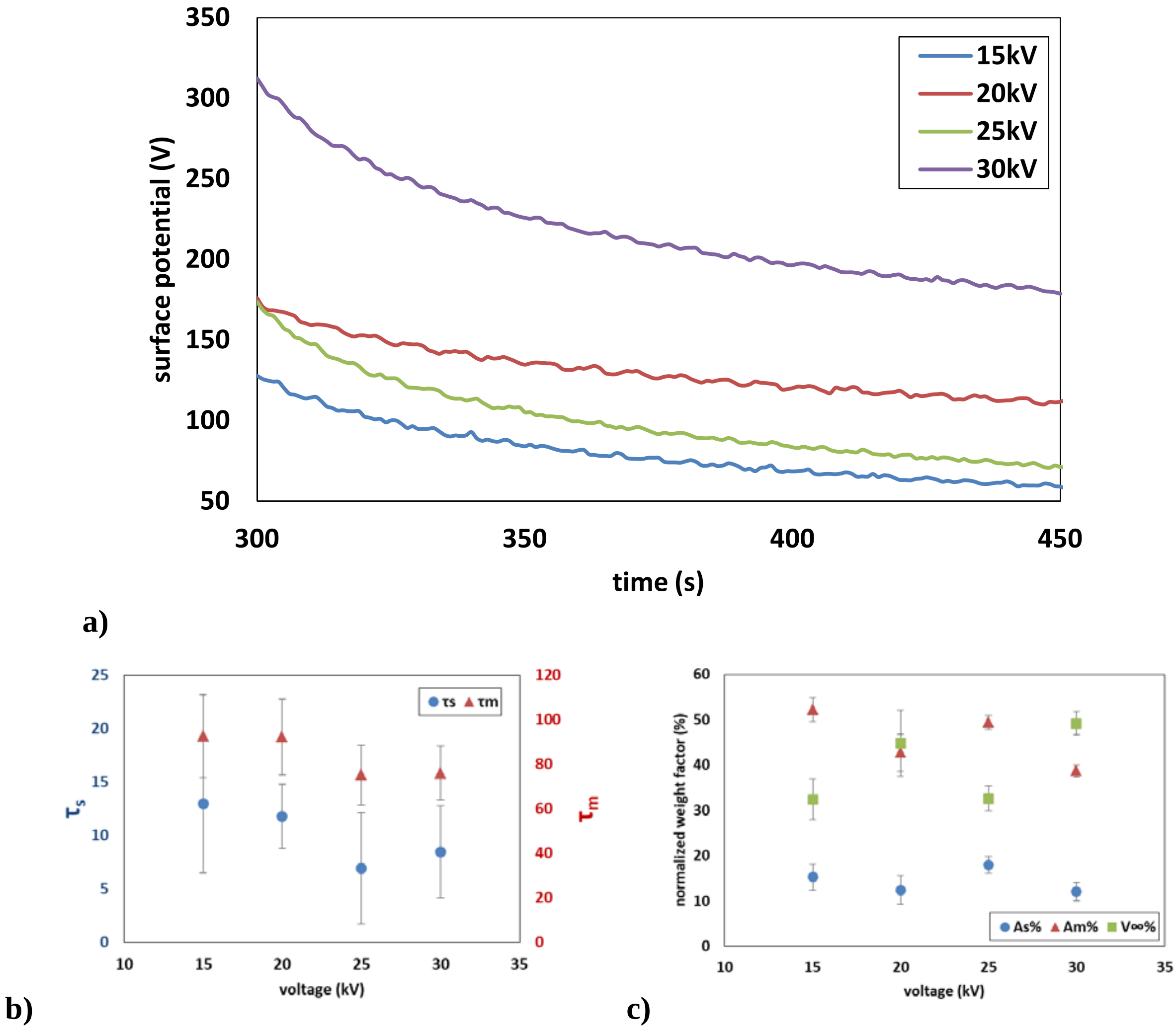

Fig. 3.15 a) Examples of curves giving the surface potential decay as a function of time for various applied voltage. b) Short and medium times and c) normalized weight factors as a function of applied voltage on the emitter.

3.4.2.2 Effect of polymer concentration

Fig. 3.16 shows τ_s and τ_m in the case of mats produced at various polymer concentration. The normalized weight factors are not significantly influenced by the polymer concentration. As observed for τ for the in-situ charging, τ_m increases with the polymer concentration. However, this trend is much less pronounced for τ_m than for τ. No tendency can be draw for the short time decay.

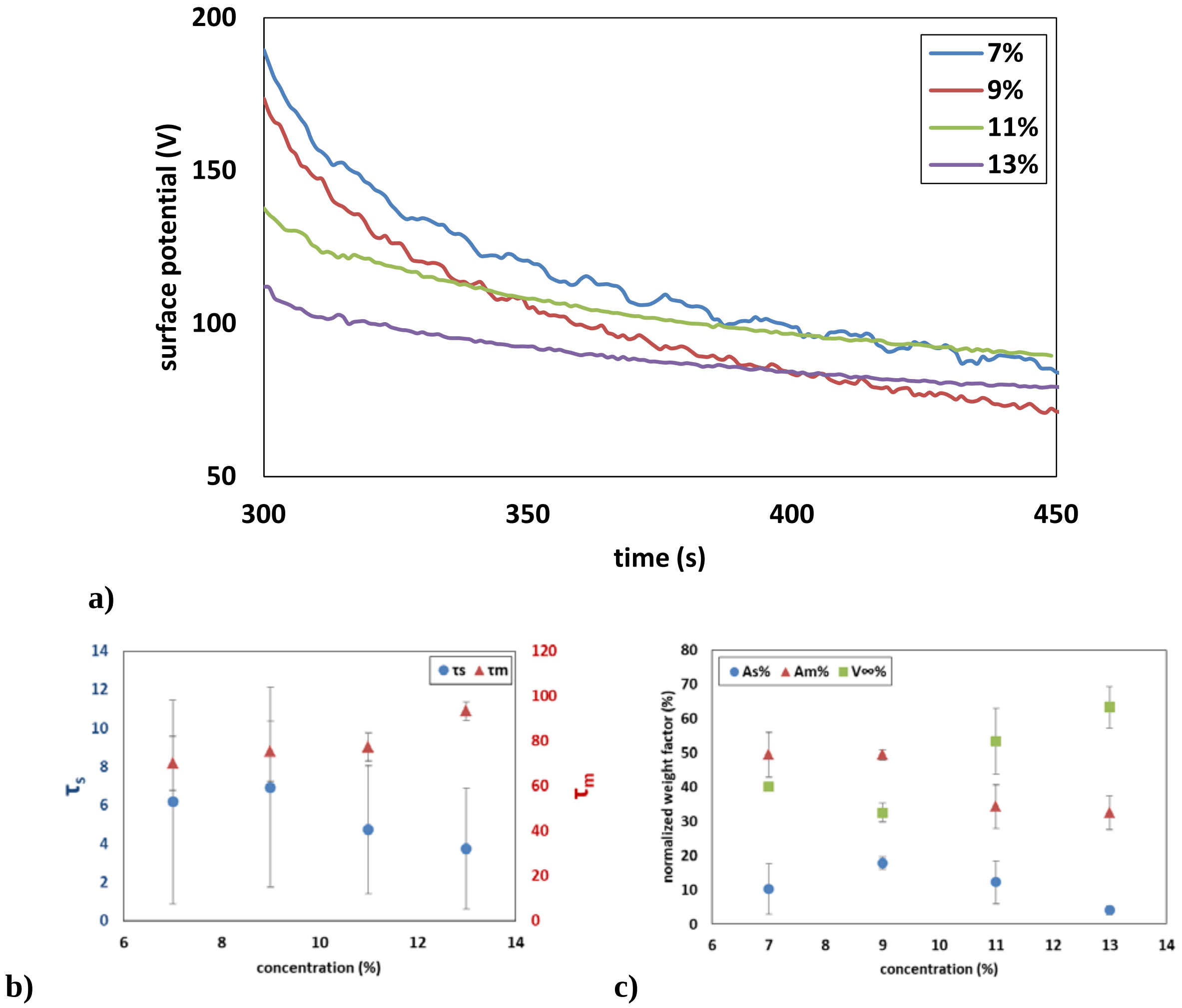

Fig. 3.16 a) Examples of curves giving the surface potential decay as a function of time for various polymer concentration. b) Short and medium times and c) normalized weight factors as a function of polymer concentration.

3.4.2.3 Effect of ambient relative humidity

Fig. 3.17 shows τ_s and τ_m obtained to fit the surface potential decay measured for various ambient relative humidity (RH). Compared with the effect of the two previous parameters (applied voltage and polymer concentration) on the characteristic times, the effect of RH is more pronounced. This should be explained by the fact that RH is imposed not only during in-situ charging by electrospinning but also after stopping electrospinning. As observed for τ, τ_m increases with RH, τ_m being in the same order of magnitude than τ. Furthermore, it is worth noting that the fact that RH influences almost only the charges located on the surface of the fibers confirms that the mechanism leading to the surface potential decay at medium time τ_m is due to the release of surface charges and not to bulk charges inside the fibers. Finally, a significant increase of $V_\infty\%$ is observed for the highest RH showing that a high amount of bulk charges, having the longest characteristic times, are stored in the matrix of the fibers.

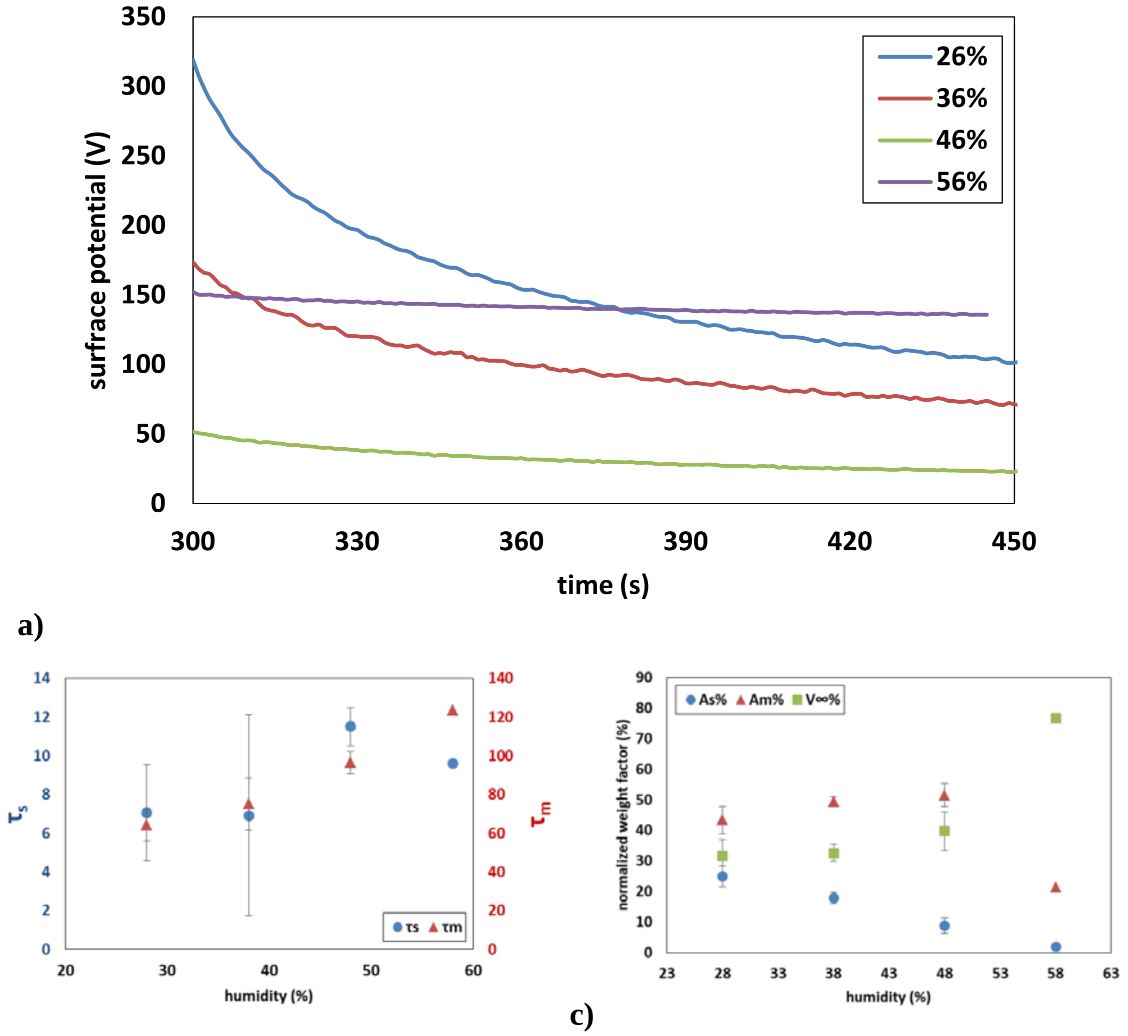

Fig. 3.17 a) Examples of curves giving the surface potential decay as a function of time for various relative humidity. b) Short and medium times and c) normalized weight factors as a function of relative humidity

3.5 Study during electrospinning of PEO

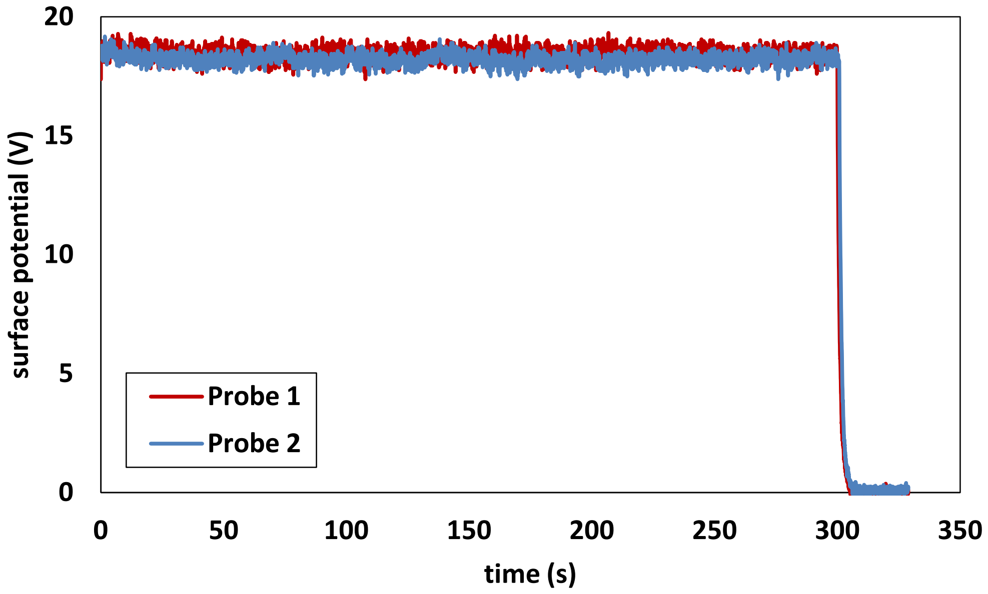

Fig. 3.18 Example of the evolution of the potential on the collector (probe 2 in blue) and the surface potential on the mat (probe 1 in red) during electrospinning of PEO in case of PEO-S2 conditions.

As shown in Fig. 3.18, there is no difference in potential between the top surface and the downside of the PEO fibrous mat. Especially, the curve achieved on the top surface presents no significant in-situ charging during the process of PEO electrospinning, indicating that no residual charges remain on PEO fibers. All charges released towards the ground immediately when PEO fibers hit the collector. From Eqn. 3.4, it indicates that $\dot{R}_m$ is almost 0 in the process of electrospinning. Indeed, as a hydrosoluble polymer, PEO is dissolved in water holding a high permittivity and conductivity favoring the charges to transfer from the PEO fibrous mat to the ground.

After stopping electrospinning, both potential declined immediately to 0 showing that PEO fibers have no capability in charge storage. In addition, due to the sharp decline, the surface potential decay cannot be modeled by the exponential function discussed in the section of PLA fibers.

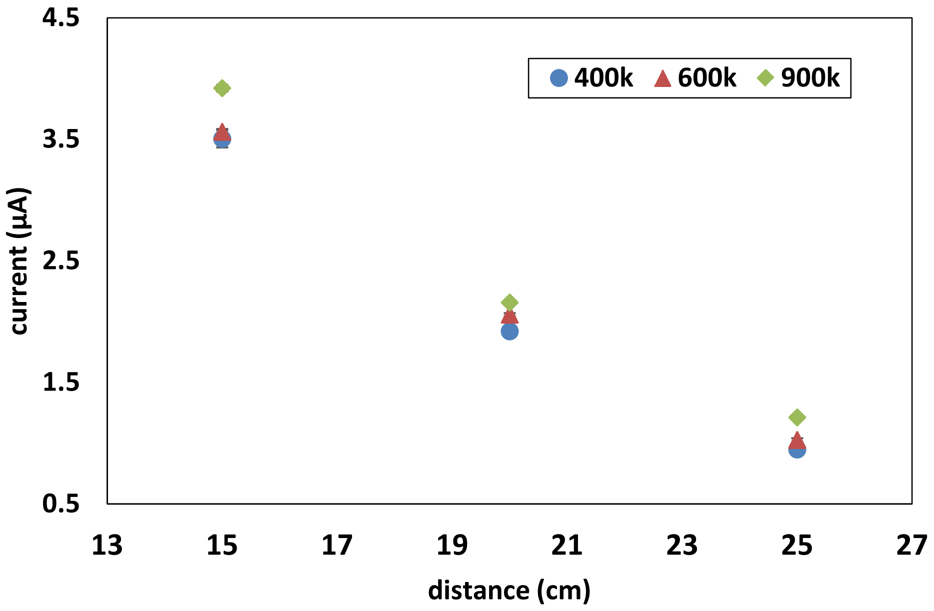

Fig. 3.19 comparison of the current formed by electrospinning PEO fibers with different molar masses in different distances

As shown in Fig. 3.19, in each condition of the processing distance, an increase of almost 10% of the current is shown with the enlargement of PEO molar mass from 400 kg/mol to 900 kg/mol, indicating that PEO fibers prepared in different molar masses held variable capabilities in charge transfer. The larger molar mass induces more entanglements among polymer chains increasing thus the viscosity of the solution resulting in thick fibers embedding more residual solvent leading to the increase of the conductivity of the fibrous mat. Therefore, fibers obtained from high molar mass PEO accelerate the charges transfer towards the ground resulting in the increment of the current.

The result in Fig. 3.19 also shows that decreasing the working distance induces a significant increase of the current. The short distance from the needle to the collector causes a strong electric force accelerating the jet, leading charges to transfer into the ground more quickly resulting to the increase of the current. In addition, a jet which experiences a shorter transporting time in the air has insufficient time for solvent evaporation. Thus, fibers with more residual solvents should have a higher conductivity increasing the overall current. In contrast, dry fibers formed under large distance have a poor ability to transfer charges thanks to complete solvent evaporation [31], [32].

In this part, we applied PEO fibers to detect the in-situ charging during the traditional electrospinning, presenting PEO fibrous mats had no ability to store residual charges. Combining with the phenomenon obtained in PLA fibers, it proved excepted the physical property of polymers, the permittivity of the solvents used in electrospinning played an important role in the behavior of in-situ charging. Solvents that with a low permittivity could maintain more charges in jets resulting in relatively low rate of charge transfer from fibers to the ground, thus facilitating charges to accumulate gradually with the extend of electrospinning.

3.6 Discussion and conclusion

Here, we showed that the measurement of the surface potential of the mat can be easily carried out online during the process using an electrostatic voltmeter. Moreover, the simultaneous measurement of the current as well as the mat surface potential is an efficient way which allows getting more insight into the overall process of electrospinning. Whereas the current is mostly related to the electrospun jet state, the surface potential is more sensitive to the behavior of the mat and especially its internal porous structure. The kinetic of the surface potential decay after stopping electrospinning is well described by three characteristic times. The short time τ_s, having a value of about ten seconds, characterizes the rapid charge release occurring on the topmost surface of the mat. The medium time τ_m, having a value of several tens of seconds up to more than one hundred of seconds, relies on the charge release inside each pore of the mat. Finally, the long time τ_l, being at least one order of magnitude higher than the medium time, characterizes the release of the charges trapped inside the fibers. This latter was not deeply studied in the present work.

Although the measurement of the surface potential decay allows to finally dissociate the kinetic in three fundamental mechanisms of charge release, it only gives an average behavior over the entire thickness of the mat. In contrary, the measurement of the surface potential during in-situ charging by electrospinning is mainly sensitive to the kinetic of charge release at medium times but with a much higher accuracy. Indeed, the medium time τ_m, obtained from the fitting of the surface potential decay measured after stopping electrospinning, is of the same order of magnitude than the time τ measured during electrospinning. Both τ_m and τ follow the same behavior as a function of the studied processing parameters: a decrease with increasing voltage and the opposite when increasing either the polymer concentration or the ambient relative humidity. However, the characteristic time τ revealed to be much more sensitive than τ_m. Such difference can be explained by the fact that the surface potential measured during electrospinning takes into account a continuously fresh deposited top surface which immediately starts to release its charges. Thus, τ may be more related to the combination of the release at short times (~ 10 s) of charges located on the top surface and the release at medium times (~ 100 s) of the charges located in the pores just below the top surface under construction. In fact, in the proposed model of in-situ charging by electrospinning (Eqn. 3.4), the τ value can be related to the electrical characteristics at the different length scales: (i) the pore, (ii) the elementary layer having the surface of the membrane and the thickness of one pore and (iii) the whole membrane under building. Each of them is related to the pore structure of the mat:

$$\tau = dR_m dC_m = R_p C_p = R_m C_m \tag{3.13}$$

Assuming the membrane electrical resistance R_m evolves linearly with time:

$$R_m = \dot{R}_m t \tag{3.14}$$

Using 3.13 and 3.14, it is possible to give an estimation of the membrane capacitance C_m:

$$C_m = \frac{\tau}{\dot{R}_m t} \tag{3.15}$$

Because the number of elementary layers in the thickness of the membrane is proportional to the time of deposition and that the current is constant during time, dR_m and dC_m scale as:

$$dR_m \propto \dot{R}_m \propto dV/dt \tag{3.16}$$

$$dC_m \propto \frac{\tau}{\dot{R}_m} \propto \frac{\tau}{dV/dt} \tag{3.17}$$

Thus, knowing that the average number of pores P for one elementary layer of membrane of surface S_m is $P = S_m/D_p^2$ and that the characteristic size of a pore D_p is proportional to the fiber diameter $D_p \sim \phi_f$ [29], the resistance and the capacitance of a pore scale respectively as:

$$R_p \;\propto\; \frac{dV/dt}{\phi_f^2} \tag{3.18}$$

$$C_p \;\propto\; \frac{\phi_f^2\,\tau}{dV/dt} \tag{3.19}$$

In order to verify that the proposed scaling law, all data points obtained in the various operating conditions (applied voltage, polymer concentration and ambient relative humidity) were represented in graphs. The first one, gives $\frac{\phi_f^2\,\tau}{dV/dt}$ as a function of the measured fiber diameter ϕ_f (Fig. 3.20a). Because of Eqn. 3.19, this graph is proportional to the graph of the pore capacitance C_p versus ϕ_f . It is shown that whatever the processing condition (highlighted by the different symbols in the graph), C_p is well correlated with the fiber diameter. The following scaling law can thus be obtained for electrospinning of PLA on a flat collector:

$$C_p \;\propto\; \phi_f^{4,87} \tag{3.20}$$

Consequently, the fiber diameter can be plotted as a function of $\frac{\tau}{dV/dt}$ a good correlation can also be obtained giving thus ϕ_f as a function of only the physical quantities obtained from the measurement of the surface potential:

$$\phi_f \propto \left[\frac{\tau}{dV/dt}\right]^{0,21} \tag{3.21}$$

In conclusion, it was shown for the first time that the measurement of the surface potential, thanks to the use of an electrostatic voltmeter, is a simple method giving accurate information at the local scale of the nanofiber diameter of an electrospun mat. Such a method should allow the detection of variations in the porous morphology of a mat during its fabrication. Furthermore, in combination with the measurement of the current, it is an efficient and complementary method to get an online monitoring of the process of electrospinning.

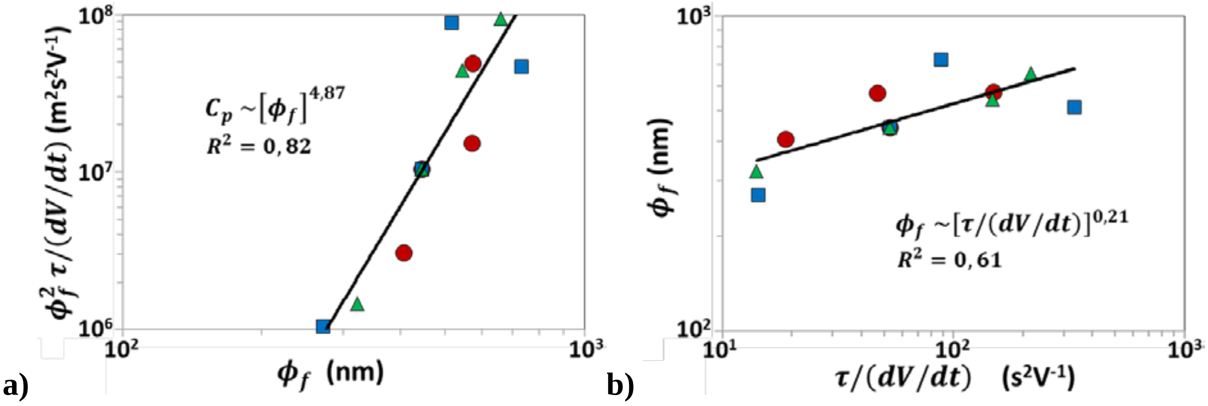

Fig. 3.20 a) Correlation between C_p and the fiber diameter ϕ_f. b) Correlation between the fiber diameter ϕ_f and $\tau/(dV/dt)$. Green triangles correspond to the experimental points obtained from polymer concentrations C = 7 %, 9 %, 11 % and 13 %, blue squares from relative humidity RH = 28 %, 38 %, 48 % and 58 % and red discus from applied voltages = 15 kV, 20 kV, 25 kV and 30 kV.

References

[1] S. Wang, X. Zhao, X. Yin, J. Yu, and B. Ding, “Electret Polyvinylidene Fluoride Nanofibers Hybridized by Polytetrafluoroethylene Nanoparticles for High-Efficiency Air Filtration,” *ACS Applied Materials & Interfaces*, vol. 8, no. 36, pp. 23985–23994, Sep. 2016, doi: 10.1021/acsami.6b08262.

[2] S. Nedjari *et al.*, “Electrostatic template-assisted deposition of microparticles on electrospun nanofibers: towards microstructured functional biochips for screening applications,” *RSC Advances*, vol. 5, no. 102, pp. 83600–83607, 2015, doi: 10.1039/C5RA15931H.

[3] J.-H. Jang, O. Castano, and H.-W. Kim, “Electrospun materials as potential platforms for bone tissue engineering,” *Advanced Drug Delivery Reviews*, vol. 61, no. 12, pp. 1065–1083, Oct. 2009, doi: 10.1016/j.addr.2009.07.008.

[4] S. Y. Chew, J. Wen, E. K. F. Yim, and K. W. Leong, “Sustained Release of Proteins from Electrospun Biodegradable Fibers,” *Biomacromolecules*, vol. 6, no. 4, pp. 2017–2024, Jul. 2005, doi: 10.1021/bm0501149.

[5] A. Thorvaldsson, H. Stenhamre, P. Gatenholm, and P. Walkenström, “Electrospinning of Highly Porous Scaffolds for Cartilage Regeneration,” *Biomacromolecules*, vol. 9, no. 3, pp. 1044–1049, Mar. 2008, doi: 10.1021/bm701225a.

[6] R. Samatham and K. J. Kim, “Electric current as a control variable in the electrospinning process,” *Polymer Engineering & Science*, vol. 46, no. 7, pp. 954–959, Jul. 2006, doi: 10.1002/pen.20565.

[7] F. Yener, B. Yalcinkaya, and O. Jirsak, “On the Measured Current in Needle- and Needleless Electrospinning,” *Journal of Nanoscience and Nanotechnology*, vol. 13, no. 7, pp. 4672–4679, Jul. 2013, doi: 10.1166/jnn.2013.7189.

[8] Y. M. Shin, M. M. Hohman, M. P. Brenner, and G. C. Rutledge, “Experimental characterization of electrospinning: the electrically forced jet and instabilities,” *Polymer*, vol. 42, no. 25, pp. 09955–09967, Dec. 2001, doi: 10.1016/S0032-3861(01)00540-7.

[10] J. Lowell, “Absorption and conduction currents in polymers: a unified model,” *Journal of Physics D: Applied Physics*, vol. 23, no. 2, pp. 205–210, Feb. 1990, doi: 10.1088/0022-3727/23/2/011.

[11] L. H. Catalani, G. Collins, and M. Jaffe, “Evidence for Molecular Orientation and Residual Charge in the Electrospinning of Poly(butylene terephthalate) Nanofibers,” *Macromolecules*, vol. 40, no. 5, pp. 1693–1697, Mar. 2007, doi: 10.1021/ma061342d.

[12] M. Ignatova, T. Yovcheva, A. Viraneva, G. Mekishev, N. Manolova, and I. Rashkov, “Study of charge storage in the nanofibrous poly(ethylene terephthalate) electrets prepared by electrospinning or by corona discharge method,” *European Polymer Journal*, vol. 44, no. 7, pp. 1962–1967, Jul. 2008, doi: 10.1016/j.eurpolymj.2008.04.027.

[13] A. Amin, A. A. Merati, S. H. Bahrami, and R. Bagherzadeh, “Effects of porosity gradient of multilayered electrospun nanofibre mats on air filtration efficiency,” *The Journal of The Textile Institute*, vol. 108, no. 9, pp. 1563–1571, Sep. 2017, doi: 10.1080/00405000.2016.1264856.

[14] B. Tabti, L. Dascalescu, M. Plopeanu, A. Antoniu, and M. Mekideche, “Factors that influence the corona charging of fibrous dielectric materials,” *Journal of Electrostatics*, vol. 67, no. 2–3, pp. 193–197, May 2009, doi: 10.1016/j.elstat.2009.01.047.

[15] A. Y. Choi, H. J. Sim, M. K. Shin, S. J. Kim, and Y. T. Kim, “Residual Charges during Electrospinning Assist in Formation of Piezoelectricity in Poly(Vinylidene Fluoride-co-Trifluoroethylene) Nanofibers,” *Journal of Nano Research*, vol. 37, pp. 13–19, Dec. 2015, doi: 10.4028/www.scientific.net/JNanoR.37.13.

[16] B. M. Cho, Y. S. Nam, J. Y. Cheon, and W. H. Park, “Residual charge and filtration efficiency of polycarbonate fibrous membranes prepared by electrospinning,” *Journal of Applied Polymer Science*, vol. 132, no. 1, Jan. 2015, doi: 10.1002/app.41340.

[17] H.-W. Tong, M. Wang, and W. W. Lu, “Enhancing the biological performance of osteoconductive nanocomposite scaffolds through negative voltage electrospinning,” *Nanomedicine*, vol. 8, no. 4, pp. 577–589, Apr. 2013, doi: 10.2217/nnm.13.51.

[18] B. Yalcinkaya, F. C. Callioglu, and F. Yener, “Measurement and analysis of jet current and jet life in roller electrospinning of polyurethane,” *Textile Research Journal*, vol. 84, no. 16, pp. 1720–1728, Oct. 2014, doi: 10.1177/0040517514528563.

[19] Z. Li, R. Liu, Y. Huang, and J. Zhou, “Effects of reversed arrangement of electrodes on electrospun nanofibers,” *Journal of Applied Polymer Science*, vol. 134, no. 15, Apr. 2017, doi: 10.1002/app.44687.

[20] G. Yan *et al.*, “Self-Assembly of Electrospun Polymer Nanofibers: A General Phenomenon Generating Honeycomb-Patterned Nanofibrous Structures,” *Langmuir*, vol. 27, no. 8, pp. 4285–4289, Apr. 2011, doi: 10.1021/la1047936.

[21] T. Yao, H. Chen, P. Samal, S. Giselbrecht, M. B. Baker, and L. Moroni, “Self-assembly of electrospun nanofibers into gradient honeycomb structures,” *Materials & Design*, vol. 168, p. 107614, Apr. 2019, doi: 10.1016/j.matdes.2019.107614.

[22] H.-W. Tong, X. Zhang, and M. Wang, “A new nanofiber fabrication technique based on coaxial electrospinning,” *Materials Letters*, vol. 66, no. 1, pp. 257–260, Jan. 2012, doi: 10.1016/j.matlet.2011.08.095.

[23] S. J. Kim, C. K. Lee, and S. I. Kim, “Effect of ionic salts on the processing of poly(2-acrylamido-2-methyl-1-propane sulfonic acid) nanofibers,” *Journal of Applied Polymer Science*, vol. 96, no. 4, pp. 1388–1393, May 2005, doi: 10.1002/app.21567.

[24] S. Nedjari *et al.*, “Electrostatic template-assisted deposition of microparticles on electrospun nanofibers: towards microstructured functional biochips for screening applications,” *RSC Advances*, vol. 5, no. 102, pp. 83600–83607, 2015, doi: 10.1039/C5RA15931H.

[25] D. Ahirwal, A. Hébraud, R. Kádár, M. Wilhelm, and G. Schlatter, “From self-assembly of electrospun nanofibers to 3D cm thick hierarchical foams,” *Soft Matter*, vol. 9, no. 11, p. 3164, 2013, doi: 10.1039/c2sm27543k.

[26] N. Lavielle *et al.*, “Controlled formation of poly(ε-caprolactone) ultrathin electrospun nanofibers in a hydrolytic degradation-assisted process,” *European Polymer Journal*, vol. 49, no. 6, pp. 1331–1336, Jun. 2013, doi: 10.1016/j.eurpolymj.2013.02.038.

[27] S. Nedjari, S. Eap, A. Hébraud, C. R. Wittmer, N. Benkirane-Jessel, and G. Schlatter, “Electrospun Honeycomb as Nests for Controlled Osteoblast Spatial Organization: Electrospun Honeycomb as Nests for Controlled …,” *Macromolecular Bioscience*, vol. 14, no. 11, pp. 1580–1589, Nov. 2014, doi: 10.1002/mabi.201400226.

[28] S. Nedjari, G. Schlatter, and A. Hébraud, “Thick electrospun honeycomb scaffolds with controlled pore size,” *Materials Letters*, vol. 142, pp. 180–183, Mar. 2015, doi: 10.1016/j.matlet.2014.11.118.

[29] H. Ma, C. Burger, B. S. Hsiao, and B. Chu, “Ultra-fine cellulose nanofibers: new nano-scale materials for water purification,” *Journal of Materials Chemistry*, vol. 21, no. 21, p. 7507, 2011, doi: 10.1039/c0jm04308g.

[31] W. K. Son, J. H. Youk, T. S. Lee, and W. H. Park, “The effects of solution properties and polyelectrolyte on electrospinning of ultrafine poly(ethylene oxide) fibers,” *Polymer*, vol. 45, no. 9, pp. 2959–2966, Apr. 2004, doi: 10.1016/j.polymer.2004.03.006.

[32] S. Moon, B.-Y. Ryu, J. Choi, B. Jo, and R. J. Farris, “The morphology and mechanical properties of sodium alginate based electrospun poly(ethylene oxide) nanofibers,” *Polymer Engineering & Science*, vol. 49, no. 1, pp. 52–59, Jan. 2009, doi: 10.1002/pen.21216.

Chapter 4 Surface potential of suspended electrospun fibers: application for the building of 3D structured scaffolds by coupling electrospinning and electrospraying

4.1 Introduction

Electrospinning is a powerful technique that enables the production of nanofibers having a diameter in the range of tens of nanometer to micrometers in the form of a non-woven mat [1]–[3]. However, it is demonstrated by several authors that the deposition of the electrospun nanofibers can be controlled thanks to the use of patterned collector instead of a flat plate. In this context, 2D and even 3D structured nanofibrous mats can be obtained paving the way for various practical applications such as the elaboration of biomimetic scaffolds mimicking bone osteons [4], [5], increasing the alignment and porosity of the mats for better cell colonization in tissue engineering [6], improving the efficiency and reepithelialization of wound healing [7], inducing the filter highly transparent to improve light transmittance and pollutant filtration [8]–[10], enhancing photocatalysts with favorable recycling characteristics [11], etc.

Among these articles, it has been mentioned that the charges carried by the suspended fibers hanging between the protuberances of patterned collectors play the most important role as they build an electrostatic template necessary for the controlled deposition of fibers. Li et al. demonstrated that suspended fibers deposited across the gap of a collector, consisting of two electrically paralleled conductive substrates, can keep charges efficiently to induce an electric force acting on the incoming electrospun fiber experiencing thus an electrostatic repulsion which enhances the fiber alignment [12]. Other researches proved that the intensity of the electric field resulting from the charges carried on the suspended fibers can be manipulated by modifying the geometry of the collector as well as the processing parameters such as the voltage, the humidity and the electrical properties of solvents. [13]–[18]. Based on this principle, 2D structured nanofibrous mats were achieved thanks to the use of various patterned collectors [19]–[21]. In addition to 2D nanofibrous mats elaborated from static patterned collectors, Kuo et al. developed a novel method which controls the direction of the electric force acting on the deposition of the electrospun jet by grounding alternately electrodes in order to modify the orientation of aligned fibers [22]. However, such a method is complex especially when micropatterning is targeted. Moreover, all these techniques lead to the fabrication of structured scaffolds which are thin because the structuration generally disappears rapidly in the thickness of the mat with extending the processing time of electrospinning.

Therefore, aiming to generate 3D scaffolds with a thickness in the order of hundreds of microns containing spatial structures is of prime importance for many applications. Deitzel, et al. observed that 3D honeycomb-like fibrous scaffolds can be obtained through a self-assembling process occurring when fabricating fibers with a wide distribution in diameter [23]. Ahirwal et al. obtained cm-thick honeycomb-like foams by such dynamic self-assembling process. They demonstrated the pivotal hole of the bimodal distribution in fiber diameter on the formation of an electrostatic template leading to the building of 3D honeycomb-like fibrous structures [24]. Nedjari et al. studied in detail the electrostatic mechanism allowing such 3D structuration. It was shown that the thick part of the jet is more charged than the thin ones. Thus, thick fiber portions are more influenced by the electrostatic forces. Moreover, during electrospinning, when the fiber is deposited, the thick fiber portions allows a good electric contact with the collector allowing an efficient charge release whereas thin fiber strands which cannot touch the collector surface remain their charges forming the electrostatic template guiding the incoming electrospun jet. [25]. Using such strategy, Yan et al. achieve very regular honeycomb-like structures by forming beaded nanofibers from the polymer solution system in low concentration and poor volatile solvents [26].

Inspired by the principle of self-assembling of bimodal electrospun nanofibers, our group developed a strategy based on the simultaneous or alternate use of electrospun nanofibers and electrosprayed microparticles [27]. This strategy relies on the difference in diameter of the produced nanofiber (few hundreds of nm) and microparticles (few microns). Indeed, at the beginning, when electrosprayed microparticles enter in contact on the flat collector, they form protuberances avoiding the incoming fiber to touch the grounded collector. The microparticles being in good contact with the collector, they can efficiently release their charges towards the ground. However, the fiber strands suspended in the air between the particles remain charged. While the discharged domains made of bundles of microparticle and fiber portions in direct contact with the collector form attractive areas, the suspended charged nanofiber strands form repulsive areas. This electrostatic template made of attractive and repulsive areas is self-sustained during the production allowing the self-organization of nanofibers and microparticles. When a flat collector is used, self-assembling does not allow the control of the electrostatic template geometry. However, if a patterned collector with regular protuberances is used, the first deposited layer of electrospun nanofibers leads to the formation of an electrostatic template which replicates the patterns of the collector. Indeed, fiber segments suspended between neighboring patterns cannot release efficiently their electric charges forming thus repulsive areas. On the other hand, the fiber segments in contact with the top surface of the protuberances can dissipate their charges forming thus attractive areas. When electrospraying is carried out onto this electrostatic template, a selective deposition of the microparticles on the attractive areas is observed, allowing maintaining the shape of the patterns and leading to the formation of an organized 3D fibrous structure after successive steps of electrospinning and electrospraying [28], [29].

The electrostatic template plays the key hole in the 2D/3D structuration of mats produced by the combination of electrospinning and electrospraying processes. Thus, in order to control the structuration over the thickness of the scaffold and also to have the best fibrous structure matching with the patterns of the collector, it is necessary to study the kinetic of the formation of the electrostatic template as well as how long time the electrostatic template can be kept after stopping electrospinning when a step of electrospraying is carried out.

In part 4.2, a model experiment was developed in order to have a deep understanding on how charges are carried and released from suspended fiber strands hanging between the protuberances of patterned collectors. To this end, electrospinning is carried out with a cylindrical rotating collector having a single adjustable gap allowing a continuous measurement of the surface potential during the process and even after stopping electrospinning. The surface potential is studied as a function of time (i.e. the surface potential during electrospinning and its decay after stopping electrospinning) as well as a function of the gap size and the kind of polymer solution system. Furthermore, a model was developed in order to get more insight into the kinetic of the surface potential generated from suspended fibers over a single gap.

In part 4.3, more complex patterned collectors are investigated for the fabrication of various kinds of structured fibrous mats dedicated to biomedical applications: (i) a striated collector with parallel grooves and gaps and (ii) grids of various sizes. In the beginning, the deposition of fibers and particles were performed on the striated collector. The objective was to investigate the generation mechanism of electrospun/electrosprayed bilayer samples by modifying the processing time of electrospinning and changing polymer solution systems to better control the distribution of particles on the fibrous layer. Then, 3D structured fibrous mats were fabricated by alternate electrospinning and electrospraying.

4.2 Charges accumulation and dissipation on electrospun fibers suspended over a single gap: experiments and modeling

4.2.1 Materials and methods

Materials and solution preparation

PLA (Mw=180k, Natureworks), PEO (Mw=400k), TEBAC, alginate (4-12 cP, 1 % in H_2O at 25 °C) and deionized water were used as received. PCL (Mw=14k and 80k), DMAC, chloroform, Dichloromethane (DCM) and N, N-Dimethylformamide (DMF) were purchased from Sigma-Aldrich.

Pure PLA solutions for electrospinning were prepared by dissolving different amounts of PLA in DMF/DCM (50:50 v/v) to get the polymer weight concentration at 9% (w/w). TEBAC (0.5% w/w) was added to PLA solution for PLA/TEBAC solution. For the fabrication of the solution, PLA or PLA+TEBAC were added in DMF/DCM in a glass bottle with stirring magnetically overnight at room temperature.

With the same method, 5% w/w PEO in deionized water was stirred 24h prior to electrospinning. PEO/alginate solution was produced by adding 1% w/w alginate in PEO solution.

For the solutions dedicated to electrospraying, PCL14k solution of 5% in DMAC (w/w) was prepared by heating the solution at 60 °C during agitation 5 h before electrospraying. PCL80k solution was achieved through dissolving PCL80k in chloroform at 2% w/w concentration and stirred overnight.

Electrospinning process

A sketch of the experimental setup is shown in Fig. 4.1. The solutions are fed using a syringe pump (Fischer scientific) with a stainless steel needle in an inner diameter of 0.5 mm. The needle was electrically connected to the positive terminal of a high voltage DC power supply (Spellman SL10). The electrospun fibers are deposited on the conducting surface of a rotating collector having a diameter D = 12 cm, connected to the ground and rotating at 120 RPM. The distance between the needle and the surface of collector is maintained constant at 15 cm. The electrospinning voltage is kept constant at 25 kV and the flow rate at 1 ml/h. The single gap collector is made of two aluminum cylinders separated by an air gap centered below the needle emitter. The gap g can be continuously adjusted from 0 to 10mm.

To measure the surface potential, a non-contacting electrostatic voltmeter ESVM (Trek Model 347-3-H-CE) connected to a computer for data acquisition was used. The measurement is based on a field-nulling technique for non-contacting voltage measurement achieving direct current stability and high accuracy, with no need for fixed probe-to-surface spacing. The technique allows an accurate measurement of the surface potential of stationary or moving surfaces. The measurement range is 0 to ± 3 kV with accuracy of 0.1% of the full range. The probe of the voltmeter (end-view probe model 6000B-7C with a speed of response of 4.5 ms for 1 kV step) having a disc surface of 11.2 mm diameter was placed 2 mm below the surface of the collector as shown in Fig 4.1. An acquisition rate of 30 measurements/s was chosen.

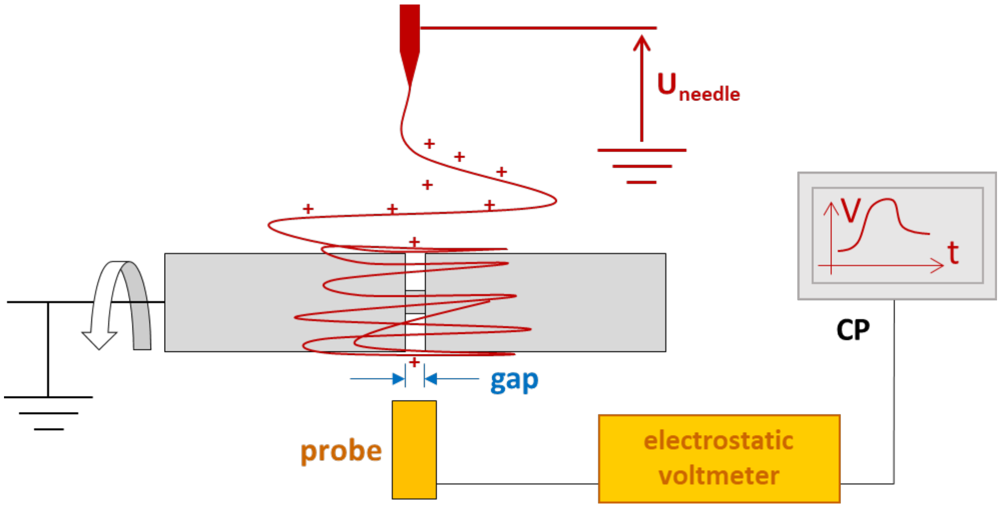

Fig. 4.1 sketch of the experimental setup for measuring the electrical voltage in electrospun jets

Calibration

Because the diameter of the sensor is larger than the gap, the voltage measured by the ESVM probe V_{probe} and the actual average voltage over the gap covered by suspended fibers V_{gap} are not identical. For this purpose, a model experiment was designed as shown in Fig. 4.2. A potential V_c was applied on two external aluminum plates having a width of 50 mm. In the central part, an aluminum plate having a width = gap was set to an imposed potential V_{gap}. The external plates were insulated from the central one by placing an insulating paper having a thickness of 70 µm. The voltage V_{probe} was measured as a function of various gap, V_c and V_{gap} values (see Table 4.1). And the following gap factor was calculated (see also Fig. 4.3):

$$f_g = \frac{V_{probe}-V_c}{V_{gap}-V_c} \tag{4.1}$$

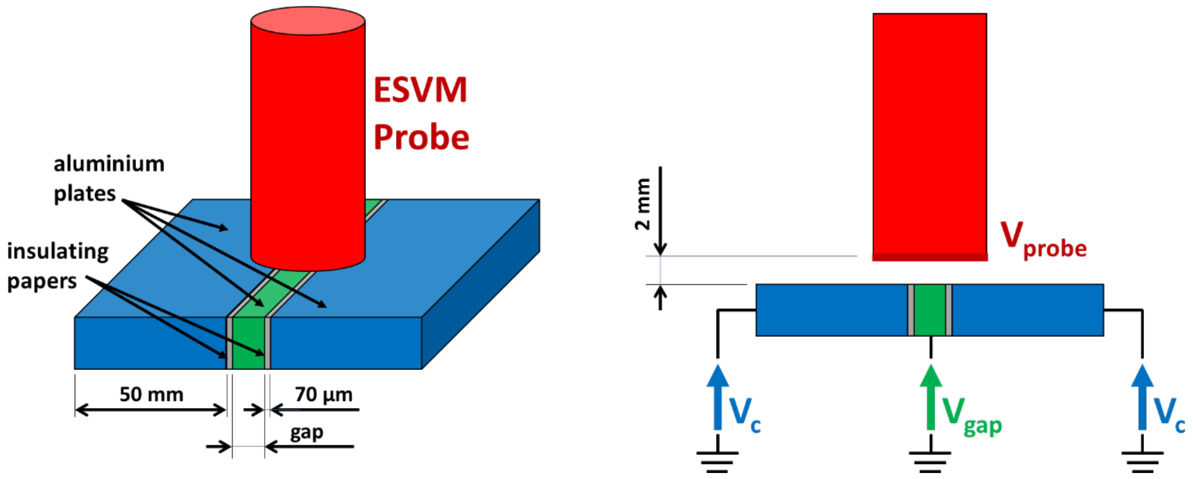

Fig. 4.2 Setup in order to find the relationship between the voltage measured by the ESVM probe $\boldsymbol{V_{probe}}$ and imposed voltages $\boldsymbol{V_c}$ and $\boldsymbol{V_{gap}}$ for various gap sizes.

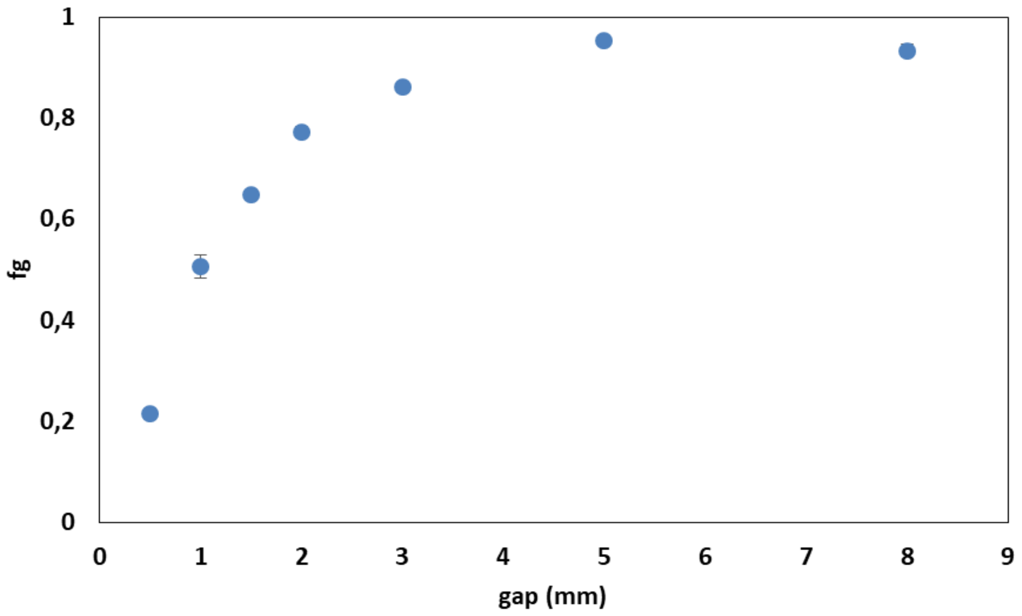

Fig. 4.3 Gap factor f_g as a function of the gap.

Tab. 4.1 all data of sensor test and the results of gap factor

L (mm)	V_c (V)	V_{gap} (V)	V_c (V)	V_{probe} (V)	Gap factor
0.5	0	20.2	0.02	4.53	0.22
0.5	0	15.2	0.03	3.25	0.21
0.5	0	10.5	-0.04	2.17	0.21
0.5	10.1	20.2	10.11	12.23	0.21
1	0	20.4	0.04	10.63	0.52
1	0	15.3	0.00	7.96	0.52
1	0	10.4	0.01	5.00	0.48
1	10.1	20.2	9.91	14.52	0.47
1.5	0	20.5	0.07	13.12	0.64
1.5	0	15.2	0.04	9.95	0.65
1.5	0	10.1	-0.04	6.54	0.65
2	0	20.3	-0.01	15.67	0.77
2	0	15.1	-0.05	11.86	0.79
2	0	10.4	0.05	7.94	0.76
3	0	20.3	0.01	17.69	0.87
3	0	15.3	0.02	13.31	0.87
3	0	10.5	0.01	9.13	0.87
3	10.2	20.6	10.02	18.98	0.86
3	5.0	10.1	4.97	9.31	0.85
3	12.2	24.5	11.94	22.56	0.86
5	0	20.3	0.09	19.49	0.96
5	0	15.0	-0.01	14.31	0.95
5	0	10.2	-0.04	9.60	0.95
8	0	20.1	0.01	18.91	0.94
8	0	15.3	-0.12	14.31	0.94
8	0	10.2	-0.12	9.26	0.92

Using eqn. 4.1, during an experiment of electrospinning (see Fig. 4.4), it is possible to calculate the local surface potential V_{gap} on suspended fibers over a gap:

$$V_{gap} = \frac{V_{p1} - V_{p2}}{f_g} + V_{p2} \tag{4.2}$$

Where V_{p1} is the surface potential measured over the gap, V_{p2} is surface potential measured over the fibers deposited on the flat part of the collector and V_{gap} is the estimated average surface potential over the suspended fibers and f_g is the gap factor taken from Fig. 4.3.

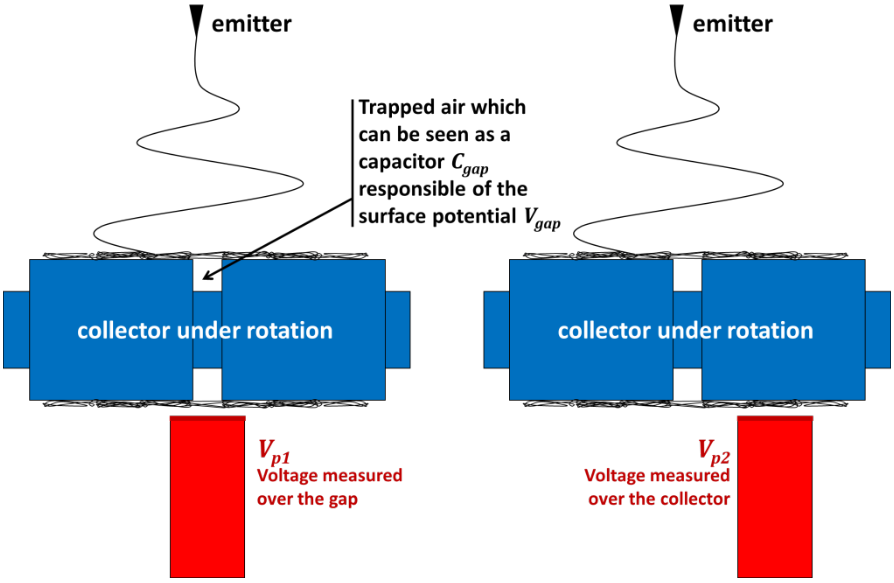

Fig. 4.4 Sketch of the experimental setup allowing the estimation of the average potential over the suspended fibers located over the gap. The scheme shows also that the surface potential is due to the presence of trapped air located between the grounded walls of the collector and the charged suspended fibrous layer. The trapped air can be seen as a capacitor $\boldsymbol{C_{gap}}$.

Characterization

Aiming to get the sample for SEM, an aluminum sheet (40mm × 25mm) with a rectangle hole (gap × 20mm) is used for collecting suspended fibers. Each side of the aluminum sheet is stick on the metal part of the collector and the rectangle hole is just placed above the gap with the longer edge of hole along the edge of gap. After finishing electrospinning, the aluminum sheet with suspended fibers over the rectangle hole is taken off from the collector. The samples are gold coated (sputter Quorum Q 150 RS, Quorum Technologies) for 2 min before SEM characterization (Vega-3, Tescan). In each sample, 5 points are chosen randomly on the suspended fibers during electrospinning for calculating the fibers density.

4.2.2 Evolution of the surface potential over PLA and PEO suspended fibers over a single gap during electrospinning

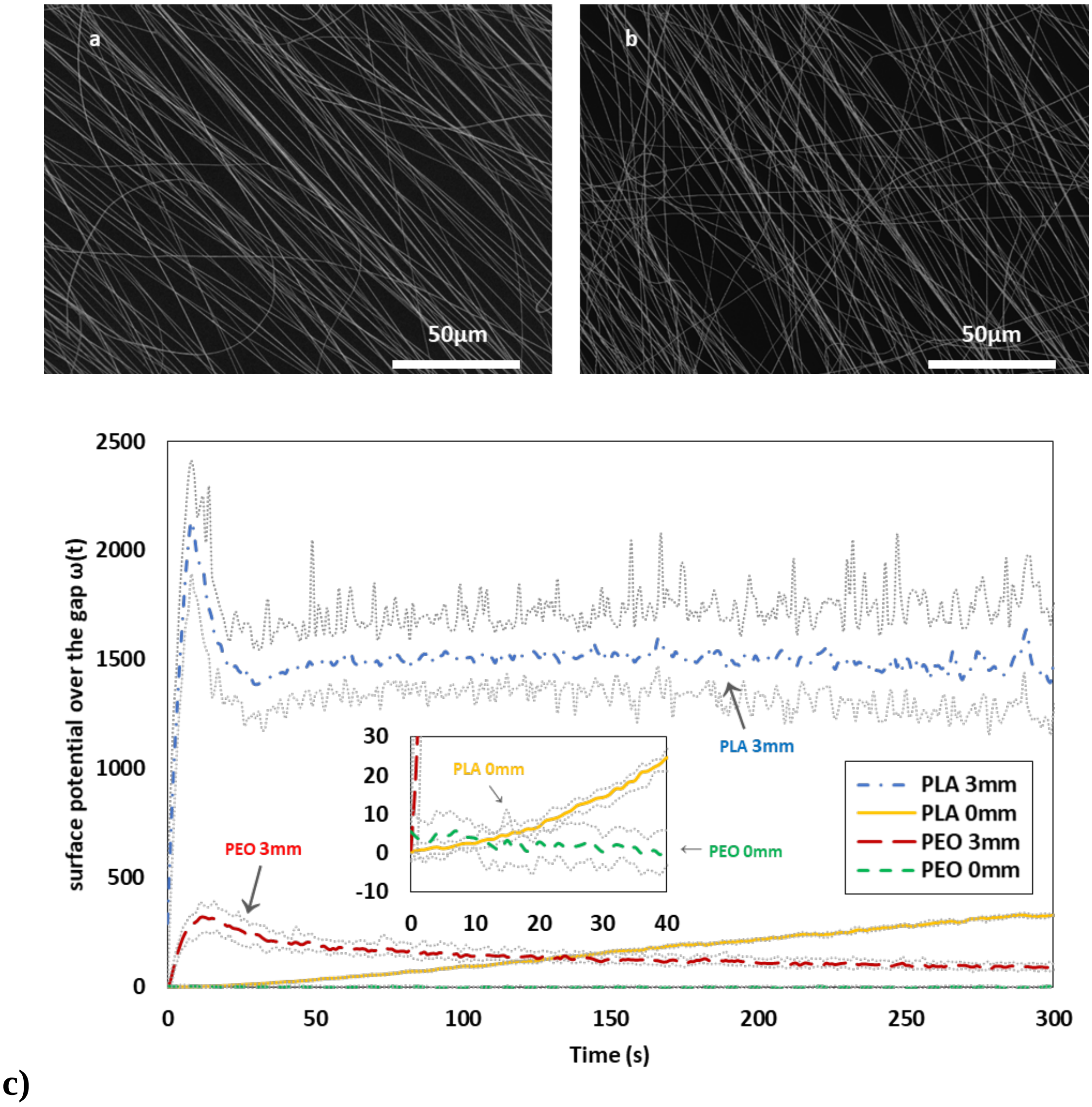

Fig. 4.5 a) SEM pictures of a) PLA and b) PEO fibers suspended over a gap of 3 mm. c) Surface potential obtained during electrospinning over a gap of 0 mm or 3 mm in the case of PLA in solution in DCM/DMF and PEO in solution in H_2O. The color dashed lines represent the average of the surface potential and the grey curves represent the envelop curves highlighting the maximum and minimum values measured during one experiment.

Fig. 4.5 shows the evolution of the surface potential of electrospun fibers either form PLA/DCM/DMF solution or PEO/H2O solution for gaps of 0 mm and 3 mm as well as SEM pictures of suspended PLA and PEO fibers over a gap of 3 mm. As expected, it is shown that fibers are mainly aligned perpendicularly to the gap [30] with a better alignment in the case of PLA fibers.

In the case of PLA fibers, a dramatic increase of the surface potential is observed immediately after switching on the power supply of the emitter. In less than 15 s the average surface potential reaches a peak at 2160 V. Then, the voltage decreases during around 20 s before reaching a plateau at 1500 V. From the peak it is shown that the surface potential fluctuates a lot with a disparity of around 400 V between the maximum and minimum. These fluctuations may be caused by uneven suspended fibers deposited over the gap inducing a nonuniform electric field. When the gap is set to 0 mm it corresponds to a simple electrospinning on a flat collector. In this case, as studied in the previous chapter, the voltage increases slowly reaching only 250 V after 300 s of electrospinning. Moreover, the fluctuations of the surface potential are very limited compared to what it is observed in the case of suspended fibers. Hence it proves that electrospun PLA fibers suspending over the gap hold electrical charges efficiently.

In the case of PEO fibers, the evolution of the surface potential can also be divided in three stages: (i) a sharp increase followed by (ii) a decrease and then (iii) a plateau regime. However, the kinetic is less sharp than what it is observed for PLA. Moreover, the surface potential values are around 7 times lower than for PLA. Such results show that suspended PEO fibers hold a much lower charge amount than PLA fibers formed in the same processing parameters. In addition, when the gap is set to 0 mm, the surface potential remains equal to 0 V indicating that charges transfer into the ground immediately when fibers fall on the collector, hence no significant charge accumulation occurs during the process of electrospinning. These results showing that PEO fibers cannot stored the charges efficiently which might be due to residual water remaining in the fibers.

4.2.3 Surface potential generated by suspended fibers over a single gap: a model

In order to get more insight into the kinetic of the surface potential generated during electrospinning over a gap is developed. A first model is proposed, it deals with the case of the deposition of non-interacting fiber strands. This model is adapted for the very first moment of electrospinning. Then, a second model is proposed allowing to take into account that the fiber strands interact with each other.

4.2.3.1 Non-interacting suspended fibers

Fig. 4.6a shows a sketch at time t when the N^{th} fiber strand is deposited. Furthermore, once a fiber strand is deposited, it immediately starts to release its charges. Indeed, a portion of fiber suspending over the gap has remained charges inducing a local surface potential, as shown in Fig. 4.6b. The distribution of potential along the strand allows the release of the charges from the central part to the edge of the collector. Because the fiber strands are not deposited at the same time, their charge amount is not the same. The air surrounded by the vertical walls of the collector and the charged fiber strand can be seen as a charged capacitor whereas the fiber strand allows the flowing of the charges as a bad conducting wire having its own resistance. Thus, a charged fiber strand located over an air gap can be considered as an RC circuit having a characteristic time $\tau = RC$.

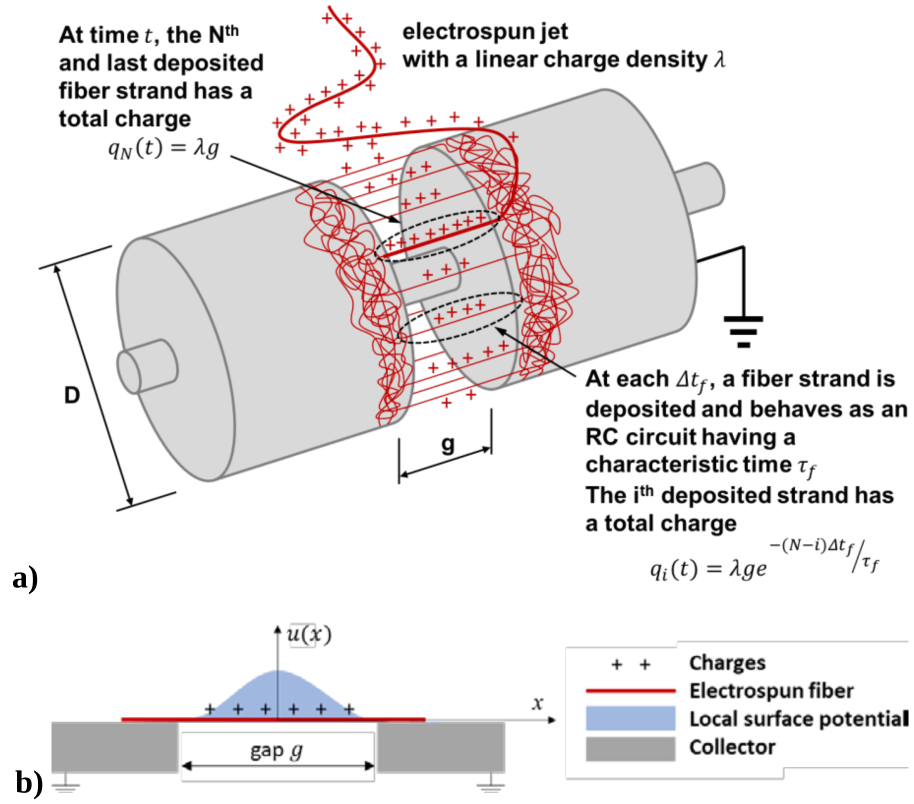

Fig. 4.6 a) Scheme showing the heterogeneous charge distribution during electrospinning on a cylindrical collector with a single gap. At time t, the last deposited fiber strand has the highest linear charge density corresponding to the linear charge of the jet just before its landing. b) Local surface potential induced by a charged suspended fiber strand.

Once deposited, the fiber strand immediately starts to release the charges as:

$$q_i(t) = q_0 e^{-(t-t_i)/\tau} \tag{4.3}$$

Where t_i is time when the i^{th} fiber strand is deposited on the collector and q_0 is the initial charge carried by the fiber strand:

$$q_0 = \lambda g \tag{4.4}$$

Where λ is the linear charge density of the electrospun jet just before hitting the collector and g is the gap size. If one strand is deposited each Δt, then:

$$q_i(t) = q_0 e^{-(N-i)\Delta t/\tau} \tag{4.5}$$

Therefore, the total amount of charges $Q(t)$ induced by N strands is:

$$Q(t) = \sum_{i=1}^{N} q_i = \sum_{i=1}^{N} \lambda g e^{-(N-i)\Delta t/\tau} = \lambda g \sum_{j=0}^{N-1} e^{-j\Delta t/\tau} \tag{4.7}$$

The average surface charge density $\bar{\sigma}(t) = Q(t)/\pi D g$ is then:

$$\bar{\sigma}(t) = \frac{\lambda}{\pi D}\sum_{j=0}^{N-1} e^{-j\Delta t/\tau} = \frac{\lambda}{\pi D}\frac{1-e^{-N\Delta t/\tau}}{1-e^{-\Delta t/\tau}} \tag{4.8}$$

Because $t = N\Delta t$ and that $\Delta t \ll \tau$, one obtains the average surface charge density as a function of time:

$$\bar{\sigma}(t) = \frac{\lambda}{\pi D}\frac{\tau}{\Delta t}\left(1 - e^{-t/\tau}\right) \tag{4.9}$$

The air trapped between the walls of the collector and the charged fibrous surface behaves as a capacitor of permittivity ε_0 (see Fig. 4.4). By numerical simulation using the finite element methods it was possible to get the relationship between the average surface potential $\bar{V}_{gap}(t)$ over the fibrous surface of suspended fibers and $\bar{\sigma}(t)$:

$$\bar{V}_{gap}(t) = k\frac{g}{\varepsilon_0}\bar{\sigma}(t) \tag{4.10}$$

Where k is a form factor which was determined by the finite element method using COMSOL software: $k \approx 0{,}15$. The trapped air can thus be seen as a capacitor C_{gap} having a capacitance such as $Q = \pi D g \bar{\sigma}(t) = C_{gap}\bar{V}_{gap}$:

$$C_{gap} = \frac{\pi D \varepsilon_0}{k} \tag{4.11}$$

If one introduces the density of deposited fiber strands $\rho_L(t)$ as the ratio between the total length of deposited fiber strands $L(t)$ and the surface of the gap $\pi D g$:

$$\rho_L(t) = \frac{L(t)}{\pi D g} \tag{4.12}$$

Knowing that the number N of fiber strands at time t is:

$$N = \frac{L(t)}{g} = \rho_L(t)\pi D \tag{4.13}$$

It leads:

$$\frac{1}{\Delta t} = \frac{d\rho_L}{dt}\pi D = \dot{\rho}_L \pi D \tag{4.14}$$

$\rho_L(t)$ can be estimated by SEM measurements stopping the process at various times and measuring the length of fiber on a SEM picture of surface S_{SEM}. Such experiment was done for PLA and PEO as well (see Fig. 4.7), they showed that $\dot{\rho}_L$ can be considered as constant. It should be noticed that from eqn. 4.12:

$$\dot{\rho}_L = \frac{d\rho_L}{dt} = \frac{1}{\pi D g}\frac{dL(t)}{dt} = \frac{\alpha v_f}{\pi D g} \tag{4.15}$$

Where v_f is the electrospun fiber velocity and $\alpha < 1$ is the fraction of fiber length which is deposited on the gap. Using eqn. 4.14 and 4.15, one can verify that the time increment Δt is:

$$\Delta t = \frac{1}{\dot{\rho}_L \pi D} = \frac{g}{\alpha v_f} \tag{4.16}$$

The second expression of Δt in eqn. 4.16 is less convenient because it seems that Δt depends on g. However, it is not the case. Indeed, it is worth noting that Δt is not the time it takes to deposit the fibrous strand but it is the time it takes to deposit two successive fiber strands. In fact, α is proportional to g.

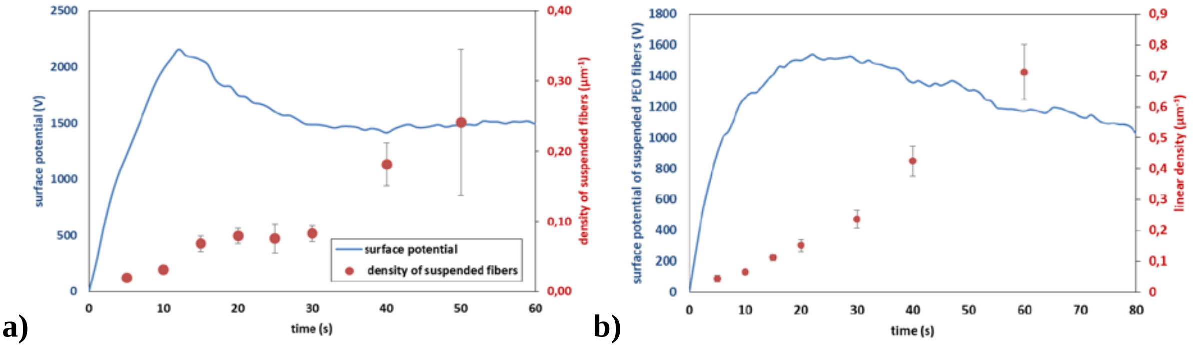

Fig. 4.7 Surface potential and density of deposited fiber strands $\rho_L(t)$ as a function of time for a) PLA with a gap g = 3 mm and b) PEO with a gap g = 7 mm.

Thus, using eqn. 4.9, 4.10 and 4.14, one obtains the average surface potential over the gap:

$$\bar{V}_{gap}(t) = \lambda \dot{\rho}_L k \frac{g}{\varepsilon_0} \tau \left(1 - e^{-t/\tau}\right) \tag{4.17}$$

Using eqn. 4.15, the surface potential over the suspended fibers can also be written as:

$$\bar{V}_{gap}(t) = \lambda \alpha v_f \frac{k}{\pi D \varepsilon_0} \tau \left(1 - e^{-t/\tau}\right) \tag{4.18}$$

When $t \ll \tau$:

$$\bar{V}_{gap}(t \ll \tau) \approx \lambda \dot{\rho}_L k \frac{g}{\varepsilon_0} t \tag{4.19}$$

Equation 4.19 shows that, at the beginning of electrospinning, the surface potential evolves linearly with time which is obvious because each deposited fiber strand brings its own charges which does not have the time to release the charges when $t \ll \tau$.

When $t \gg \tau$:

$$\bar{V}_{gap}(t \gg \tau) \approx \bar{V}_{\infty} = \lambda \dot{\rho}_L k \frac{g}{\varepsilon_0} \tau \tag{4.20}$$

Using eqn. 4.19, an estimation of the linear charge density λ can be done:

With:

g = 3 mm, ε_0 = 8,85 10^{-12} $m^{-3}kg^{-1}s^4A^2$, k = 0,15

$$\dot{\rho}_L = 4166\ \mathrm{m^{-1}s^{-1}} \text{ and } \frac{d\bar{V}_{gap}}{dt} = 250\ \mathrm{Vs^{-1}}$$

One obtains:

$$\lambda = \frac{\varepsilon_0}{\dot{\rho}_L kg}\frac{d\bar{V}_{gap}}{dt} \approx 1{,}2\ 10^{-9}\ \mathrm{Cm^{-1}}$$

Using eqn. 4.20, an estimation of the characteristic time is then possible by taking $\bar{V}_\infty$ = 1422 V:

$$\tau = \frac{\bar{V}_\infty \varepsilon_0}{\lambda \dot{\rho}_L kg} \approx 5{,}6\ \mathrm{s}$$

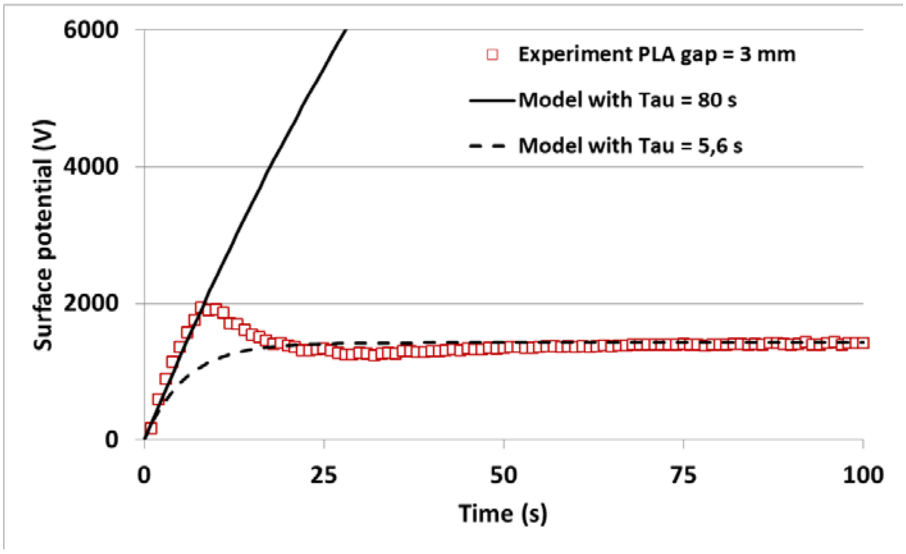

Fig. 4.8 Surface potential of suspended PLA fiber strands with a gap of 3 mm. Experimental points (red squares), model from eqn 4.17 with τ = 80 s (solid black line) model from eqn 4.17 with τ = 5,6 s (dashed black line).

From Fig. 4.8 it is shown that with τ = 5,6 s the model cannot fit the first and the second stage of the experimental curve. If we try to fit the first stage, a much greater τ value must be considered (τ = 80 s), but in this case $\bar{V}_\infty \approx 20$ kV! Thus, it appears that τ must be high at the first time of the deposition and must decrease. For this purpose, another model is proposed.

4.2.3.2 Interacting suspended fibers

A close view shows that the suspended fiber strands are touching together forming thus closed loops equivalent to resistor-capacitor circuits of resistance R_{loop} and capacitance C_{loop}. The thin deposited layer of fiber strands can be seen as the association of a large number of RC circuits having an equivalent resistance $R(t)$ and a capacitance C_{gap}. Because $R(t)$ characterizes the fibrous layer, it varies during electrospinning due to the fiber densification. However, as already mentioned, C_{gap} characterizes the capacitance of the trapped air between the walls of the collector and the suspended fibrous layer (see Fig. 4.4), it is thus a constant during the time of electrospinning. The characteristic time of the charged suspended fibrous layer is:

$$\tau(t) = R(t)C_{gap} \tag{4.21}$$

Using eqn. 4.11, the characteristic time can be written as:

$$\tau(t) = \frac{\pi D \varepsilon_0}{k} R(t) \tag{4.22}$$

The amount of charges deposited over the gap per unit time is the fraction α of total current i_{jet} coming from the jet, α being the same as introduced for eqn. 4.16:

$$i = \alpha i_{jet} = \alpha \lambda v_f \tag{4.23}$$

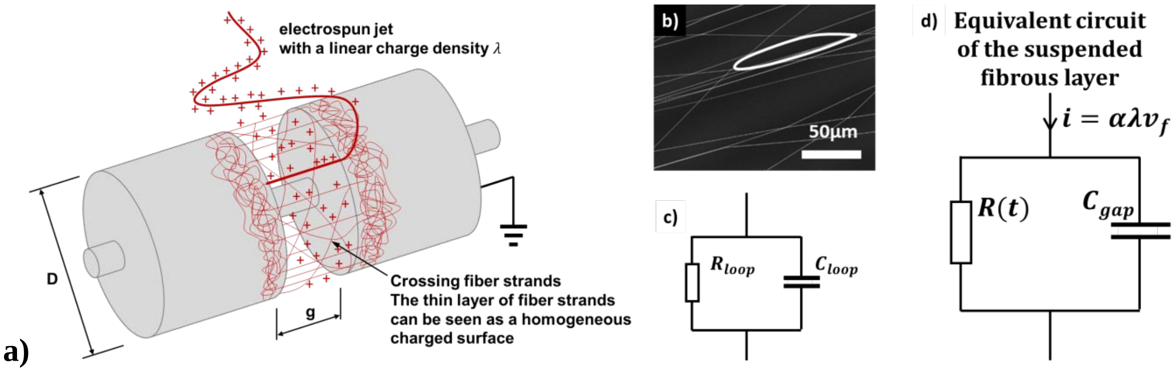

Fig. 4.9 a) Sketch at time when fiber strand is deposited over the gap. b) SEM showing crossing fibers forming loops. c) Each loop can be seen as a short RC circuit. d) Equivalent circuit of the thin suspended fibrous layer.

Thus, the differential equation characterizing the behavior of the equivalent RC circuit of suspended fibrous layer is obviously the following:

$$\frac{d}{dt}\left(\bar{V}_{gap}\right) + \frac{1}{\tau(t)}\bar{V}_{gap} = \frac{i}{C_{gap}} \tag{4.24}$$

Eqn. 4.24 cannot be solved directly due to the characteristic time is not a constant. The form of the function $\tau(t)$ must be proposed in order to solve eqn. 4.24. First, we will discuss the case for which $\tau(t)$ is a constant τ. In this case, the solution of eqn. 4.24 is obvious:

$$\bar{V}_{gap}(t) = \frac{i}{C_{gap}}\tau\left(1 - e^{-t/\tau}\right) \tag{4.25}$$

In this simple case, using eqn. 4.11 and 4.23, it can be seen that the average surface potential was already given by eqn. 4.18. In fact, this result is consistent. Indeed, in the previous section dealing with non-interacting fiber strands we calculated the average surface charge density $\bar{\sigma}(t)$ in eqn. 4.8. Such average means that in fact one assumes that the suspended fibrous layer is homogeneous.

$$\bar{V}_{gap}(t) = \frac{ik}{\pi D\varepsilon_0}\tau\left(1 - e^{-t/\tau}\right) \tag{4.26}$$

It was thus shown that eqn. 4.25 is not able to model the kinetic of $\bar{V}_{gap}(t)$, the characteristic time must vary during time. Thus, we propose the following empiric equation:

$$\tau(t) = \tau_\infty + \frac{(\tau_0 - \tau_\infty)^2}{|\tau_0'|t + \tau_0 - \tau_\infty} \tag{4.27}$$

Where $\tau_0 = \tau(t = 0)$, τ_∞ is the asymptote of $\tau(t)$ and $|\tau_0'|$ is the absolute value of the initial slope (see also Fig. 4.10).

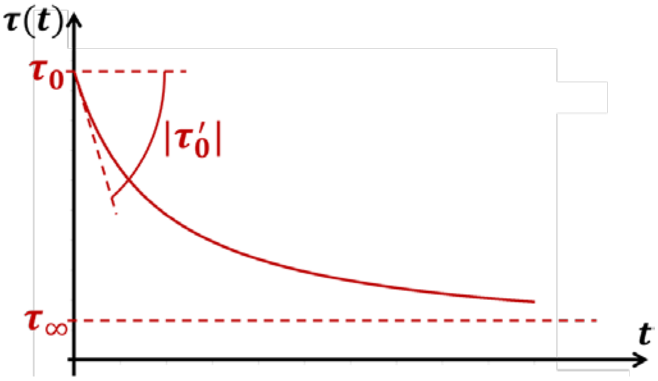

Fig. 4.10 Proposed behavior of the characteristic time versus time.

Using eqn. 4.27, it is possible to solve the differential equation 4.24. After integration and imposing the initial condition, the complete solution is:

$$\bar{V}_{gap}(t) = K(t)G(t) \tag{4.28}$$

$$G(t) = \left[\tau_\infty|\tau_0'|t + \tau_0(\tau_0 - \tau_\infty)\right]^\gamma e^{-t/\tau_\infty} \tag{4.29}$$

$$K(t) = \frac{i}{C_{gap}} \int_0^t [\tau_\infty |\tau_0'| t + \tau_0(\tau_0 - \tau_\infty)]^{-\gamma} e^{t/\tau_\infty} dt \tag{4.30}$$

$$\gamma = \frac{(\tau_0 - \tau_\infty)^2}{\tau_\infty^2 |\tau_0'|} \tag{4.31}$$

The integration of 4.30 must be evaluated numerically using for example a Simpson method. In order to avoid any numerical divergence when exponent γ is high, $G(t)$ is put inside the integral of $K(t)$.

4.2.4 Surface potential of suspended fibers made of various polymers

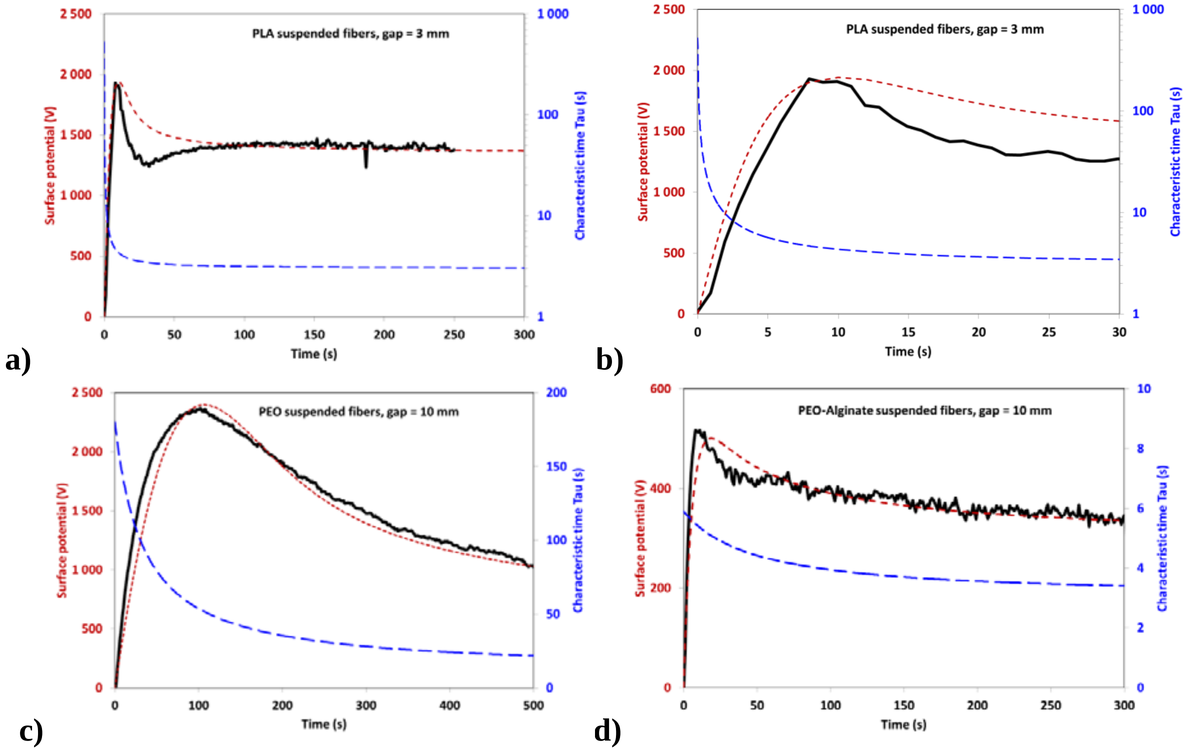

Fig. 4.11 Surface potential (black solid lines: experimental result, red dashed lines: model from eqn. 4.28) and the characteristic time $\tau(t)$ (blue dashed line) as a function of time. a and b) PLA gap = 3 mm. c) PEO, gap = 10 mm. d) PEO-alginate gap = 10 mm.

Table 4.2: Parameters of $\tau(t)$ obtained for the fitting

	PLA	PEO	PEO-Alginate
τ_0 (s)	520	180	5,9
τ_∞ (s)	3	11	3
$\lvert\tau_0'\rvert$ (s/s)	20000	5	0,06

Fig. 4.11 shows the evolution of the surface potential measured for various polymer systems and the model curves obtained after adjusting the parameters τ_0, τ_∞ and $|\tau'_0|$ allowing the best matching (see also Table 4.2). It is shown that each polymer has its own specific behavior. Fig. 4.11 shows that all three curves are modeled precisely by eqn. 4.28. In Table 4.2, τ_0 holds a dramatically high value of 520s in the condition of PLA fibers which is remarkably larger than those of PEO fibers (τ_0 = 180s) and PEO/Alginate (τ_0 = 5.9s). As mentioned in eqn. 4.21, the characteristic time is related to the intensity of the capacitance of the trapped air C_{gap} and the equivalent resistance $R(t)$. Because C_{gap} is no related to the polymer properties, the variation of τ_0 is due to the change of $R(t)$ which is related with the kind of polymer, the possible content of residual solvents used in electrospinning and the quality of the fiber-fiber contact points. In the case of PEO/Alginate fibers, besides water used for the solvent, because alginate is a polyanion, it improves the conductivity of the fibers efficiently. Thus $R(t)$ is remarkably low resulting in a very small τ_0 of 5.9s. Compared with PEO/Alginate fibers, pure PEO system has a higher $R(t)$ resulting in an increase of τ_0 to 180s. In the case of PLA, the used solvents (DCM and DMF) have very lower conductivities than water. Thus $R(t)$ increases significantly to enhance τ_0 to 520s for PLA fibers.

All three cases hold a low τ_∞ attributed to more intersections occurring among suspended fibers with the extend of electrospinning duration. Thus, the size of loops formed by crosslinked fibers decreases gradually resulting in the decline of $R(t)$. However, for long time of electrospinning, the size of the loops reaches a critical value related to the fiber diameter [31] leading to a constant $R(t)$. Therefore, τ_∞ reaches a low and stable value.

Regarding $|\tau'_0|$, it reflects the decrease of τ at the beginning of electrospinning. Taking PEO/Alginate fibers as the example, the low $R(t)$ induces almost no change in $\tau(t)$. Meanwhile, highly conducting fibers can transfer charges from suspended fibers to the grounded collector instantaneously. Moreover, the deposited fiber having a high conductivity can remove the uneven electric field above the patterned collector fleetly. Thus, PEO/Alginate fibers can fall over the gap randomly meaning that the change of size of loops formed by crosslinked fibers hold poor impact on $R(t)$. Hence, there is almost no change of $|\tau'_0|$ for PEO/Alginate fibers. Regarding PEO fibers, $|\tau'_0|$ is higher than for PEO/Alginate but still low, which is attributed to water as the solvent holding a high conductivity which deceases $R(t)$. However, PLA fibers presents a dramatically high $|\tau'_0|$. Due to PLA fibers having a relatively high resistivity, the local resistance value of the loop induced by crosslinked fibers can decrease significantly regarding the charge release mechanism impacting the suspended fibers. Thus, R(t) may decline dramatically and very rapidly characterized by a high $|\tau_0'|$ value.

4.2.5 Effect of the gap size on the surface potential

4.2.5.1 Effect of the gap in the case of PLA

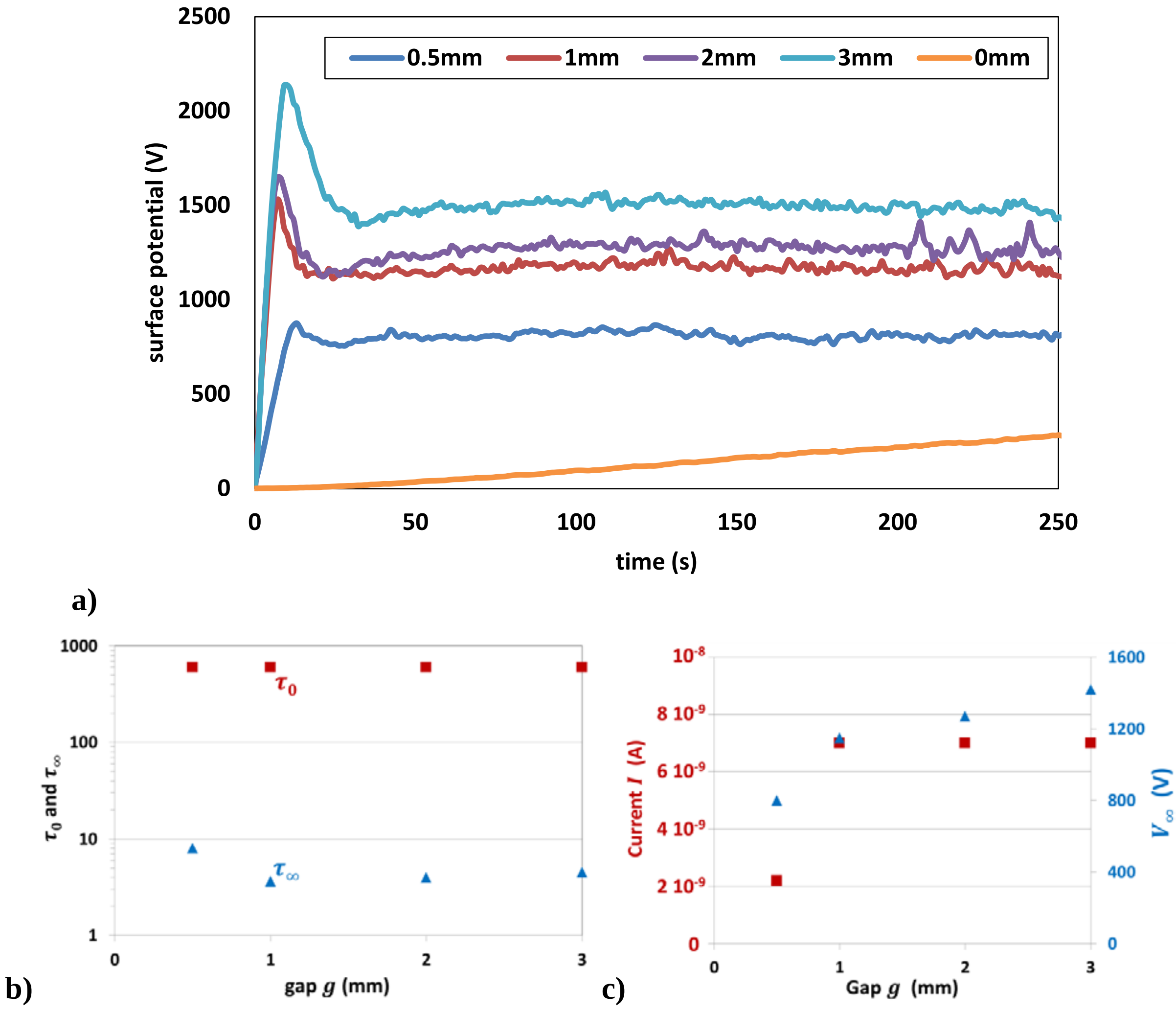

Fig. 4.12 a) Surface potential in the case of PLA for various gaps. b) τ_0 (red squares) and τ_∞ (blue triangles) as a function of the gap. c) Current I (red squares) and potential V_∞ (blue triangles) as a function of the gap.

Fig. 4.12a shows the evolution of the surface potential as a function of the gap size for PLA fibers. The gap size was set at 0mm, 0.5mm, 1mm and 2mm and 3mm respectively. For larger gaps, the surface potential was too high to be measured by the voltmeter. Whatever the gap value, the surface potential can be divided in three distinct stages.

Regarding the first stage, the slope increases sharply with the size of gap. From the model it is seen that at the very beginning of the electrospinning, when $t \ll \tau$, the surface potential should scales as $\lambda \dot{\rho}_L k \frac{g}{\varepsilon_0} t = \frac{i}{C_{gap}} t$ (see eqn. 4.19). However, surprisingly as shown in Fig. 4.12c, this behavior is not verified as the current i is almost constant with the gap. A decrease was only observed in the case of the smallest gap of 0.5mm.

In the second stage, the surface potential decreases sharply. The decrease of the surface potential is explained by the f act that the characteristic time decreases as a function of time. However, it is observed that the gap has no significant effect on τ_0 and τ_∞ (see Fig. 4.12b) meaning that the kinetic of the surface potential is not affected in the second stage and the third stage.

The third stage is reached very rapidly after only 30s. Larger the gap, larger the time it takes to reach the surface potential plateau. However, the prediction of the model is not verified as $\bar{V}_\infty = \lambda \dot{\rho}_L k \frac{g}{\varepsilon_0} \tau_\infty$ should increases linearly with the gap (see Fig. 4.12c) while the increase is lowered for the largest gap sizes. This effect may be due to rapid charge release in the air from the charges located at the topmost surface of the suspended fibrous layer.

In general, the fact that PLA does not behaves perfectly as predicted by the model suggests that charge release or neutralization may occur significantly with the fibers located at the topmost surface.

4.2.5.2 Effect of the gap in the case of PEO

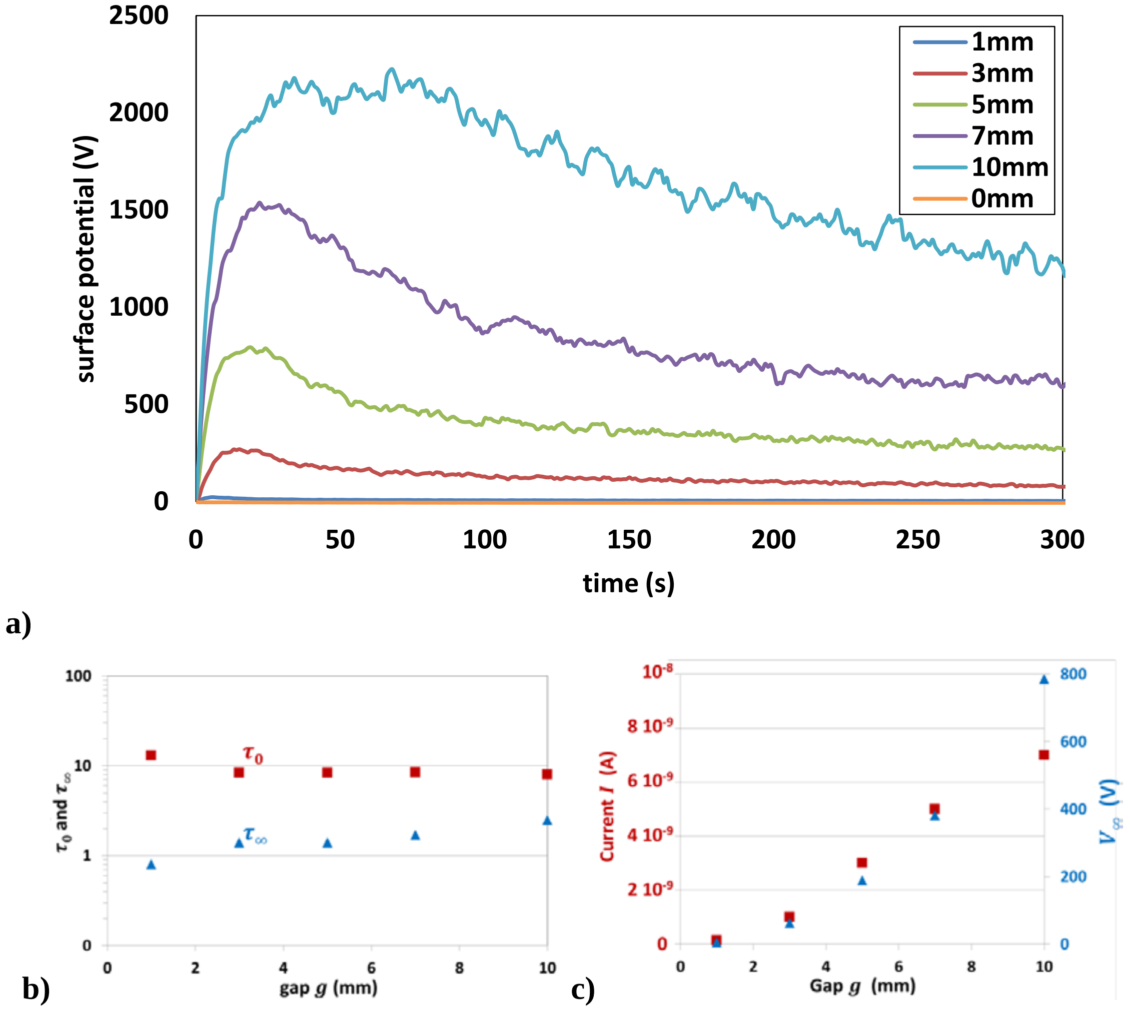

Fig. 4.13 a) Surface potential in the case of PEO for various gaps. b) τ_0 (red squares) and τ_∞ (blue triangles) as a function of the gap. c) Current I (red squares) and potential V_∞ (blue triangles) as a function of the gap.

Fig. 4.13a shows the evolution of the surface potential as a function of the gap size for PEO fibers. The gap size was set at 1mm, 3mm and 5mm, 7mm and 10mm respectively. Whatever the gap value, the surface potential can be divided in three stages but with smoother variations as what it is observed for PLA.

Regarding the first stage, the slope increases with the size of gap. From the model it is seen that at the very beginning of the electrospinning, when $t \ll \tau$, the surface potential scales as $\lambda \dot{\rho}_L k \frac{g}{\varepsilon_0} t = \frac{i}{C_{gap}} t$ (see eqn. 4.19). This behavior is well verified as the current i

increases linearly with the gap as shown in Fig. 4.13c. Thus, larger the gap, larger the current, assuming that in the studied range of gaps $\dot{\rho}_L$ is constant. This may be explained by the fact that larger gap provides a larger surface and thus more charges affecting the capacitor C_{gap} formed by the air trapped between the collector walls and the suspended charged fibrous layer.

The second stage is very smooth compared to what it is observed for PLA. The decrease of the surface potential is explained by the fact that the characteristic time decreases as a function of time. However, it is observed that the gap has no significant effect on τ_0 and τ_∞ (see Fig. 4.13b) meaning that the kinetic of the surface potential is not affected in the second stage and the third stage. It should be noticed that the characteristic times τ_0 and τ_∞ obtained in this case are much shorter than the ones obtained for the experiment carried out in the previous section (reported values in Table 4.2). In this series of experiments, the current was more than 7 times larger than in the previous section due to probably different conditions in relative humidity.

The third stage is reached at very long times. Larger the gap, larger the time it takes to reach the surface potential plateau. The prediction of the model is well verified as $\bar{V}_\infty = \lambda \dot{\rho}_L k \frac{g}{\varepsilon_0} \tau_\infty$ increases linearly with the gap (see Fig. 4.13c).

As opposed to PLA, the model can predict the behavior of PEO fibers with a very good accuracy. Thus, the main charge exchanges occur inside the fibrous mesh formed by the suspended fibers. Charge transfer in the air seems to be negligible in this case.

4.2.6 Effect of the duration of electrospinning on the kinetic of the surface potential decay of suspended PLA and PEO fibers

The kinetic of the surface potential decay is of prime importance when the process needs to keep the electrostatic template effect for long times. Thus, we studied this kinetic and how it is affected by duration of electrospinning that precedes the surface potential decay. This study was carried out for PLA and PEO fibers as well.

4.2.6.1 PLA fibers

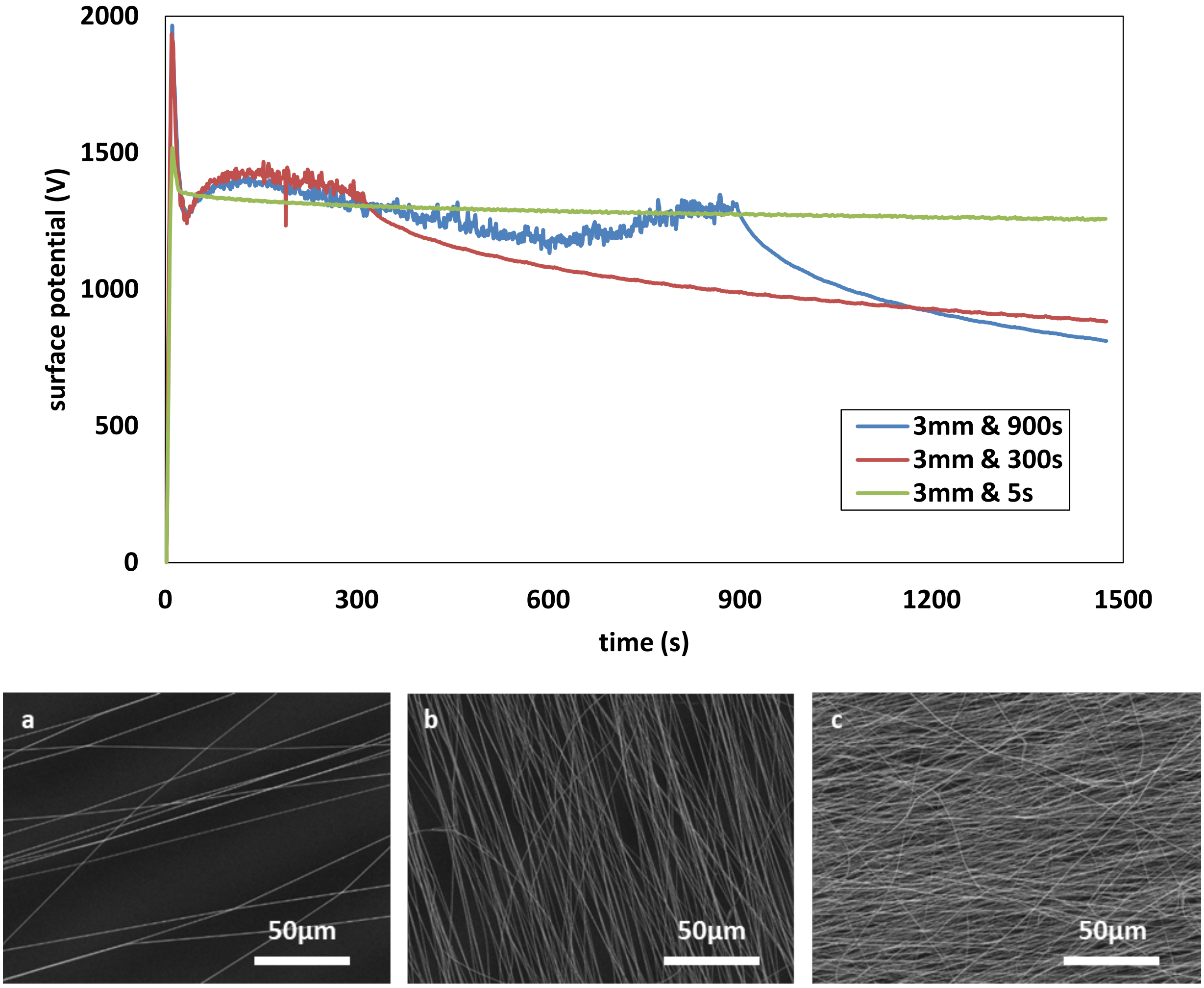

Fig. 4.14 Voltage curves and morphologies of suspended PLA fibers for a gap g = 3 mm and different duration t_{spin} of electrospinning. a) t_{spin} = 5 s. b) t_{spin} = 300 s. c) t_{spin} = 900 s

Fig. 4.14 presents the relationship between the number of suspended PLA fibers and the surface potential decay when the process of electrospinning is shut down after a time t_{spin}. We can see that the initial surface potentials are almost the same at moment of shutting down the power supply of the electrospinning emitter. As previously discussed, a sharp increase of the surface potential is observed during the first stage of electrospinning. In the case of t_{spin} = 5s, the electrospinning is stopped at the very beginning of the process, when only few suspended fibers cover the gap of the collector. In this case, the voltage stays constant over the gap and no charge dissipation is thus observed after t_{spin}. For longer time of electrospinning t_{spin} (ie. 300 and 900 s), a decrease of the voltage is observed with a more rapid decrease for the largest t_{spin}. It proves that the kinetic of charge dissipation has a direct correlation with the duration of electrospinning preceding the free charge release. As discussed in the previous chapter, several mechanisms of charge release can explain the surface potential decay. First, charges located at the topmost surface of the mat are subjected to ion neutralization with air. This charge release phenomenon may occur at short times. Second, charges mostly located at the surface of the fibers, but inside the porosity of the mat, should release their charges within each pore having already participated to the kinetic of in-situ charging by electrospinning. It is thus expected that this second characteristic time of decay is in the same order than the characteristic time τ estimated during electrospinning. Third, in-situ electrospinning may lead the production of charges efficiently trapped in the bulk of the fibers. This charge release phenomenon may occur at long times.

To characterize the difference in the charge dissipation rate obtained in the three conditions, a double exponential function is introduced to fit the results:

$$V(t) = V_{\infty} + A_s e^{-\left(\frac{t-t_{spin}}{\tau_s}\right)} + A_l e^{-\left(\frac{t-t_{spin}}{\tau_l}\right)} \tag{4.32}$$

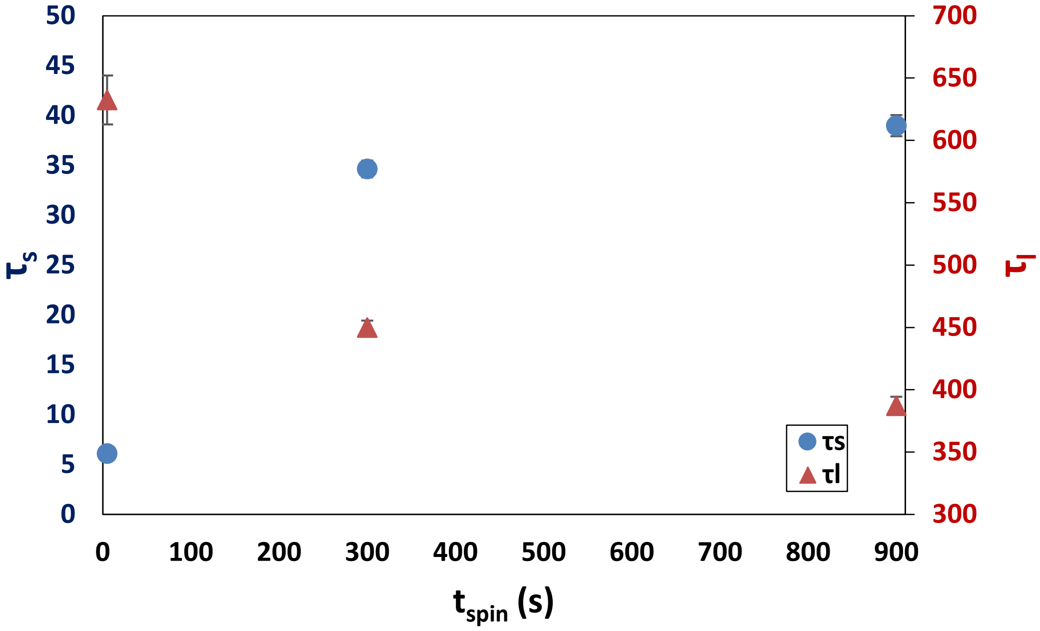

Fig. 4.15 Short τ_s and long τ_l characteristic times of the surface potential decay of suspended PLA fibers for a gap g = 3 mm and for different electrospinning times t_{spin}

Fig. 4.15 shows that the kinetic of the surface potential decay follows a double exponential decay with distinct times, i.e. τ_s and τ_l are significantly different (τ_l being 10 to 100 times larger than τ_s). Furthermore, it is worth noting that the characteristic time determined during electrospinning corresponds approximatively to the values of τ_s. The mechanism of charge release characterized by τ_l at long times does not occur during electrospinning or only at the very first time of electrospinning as a high τ_0 (see Table 4.2 and Fig. 4.12b) was necessary to fit the experimental data. In the process of surface potential decay, τ_s holds an increasing trend with extending the process time of electrospinning, implying that the surface charges dissipate much faster on fibers fabricated in a shorter time, which may be caused by more contact area between fibers and air to accelerate the release of charges. Due to more suspended fibers formed over the gap when electrospinning was carried out during 300s and 900s, up-layer fibers cover down-layer fibers may restrict the dissipation of surface charges from down-layer fibers resulting in the low release rate of surface charges. In addition, more suspended fibers in the condition of longer electrospinning time means higher density of charges around fibers in air which restrict surface charges to release to the around efficiently. Hence fibers prepared in 5s take an extremely short time to dissipate surface charges.

Regarding the long-time decay kinetic characterized by τ_l, a decrease with the duration of electrospinning time is observed which proves that the dissipation rate of charges is directly linked with the amounts of suspended fibers. Indeed, suspended fibers in a larger density induce more overlaps among fibers which is the decisive factor affecting the dissipation rate. Because for longer time of electrospinning more fibers are produced and thus also more bulk charges are produced, it is expected that bulk charge release should increases with t_{spin}. The fact that τ_l decreases with increasing t_{spin} proves that the surface potential decay is not due to the release of bulk charges. The kinetic characterized by τ_l is more linked with the fibrous structure of the suspended layer characterized by its resistance $R(t)$ as previously introduced in the model. As also mentioned before, the capacitance C_{gap} is linked with the geometry of the collector and especially the gap size. Nevertheless, the difference between τ_l and the characteristic time $\tau = R(t)C_{gap}$ determined during electrospinning just before shutting down the power supply remains an open question. The effect of the presence of the electrospun jet during electrospinning may also change the air property and could create ions favoring the discharge during electrospinning. When stopping electrospinning, the air is no longer affected by the electrospun jet resulting in a different kinetic.

4.2.6.2 PEO fibers

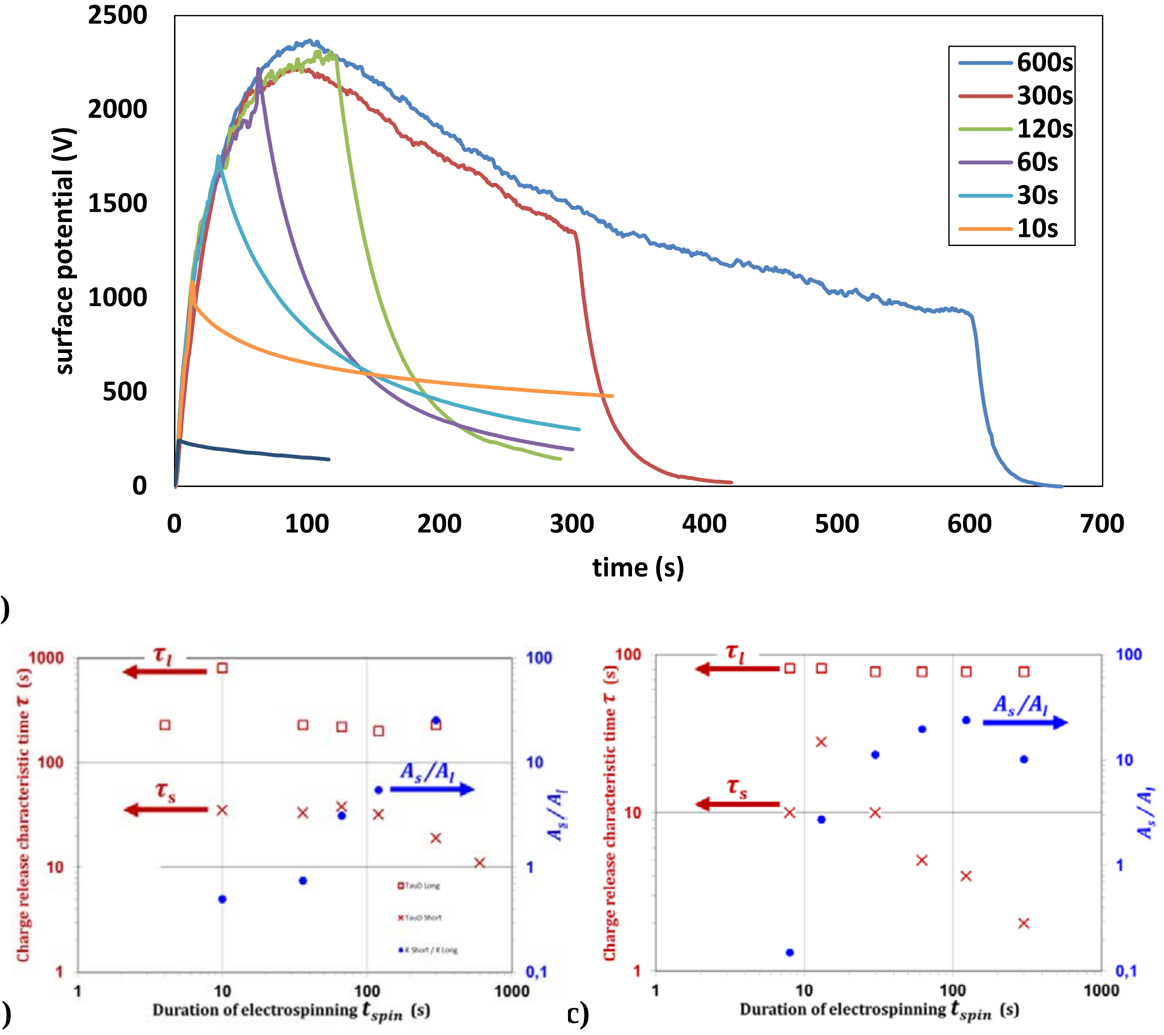

Fig. 4.16 a) Surface potential measured in the case of PEO for a gap $g = 10\ mm$ for various duration of electrospinning t_{spin}. τ_s (red squares), τ_l (red cross) and A_s/A_l (blue discus) for various duration of electrospinning t_{spin} in the case of b) $g = 10\ mm$ and c) $g = 7\ mm$

The duration of electrospinning on the surface potential decay after shutting down the power supply was also studied in the case of PEO fibers (Fig. 4.16). Here, two series of experiments were carried out: with a gap of 10 mm and with a gap of 7 mm. The conditions of electrospinning were similar with that used in section 4.2.4 (Fig. 4.11 and Table 4.2). Furthermore, it should be noticed that the series of experiments at gap = 7mm were carried out several months after series carried out at gap = 10 mm. Both experiments show the same trend (Fig. 4.16b-c). Compared with the surface potential decay of PLA fibers, PEO fibers present a much faster kinetic. In the case of PEO, the following equation was used to fit the experimental data:

$$V(t) = A_s e^{-\left(\frac{t-t_{spin}}{\tau_s}\right)} + A_l e^{-\left(\frac{t-t_{spin}}{\tau_l}\right)} \tag{4.33}$$

As opposed to PLA, the short time decreases with the duration of electrospinning t_{spin}. Furthermore, the long characteristic time τ_l is in the same order of magnitude than τ_0=180s measured during electrospinning for gap =10mm. The decay kinetic is faster for larger t_{spin} as the ratio of A_s/A_l, characterizing the impact of the short time kinetic, increases with t_{spin}. This result is in agreement with the fact that $\tau = R(t)C_{gap}$ estimated during electrospinning decreases with t_{spin}. For the shortest times of electrospinning, before reaching the maximum of the surface potential ($t_{spin} < 100\ s$), the surface potential is retained for much longer times. This can be explained by the fact that before 100 s of electrospinning there is a low number of crossing suspended fibers allowing keeping the resistance of the fibrous suspended layer $R(t)$ at a high level leading to larger characteristic time $\tau = R(t)C_{gap}$. For the longest times of electrospinning a good agreement is also observed between τ_∞ and τ_s proving the fast kinetic during surface potential decay as well as during electrospinning.

4.2.7 Conclusion

This section presents a novel strategy to analyze the variation of charges and surface potential on suspended fibers. The results show that the geometry of the collector has an obvious influence on the surface potential of suspended fibers. The surface potential induced by suspended PLA fibers has a sharp rise at moment of starting electrospinning before entering in a regime of constant potential. However, suspended PEO fibers fabricated under the same processing parameters hold much lower ability in charge storage. The size of the gap can modify the length of suspended fibers affecting the amount of stored charges. This result implies that the surface potential increases with the gap size. Regarding the charge release happening from the moment of stopping electrospinning, the dissipation rate is enhanced with extending the processing time. This effect is attributed to the high density of the contact among suspended fibers favoring the surface potential decay, this phenomenon happens in both PLA fibers and PEO fibers.

4.3 Application for the building of 3D structured scaffolds by electrospinning/electrospraying on patterned collectors

4.3.1 Introduction

The former part of this chapter discussed how the surface potential of suspended fibers changed over a single gap. In order to analyze the effect of suspended fibers on the particle trajectories when electrospraying over a layer of electrospun fibers, electrospinning/electrospraying experiments were operated using patterned collectors of various geometries. We studied how the interactions between the suspended fibers and the electrosprayed particles influence their precise deposit on selective areas.

In this section, two kinds of patterned collectors were tested: a striated collector and grids. In the beginning, the formation of fibers and particles were performed on the striated collector which only contained paralleled grooves and gaps, the objective was to investigate the generation mechanism of bilayer samples by modifying the processing time of electrospinning and changing the polymer solution systems to better control the distribution of particles on the fibrous mats. Eventually, the result proved that the strategy was feasible by alternately generating fibers and particles on grids to construct multilayer scaffolds.

4.3.2 Fabrication of bilayer samples on a striated collector

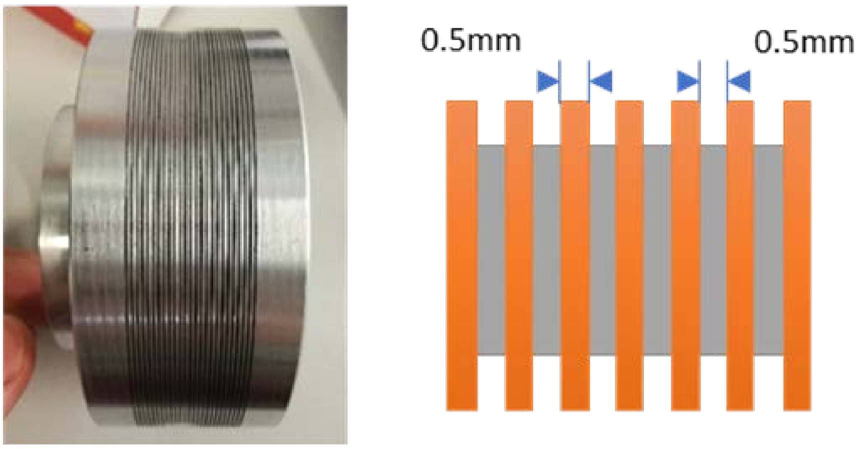

Fig. 4.17 Picture showing the geometry of gaps and grooves of the striated collector

In the previous chapter, the variation of surface potential induced by suspended fibers was analyzed deeply in the case of a simple gap geometry. For potential applications, a new striated collector with 20 gaps and 20 grooves of 0.5mm was fabricated as shown in Fig. 4.17, which is used for studying the surface potential of suspended fibers on the construction of 3D scaffolds by coupling electrospinning and electrospraying, In this section, fibers and particles are prepared at each side of the striated collector for the generation of bilayer scaffolds with patterned structures. Aiming to study the effect of polymer solution system on the morphology of bilayer samples, PLA fibers and PEO fibers were used with PCL 14k particles. The goal is to find and understand the best conditions allowing the controlled deposition of particles only on the grooves of the collector.

As mentioned previously, suspended fibers played the important role in the construction of structured scaffolds. Due to charge dissipation happening concurrently during electrospinning, the variation of surface potential induced by fibers on the striated collector was measured as well.

4.3.2.1 Materials and methods

Materials and solution preparation

PLA (Mw=180k, Natureworks) and PEO are used as received. Dichloromethane (DCM) and N, N-Dimethylformamide (DMF) are all reagent grades. PLA polymer (9% by weight) is dissolved in DMF/DCM (50:50 v/v) at room temperature with magnetic stirrer for 24h to obtain the spinning solution. With the same method, 5% PEO in deionized water is prepared 24h prior to electrospinning. PCL (14kDa) is purchased from Sigma-Aldrich. Dimethylacetamide (DMAC) is used as received. PCL solution of 5% in DMAC (w/w) is prepared and heated at 60 °C during the agitation 5 h prior to electrospraying.

Electrospinning process

The solution in the syringe is pushed by a pump (Fischer scientific) and passes through the plastic tube that connected from the nozzle of syringe to a stainless steel needle in an inner diameter of 0.5 mm. The needle is connected to a high voltage DC power supply (Spellman SL10). All polymer solutions are operated in the same parameter during electrospinning. The distance from the nozzle to the plane for collecting fibers is set at 15 cm. The rotation rate is 120 rpm. The voltage is controlled at 25kv and the feed rate of solution is 1ml/h. The experiment is carried out at room temperature and humidity.

Electrospraying process

As to electrospraying PCL 14k particles, PCL 14k solution is delivered with a flow rate of 0.6 ml/h. Positive potential is performed at 30 kV and the distance is 15cm. The experiment is operated at room temperature and humidity.

Combination of electrospinning and electrospraying

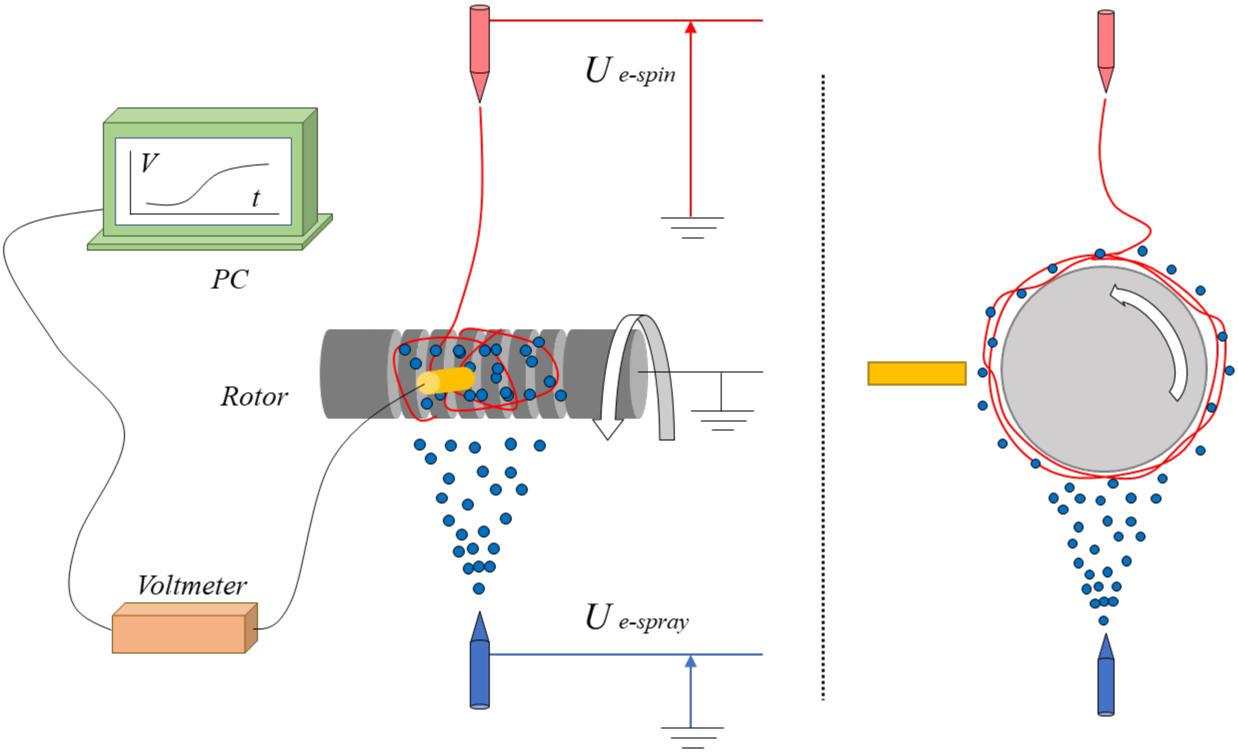

Fig. 4.18 Sketch showing the coupling of electrospun fibers and electrosprayed particles on the striated collector

The operation sketch is shown in Fig. 4.18, aiming to observe the change of morphology of scaffolds after modifying the parameters of electrospinning and electrospraying, fibers and particles are fabricated alternately in this section. In the beginning, fibers are prepared on the striated collector with the parameters mentioned in the former part. The time to start electrospraying is the moment of shutting down electrospinning. As shown in Fig. 4.18, the intensity of surface potential is also measured during the process.

Characterization

The morphology of fibers suspending over the gap is studied by using scanning electron microscope (SEM) (Vega-3, Tescan) after gold coating (Quorum Q 150 RS, Quorum Technologies).

4.3.2.2 Effect of processing time on the variation of surface potential of suspended PLA and PEO fibers

Electrospraying over a layer of PLA electrospun fibers on the striated collector

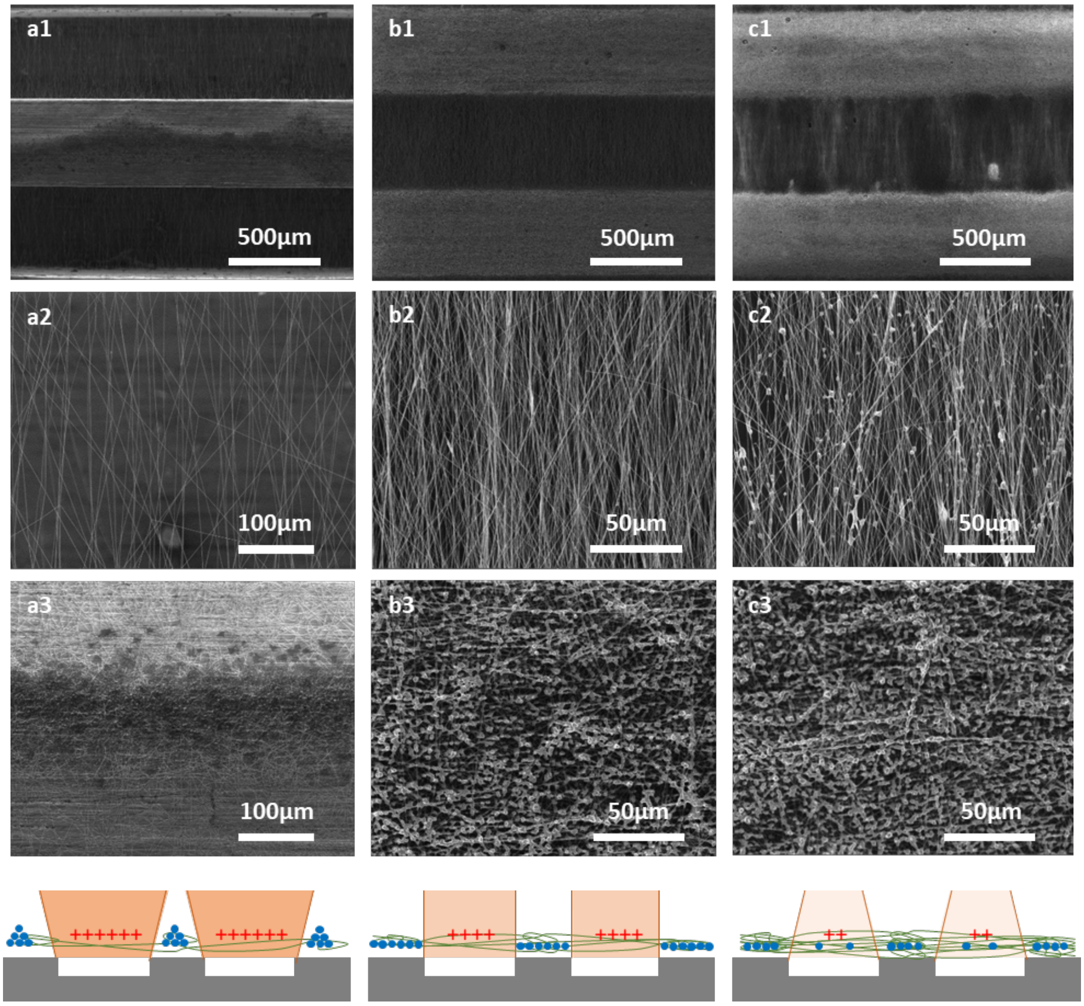

Fig. 4.19 Bilayer samples obtained from the deposition of a first layer of PLA fibers electrospun during a time t_{spin} covered by a layer of electrosprayed PCL 14k particles on the striated collector (a: t_{spin} = 15s, b: t_{spin} = 3min and c: t_{spin} = 5min). a1, b1, c1 show grooves and gaps; a2, b2, c2 are pictures taken over the suspended fibers; a3, b3, c3 are pictures taken over the grooves.

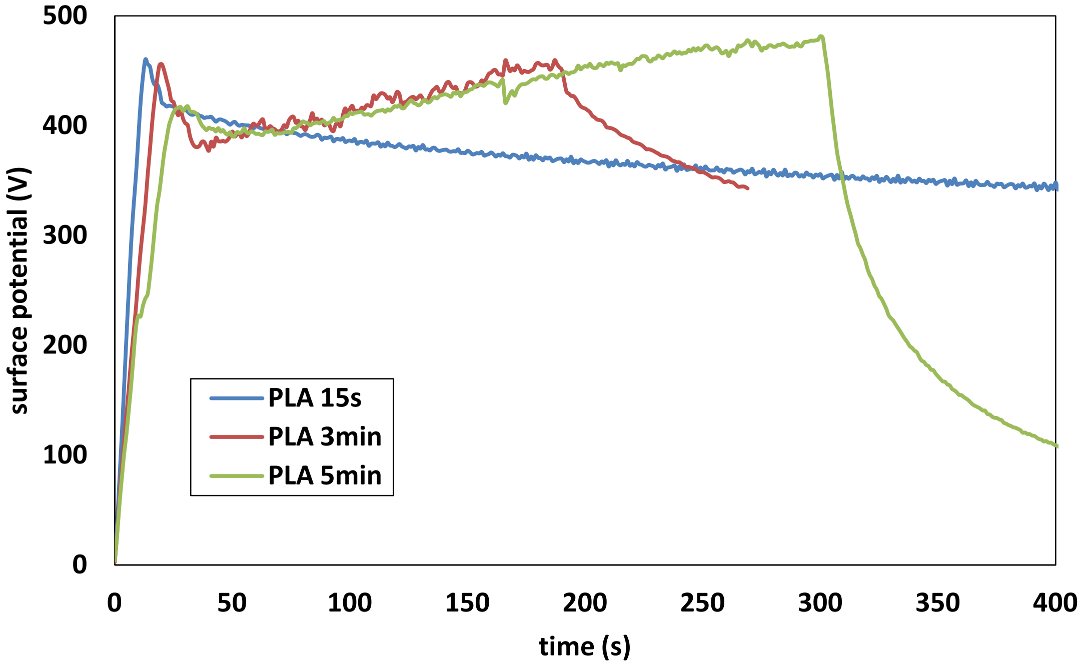

Fig. 4.20 Surface potential curves achieved when preparing PLA fibers in three electrospinning times on the striated collector: Electrospinning from 0 to t_{spin} then surface potential decay for $t > t_{spin}$. Blue: t_{spin} = 15 s, red: t_{spin} = 3 min, green: t_{spin} = 5 min.

Fig. 4.19 shows bilayer samples obtained from the deposition of electrospun PLA fibers on a striated collector with different times of electrospinning covered by a layer of electrosprayed PCL 14k particles. Furthermore, the variation of surface potential of fibers formed on the striated collector in each condition is also measured (Fig. 4.20). In the cases of t_{spin} > 1 min, comparing the surface potentials in Fig. 4.20 and Fig. 4.12a, a similar trend is obtained. First a sharp increase is observed due to charge accumulation, then in the second stage it is observed a surface potential decrease due to crossing fibers leading to the decrease of the overall suspended fiber resistance $R(t)$. In the third stage a slow increase of the surface potential is shown for the striated collector instead of a plateau value as observed in the case of the single gap collector. This slow increase can be explained by the fact that after 3 min of electrospinning a dense fibrous mat is already formed over the gaps of the striated collector. Thus, the behavior looks like more the behavior of charge accumulation during electrospinning on flat collector.

Then, when stopping electrospinning, a significant surface potential decay is shown. The gap size of 0.5mm in the striated collector shortens the length of suspended fibers with fewer charges increasing also the contact probability and crossing of suspended fibers which decreases the fibrous layer resistance $R(t)$ and shorten the characteristic time $\tau = R(t)C_{gaps}$ of the surface potential decay, where C_{gaps} is the capacitance generated by the gaps of the collector. Finally, faster charge release is observed for longer duration of electrospinning t_{spin}. The coulombic force resulting from a lower surface potential is weaker and decreases with increasing t_{spin} . Thus, particles which are electrosprayed after a long time of electrospinning are subjected to weak repulsive force and poor electrostatic template effect leading to bad control of their deposition on the grooves of the collector. However, when electrospinning is carried out during a short time, such as $t_{spin} = 15\ s$, a perfect electrostatic template is formed. In this case, as shown in Fig. 4.19 a1, a2 and a3, no particles fell on the suspended fibers and all particles were deposited on the grooves. More precisely, the particles are deposited on the central part of the grooves without covering their whole surface. This effect is attributed to the strong repulsive force induced by the suspended fibers and also the strong attractive force generated from the central part of the grooves. When electrospraying is carried out after 3min of electrospinning, the charges release faster leading to the weakening of the electrostatic template forces (i.e. the attractive force on the grooves and the repulsive one on the suspended fibers). In this condition, the weaker electrostatic template forces cause the enlargement of the distributing area of PCL 14k particles covering the whole surface of the grooves, but no particles are deposited on the suspended fibers over the gaps (Fig. 4.19 b2) proving that the repulsive strength is still strong enough to push all particles on the grooves. When extending the electrospinning time to 5 min, the electrostatic template effect is no longer acting on the electrosprayed particles which are deposited on the whole surface of the collector (4.19d): repulsive and attractive forces disappear dramatically in such condition.

Electrospraying over a layer of PEO electrospun fibers on the striated collector

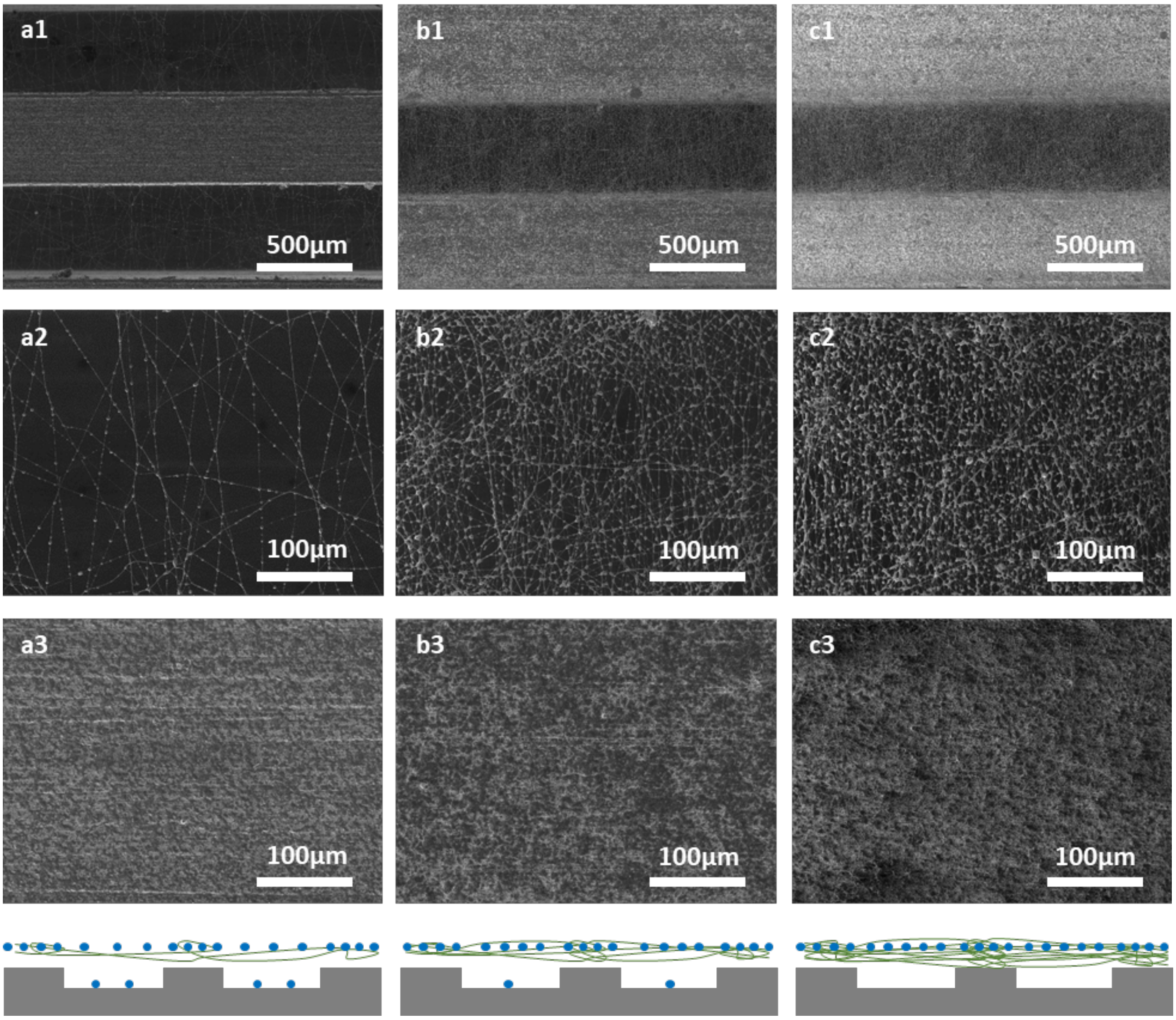

Fig. 4.21 Bilayer samples obtained from the deposition of a first layer of PEO fibers electrospun during a time t_{spin} covered by a layer of electrosprayed PCL 14k particles on the striated collector (a: t_{spin} = 15s, b: t_{spin} = 3min and c: t_{spin} = 5min). a1, b1, c1 show grooves and gaps; a2, b2, c2 are pictures taken over the suspended fibers; a3, b3, c3 are pictures taken over the grooves.

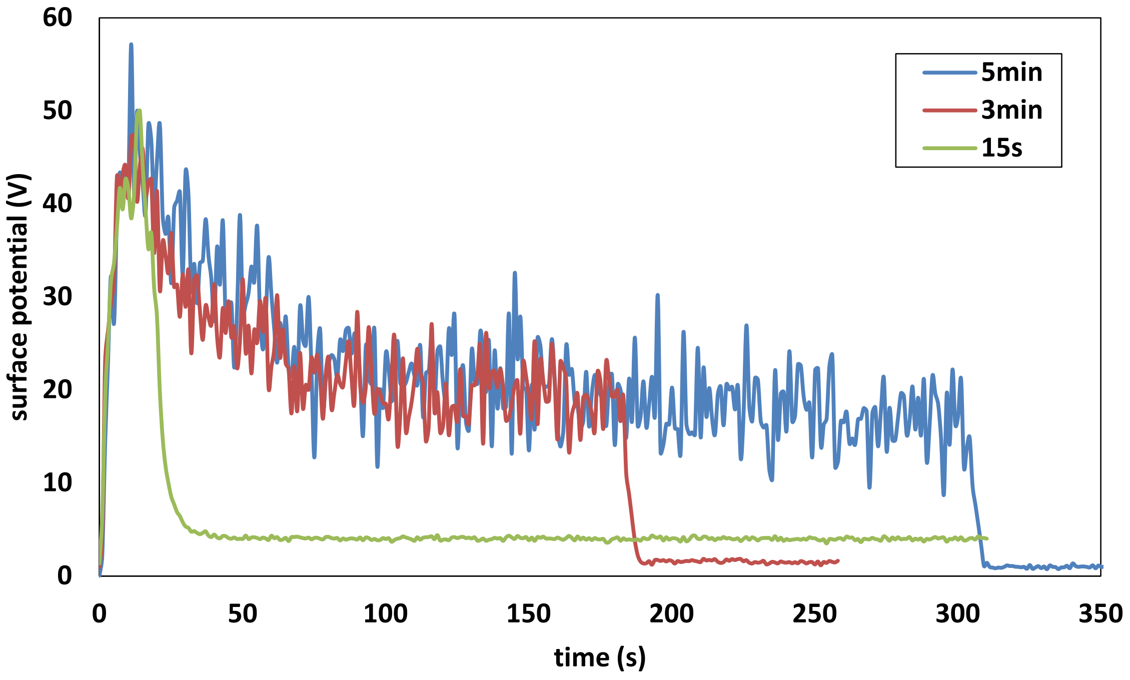

Fig. 4.22 Surface potential curves achieved when preparing PEO fibers in three electrospinning times on the striated collector: Electrospinning from 0 to t_{spin} then surface potential decay for $t > t_{spin}$. Blue: t_{spin} = 15 s, red: t_{spin} = 3 min, green: t_{spin} = 5 min.

Fig. 4.21 shows the bilayer samples obtained after electrospraying PCL14k particles on PEO fibers deposited on the striated collector with an electrospinning duration of 15s, 3min and 5min, respectively. Fig. 4.22 shows that the surface potential induced by the suspended PEO fibers is extremely low and is not strong enough to repel the PCL14k particles on the grooves of the collector. No efficient electrostatic template effect is induced in these cases. This phenomenon is proved by the morphologies of the three bilayer samples in Fig. 4.21 showing that PCL14k particles appear on suspended PEO fibers in all three samples. Taking the condition of electrospinning during 15s as an example (Fig. 4.21 a1-a3), due to the low repulsive force formed by suspended PEO fibers, PCL14k particles cover the whole surface of the grooves as well as the suspended PEO fibers. Extending the electrospinning duration does not lead to any change of the particles deposition (Fig. 4.16 b1-b3, c1-c3). Therefore, PEO fibers are not suitable for building structured 3D scaffolds with patterned collectors.

4.3.2.3 Conclusion

In summary, bilayer samples were generated by combining electrospun fibers and electrosprayed particles using the striated collector. It was proven that PEO fibers cannot modify the trajectory of PCL14k particles due to low residual charges resulting to poor electrostatic template effect. However, the situation is completely different when PLA is used instead of PEO. Indeed, the charges of suspended PLA fibers play a necessary role in the selective deposition of PCL14k particles. The controlled deposition of electrosprayed PCL14k particles on the grooves of the striated collector covered by PLA fibers is enhanced when a thin layer (instead of a thick one) of fibers is deposited, ensuring thus an efficient electrostatic template effect. Bilayer samples produced on the striated collector shows a great value in the future fabrication of the structured scaffolds.

4.3.3 Fabrication of multilayer 3D samples on grid collectors

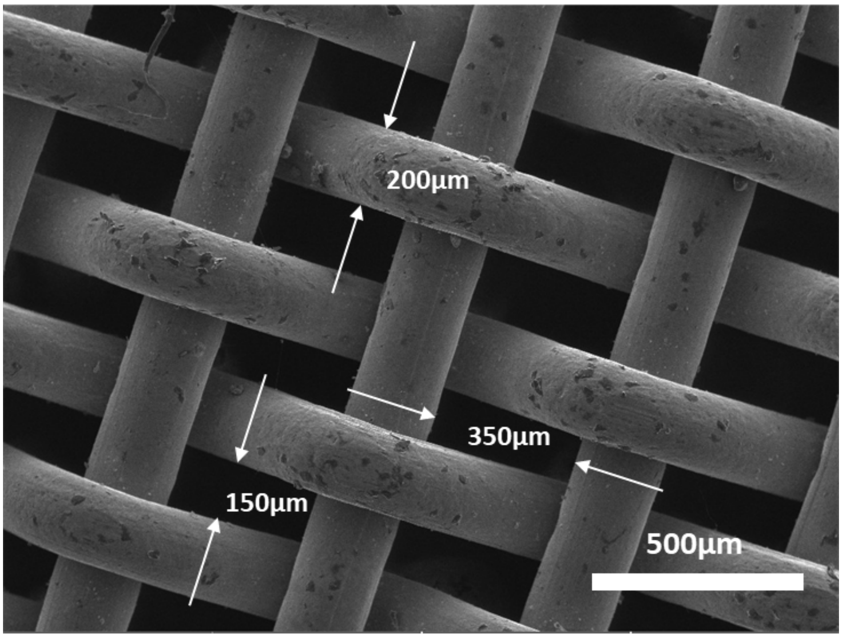

Fig. 4.23 SEM image of the grid collector

The former section discussed the feasibility of the formation of bilayer samples on a striated collector. In order to build another kind of fibrous structure, grid collectors were used. As shown in Fig. 4.23, the walls and valleys of the grid held smaller sizes than those in the striated collector. In addition, except PLA fibers and PEO fibers, PLA/TEBAC fibers and PEO/Alginate fibers were also investigated for the fabrication of structured scaffolds. Regarding the electrosprayed particles, both PCL14k and PCL80k were processed to enrich the types of composite scaffolds.

4.3.3.1 Materials and methods

Materials

PLA (Mw=180k, Natureworks), PEO (Mw=400k), TEBAC, alginate and deionized water were used as received. PCL (Mw=14k and 80k), DMAC, chloroform, Dichloromethane (DCM) and N, N-Dimethylformamide (DMF) were purchased from Sigma-Aldrich.

Preparation of solution

Pure PLA solutions for electrospinning were prepared by dissolving PLA in DMF/DCM (50:50 v/v) to get a 9% w/w polymer concentration. TEBAC (0.5% w/w) was added to PLA solution for PLA/TEBAC solution. For the fabrication of the solution, PLA or with TEBAC were added in DMF/DCM in a glass bottle with stirring magnetically overnight at the room temperature. With the same method, 5% w/w PEO in deionized water was stirred 24h prior to electrospinning. PEO/alginate solution was produced by adding 1% w/w alginate in PEO solution.

For electrospraying, PCL14k solution of 5% in DMAC (w/w) was prepared by heating the solution at 60 °C during agitation 5 h before electrospraying. PCL80k solution was achieved through dissolving PCL80k in chloroform with 2% w/w concentration to stir overnight.

Electrospinning process

The solution in the syringe was pushed by a pump (Fischer scientific) and passed through the plastic tube connected from the nozzle of a syringe to a stainless steel needle with an inner diameter of 0.5 mm. The needle was connected to a high voltage DC power supply (Spellman SL10). The distance from the nozzle and the plane for collecting fibers was set at 15 cm. The rotation rate was 120 rpm. The voltage was controlled at 25kv and the feed rate of solution was 1ml/h. The experiment was carried out at room temperature and humidity. All polymer solutions were operated with the same parameters during electrospinning.

Electrospraying process

In the case of electrospraying PCL14k particles, PCL 14k solution was delivered with a flow rate of 0.6 ml/h. Experiment were performed with positive potential at 30 kV and the distance of 15cm. For the electrospraying of PCL80k particles, the solution was delivered at a flow rate of 0.8 ml/h. The distance was 15 cm from the needle to the collector and the positive voltage was set at 12kV. The experiment was operated at room temperature and humidity.

Combination of electrospinning and electrospraying

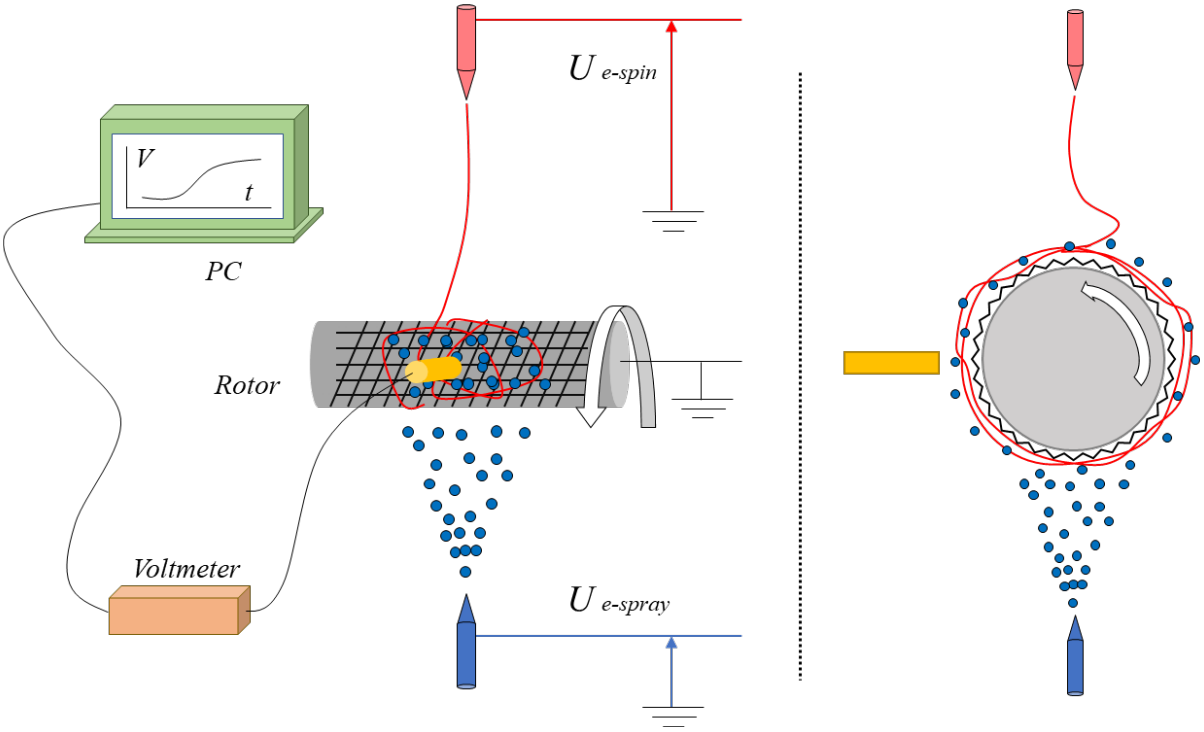

Fig. 4.24 the sketch of the operation to prepare bilayer samples by coupling electrospinning and electrospraying on the grid

As shown in Fig. 4.24, a grid with patterned structure is covering a metallic rotor for the collection of fibers and particles. During the experiment, electrospinning and electrospraying were operated at each side of the collector to form fibers and particles alternately. Fibers were produced on the grid at first. Then, electrospraying is starting immediately at moment of shutting down electrospinning. In order to compare the intensity of surface potential induced by four types of suspended fibers clearly, the experiment setup of Fig. 3.1 was used with the gap size at 3mm.

Characterization

The morphology of fibers and particles was characterized by scanning electron microscope (SEM) (Vega-3, Tescan) using an accelerating voltage at 5KV, the samples were taken sputter coating (Quorum Q 150 RS, Quorum Technologies) for 2min prior to take microscope.

4.3.3.2 Bilayer samples obtained from various polymer fibers covered by PCL14k particles

In the 2nd chapter, we compared the amount of charges carried by an electrospun jet of PLA, PLA/TEBAC, PEO and PEO/Alginate. It was proven that the current is related with the conductivity of the corresponded solutions. Due to the presence of more ionic charge carriers, increasing the conductivity of a polymer solution, the electrospun jet could be highly charged under the electric field enhancing the intensity of the current. However, as discussed previously, the charge dissipation occurs immediately when the jet hits the collector. So, it is essential to measure the surface potential of the four types of fibers deposited on the grid to get more insight into the electrostatic template effect.

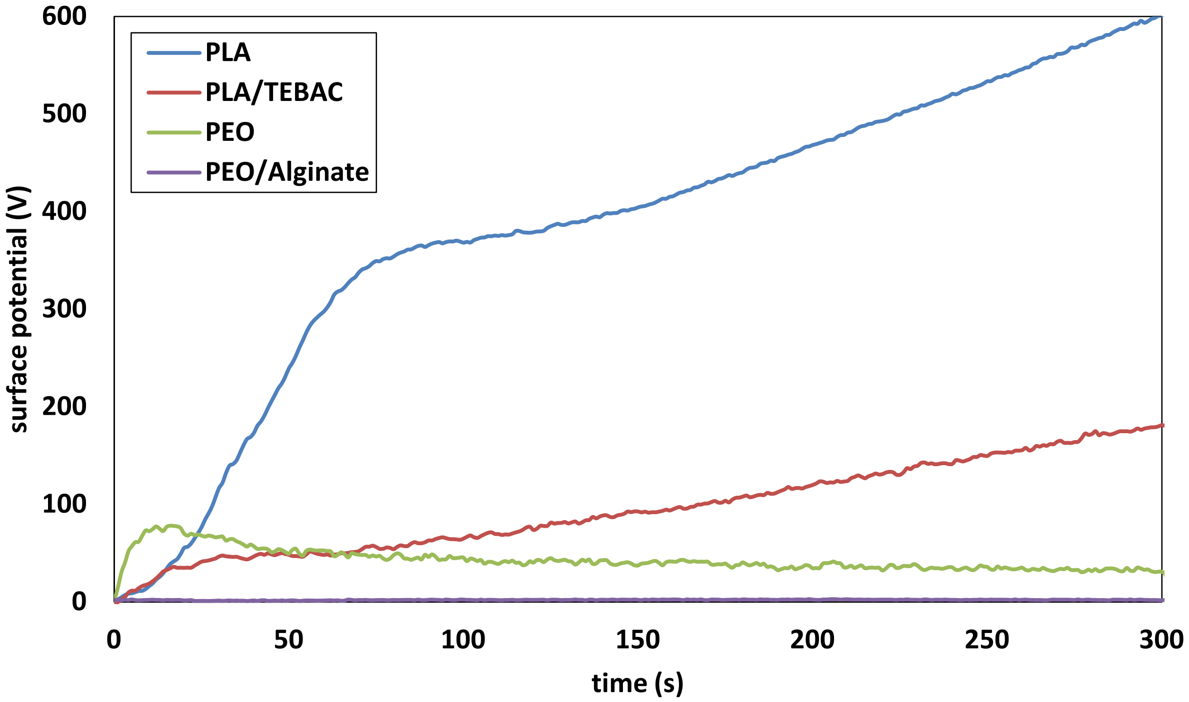

Fig. 4.25 Curves of surface potential of four types of fibers generated on the grid collector.

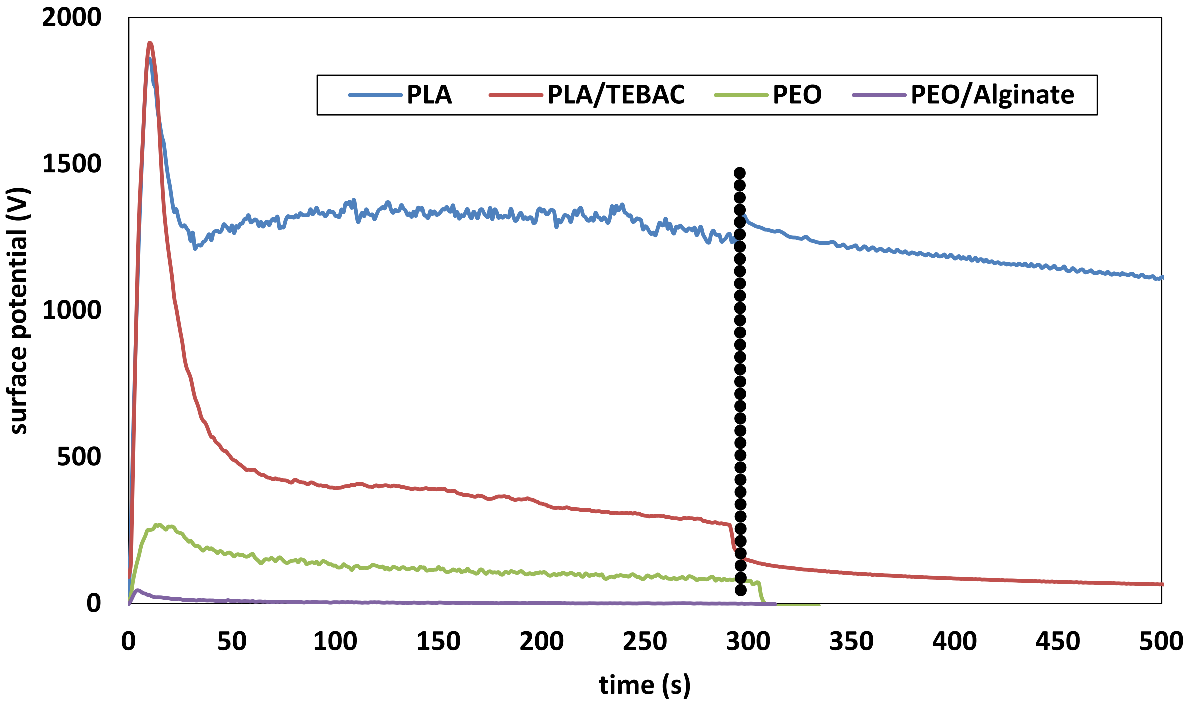

Fig. 4.26 Curves of surface potential of four types of fibers generated on a single gap collector with a gap of 3mm. The dotted line indicates the end of electrospinning.

Fig. 4.25 presents the variation of the surface potential for four kinds of fibers electrospun on the grid. It is shown that when a solution having a high conductivity is electrospun, the high amount of charges is released very rapidly. The electrical resistance $R(t)$ of the fibrous mat obtained from conducting systems is low resulting in short characteristic times leading to low surface potential as shown in the previous chapter. Consequently, the surface potential decay after stopping electrospinning is fast for conducting systems.

For example, the addition of alginate, a polyanion, increases the conductivity of the PEO solution, thus almost no increase of the surface potential occurred on suspended PEO/Alginate fibers during electrospinning.

Compared with PEO/Alginate fibers, because of the decrease of the conductivity, PEO fibers held an increasing surface potential with a peak at around 72V. In the 3rd chapter, it was proven that PEO fibers cannot remain the charges during simple electrospinning. Additionally, the increasing density of suspended fibers accelerates the dissipation rate of residual charges. Both factors led to fewer charges maintaining on PEO mats resulting in the decay of surface potential with extending electrospinning.

PLA fibers showed a significant rise in the initial stage of electrospinning resulting from the low conductivity allowing the charges to maintain on the suspended fibers, explaining the increasing amount of charges accumulating on the suspended fibers. Then, after reaching a shoulder (350 V, 80 s), a second increase is observed. As discussed previously, the density of suspended fibers enhanced the charge dissipation, and even more rapidly due to the small size of the grid patterns. Furthermore, due to the small size of the grid patterns, the repulsive force from the suspended fibers would disappear quickly as time went on. Hence, the new coming fibers started to deposit on the grid randomly without any interaction between the falling fibers and the suspended potions on the grid. This situation is similar with the deposition of an electrospun jet on a randomly deposited mat on flat collector. As a result, the surface potential increases due to charge accumulation as discussed in chapter 3.

Electrospinning of PLA/TEBAC fibers leads to a surface potential following the same trend as what it is observed in the case of PLA but with much lower intensity. Indeed, the shoulder characteristic to the end of the first stage appears after 20 s for a potential of only 35 V. This behavior is attributed to the enlargement of the conductivity due to the addition of TEBAC salt improving the charge release [32], [33].

These behaviors were also confirmed when the four kind of polymer are electrospun over a single gap collector (Fig. 4.26). Fig. 4.26 presents the evolution of the surface potential for the four types of fibers prepared on the single gap collector with a gap of 3 mm. The behavior of PLA, PEO and PEO/alginate were already discussed. For PLA/TEBAC, it is worth noting that after stopping electrospinning, the fibers can remain the charges for long time even though the initial potential is low.

Next step was to prepare fibers and particles alternately on the grid to understand the dramatic role of the surface charges carried by the suspended fibers on the construction of bilayer electrospun/electrosprayed samples. In addition, the effect of fibers fabricated from different polymer solutions on the morphology of the bilayer samples was also considered.

4.3.3.2.1 PLA fibers & PCL14k particles

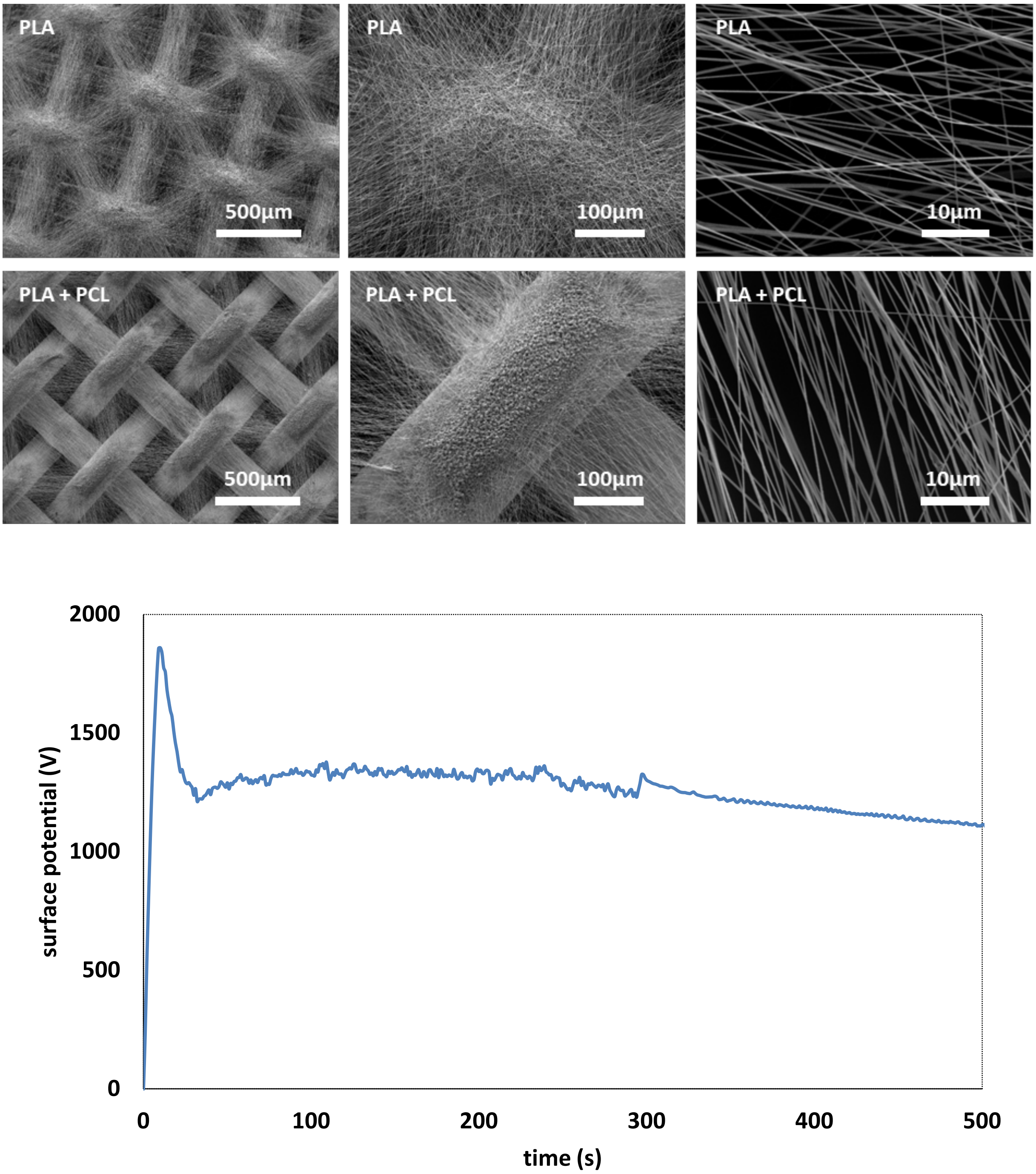

Fig. 4.27 Comparison of morphology of bilayer samples generated by coupling PLA fibers with PCL 14k particles on the grid and the intensity of surface potential induced by PLA fibers on a single gap collector with a gap = 3 mm. Electrospinning stopped at 300 s.

SEM images showed that only PLA fibers affected PCL 14k particles to land on specific areas of fibrous mats remarkably. This was attributed to the capability of suspended

PLA fibers to store the charges. As discussed in the aforementioned result, patterned geometry caused a lensing electric field above the collector with a strong attractive force over the surface of protrusions. In addition, fibers discharged efficiently when touch the collector without forming significant repulsive force to the new coming fibers, thus most of falling fibers converged randomly on the convex part of collector. At the same time, portions of fibers crossing over the concaves domains remain charged inducing an electrostatic repulsion among the suspended fibers which results in the generation of aligned fibers suspending the cavities of the collector. Due to the different dissipating rates of charges between fibers landed on protrusions of collector and suspended portions, uneven electric field occurred near the surface of fibrous mat which impacted the distribution of electroprayed PCL 14k particles. During the process of electrospraying, weak domains of electric field above the discharged fibers at the protrusions attract the deposited particles. However, highly charged fibers suspended over the gap cause strong domains that repels particles to fall on weak domains, resulting in the specific deposition of PCL 14k particles on PLA fibers. The high intensity of repulsive force induced by suspended PLA fibers was proven by the high value of the surface potential over the suspended PLA fibers (Fig. 4.27). Therefore, PLA fibers were a suitable candidate for the building of structured scaffolds by coupling electrospinning and electrospraying.

4.3.3.2.2 PLA/TEBAC fibers & PCL 14k particles

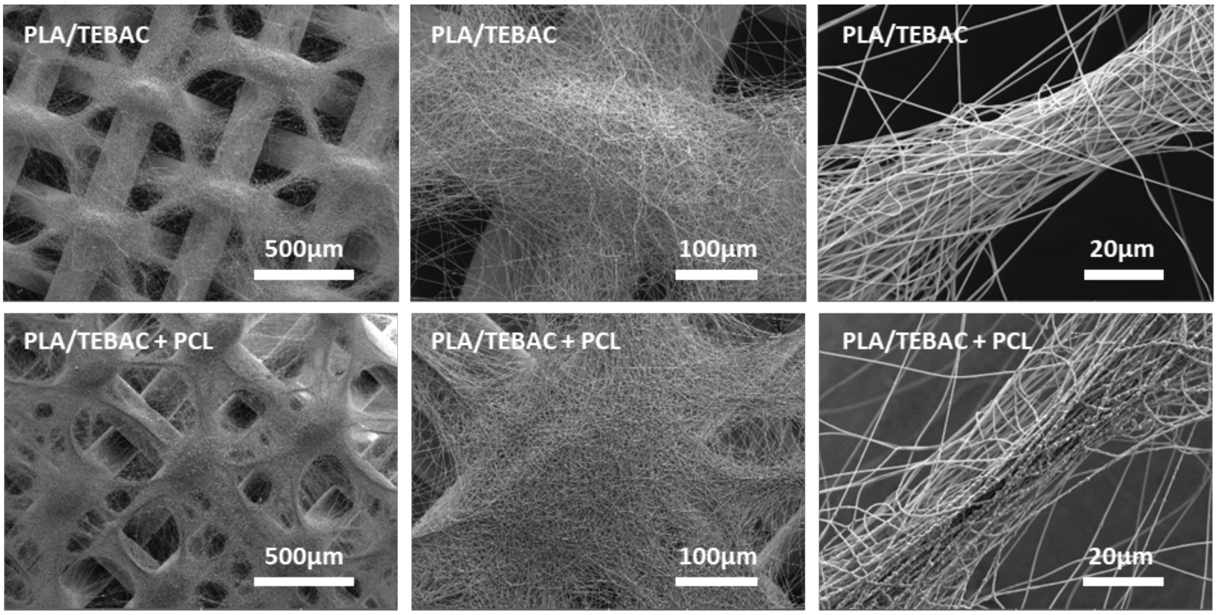

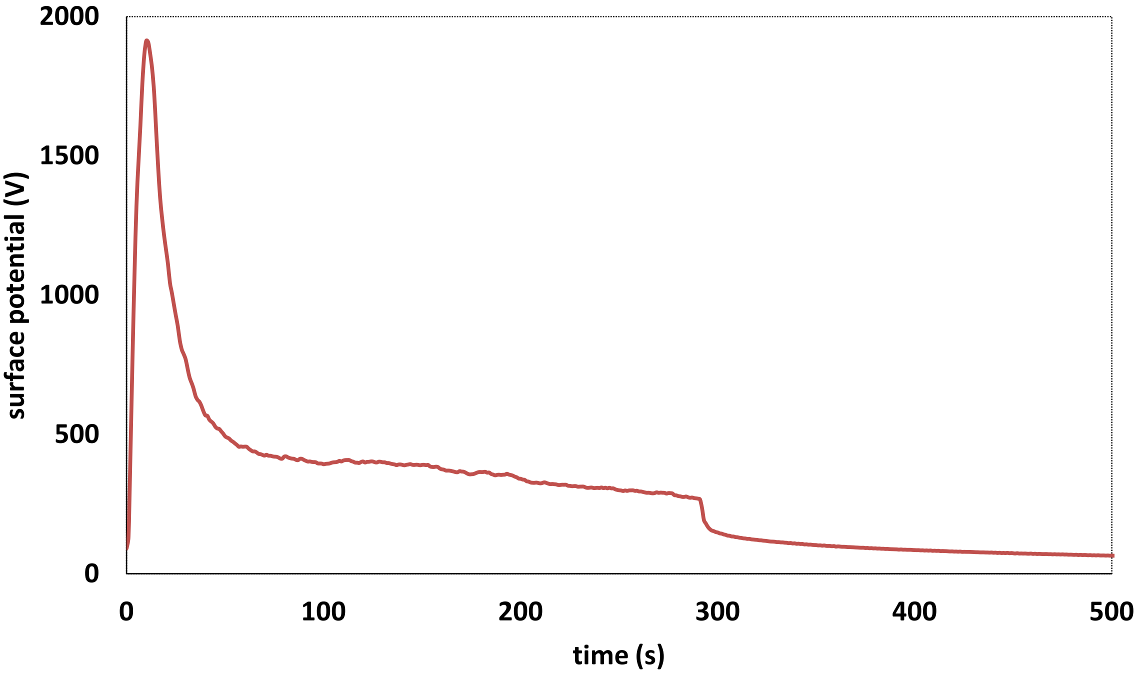

Fig. 4.28 comparison of morphology of bilayer samples generated by coupling PLA/TEBAC fibers with PCL 14k particles on the grid and the intensity of surface potential induced by PLA/TEBAC fibers on a single gap collector with a gap = 3 mm. Electrospinning stopped at 300 s.

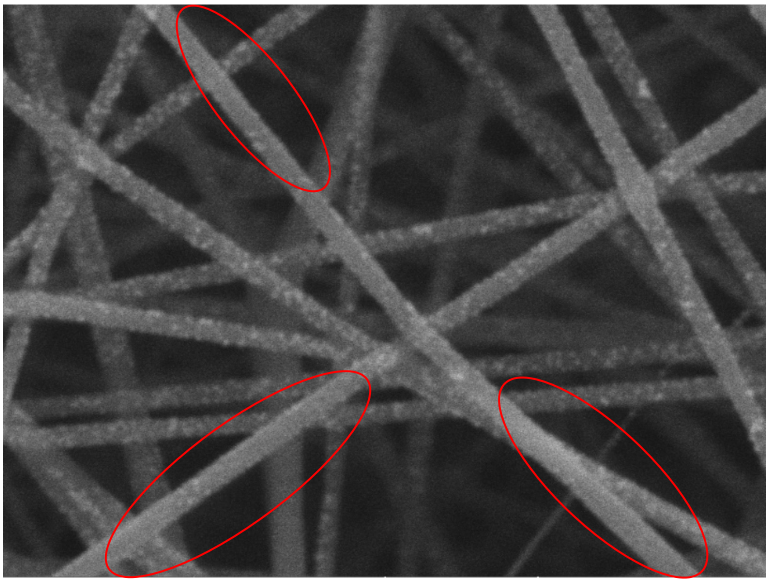

Fig. 4.29 morphology of fibers produced from PLA/TEBAC solution

In the case of PLA/TEBAC fibrous mat, the major fibers also converged on the protrusions of collector. Unlike the condition of pure PLA fibers, PLA fibers containing TEBAC salt assembled over the gaps, this strange phenomenon might be attributed to the non-uniform surface potential of suspended PLA fibers after introducing TEBAC. The morphology of PLA/TEBAC fibers is shown in Fig. 4.29. It is clearly shown that TEBAC salt is heterogeneously distributed along the fibers with TEBAC-rich and poor domains. The introduction of TEBAC increases the ionic charge carriers leading to highly charged fibers during their deposition. The TEBAC-rich domains contain a high amount of charges that cannot be efficiently released due to the presence of TEBAC-poor domains. So repulsive and attractive forces may happen along the suspended fiber strands resulting in the formation of fibrous clusters. The obvious discharge of suspended PLA/TEBAC fibers was observed in Fig. 4.28, the curve of surface potential dropped down sharply after reaching the peak with the value varying from around 1900V to 470V, which results from the high conductivity of fibers accelerating the charge migration when they start to interact through their contact points. After the quick decay, the curve entered in a slow decay stage before shutting down the power supply at 300 s. This might be caused by the increasing aggregation of suspended fibers during electrospinning. After stopping the power, surface potential decreases to less than 70V after 3min. Therefore, the deposition area of PCL 14k particles increases significantly due to low surface potential maintained on PLA/TEBAC fibers. As shown in Fig. 4.28, except on fibers fabricated on the protrusions of the grid, PCL 14k particles also appeared on the aggregated fibers suspended over the gaps.

4.3.3.2.3 PEO fibers & PCL 14k particles and PEO/alginate & PCL 14k particles

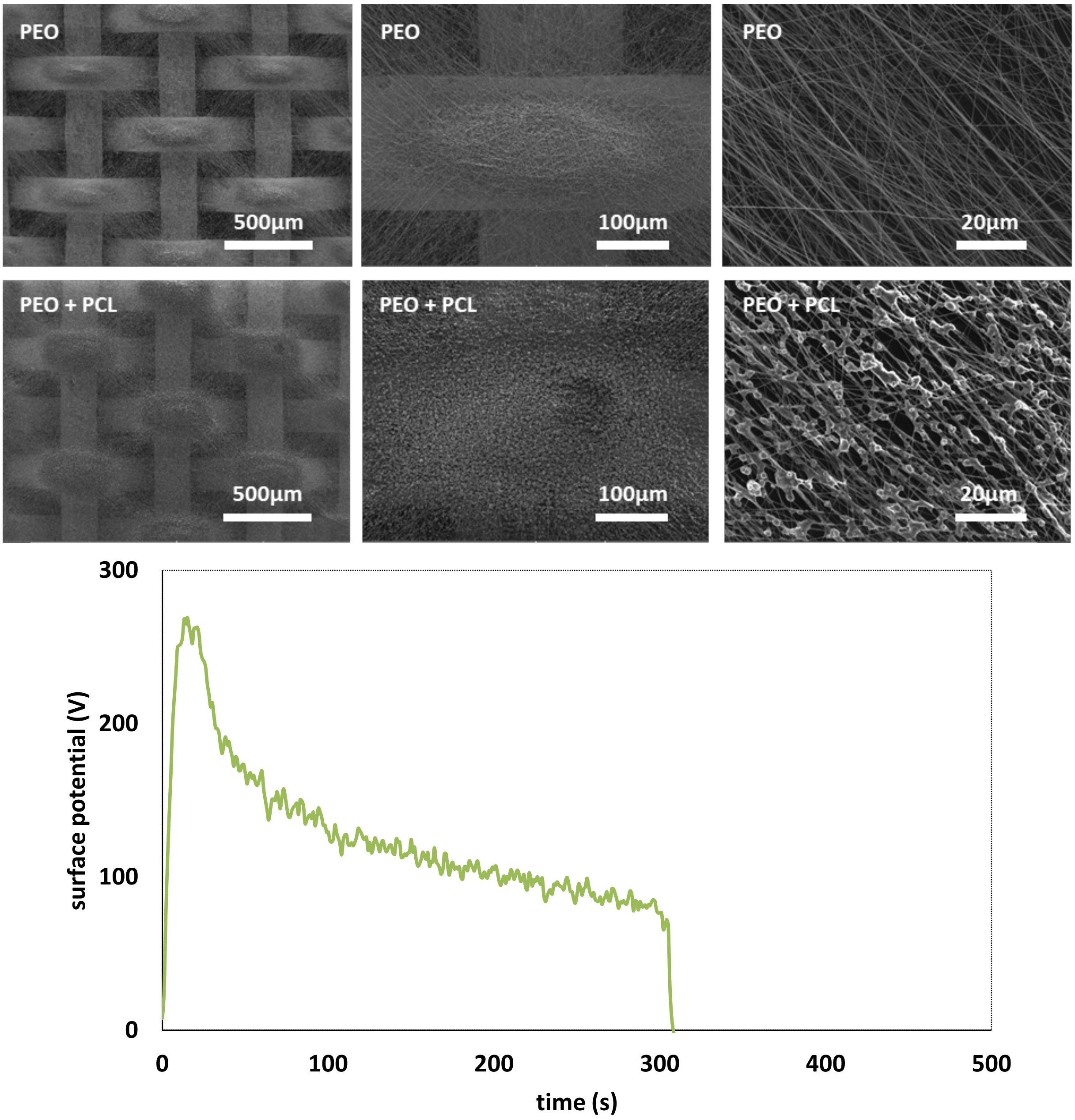

Fig. 4.30 comparison of morphology of bilayer samples generated by coupling PEO fibers with PCL 14k particles on the grid and the intensity of surface potential induced by PEO fibers on a single gap collector with a gap = 3 mm. Electrospinning stopped at 300 s.

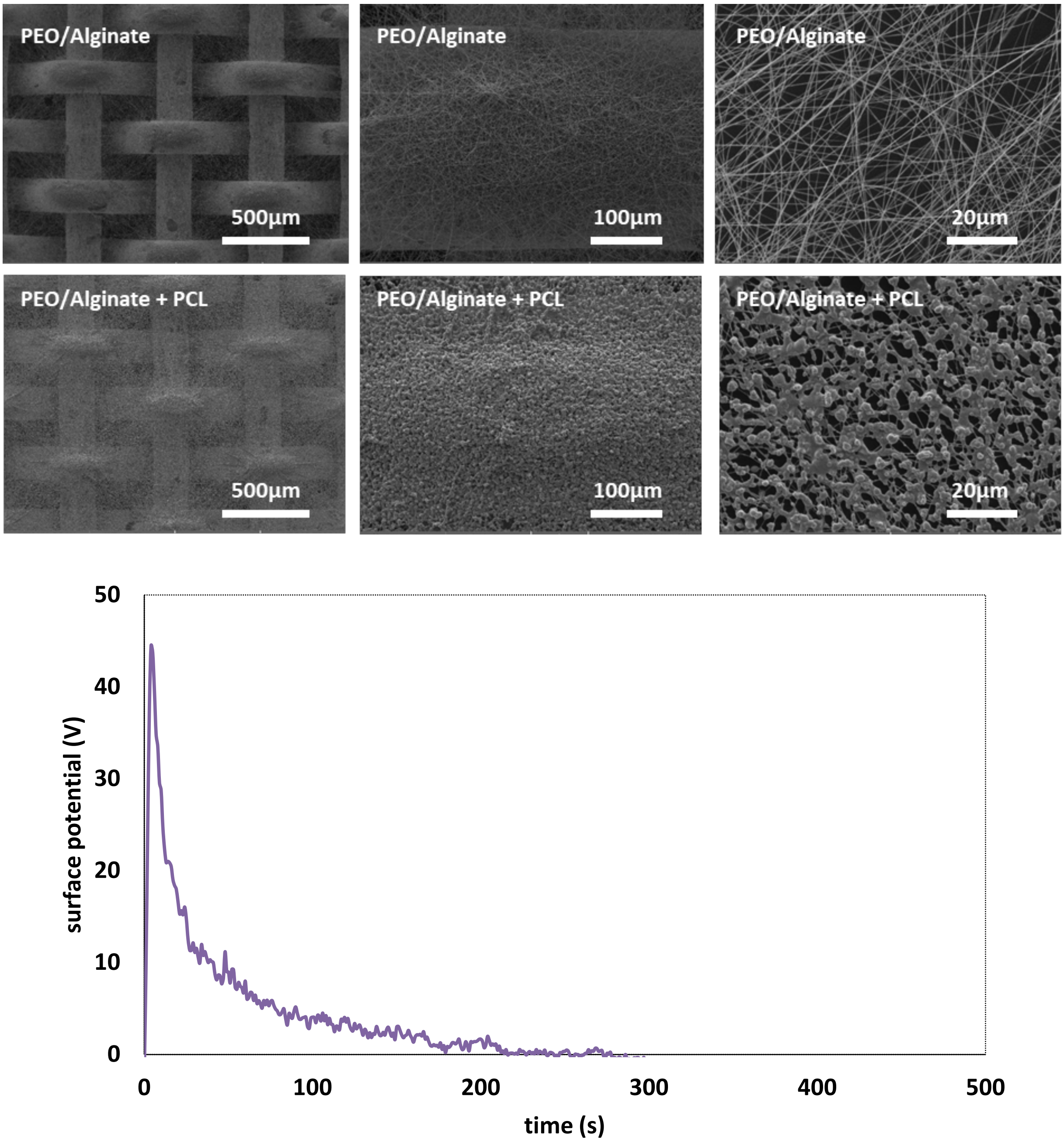

Fig. 4.31 comparison of morphology of bilayer samples generated by coupling PEO/Alginate fibers with PCL 14k particles on the grid and the intensity of surface potential induced by PEO/alginate fibers on a single gap collector with a gap = 3 mm. Electrospinning stopped at 300s.

The case of PEO fibers & PCL and the particles case of PEO/alginate fibers & PCL are similar shown as shown in Fig. 4.30 and 4.31. In the two cases, a mass of PCL 14k particles fell on suspended fibers, indicating that fibers crossed the concaves without offering sufficient electric force to affect the trajectory of PCL 14k particles. The poor capability of these fibers in remaining charges during electrospinning was proven by the curves of surface potential of suspended fibers in Fig. 4.30 and 4.31 showing that the surface potential decreases very quickly after stopping electrospinning in the case of PEO fibers and even before in the case of PEO/alginate for which the conductivity is higher. Therefore, no repulsive force came from suspended PEO fibers and PEO/alginate as well when PCL 14k particles are produced, resulting in the formation of uniform distribution of PCL 14 particles on PEO and PEO/alginate fibrous mats.

4.3.3.3 The effect of the density of suspended PLA fibers on the distribution of PCL particles

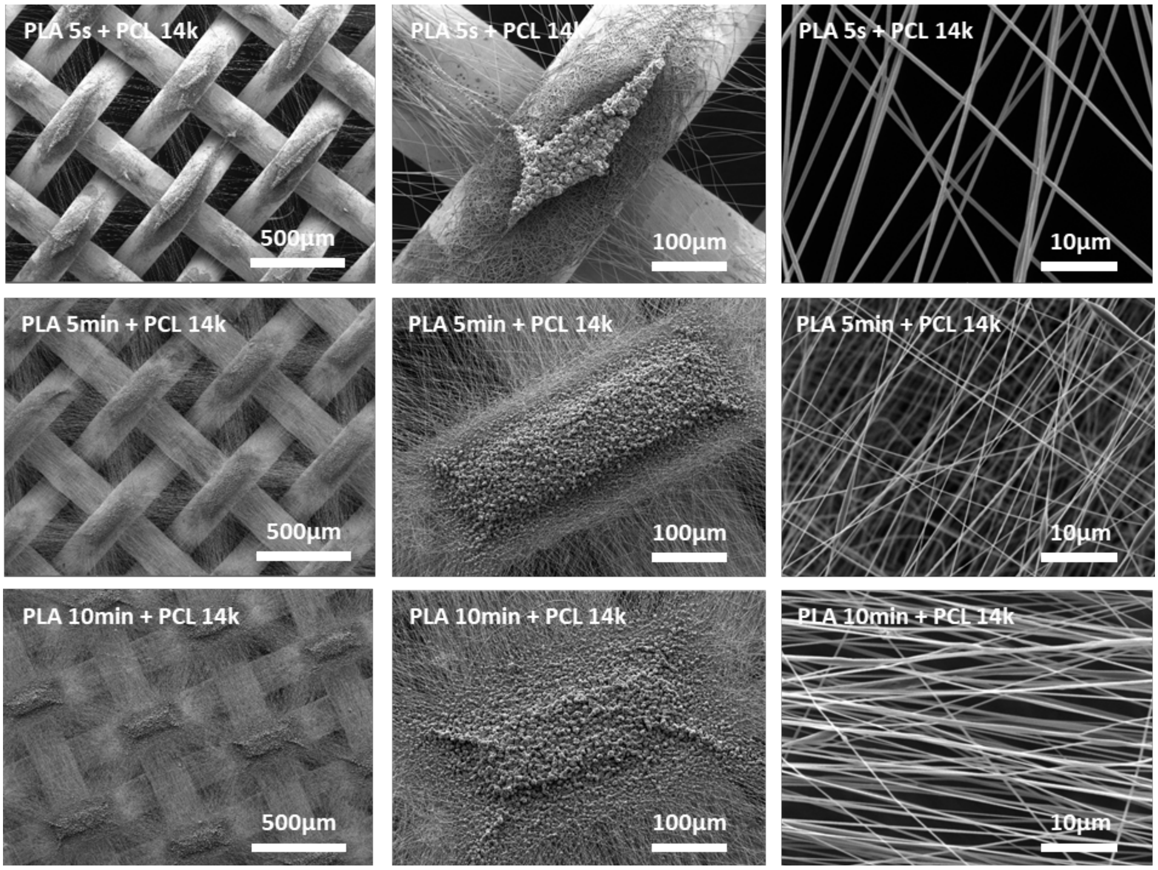

Fig. 4.32 morphologies of bilayer samples that PLA fibrous mats formed in three processing times on the grid covered by PCL 14k particles

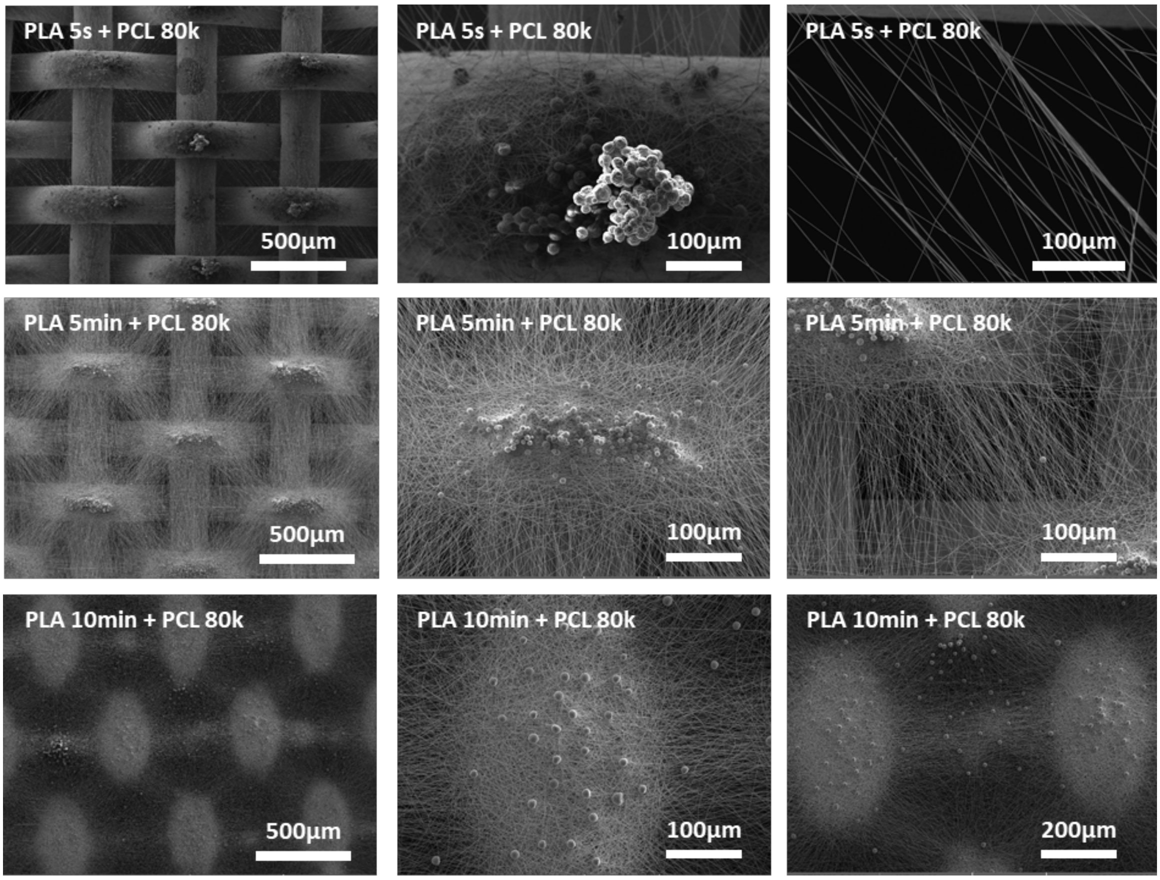

Fig. 4.33 morphologies of bilayer samples that PLA fibrous mats formed in three processing times on the grid covered by PCL 80k particles

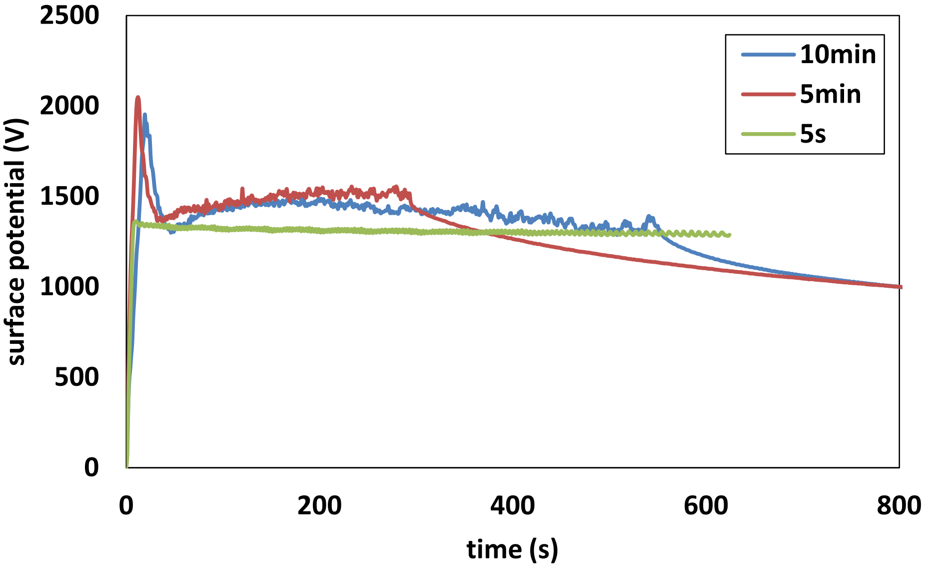

Fig. 4.34 the graph of variation of surface potential observed in electrospinning PLA fibers in three processing times

Fig. 4.32 and Fig. 4.33 showed the effect of the density of suspended PLA fibers on the distribution of PCL 14k and PCL 80k particles, respectively. The time of electrospinning was set at 5s, 5min and 10min to achieve suspended fibers in different densities. The time of electrospraying PCL 14k and 80k particles was 5min. The two kinds of bilayer samples prepared after t_{spin} = 5s from the two types of PCL particles present the same morphology showing aggregated particles which were deposited on specific small areas where the fibers touch the collector. With extending the processing time of electrospinning to produce more fibers on the grid, the deposition areas of particles enlarged gradually. For example, in the condition of electrospinning PLA fibers for 5min, the aggregation of particles disappeared which was attributed to the extension of deposition area of particles on PLA fibers. For prolonged electrospinning time at 10min, the area of particles deposition enlarged continuously, especially in the case of bilayer sample formed with PCL 80k particles. Indeed, these samples show PCL 80k particles homogenously deposited on PLA fibers without locating on specific areas. The phenomenon explaining the effect of the processing time on the distribution of particles is related with the decay rate of surface potential of suspended fibers. Indeed, it was shown in the previous part that the characteristic decay time decreases with the time of production due to the increase of crossing fibers leading to the enhancement of the suspended fibers conductivity. Fig. 4.34 presents the difference in charge release when electrospinning fibers in different processing times. In the case of 5s, at the very beginning of the process, only few suspended fibers were formed over the gap of the grid when shut down the power. Surface potential of suspended fibers stayed stable for a relatively long period to offer repulsive force intensely and constantly to the falling PCL particles. At the same time, the portion of PLA fibers deposited on the convex parts of the grid attracted PCL particles, resulting in the aggregation of PCL particle in small areas on PLA fibers. After extending the processing time, a decay of the surface potential occurs with a more rapid decrease for more suspended PLA fibers generated on the grid. It indicates that the kinetic of charge release has a positive correlation with the processing time of electrospinning. Therefore, weaker repulsive power appeared with more fibers suspended over the gap after prolonging the processing time, resulting in the enlargement of deposition area of PCL particles on PLA fibers, even portions of PCL particles fell on suspended PLA fibers. As discussed previously, the intersections between suspended fibers induced the formation of the loops among the suspended fibers behaving electrically as an RC circuit. R being the crucial factor impacting the kinetic of charge release. After extending the processing time, R decreased gradually due to the increase of crossing fibers over the gaps accelerating the charge dissipation. As a result, a fast charge release occurs in the condition of high density of suspended PLA fibers resulting in the weakening of the repulsive force induced by suspended fibers. Thus, PCL particles are distributed in larger areas on PLA fibers.

4.3.3.4 Electrostatic template effect for long times of electrospraying

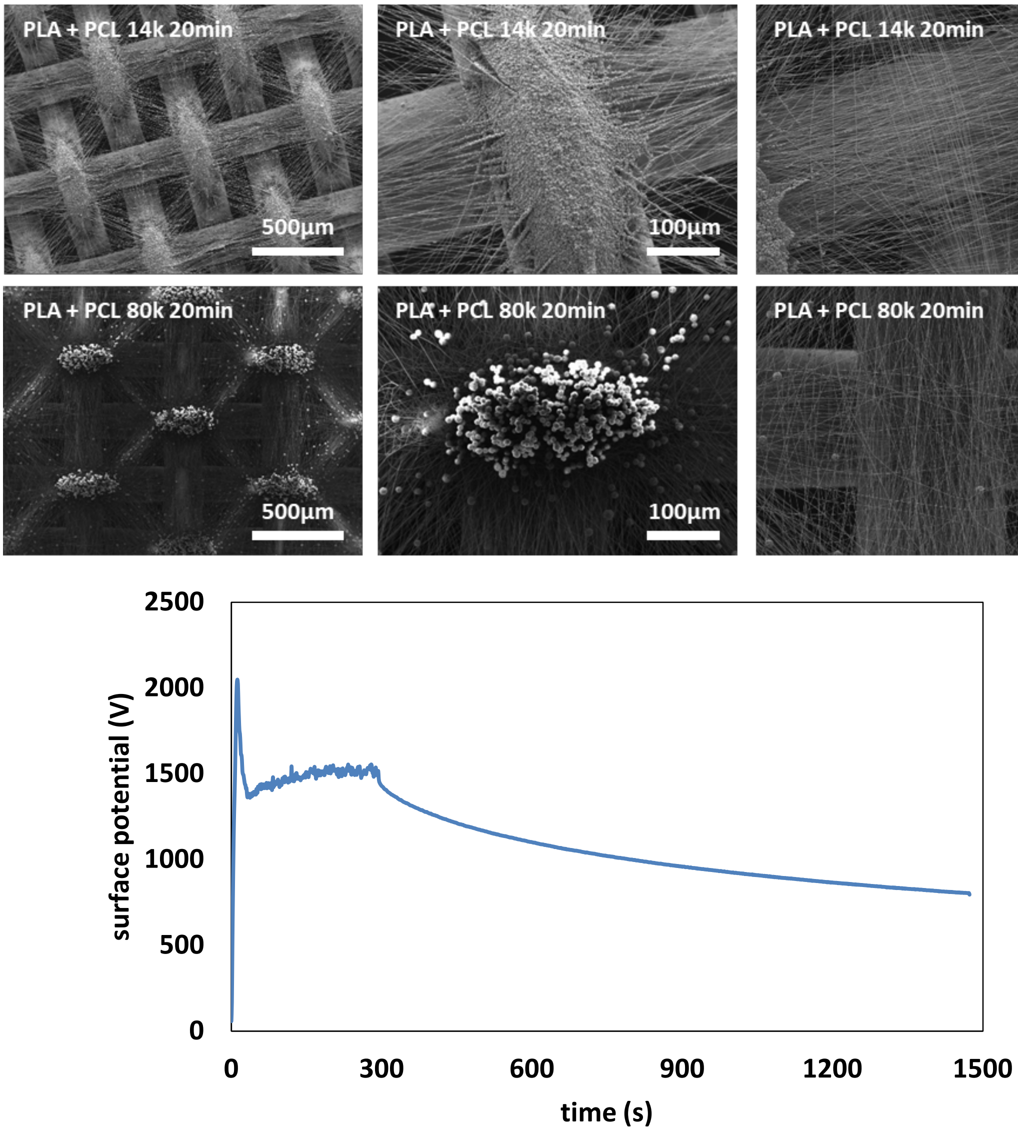

Fig. 4.35 morphologies of bilayer samples that PLA fibrous mats formed on the grid covered by PCL 14k and 80k particles generated in 20min, respectively and the graph of the dissipation of surface potential on suspended PLA fibers in 20min

The previous section explained the effect of density of suspended PLA fibers on the distribution of PCL particles, and proved that suspended PLA fibers in fewer amounts are able to control efficiently the deposition of PCL particles on specific areas. Here, we focus on the effect of the electrospraying time on the distribution of PCL particles. In this section, the processing time of electrospraying was increased to 20min. Fig. 4.35 presents the morphologies of bilayer samples generated by electrosparying PCL 14k and 80k particles in 20min on PLA fibers. Similar results are obtained for both kind of particles: PCL particles fall on the “attractive” areas of PLA fibers persistently after electrospraying 20min. It is shown that no PCL 14k particles are deposited on the suspended fibers after electrospraying 20min. In the case of PCL 80k particles, few of them are deposited on suspended PLA fibers. The controlled structure of bilayer samples generated in this section implied that electrostatic template effect induced by the surface potential on suspended PLA fibers can be maintained during 20min which was also proven by the graph showing the decay of the surface potential of PLA fibers in Fig. 4.35, the value still kept around 800V after decreasing from 1500V in 20min. Compared with the bilayer samples in Fig. 4.32 and Fig. 4.33, it is obvious from Fig. 4.35 that more PCL particles stacked on the targeted attractive areas. Such feature is of importance for the preparation of 3D structured scaffolds with a certain thickness.

4.3.3.5 Fabrication of multilayer samples by alternate PLA fibers and PCL particles deposition

In the previous section, the results proved that suspended PLA fibers in few amounts store efficiently the charges controlling the deposition of PCL particles on PLA fibers remarkably. Herein, in order to get 3D structured scaffolds with a certain thickness for potential biological applications, electrospinning and electrospraying was carried out alternately.

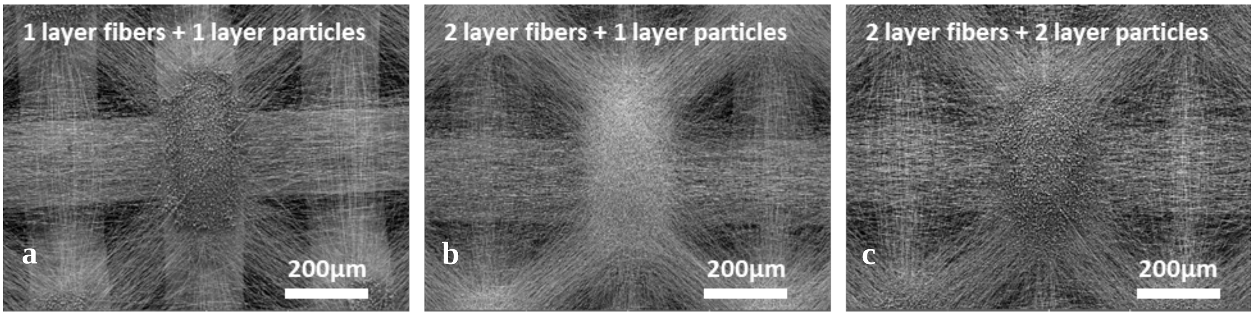

Fig. 4.36 SEM images of multilayer samples formed by coupling different layers of PLA fibers and PCL 14k particles (a: bilayer samples by coupling one layer of PLA fibers and one layer of PCL 14k particles; b: two layers of PLA fibers and one layer of PCL particles alternately; c: two layers of PLA fibers and two layers of PCL particles alternately)

Fig. 4.36 presented the morphologies of multilayer samples generated by two successive bilayers of PLA fibers and PCL 14k particles. The time for electrospinning and electrospraying were both 5min. Obviously, it was show in Fig. 4.36 b that the second layer of PLA fibers covered the first layer of PCL 14k particles fully after the second time of electrospinning on the first bilayer sample. The major portion of the second layer of PLA fibers still landed on the convex parts of the grid with suspended fibers appearing over the concave parts of the grid proving that PCL 14k particles “prolong” the effects of the protuberances of the grids. fibers. In addition, the alignment of fibers over the gap indicates that the electric field at the vicinity of grid is enough high to control the deposition of the second layer of PLA fibers, resulting in suspended PLA fibers keeping the surface potential. This latter offers a repulsive force to the falling PCL 14k particles which induce the formation of a novel stage of protuberances. The succeed in the fabrication of multilayer samples in this section indicates the feasibility to build 3D structured scaffold with a certain thickness by alternate deposition of PLA fibers and PCL 14k particles.

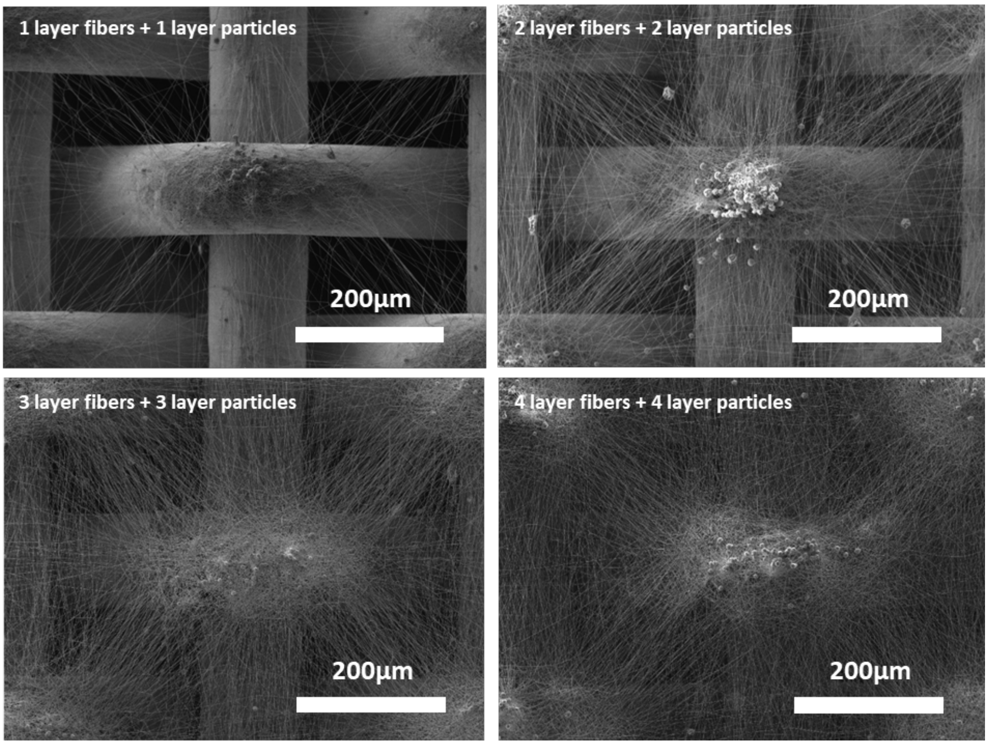

Fig. 4.37 SEM images of multilayer samples formed by coupling different layers of PLA fibers and PCL 80k particles (a: bilayer samples by coupling one layer of PLA fibers and one layer of PCL 80k particles; b: two layers of PLA fibers and two layers of PCL particles alternately; c: three layers of PLA fibers and three layers of PCL particles alternately; d: four layers of PLA fibers and four layers of PCL particles alternately)

In order to increase the efficiency of 3D structured scaffolds formation, the time for electrospinning and electrospraying were set to 150s and 300s, respectively. Fig. 4.37 shows the samples after the several steps of the process. It is revealed that all samples held a good morphology with spatial structures which implied efficient interactions between PCL 80k particles and suspended PLA fibers still existed after repeating electrospinning and electrospraying few times alternately.

Overall, the morphology of multilayer samples was well controlled after fabricating few layers of PLA fibers and PCL particles alternately on the grid. Thus, 3D scaffolds with specific spatial structures and thickness were achieved by controlling the accumulation and dissipation of surface charges during electrospinning and electrospraying.

4.3.3.6 Conclusion

After comparing the intensity of surface potential of suspended fibers generated from four types of polymer solutions, it is shown that high conductivity of polymer solution weakened the charge storage of fibers over the valley of the grid, resulting in poor repulsive force avoiding the controlled deposition of PCL particles. For example, compared with other three samples, alginate increases the ionic nature of PEO solution generating a highly charged jet under the electric field. However, due to the addition of alginate, the fast transfer of charges from suspended PEO/Alginate fibers to the ground occurs, resulting in the weak interactions between the falling PCL particles and the suspended PEO/Alginate fibers. As a result, the PCL particles deposited uniformly on the PEO/Alginate fibrous mats. The best controllability on the deposition of PCL particles came out on PLA fibers: the poor conductivity allows remaining efficiently the charges on suspended PLA fibers. Thus, the new coming PCL particles underwent a strong repulsive force from the suspended PLA fibers to be repelled to the “attractive” areas. Therefore, the selective distribution of PCL particles on PLA fibrous mats was achieved as a result. In addition, the strength of surface potential could be modified by changing the density of suspended fibers, the large density enhanced the charge release on suspended fibers leading to a poor control on the distribution of PCL particles. The interaction between the falling PCL particles and PLA fibers could be controlled during 20min. In the end, multilayered structured 3D scaffolds were prepared successfully by combining PLA fibers and PCL particles alternately on a grid collector, proving that the electrostatic template effect can be maintained along all the process of deposition of each layer.

4.4 Conclusion

In this chapter we designed a collector with one central adjustable gap in order to analyze the surface potential of suspended fibers. The results showed that the geometry of the collector had an obvious influence on the surface potential of suspended PLA. However, suspended PEO fibers fabricated under the same processing parameters held a much lower ability in charge storage. The intensity of surface potential held a positive correlation with the gap size. Regarding the charge release from the moment of stopping electrospinning, the dissipation rate was enhanced with extending the processing time which was attributed to the high density of the contact among suspended fibers stimulating the charge decay, this phenomenon happened in both suspended PLA fibers and suspended PEO fibers.

When bilayer samples are prepared by combining electrospun fibers and electrosprayed particles on a striated collector, it is proved that PEO fibers had no effect on the deposition of PCL14k particles due to from the low electric force of suspended PEO fibers avoiding repelling PCL14k particles. While suspended PLA fibers had a positive effect on the selective deposition of PCL particles.

Then, a grid collector with small size in the valleys and walls was used for the fabrication of structured composite scaffolds. Here, PLA fibers and PEO fibers as well as two other types of fibers made either of PLA/TEBAC or and PEO/Alginate were applied in this section to examine the effect of the conductivity on the controlled deposition of PCL particles. It indicates that high conductivity of polymer solution weakened the charge storage of fibers over the valley of the grid, resulting in poor repulsive force allowing an efficient controlled deposition of the PCL particles. Thanks to the low conductivity of the PLA solution, an optimum controllability on the deposition of PCL particles was observed. This effect was attributed to the fact that charges remain efficiently and for long times on suspended PLA fibers. Thus, the in-coming PCL particles underwent a strong repulsive force induced by the suspended PLA fibers repelling them to the attractive walls of the collectors. Such interactions between the falling PCL particles and the deposited PLA fibers can be maintained during 20min. In the end, multilayer samples were prepared successfully by the alternate deposition of PLA fibers and PCL particles on the grid collector.

References

[1] D. H. Reneker and A. L. Yarin, “Electrospinning jets and polymer nanofibers,” *Polymer*, vol. 49, no. 10, pp. 2387–2425, May 2008, doi: 10.1016/j.polymer.2008.02.002.

[2] D. Li and Y. Xia, “Electrospinning of Nanofibers: Reinventing the Wheel?,” *Advanced Materials*, vol. 16, no. 14, pp. 1151–1170, Jul. 2004, doi: 10.1002/adma.200400719.

[3] D. H. Reneker and I. Chun, “Nanometre diameter fibres of polymer, produced by electrospinning,” *Nanotechnology*, vol. 7, no. 3, pp. 216–223, Sep. 1996, doi: 10.1088/0957-4484/7/3/009.

[4] F. Hejazi and H. Mirzadeh, “Novel 3D scaffold with enhanced physical and cell response properties for bone tissue regeneration, fabricated by patterned electrospinning/electrospraying,” *Journal of Materials Science: Materials in Medicine*, vol. 27, no. 9, Sep. 2016, doi: 10.1007/s10856-016-5748-8.

[5] A. Garcia Garcia *et al.*, “Poly(ε-caprolactone)/Hydroxyapatite 3D Honeycomb Scaffolds for a Cellular Microenvironment Adapted to Maxillofacial Bone Reconstruction,” *ACS Biomaterials Science & Engineering*, vol. 4, no. 9, pp. 3317–3326, Sep. 2018, doi: 10.1021/acsbiomaterials.8b00521.

[6] Q. Cheng, B. L.-P. Lee, K. Komvopoulos, and S. Li, “Engineering the Microstructure of Electrospun Fibrous Scaffolds by Microtopography,” *Biomacromolecules*, vol. 14, no. 5, pp. 1349–1360, May 2013, doi: 10.1021/bm302000n.

[7] H. Xu *et al.*, “Hierarchically micro-patterned nanofibrous scaffolds with a nanosized bio-glass surface for accelerating wound healing,” *Nanoscale*, vol. 7, no. 44, pp. 18446–18452, 2015, doi: 10.1039/C5NR04802H.

[8] N. Pan, J. Qin, P. Feng, and B. Song, “Window screen inspired fibrous materials with anisotropic thickness gradients for improving light transmittance,” *Nanoscale*, vol. 11, no. 28, pp. 13521–13531, 2019, doi: 10.1039/C9NR02810B.

[9] J. Xu *et al.*, “Roll-to-Roll Transfer of Electrospun Nanofiber Film for High-Efficiency Transparent Air Filter,” *Nano Letters*, vol. 16, no. 2, pp. 1270–1275, Feb. 2016, doi: 10.1021/acs.nanolett.5b04596.

[10] R. Chen *et al.*, “Transparent thermoplastic polyurethane air filters for efficient electrostatic capture of particulate matter pollutants,” *Nanotechnology*, vol. 30, no. 1, p. 015703, Jan. 2019, doi: 10.1088/1361-6528/aae611.

[11] M. Shang, W. Wang, L. Zhang, S. Sun, L. Wang, and L. Zhou, “3D Bi_2WO_6/TiO_2 Hierarchical Heterostructure: Controllable Synthesis and Enhanced Visible Photocatalytic Degradation Performances,” *The Journal of Physical Chemistry C*, vol. 113, no. 33, pp. 14727–14731, Aug. 2009, doi: 10.1021/jp9045808.

[12] D. Li, Y. Wang, and Y. Xia, “Electrospinning of Polymeric and Ceramic Nanofibers as Uniaxially Aligned Arrays,” *Nano Letters*, vol. 3, no. 8, pp. 1167–1171, Aug. 2003, doi: 10.1021/nl0344256.

[13] H. Yan, L. Liu, and Z. Zhang, “Alignment of electrospun nanofibers using dielectric materials,” *Applied Physics Letters*, vol. 95, no. 14, p. 143114, Oct. 2009, doi: 10.1063/1.3242378.

[14] V. Chaurey, P.-C. Chiang, C. Polanco, Y.-H. Su, C.-F. Chou, and N. S. Swami, “Interplay of Electrical Forces for Alignment of Sub-100 nm Electrospun Nanofibers on Insulator Gap Collectors,” *Langmuir*, vol. 26, no. 24, pp. 19022–19026, Dec. 2010, doi: 10.1021/la102209q.

[15] R. Jalili, M. Morshed, and S. A. H. Ravandi, “Fundamental parameters affecting electrospinning of PAN nanofibers as uniaxially aligned fibers,” *Journal of Applied Polymer Science*, vol. 101, no. 6, pp. 4350–4357, Sep. 2006, doi: 10.1002/app.24290.

[16] D. Li, G. Ouyang, J. T. McCann, and Y. Xia, “Collecting Electrospun Nanofibers with Patterned Electrodes,” *Nano Letters*, vol. 5, no. 5, pp. 913–916, May 2005, doi: 10.1021/nl0504235.

[17] A. Zucchelli, D. Fabiani, C. Gualandi, and M. L. Focarete, “An innovative and versatile approach to design highly porous, patterned, nanofibrous polymeric materials,” *Journal of Materials Science*, vol. 44, no. 18, pp. 4969–4975, Sep. 2009, doi: 10.1007/s10853-009-3759-2.

[18] D. Zhang and J. Chang, “Electrospinning of Three-Dimensional Nanofibrous Tubes with Controllable Architectures,” *Nano Letters*, vol. 8, no. 10, pp. 3283–3287, Oct. 2008, doi: 10.1021/nl801667s.

[19] P. S. Ginestra, S. Pandini, A. Fiorentino, P. Benzoni, P. Dell’Era, and E. Ceretti, “Microstructured scaffold for guided cellular orientation: Poly(ε-caprolactone) electrospinning on laser ablated titanium collector,” *CIRP Journal of Manufacturing Science and Technology*, vol. 19, pp. 147–157, Nov. 2017, doi: 10.1016/j.cirpj.2017.08.002.

[20] H. Xu, W. Cui, and J. Chang, “Fabrication of patterned PDLLA/PCL composite scaffold by electrospinning,” *Journal of Applied Polymer Science*, vol. 127, no. 3, pp. 1550–1554, Feb. 2013, doi: 10.1002/app.37505.

[21] S. Zhao, Q. Zhou, Y.-Z. Long, G.-H. Sun, and Y. Zhang, “Nanofibrous patterns by direct electrospinning of nanofibers onto topographically structured non-conductive substrates,” *Nanoscale*, vol. 5, no. 11, p. 4993, 2013, doi: 10.1039/c3nr00676j.

[22] C.-C. Kuo, C.-T. Wang, and W.-C. Chen, “Highly-Aligned Electrospun Luminescent Nanofibers Prepared from Polyfluorene/PMMA Blends: Fabrication, Morphology, Photophysical Properties and Sensory Applications,” *Macromolecular Materials and Engineering*, vol. 293, no. 12, pp. 999–1008, Dec. 2008, doi: 10.1002/mame.200800224.

[23] J. M. Deitzel, J. Kleinmeyer, D. Harris, and N. C. Beck Tan, “The effect of processing variables on the morphology of electrospun nanofibers and textiles,” *Polymer*, vol. 42, no. 1, pp. 261–272, Jan. 2001, doi: 10.1016/S0032-3861(00)00250-0.

[24] D. Ahirwal, A. Hébraud, R. Kádár, M. Wilhelm, and G. Schlatter, “From self-assembly of electrospun nanofibers to 3D cm thick hierarchical foams,” *Soft Matter*, vol. 9, no. 11, p. 3164, 2013, doi: 10.1039/c2sm27543k.

[25] S. Nedjari, G. Schlatter, and A. Hébraud, “Thick electrospun honeycomb scaffolds with controlled pore size,” *Materials Letters*, vol. 142, pp. 180–183, Mar. 2015, doi: 10.1016/j.matlet.2014.11.118.

[26] G. Yan *et al.*, “Self-Assembly of Electrospun Polymer Nanofibers: A General Phenomenon Generating Honeycomb-Patterned Nanofibrous Structures,” *Langmuir*, vol. 27, no. 8, pp. 4285–4289, Apr. 2011, doi: 10.1021/la1047936.

[27] N. Lavielle, A. Hébraud, G. Schlatter, L. Thöny-Meyer, R. M. Rossi, and A.-M. Popa, “Simultaneous Electrospinning and Electrospraying: A Straightforward Approach for Fabricating Hierarchically Structured Composite Membranes,” *ACS Applied Materials & Interfaces*, vol. 5, no. 20, pp. 10090–10097, Oct. 2013, doi: 10.1021/am402676m.

[28] C. R. Wittmer, A. Hébraud, S. Nedjari, and G. Schlatter, “Well-organized 3D nanofibrous composite constructs using cooperative effects between electrospinning and electrospraying,” *Polymer*, vol. 55, no. 22, pp. 5781–5787, Oct. 2014, doi: 10.1016/j.polymer.2014.08.044.

[29] A. Garcia Garcia *et al.*, “Poly(ε-caprolactone)/Hydroxyapatite 3D Honeycomb Scaffolds for a Cellular Microenvironment Adapted to Maxillofacial Bone Reconstruction,”

ACS Biomaterials Science & Engineering, vol. 4, no. 9, pp. 3317–3326, Sep. 2018, doi: 10.1021/acsbiomaterials.8b00521.

[30] H. Yan, L. Liu, and Z. Zhang, “Alignment of electrospun nanofibers using dielectric materials,” *Applied Physics Letters*, vol. 95, no. 14, p. 143114, Oct. 2009, doi: 10.1063/1.3242378.

[31] H. Ma, C. Burger, B. S. Hsiao, and B. Chu, “Ultra-fine cellulose nanofibers: new nano-scale materials for water purification,” *Journal of Materials Chemistry*, vol. 21, no. 21, p. 7507, 2011, doi: 10.1039/c0jm04308g.

[32] J.-A. Park and S.-B. Kim, “Preparation and characterization of antimicrobial electrospun poly(vinyl alcohol) nanofibers containing benzyl triethylammonium chloride,” *Reactive and Functional Polymers*, vol. 93, pp. 30–37, Aug. 2015, doi: 10.1016/j.reactfunctpolym.2015.05.008.

[33] K. Nartetamrongsutt and G. G. Chase, “The influence of salt and solvent concentrations on electrospun polyvinylpyrrolidone fiber diameters and bead formation,” *Polymer*, vol. 54, no. 8, pp. 2166–2173, Apr. 2013, doi: 10.1016/j.polymer.2013.02.028.

General conclusion

The objective of this thesis was to study the electric charges carried by fibers during and after their processing by electrospinning and how these charges may affect the surface potential and furthermore, the resulting morphology of the produced fibrous mat. In this perspective, two cases were deeply studied: (i) the surface potential formation kinetic and decay of non-woven mat produced on a flat collector and (ii) the formation kinetic of the electrostatic template generated on electrospun fibers deposited on patterned collectors.

In a first part, we investigated the charge density carried by the single PLA electrospun fiber thanks to a novel approach providing details on the effects of various processing conditions (polymer concentration, applied voltage, conductivity, ambient humidity and flow rate) on the rate of charge accumulation and the formation velocity of fibers. The amount of charges carried by PEO, PEO/Alginate fibers and PCL particles were measured as well. By the new approach consisting in the connection of a capacitor between the collector and the ground, it allowed to keep and measure all charges on the surface of the collector. The total amount of charges carried by a single fiber or an individual particle was thus calculated precisely. In addition, the length of fibers and the number of particles deposited on the collector were measured by SEM allowing an accurate estimation of the charge density of fibers and particles. It was proven that the charge density of fibers held a positive correlation with the permittivity of solvent used in polymer solution. Fibers fabricated from a PEO/H_2O solution presented a higher charge density than those prepared from a PLA/DCM/DMF solution, the addition of alginate and TEBAC increased the amount of charge carriers leading to a dramatic increase of the charge density of PEO/Alginate and PLA/TEBAC respectively. Although the increased conductivity of the solution enhanced the charge density on fibers, high conductivity also induced efficient charge transfer from fibers to the grounded collector. In addition, the linear charge density of a single PLA fiber was enhanced with high polymer concentration, large solution conductivity, low applied voltage, high ambient humidity and low solution feeding rate. The results obtained in this part are of prime importance to better anticipate the building of structured fibrous membranes by alternate electrospinning and electrospraying on patterned collectors for which the formation of an electrostatic template is the necessary condition.

In-situ charging of fibrous mats during their fabrication by electrospinning is an efficient way which prolong remarkably the release time of bulk charges. Thus, the in-situ charging kinetic by electrospinning as well as the charge release kinetic were studied deeply by the online measurement of the mat surface potential in the case of simple electrospinning on flat collector. In the same time, the electric current was measured as well during the process of electrospinning. The result proved that the intensity of the current was affected by the electrospun jet state, the surface potential was more related to the internal porous structure of fibrous mats. Regarding the accumulation of surface potential during electrospinning, fibers generated in different conditions held different morphologies in terms of fiber diameter, quality of the fiber-fiber contact points, etc. A model was proposed in order to get more insight into the electrostatic behavior of the mat during its fabrication and after stopping electrospinning. Thanks to the model, it is shown that the measurement of the surface potential during in-situ charging by electrospinning is characterized by a characteristic time τ which can be related to the electrical characteristics at the different length scales: (i) the pore, (ii) the elementary layer having the surface of the membrane and the thickness of one pore and (iii) the whole membrane under building. It was shown that a scaling law is able to predict the variation in fiber diameter as a function of the measured characteristic time. The study of the surface potential decay after stopping electrospinning allows the fine dissociation of the kinetic in three fundamental mechanisms of charge release. The rapid charge release with only few seconds occurring on the topmost surface of the mat caused the initial stage, then a relative slow decay arranging from tens of seconds up to more than one hundred of seconds results from the charge dissipation of the pores of the mats. And the dissipation of charges which are trapped in the bulk of the fibers form the third stage which was at least one order of magnitude higher than the medium time. The persistence of charge decay, especially the second and third stages, are of importance for the building of a constant electrostatic template improving the construction of composite scaffolds with a controlled structure. Finally, in this part, it was shown for the first time that the measurement of the surface potential, thanks to the use of an electrostatic voltmeter, is a simple method which gives an accurate information at the local scale of the pore and fiber diameter of an electrospun mat. Such a method should allow the detection of variations in the porous morphology of a mat during its fabrication. Furthermore, in combination with the measurement of the current, it is an efficient and complementary method to get an online monitoring of the process of electrospinning.

In the last part of the thesis, we focused on the surface potential generated by suspended fibers. Such study is of prime importance for the controlled elaboration of structured fibrous membranes. We designed an experiment allowing a deep understanding of the formation kinetic of the surface potential of suspended fibers. This experiment consisted in the electrospinning on a rotating collector with a single gap continuously adjustable from 0 to 10 mm. Furthermore, a model was proposed to explain the formation kinetic of the surface potential during electrospinning on a single gap. The results show that the deposition of suspended electrospun fibers is characterized by a characteristic time which sharply decreases at the first times of production before reaching a plateau value. It was also shown that this characteristic time is attributed to the density of contacts between the suspended fibers. After a sharp increase of the surface potential controlled by the rate of incoming fibers, a decrease of the surface potential was always observed due to the increasing number of crossing fibers formed over the gap. Then, a plateau regime is observed. These results were used in the second section of this part to get more insight into the controlled fabrication of structured composites by electrospinning and electrospraying on patterned collectors. A strong electrostatic template could be formed when suspended fibers having a low density of crossing fibers is achieved. This was proven by the fact that PCL particles are selectively deposited on PLA fibrous mats formed on patterned collector. Suspended PLA fibers could generate repulsive force leading to change the trajectory and thus drive the deposition of PCL particles. This effect became gradually worse with the enlargement of the density of suspended fibers resulting from faster charge release. By modifying the processing time of electrospinning to control the density of suspended PLA fibers, the results showed that the electrostatic template effect experienced by the falling PCL particles could be kept during 20min. Moreover, the selective deposition could be repeated after producing few layers of PLA fibers and PCL particles alternately. Hence, 3D composite scaffolds with controlled spatial structures were successfully obtained by the alternate deposition of PLA fibers and PCL particles on a patterned collector.

Actually, the work is not end. As mentioned in the beginning, linear charge density of PLA fibers showed a high value in the condition of high polymer concentration, low applied voltage, high ambient humidity and low solution feeding rate. Applying these parameters in preparing patterned scaffolds might induce better electrostatic template to facilitate the construction of 3D composite scaffolds with controlled special structures. In order to enhance the spatial structure, the deposition time of fibers and particles should be studied further. Additionally, various raw materials can be applied by this approach to enlarge the category of products, making it more prospective in targeted fields such as tissue engineering, filtration, wound healing, etc.

UNIVERSITÉ DE STRASBOURG

École doctorale
Physique, chimie-physique
ED 182
Université de Strasbourg

Meng LIANG

Spatial organization of electric charges and discharge kinetics during electrospinning: application to the elaboration of 3D structured nanofibrous materials

Résumé

L’electrospinning est un procédé permettant la production de matériaux nanofibreux sous l'action d'un champ électrostatique intense. Au cours du procédé, une solution de polymère en régime semi-dilué enchevêtré est introduite dans une aiguille métallique soumise à un potentiel électrique élevé. Lorsque le champ électrique entre l'aiguille et une contre-électrode métallique reliée à la terre électrique, appelée collecteur, est suffisamment fort (de l’ordre de 1 kV/cm), un jet de la solution est violemment éjecté vers le collecteur. Pendant le vol entre l'aiguille et le collecteur, le jet est soumis à des instabilités électro-hydrodynamiques qui provoquent des mouvements de fouet favorisant l'évaporation du solvant et la réduction du diamètre. Après un temps de vol de quelques ms, une nanofibre polymère solide est déposée sur le collecteur sous la forme d’un scaffold non-tissé. Lorsque la nanofibre chargée électriquement est mise en contact avec le collecteur, elle se décharge progressivement. La cinétique de la décharge électrique mais aussi la façon dont les charges sont réparties à la surface du matériau pendant le procédé déterminent l'organisation et la structuration 3D finale du scaffold.
Les travaux de cette thèse ont consisté à mesurer les charges électriques portées par la nanofibre lors de son dépôt mais aussi à étudier comment ces charges se dissipent dans la membrane et dans le temps, une fois la nanofibre déposée. Cette étude a ensuite été appliquée au développement de scaffolds nanofibreux de structure contrôlée en 3D.

Mots-clés : *electrospinning, electrospraying, densité de charge, potentiel de surface, scaffolds structurés 3D*

Abstract

Electrospinning is a process allowing the production of nanofibrous materials under the action of an intense electrostatic field. During the process, a polymer solution in a semi-diluted entangled regime is fed to a metal needle submitted to a high electrical potential. When the electric field between the needle and a metal counter electrode connected to the electrical ground, called a collector, is strong enough (i.e. about 1 kV/cm), a jet of the solution is violently ejected towards the collector. During the flight between the needle and the collector, the jet is subjected to electro-hydro-dynamic instabilities resulting in whipping movements that promote solvent evaporation and diameter reduction. After a flight time of a few ms, a solid polymer nanofiber in the form of a non-woven membrane is deposited on the collector. When the electrically charged nanofibre is brought into contact with the collector, it gradually discharges. The kinetics of electrical discharge but also the way in which the charges are distributed on the surface of the material during the process determine the organization and the final 3D structuring of the membrane.
The work of this thesis consisted in measuring the electrical charges carried by the nanofibre during its deposition but also in studying how these charges dissipate in the membrane and over time once the nanofibre has been deposited. This study was then applied to develop nanofiber membranes with a controlled 3D structure.

Keywords: *electrospinning, electrospraying, charge density, surface potential, 3D structured scaffold*